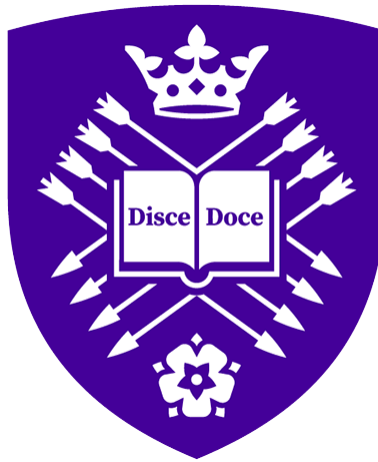


University of Sheffield

**Single Scatter Neutron Background
Estimates using Multiple Scatters of
Neutrons in the LUX-ZEPLIN
Experiment**



Jonathan Orpwood

Supervisor: Dan Tovey

School of Mathematical and Physical Sciences

March 25, 2025

Declaration

All sentences or passages quoted in this document from other people's work have been specifically acknowledged by clear cross-referencing to author and work.

The personal contribution of the author to the work described in this thesis was as follows. The author was responsible for all development of the $\Delta\chi^2$ analysis described in chapter 3, but the photopeak measurements used for the S1 S2 anti-correlation work, discussed in section 3.3.1, were made by G. Pereira, with only some verification, detailed in this thesis, performed by the author. For the $\Delta\chi^2$ SS neutron estimates discussed in chapters 4 and 6, all analysis steps discussed in the thesis were carried out by the author. The author did not run the WS2024 neutron background simulation (this work was done by A. Usón), and in some instances across the two analyses cuts were pre-applied to datasets before use by the author (by E. Fraser).

For the LZ WS2024 SS neutron estimate discussed in chapter 5, the author contributed to the selection of MS events from WIMP search data, by use of the $\Delta\chi^2$ method, in collaboration with E. Fraser.

In addition to the work described in this thesis, the author also carried out other work during the course of their PhD as part of the LZ collaboration, some of which will be detailed here. Firstly, PMT monitoring shifts were undertaken throughout the PhD, and with an increased frequency during the author's time at SURF, working with the hardware of the detector and its subsystems. This work comprised a number of different tasks across the different subsystems, and included the following: carrying out testing of all backing pumps used for the vacuum systems, leak checking vacuum spaces to ensure good vacuums were maintained, assisting with both calibration source deployment (CSD) and source injection calibrations, helping to maintain the infrastructure of the purified water system, and assisting with the maintenance of the detector electronics. This time spent on site, along with the increased cadence of PMT shifts whilst there, meant that the author was given the role of PMT shift supervisor. For the last 1.5 years of this PhD, the author has supervised numerous weeks of PMT shifts and remained on-call in case of any detector issues (on several occasions being one of the first responders).

Finally, throughout the PhD the author also worked occasionally with the simulations group, running data-simulation comparisons for different calibrations sources which the simulations group would use to improve the tuning of the detector simulation.

Name: Jonathan Orpwood

Signature:

Date: 25/03/2025

Acknowledgments

The work presented in this thesis would not have been possible had it not been for the support and work of countless people both in and outside of the LZ collaboration, and I am extraordinarily grateful to all of those who made this PhD even remotely possible.

First and foremost, I would like to thank my supervisor Dan Tovey for his unwavering support and guidance throughout the last three and a half years. I always felt supported and that I could be open with you about any part of the analysis that was playing on my mind and causing me more stress than may have been strictly necessary. I always left our meetings feeling supported and reassured, and for this I am extremely grateful.

I would also like to thank everyone in the LZ collaboration to whom I spoke about any aspect of this analysis, as being able to talk ideas through and gain different viewpoints was truly invaluable and was a huge advantage of working in such a friendly, helpful collaboration. In particular though, Ewan Fraser was a colossal support and provided enormous amounts of guidance, especially throughout WS2024. Thank you for always being up for a chat about whatever analysis rabbit hole I had got myself stuck down, and replying to my regular questions on slack. Thank you as well to Tom Rushton who acted as a local source of endless wisdom about completing a PhD in LZ and at the University of Sheffield, and particularly regarding my LTA, going out to South Dakota to work on-site with the detector.

On which note, I cannot thank the on-site LZ team at SURF enough for how welcoming and accommodating you all were for the four months that I spent out there. I felt like I learned so much about the detector, and also quite a lot about life in South Dakota! Gavin, Julia, and Alex are all integral to the daily operations of LZ, but beyond that are just really fun people to spend time with.

Thank you as well to Jack who has been a constant comfort and reassurance as we progressed through our PhDs at Sheffield. I really appreciated having someone in the same position as me that I could talk to about whatever was stressing me out at the time, and you never failed to put things in context for me and help me see that things were usually ok. I was always smiling more on a Friday morning than I was on a Thursday afternoon thanks to our Thursday meet ups!

I would of course like to thank my parents for their continued support while I have been in Sheffield, and for providing dinner on Friday nights!

Finally, I'd like to thank Bekah for putting up with me throughout the highs and lows of the PhD process. It's hard to overstate just how grateful I am and how lucky I feel.

Abstract

Dark matter constitutes around 85% of the matter in the universe, and yet its exact nature remains unknown. Numerous experiments across the world have sought to discover either direct or indirect evidence for a viable dark matter candidate. The LUX-ZEPLIN (LZ) experiment uses a dual-phase xenon time projection chamber to search for direct evidence of WIMP dark matter. In rare event searches, comprehensive understanding of background signals is essential, and a particularly important background is neutrons, since they can produce a signal in the detector that is indistinguishable from a WIMP. However, unlike WIMPs neutrons have a high probability of scattering multiple times in the detector, and this can be used to infer the rate at which they would be expected to produce WIMP-like single scatter events. In this work, the multiple scatters of neutrons in LZ are studied in depth with the aim of being able estimate the number of neutrons that remain in the WIMP search data.

Contents

1	Introduction	1
1.1	A History of Dark Matter	2
1.1.1	Galaxy Clusters	2
1.1.2	Galactic Rotation	3
1.1.3	The Bullet Cluster	5
1.1.4	Cosmic Microwave Background	8
1.1.5	Big Bang Nucleosynthesis	11
1.2	Properties of Dark Matter	14
1.3	Dark Matter Candidates	15
1.3.1	MACHOs	16
1.3.2	WIMPs	16
1.3.3	Further Dark Matter Candidates	18
1.4	Searching for Dark Matter	19
1.4.1	Collider Searches	20
1.4.2	Indirect Detection	20
1.4.3	Direct Detection	21
2	The LUX-ZEPLIN (LZ) Detector	25
2.1	The Time Projection Chamber (TPC)	26
2.2	The Skin	28
2.3	The Outer Detector (OD)	30
2.4	Electric Fields in LZ	31
2.5	Xenon Circulation System	33
2.6	Cryogenics and Vacuum Systems	34
2.7	Electronics	35
2.8	Calibrations	36
2.8.1	CSDs	36
2.8.2	Alpha Neutron Sources	37
2.8.3	Source Injection	38

2.8.4	DD Neutron Generation	39
2.9	Interpreting Signals	40
2.9.1	Waveforms and Triggering	41
2.9.2	LZAP	43
2.9.3	Reduced Quantities (RQs)	44
2.10	Simulations	46
2.10.1	NEST	46
2.10.2	BACCARAT	47
2.10.3	LZLAMA	48
2.11	Background Signals	48
2.11.1	Electron Recoil Events	48
2.11.2	Accidental Coincidences	51
2.11.3	Neutrinos	54
2.11.4	Neutrons	55
2.12	Statistics	57
2.12.1	χ^2 Tests	57
2.12.2	PLR Tests	59
2.13	LZ Performance Parameters	60
3	Multiple Scatter Neutrons	61
3.1	Neutrons	61
3.1.1	Outer Detector and Skin Vetoes	61
3.1.2	Multiple Scatters to Estimate Single Scatters	63
3.2	The Multiple Scatter Problem	64
3.3	The $\Delta\chi^2$ Method	67
3.3.1	Incorporating S1 S2 Correlations into the $\Delta\chi^2$ Parameter	71
3.4	Multiplicity of MS Events	81
3.5	Previous Recombination Fluctuation Studies	82
4	WIMP Search 2022 Neutron Single Scatter Estimate	86
4.1	LZ WS2022	86
4.2	Analysis Cuts for the $\Delta\chi^2$ SS Neutron Estimate	87
4.2.1	Fiducial Volume	88
4.2.2	Field Cage Resistor Cut	91
4.2.3	Region of Interest	92
4.2.4	OD and Skin Veto Cuts	92
4.2.5	Accidental Coincidence Cuts	92
4.2.6	Electron Train Veto	93

4.2.7	Muon Cut	95
4.2.8	Exclusion Periods	95
4.2.9	OD Burst Cut	96
4.2.10	Additional Cuts	96
4.3	NR and ER Band Definitions	96
4.4	Exploring $\Delta\chi^2$ Space	100
4.4.1	The Band Above the ER Band	100
4.4.2	The Band Below the NR Band	101
4.4.3	Low Energy Cluster of Events	104
4.4.4	'Fish Bone' Structure	104
4.5	Neutron Background Simulation SS/MS Ratio	108
4.6	Correcting SS/MS Ratio Differences in Simulation and Data	109
4.7	Multiple Scatter Neutron Candidates in Data	112
4.8	WS2022 $\Delta\chi^2$ SS Neutron Estimate	116
4.9	Choice of Neutron Interaction Cross-Section Library	117
5	LZ WIMP Search 2024 Single Scatter Neutron Estimate	119
5.1	Differences Between the LZ and $\Delta\chi^2$ Single Scatter Neutron Estimates	120
5.2	Use of the $\Delta\chi^2$ Method	123
5.3	Multiple Scatter Neutron Candidates in Data	125
5.4	Single Scatter Neutron Estimate	125
6	$\Delta\chi^2$ WIMP Search 2024 Neutron Single Scatter Estimate	129
6.1	$\Delta\chi^2$ Update	129
6.2	Analysis Cuts for the $\Delta\chi^2$ SS Neutron Estimate	130
6.2.1	Fiducial Volume	131
6.2.2	Field Cage Resistor Cut	132
6.2.3	Region of Interest	132
6.2.4	OD and Skin Veto Cuts	133
6.2.5	Ghost Train Veto	133
6.2.6	PMT Trip Cut	133
6.2.7	High SPE Rate Cut	134
6.2.8	Additional Cuts	134
6.2.9	Accidental Coincidences	134
6.3	NR and ER Band Definitions	134
6.4	Neutron Background Simulation SS/MS Ratio	140
6.5	Correcting SS/MS Ratio Differences in Simulation and Data	144
6.5.1	SS Energy Definition Investigation	146

6.6	Multiple Scatter Neutron Candidates in Data	148
6.7	WS2024 $\Delta\chi^2$ SS Neutron Estimate	154
6.8	Choice of Neutron Interaction Cross-Section Library	155
6.9	Further $\Delta\chi^2$ Method Optimisation Studies	160
7	Conclusion	169
7.1	$\Delta\chi^2$ Method	169
7.2	WS2022 SS Neutron Estimate	170
7.3	WS2024 SS Neutron Estimate	170
7.4	WS2022, WS2024 and Implications for Future LZ Runs	172
7.5	Future Work	173
	Appendices	187
A	$\Delta\chi^2$ Method Technical Details	188
A.1	Python	188
A.2	C++	196
B	Derivation of the $\sigma_m(S1)$, $\sigma_m(S2)$, and σ_c Equations	210

List of Figures

1.1	Measurements of the rotation curve of the Andromeda (M31) galaxy.	4
1.2	Geometric diagram of gravitational lensing.	5
1.3	False colour composite image of the Bullet Cluster.	7
1.4	Illustration of the history of the Universe as observed by looking out to greater distances.	8
1.5	Mapping of the temperature anisotropy of the CMB across the sky by the Planck telescope	9
1.6	CMB anisotropy shown by temperature fluctuations as a function of angular scale. .	11
1.7	Primordial abundance with respect to baryon-photon ratio η , (or equally the baryon density, $\Omega_b h^2$) for ${}^4_2\text{He}$, ${}^2_1\text{H}$ (alternatively referred to as deuterium, D), ${}^3_2\text{He}$, and ${}^7_3\text{Li}$	13
1.8	Diagram illustrating the freeze-out process in the early Universe.	15
1.9	Illustration of the different approaches to detecting dark matter.	19
2.1	Diagram of the LZ detectors.	25
2.2	Diagram illustrating how signals are generated in a dual-phase noble element time projection chamber.	27
2.3	NR and ER calibration data events illustrating the power to differentiate events by their position in $\log(\text{S2c})$ vs. S1c space.	29
2.4	Visualisation of the dome and lower side sections of the Skin veto detector, along with the mounting of the Skin PMTs in these regions.	29
2.5	Layout of the outer detector system used in LZ.	30
2.6	Diagram illustrating the position of the electrode grids in LZ and the resultant regions of electric field.	32
2.7	Cutaway of the LZ TPC, with the flow paths and circulation system elements indicated.	34
2.8	Diagram of the signal processing for the TPC PMTs.	35
2.9	Design of the CSD system.	37
2.10	The spatial distribution, after analysis cuts, of WS2024 SS AmLi calibration data, with the source lowered to 700 mm in the CSDs.	38

2.11	The spatial distribution of WS2024 SS DD calibration data, after analysis cuts. . . .	41
2.12	Examples of the typical shapes of S1, S2, SPE, and SE pulses in a dual-phase TPC. . . .	42
2.13	Example waveform for an SS event containing an S1, an S2, and multiple SEs and SPEs.	43
2.14	The light and charge yields, as functions of recoil energy, produced by NEST for both NRs and beta ERs.	47
2.15	U-238 decay chain that produces Rn-222, along with subsequent decays.	50
2.16	Maximum drift time of 10 runs of WS2022 MS data with no analysis cuts applied, shown with respect to the UDT limit, the pre-trigger window, and the post-trigger window.	51
2.17	Visualisation of the neutrino fog relative to exclusion limits set by experiments preceding LZ.	54
2.18	The χ^2 distribution for different numbers of degrees of freedom, k	58
3.1	DD and Th-232 simulated MS data illustrating the overlapping of the MS NR and ER bands in $\log(S2c)$ vs. S1c space.	65
3.2	Total $\log(S2c)$ value and S1c value as a function of the number of scatters for WS2022 MS DD NR calibration data, with the mean value for each number of scatters indicated.	66
3.3	Leakage of simulated Th-232 MS ER events into the MS NR band in $\log(S2c)$ vs. S1c space as a function of S1c.	67
3.4	Flowchart illustrating the $\Delta\chi^2$ analysis method.	68
3.5	WS2024 photopeak data within the range of $0 \text{ phd} < S1c < 2000 \text{ phd}$, $2.5 < \log(S2_{bc} / \text{phd}) < 5.5$	73
3.6	Verification of the S1c, $S2_{bc}$, and electron equivalent energy measurements of the 40.95 keV Kr-83m photopeak from WS2024 data.	75
3.7	Verification of the S1c, $S2_{bc}$, and electron equivalent energy measurements of the 163.780 keV Xe-131m photopeak from WS2024 data.	76
3.8	Verification of the S1c, $S2_{bc}$, and electron equivalent energy measurements of the 236.192 keV Xe-127 + Xe-129m photopeak from WS2024 data.	77
3.9	Distribution of the resolution of $\sigma_m(S1c)$ as a function of the mean S1c value for WS2024 photopeaks, fitted with the standard calorimeter resolution function.	79
3.10	Distribution of the resolution of $\sigma_m^2(S2_{bc})$ as a function of the mean $S2_{bc}$ value for WS2024 photopeaks, fitted with the square of the standard calorimeter resolution function.	80
3.11	Distribution of σ_c as a function of the number of ions for WS2024 photopeaks, fitted with a polynomial with non-zero coefficients for powers of 1/2 and 1, and with a tanh function of that polynomial.	81

3.12	Multiplicity of DD calibration events in WS2024 after data quality cuts, shown as a fraction of the total number of events.	83
3.13	Recombination fluctuations, σ_r , plotted as a function of the number of ions, as measured by the LUX collaboration.	84
3.14	Re-plotting of the number of ions vs. σ_c to compare to the LUX result for measurement of the same parameter.	85
4.1	The WS2022 LZ spin-independent limit in WIMP cross section vs. WIMP mass space.	87
4.2	R^2 vs. drift time spatial distribution for a sample of WS2022 MS events passing the data quality cuts that have a UDT scatter on the cathode.	89
4.3	Illustration of how a mis-classified pile-up event can be interpreted as a vertical MS event.	90
4.4	The time difference between S2 pulse starts (Δt) for MS events that have a scatter on the cathode.	91
4.5	The 90-10 CL Gaussian NR and ER bands in $\Delta\chi^2$ vs. total fitted NR energy space, used for the $\Delta\chi^2$ WS2022 analysis, overlaid on the respective DD and Th-232 simulations used to create them.	97
4.6	A demonstration of the difference in MS NR ER discrimination between the $\log(S2c)$ vs. S1c parameter space, and the $\Delta\chi^2$ vs. total fitted NR energy parameter space using NR (DD) and ER (Th-232) simulated data for WS2022.	97
4.7	A comparison of the leakage of ER events into the NR band in $\log(S2c)$ vs. S1c space and $\Delta\chi^2$ vs. total fitted NR energy space for WS2022.	98
4.8	WS2022 $\Delta\chi^2$ space NR band verification using DD and AmLi MS calibration data.	99
4.9	All WS2022 events in $\Delta\chi^2$ vs. total fitted NR energy space.	100
4.10	The sample of $\sim 23,000$ WS2022 events, with only an ROI cut applied, used for further study of features in $\Delta\chi^2$ space.	101
4.11	The band feature above the ER band in $\Delta\chi^2$ space, shown in a range of parameter spaces.	102
4.12	The band feature below the NR band in $\Delta\chi^2$ space, shown in a range of parameter spaces.	103
4.13	The low energy cluster of events in $\Delta\chi^2$ space, shown in a range of parameter spaces.	105
4.14	Samples of the ‘fish bone’ structure of events in $\Delta\chi^2$ space, shown in a range of parameter spaces.	106
4.15	$\Delta\chi^2$ values of events in the ‘fish bone’ structure, as a function of the number of scatters in the event. Also shown is the average number of scatters in each subgroup of the selection.	107

4.16	Weighted energy distributions of SS and MS events in the WS2022 neutron background simulation.	109
4.17	SS/MS ratio as a function of energy, as calculated for the WS2022 neutron background simulation after cuts.	110
4.18	Energy distributions of WS2022 DD SS and MS events for data and simulation after analysis cuts.	111
4.19	WS2022 energy distributions of the SS/MS ratio for DD data and simulation and r_{DD} , after analysis cuts.	112
4.20	WS2022 MS events passing all data quality cuts with an S2c-weighted FV, with events in the $\Delta\chi^2$ NR band highlighted.	113
4.21	The MS neutron candidates identified by the independent, OD-based LZ WS2022 neutron study, shown in $\Delta\chi^2$ space.	115
4.22	Visualisation of the cuts failed by the MS neutron candidates identified by the independent, OD-based LZ WS2022 neutron study. Only cuts failed by an event are shown, along with the weighted FV.	116
4.23	The 20 process-material-component simulations that contribute the most to the WS2022 SS neutron background, after weighting and cuts were applied.	118
5.1	The LZ WS2024 and WS2022 combined spin independent WIMP-nucleon cross-section limit as a function of WIMP mass.	120
5.2	The effect of expanding the strict FV cut on the selection of MS events from WS2024 data.	122
5.3	An example waveform for a good and bad MS neutron candidate.	124
5.4	The 14 MS NR candidates selected from the WS2024 dataset in the strict FV extended out to 2 cm from the ideal wall.	127
5.5	The 9 MS NR candidates selected from the WS2024 dataset in the strict FV extended out to the ideal wall, requiring a delayed OD veto signal.	128
6.1	The 90-10 CL Gaussian NR and ER bands used for the $\Delta\chi^2$ WS2024 analysis, overlaid on the respective DD and Na22 simulations used to create them.	135
6.2	A demonstration of the difference in MS NR ER discrimination between the log(S2c) vs. S1c parameter space, and the $\Delta\chi^2$ vs. total fitted nuclear recoil energy parameter space using NR (DD) and ER (Na-22) simulated data for WS2024.	136
6.3	A comparison of the leakage of ER events into the NR band in log(S2c) vs. S1c space and $\Delta\chi^2$ vs. total fitted NR energy space for WS2024.	137
6.4	A verification of the DD simulation-produced NR band using DD, AmLi, and AmBe data.	138

6.5	WS2024 Na-22 calibration data shown across different parameter spaces, aiming to verify the ER band.	139
6.6	WS2024 Th-228 simulated data shown across different parameter spaces, aiming to verify the ER band.	141
6.7	Weighted energy distributions of SS and MS events in the WS2024 neutron background simulation.	142
6.8	SS/MS ratio as a function of energy, as calculated from the WS2024 neutron background simulation.	143
6.9	NR energy distributions of WS2024 DD SS and MS events for data and simulation after analysis cuts.	145
6.10	WS2024 energy distributions of the SS/MS ratio for DD data and simulation and r_{DD} after analysis cuts.	146
6.11	WS2024 energy distributions of the SS/MS ratio for AmLi data and simulation and r_{AmLi} after analysis cuts.	147
6.12	Energy distributions of WS2024 DD SS events, for data and simulation after analysis cuts, comparing the $\Delta\chi^2$ fitted energy definition and the non-fitted energy definition. This is then propagated to the calculation of r_{DD}	148
6.13	The 17 MS NR candidates selected from the WS2024 dataset.	149
6.14	An example of the S2 pulses from a gate photoionisation event.	151
6.15	An example of a potential alpha event.	152
6.16	An example of a split S2 pulse.	153
6.17	The waveform of a suspected MS accidental coincidence event.	154
6.18	The NR energy distribution of simulated SS neutron events with the G4NDL-4.5 and JEFF-3.3 interaction cross-section libraries.	157
6.19	The NR energy distribution of simulated MS neutron events with the G4NDL-4.5 and JEFF-3.3 interaction cross-section libraries.	158
6.20	The NR energy dependent distribution of the SS/MS ratio of simulated neutron events with the G4NDL-4.5 and JEFF-3.3 interaction cross-section libraries.	159
6.21	The MS χ^2 distributions from both the NR and ER models of the $\Delta\chi^2$ method, compared to the theoretical $k = 1$ χ^2 distribution, shown for DD data, DD simulation, and Na-22 simulation.	160
6.22	The SS χ^2 distributions from both the NR and ER models of the $\Delta\chi^2$ method, compared to the theoretical $k = 1$ χ^2 distribution, shown for DD data, DD simulation, and Na-22 simulation.	162
6.23	The SS χ^2 distributions from both the NR and ER models of the $\Delta\chi^2$ method, compared to the theoretical $k = 1$ χ^2 distribution, shown for the ER photopeak data on which the model was tuned.	163

6.24	The SS χ^2 distribution from both the NR and ER models of the $\Delta\chi^2$ method, compared to the theoretical $k = 1$ χ^2 distribution, shown for a CH3T beta source. .	164
6.25	The distribution of observed minus mean S2 values as a function of the mean S2 value for simulated DD data. Also shown is how the width of this distribution varies with the mean S2 value.	165
6.26	The distribution of observed minus mean S1 values as a function of the mean S1 value for simulated SS DD data. Also shown is how the width of this distribution varies with the mean S1 value.	166
6.27	The MS χ^2 distribution from both the NR and ER models of the $\Delta\chi^2$ method using a DD simulation-based error covariance matrix for the NR model, shown for 10 000 DD calibration events. Also shown is the $\Delta\chi^2$ space with this redefinition of the method.	167
6.28	MS Na-22 simulation events in $\Delta\chi^2$ space with the NR covariance matrix redefinition of the method.	168

List of Tables

1.1	Summary of the parameters in the standard cosmological model using the marginalised mean and 68% error using the ‘Plik’ likelihood [1].	14
2.1	Simulated datasets used throughout the work presented in this thesis.	46
2.2	Summary of the main radioactive contaminants contributing to the ER background of LZ.	49
2.3	LZ detector parameters for WS2022 and WS2024. The parameters in the bottom half of the table are from NEST calculations.	60
3.1	Comparison of WS2022 and WS2024 prompt and delayed veto cuts for the Skin and OD veto detectors.	62
3.2	WS2024 photopeak data used for the study of the distributions of $\sigma_m^2(E_1)$, $\sigma_m^2(E_2)$, and σ_c^2 , provided by G. Pereira.	74
3.3	Comparison of WS2024 photopeak measurements made by G. Pereira with the verification measurements made by the author of this thesis.	78
4.1	LZ WS2022 accidental coincidence cuts that required MS adaptation, and how they were adapted for application to MS events. The valid xy reconstruction cut is also included since this required MS adaptation.	94
4.2	Results of the $\Delta\chi^2$ SS neutron estimate for WS2022. Errors are the 90% CL upper limits on the estimates.	117
4.3	Results of the WS2022 neutron simulation cross-section library study, and final $\Delta\chi^2$ SS neutron estimates for WS2022, including both systematic and statistical errors. Errors are the 90% CL upper limits on the estimates.	118
5.1	LZ WS2024 MS-driven SS neutron estimate results.	125
6.1	The leakage of ER simulation events into the NR band in $\Delta\chi^2$ space for WS2022 and WS2024, for events with $S1c < 250$ phd.	130
6.2	WS2024 MS events in the NR band, and whether analysis of their waveform leads to their selection as a neutron candidate.	150

6.3	WS2024 $\Delta\chi^2$ SS neutron estimate results. Errors quoted are 1σ using Poisson statistics.	155
6.4	Results of the WS2024 neutron simulation cross-section library study.	158
7.1	Comparison of WS2022 and WS2024 $\Delta\chi^2$ SS neutron estimate results, and extrapolation of WS2024 results. WS2022 errors are 90% upper limits, and all other errors are 1σ , based on Poisson statistics.	172

List of Acronyms

BACCARAT ‘Basically A Component-Centric Analogue Response to AnyThing’

BBN Big Bang Nucleosynthesis

CDF cumulative distribution function

CE ν NS coherent elastic neutrino-nucleus scattering

CL confidence limit

CMB cosmic microwave background

CSD calibration source deployment

DD deuterium-deuterium

DAQ data acquisition

ER electron recoil

FV fiducial volume

GdLS gadolinium-loaded liquid scintillator

LZ LUX-ZEPLIN

LZAP LZ Analysis Package

LZLAMA ‘LZ Light Analysis Montecarlo Application’

MACHO massive compact halo object

MOND Modified Newtonian Dynamics

MS multiple scatter

NEST the Noble Element Simulation Technique

NR nuclear recoil

OD Outer Detector

PDT physical drift time

- PDF** probability density function
- PLR** profile likelihood ratio
- PMT** photomultiplier tube
- PTFE** polytetrafluoroethylene
- QCD** quantum chromodynamics
- RFR** reverse field region
- ROI** region of interest
- RQ** reduced quantity
- SE** single electron
- SHM** Standard Halo Model
- SPE** single photoelectron
- SS** single scatter
- SURF** the Sanford Underground Research Facility
- TPC** time projection chamber
- UDT** unphysical drift time
- WIMP** weakly interacting massive particle
- WS2022** 2022 LZ WIMP search
- WS2024** 2024 LZ WIMP search

Chapter 1

Introduction

Ordinary baryonic matter is thought to constitute only 4.9% [1] of the energy density of the universe, with 68.5% being ‘dark energy’¹ [2], and the remaining 26.4% being ‘dark matter’. The presence of this matter that does not interact with electromagnetic radiation, hence the name ‘dark matter’, can be inferred from its gravitational interactions in the large-scale cosmological structures of the universe. The history of observations that led to the suggested existence of dark matter will be outlined in section 1.1.

Given that approximately 85% of the matter in the universe is yet to be observed, the question immediately follows as to what constitutes this so-called dark matter. Since the speculation of its existence there have been numerous proposed candidates for dark matter [3], of which a selection are highlighted in section 1.3.

The main focus of this thesis, however, will be on weakly interacting massive particles (WIMPs) as a dark matter candidate. There are a few different ways in which different experiments aim to detect WIMP dark matter, covered in section 1.4, but the subject of this work will be direct detection, specifically by the dual-phase xenon time projection chamber (TPC) of the LUX-ZEPLIN (LZ) experiment [4].

LZ is based at the Sanford Underground Research Facility (SURF) in Lead, South Dakota, USA. The detector itself is located 4850 ft (~ 1.5 km) underground so as to provide a significant overburden of rock to shield the detector from cosmogenic backgrounds. Full details of the functionality of the detector will be covered in chapter 2 of this thesis.

Crucial to rare event searches, such as that of LZ for WIMP dark matter, is a comprehensive understanding of all of the signals that will be detected that are not WIMPs, but rather just background signals from other processes occurring in the detector and its surrounding environment. A particularly important background to understand is the neutron background, as a neutron produces a signal in the detector that is indistinguishable from a hypothetical WIMP. However, since neutrons have a much greater interaction probability with baryonic matter than WIMPs

¹A quantity thought to drive the accelerated expansion of the Universe.

have (WIMPs by definition interact very rarely with regular matter), they are often seen to scatter multiple times in the detector. Therefore, these multiple scatter (MS) neutron events can be used to infer the number of WIMP-like single scatter (SS) neutron events expected in a given dataset, and that is the focus of the work discussed in this thesis in chapters 3-7.

1.1 A History of Dark Matter

1.1.1 Galaxy Clusters

Speculation about the existence of invisible matter in the Universe could be argued to go as far back as ancient Greece [5], but the first major piece of evidence for the existence of dark matter is usually considered to be the observations of galaxy clusters by F. Zwicky in 1933 [6] (republished and translated in Ref [7]). Zwicky was studying the redshift of different galaxies within the Coma galaxy cluster, and observed velocity dispersion² values for individual galaxies of 1500 km s^{-1} to 2000 km s^{-1} . This work relied on that of E. Hubble [8] in which the amount of redshift observed for a light source was related to the distance of the source. Zwicky is thought to have been the first to determine the mass of a galaxy cluster through a novel application of the virial theorem [9]:

$$\bar{\epsilon}_k = -\frac{1}{2}\bar{\epsilon}_p, \quad (1.1)$$

where $\bar{\epsilon}_k$ and $\bar{\epsilon}_p$ represent the average kinetic and potential energies respectively of galaxies within a cluster. This required the assumption that the Coma cluster had reached a mechanically stationary state [7]. Zwicky was able to estimate the total potential energy, Ω , of the Coma cluster [7] using:

$$\Omega = -\frac{3}{5}G\frac{M^2}{R}, \quad (1.2)$$

with an estimate of the radius of the cluster, R , and an estimate of the mass, M , based on the amount of visible matter. G here is the gravitational constant. By dividing by M , the average potential energy, $\bar{\epsilon}_p$, can be found, and therefore so can the average kinetic energy, $\bar{\epsilon}_k$, and hence the mean velocity dispersion. When he carried out this calculation, Zwicky found the expected velocity dispersion, given the amount of visible mass in the Coma cluster, to be 80 km s^{-1} . This is notably different from the observed values of $\sim 1000 \text{ km s}^{-1}$, and therefore can be interpreted to imply that there is in fact more mass in the galaxy cluster than just that which is visible. Further study by Zwicky showed that the mass-to-light ratio of the Coma cluster was around 500 [10], although this was later seen to be an overestimation by a factor of approximately 8.3 if the modern value of the Hubble constant is used. This is still a very high ratio however, since this

²Velocity dispersion was observed here as this measures the velocity of individual galaxies with respect to the overall mean velocity of the galaxy cluster. This means that the galaxy velocities can be considered in a stationary reference frame.

means that there is a lot more mass than that which is visible, and therefore this provides strong evidence for the existence of dark matter.

1.1.2 Galactic Rotation

After the work of Zwicky on galaxy clusters, additional evidence was provided by the study of galactic rotation curves [11, 12], which helped convince much of the scientific community as to the existence of dark matter.

Some of the first measurements of galactic rotation curves that suggested the existence of missing mass at larger radii came from H. Babcock in 1939 [13], specifically of the rotation curve of Andromeda (M31), and several further studies of numerous galaxies followed [14].

Kepler's third law [15] states that the orbital period, T , depends on the orbital radius, r , according to $T^2 \propto r^3$. Newton's version of Kepler's third law then uses Newton's law of gravitation, given by:

$$F = \frac{GM(r)m}{r^2}, \quad (1.3)$$

to quantify Kepler's constant of proportionality for an orbiting body (orbital acceleration $a = v^2/r$, with r being the semi-major axis for a non-circular orbit), assuming spherical symmetry, the result of which is shown by:

$$T^2 = \left(\frac{4\pi^2}{GM(r)} \right) r^3. \quad (1.4)$$

Here, G is the gravitational constant as before, and $M(r)$ is the mass of the body being orbited, which in this case corresponds to the amount of the mass of a galaxy that is within a given radius, r . Note that the orbital period can also be expressed in terms of the orbital velocity, v , as $T = 2\pi r/v$. Equation 1.3 introduces the gravitational force, F , and the mass of the orbiting body, m . The final element required for this calculation is Newton's second law. Therefore, the expected orbital velocity with radius can be estimated, based on the amount of visible matter in the galaxy at different radii, according to:

$$v = \sqrt{\frac{GM(r)}{r}}. \quad (1.5)$$

Observations of galactic rotational velocity can be made by using the redshift of visible stars, but more commonly use the hydrogen 21 cm emission line, especially at larger radii where visible starlight decreases. The findings of the aforementioned studies were all that the observed rotation curves of spiral galaxies remain relatively flat out to large radii. However, the expected rotational velocity, based on visible matter, is a curve that drops off at larger radii [19]. This implies that there must be more mass than that which is visible in the galaxy to account for this higher than expected rotational velocity.

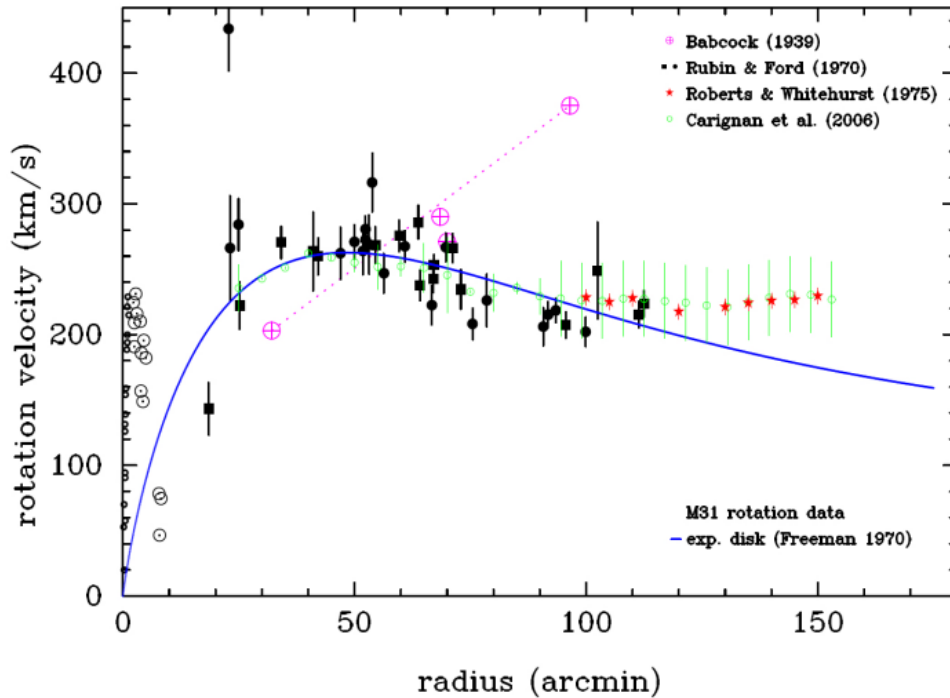


Figure 1.1: Measurements of the rotation curve of the Andromeda (M31) galaxy. Pink points show the emission line measurements by Babcock (1939) [13]. Black points (squares show southwest data, filled circles show northeast data, and open circles show data in the inner parts of the galaxy) are measurements by Rubin and Ford (1970) [16]. The red and green points are hydrogen 21 cm emission line measurements by Roberts and Whitehurst (1975) [17] and Carignan *et al.* (2006) [18] respectively. The solid blue line allows comparison of these datasets to the rotation curve of an exponential disc (scale length taken from Freeman (1970) [19], and scaled appropriately in velocity). This figure is taken from Ref [5].

The expected rotational velocity curve for an exponential disc, and the observed curves across a range of measurements, are shown for Andromeda (M31) in Figure 1.1, which is taken from Ref [5]. This figure includes the original measurements by Babcock [13] (pink), which show an increasing rotational velocity with radius. While this was the first hint that dark matter was present in M31, these measurements can be seen to be in disagreement with more modern measurements. Measurements by Rubin and Ford (1970) [16] are shown in black, and these include data points collected from opposite sides of the galaxy (squares show southwest data, filled circles show northeast data), as well as in the inner parts of the galaxy (open circles), although non-circular motions of the latter measurements introduced an additional uncertainty. The red and green datasets were collected at larger radii, and hence utilised the hydrogen 21 cm line method for measuring orbital velocity. These are datasets collected by Roberts and Whitehurst (1975) [17] and Carignan *et al.* (2006) [18] respectively.

The distribution of dark matter required in the galaxy to account for the observed rotation curve can be found by subtracting the expected distribution from the observed distribution. The resultant contribution of the missing matter to the observed velocity distribution increases with distance from the galactic centre. In order to make observation agree with theory, there must be a so-called dark matter halo surrounding galaxies [19].

1.1.3 The Bullet Cluster

There was still an alternative theory to explain the observations discussed so far however, and this was Modified Newtonian Dynamics (MOND) [20], which suggests that rather than the usual version of Newton's second law, the force due to gravity could scale as $F = ma^2/a_0$ in the limit of low accelerations, with $a_0 \sim 1.2 \times 10^{-10} \text{ m s}^{-2}$ [5]. This would explain flat galactic rotation curves, but has difficulty describing observations of galaxy clusters, and arguably cannot explain x-ray and gravitational lensing images of the Bullet Cluster, taken in 2006, which provided one of the most convincing pieces of evidence for dark matter.

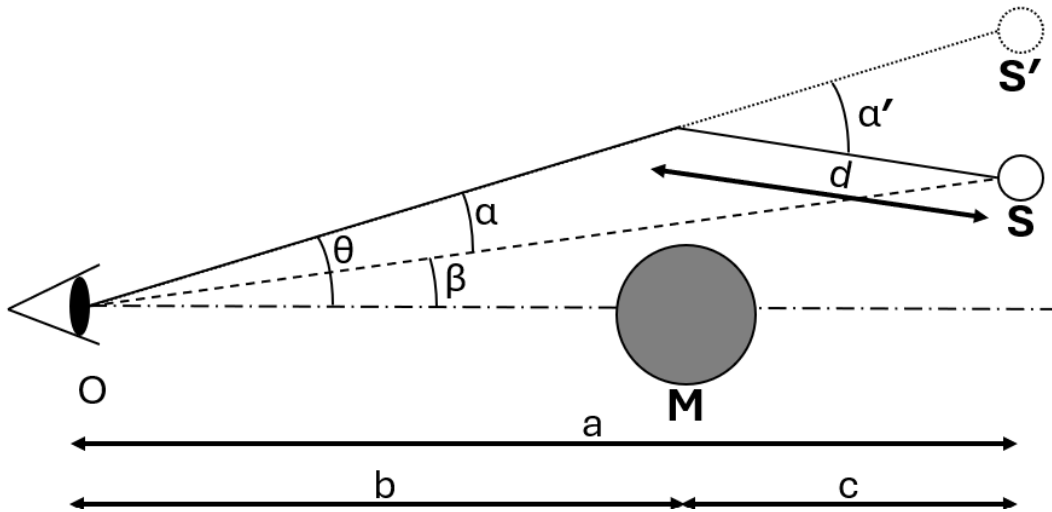


Figure 1.2: Geometric diagram of gravitational lensing due to a mass, M , of light from an obscured source, S , as seen by an observer at O . The observer sees the image of the source as being at S' . Also marked are the horizontal distances along the optical axis between the observer and the source, a , between the observer and the mass, b , and between the mass and the source, c . The distance between the source and the point at which the mass bends the light is denoted d . With respect to the optical axis, the image of the source is at angle θ , and the source is at angle β . The mass has bent the light from the source through an angle α' . The angle α between the source and the image is also shown. The original version of this figure is in Ref [21].

Before discussing in detail how the Bullet Cluster strongly suggests the presence of dark matter, it is first necessary to understand the concept of gravitational lensing. Gravitational lensing [21]

is an effect that occurs due to the fact that light, as well as mass, is affected by the laws of gravity, according to Einstein's theory of general relativity. Therefore, if an object has a sufficiently large mass, it will cause an observable distortion of the light from sources located behind it, relative to an observer. There are three different types of gravitational lensing: strong lensing, weak lensing, and microlensing. In the case of strong lensing the amount that a known light source appears to move in the sky can be related to the mass of the object in front of it. This concept is illustrated by Figure 1.2 for a mass M (modelled as a point mass) causing light from an obscured source, S , to appear to be coming from a different point, S' , for an observer located at O .

From the geometry of the figure, and using the small angle approximation that $\tan(x) \approx x$, it can be derived that:

$$\theta a = \beta a + \alpha' c. \quad (1.6)$$

This also requires the approximation that $d \approx c$ for small angles, which is derived from the fact that $\cos(x) \approx 1$.

If the reduced deflection angle, α is defined according to:

$$\alpha \equiv \alpha' \frac{c}{a}, \quad (1.7)$$

then the relationship between the true and apparent locations of the light source can be written as the lens equation, given by:

$$\beta = \theta - \alpha, \quad (1.8)$$

which can trivially be seen to be true when α is marked on the diagram. The conditions for strong lensing are that the angle β is small and the mass M is large, such that the source is hidden behind the mass. This results in distinct arcs of light being seen from the source, or rings in the idealised case where $\beta = 0$.

Weak lensing occurs when the mass M is large but β is also large, hence the source is not obscured by the mass. In this case, light from the source is slightly elongated perpendicular to the direction of the lens. For individual sources, this effect is not measurable, but for a group of many sources a non-random distortion can be seen that can be statistically analysed to map the mass M .

Finally, microlensing occurs when β is very small but the mass M is also small. This means that the ring feature visible from strong lensing cannot be resolved, but there is an observable increase in the luminosity of the source.

Returning to the Bullet Cluster of galaxies, this is in fact two galaxy clusters that have recently passed through each other. The visible light from this cluster shows all of its constituent galaxies. By viewing the x-ray emissions of this galaxy cluster, the intracluster medium that makes up most

of the baryonic mass can be mapped. In addition to this, weak gravitational lensing allows all of the mass of the cluster to be mapped.

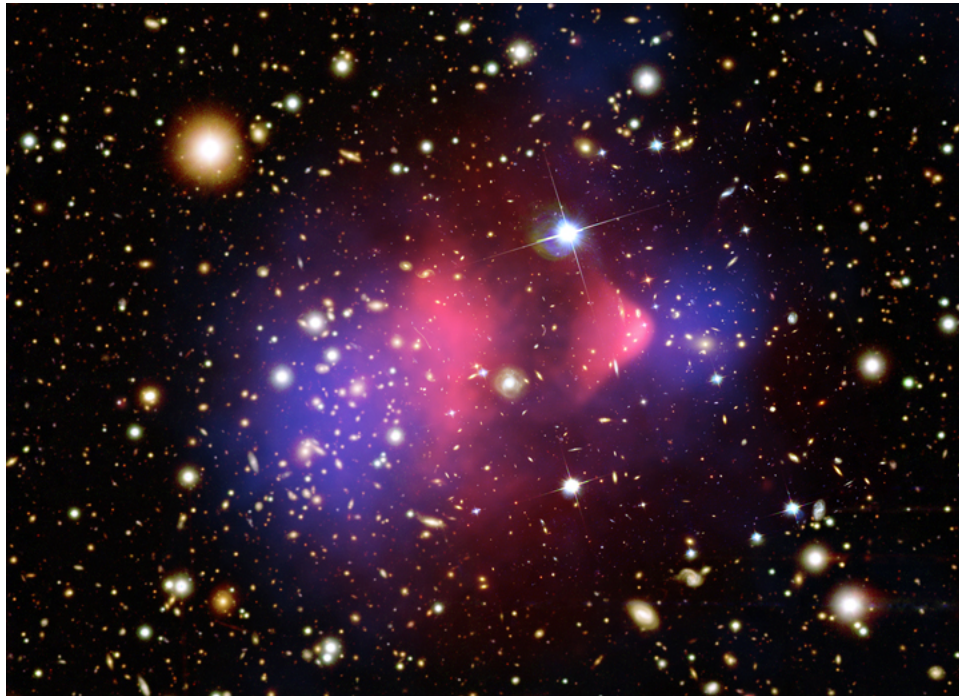


Figure 1.3: *False colour composite image of the Bullet Cluster. X-ray imaging of hot baryonic gas is shown in pink and was measured by the Chandra X-ray observatory [22] (from NASA/CXC/CfA/ M.Markevitch et al.). In white and orange is the optical image from Magellan [23] and the Hubble Space Telescope [24] (from NASA/STScI; Magellan/U.Arizona/D.Clowe et al.). In blue is a mapping of all of the mass of the cluster using gravitational lensing, (from NASA/STScI). This composite image was acquired from Ref [25].*

When the optical image, gravitational lensing, and x-ray mapping are superimposed onto each other, as is shown in Figure 1.3, it can be seen that the baryonic matter has been held back as the two clusters passed through each other, but conversely the majority of matter has passed through without interacting. This implies that the majority of the mass in one of the two constituent clusters had very weak interactions with the mass of the other cluster. This is widely seen as one of the strongest pieces of evidence against the aforementioned alternative theory to dark matter of MOND, as altered laws of gravitation struggle to explain this phenomenon. There are claims, however, that multicentred potentials, rather than spherically symmetrical versions of MOND, could explain the Bullet Cluster [26], and further that the collision velocity of the Bullet Cluster is more compatible with the MOND hypothesis than the dark matter hypothesis [27].

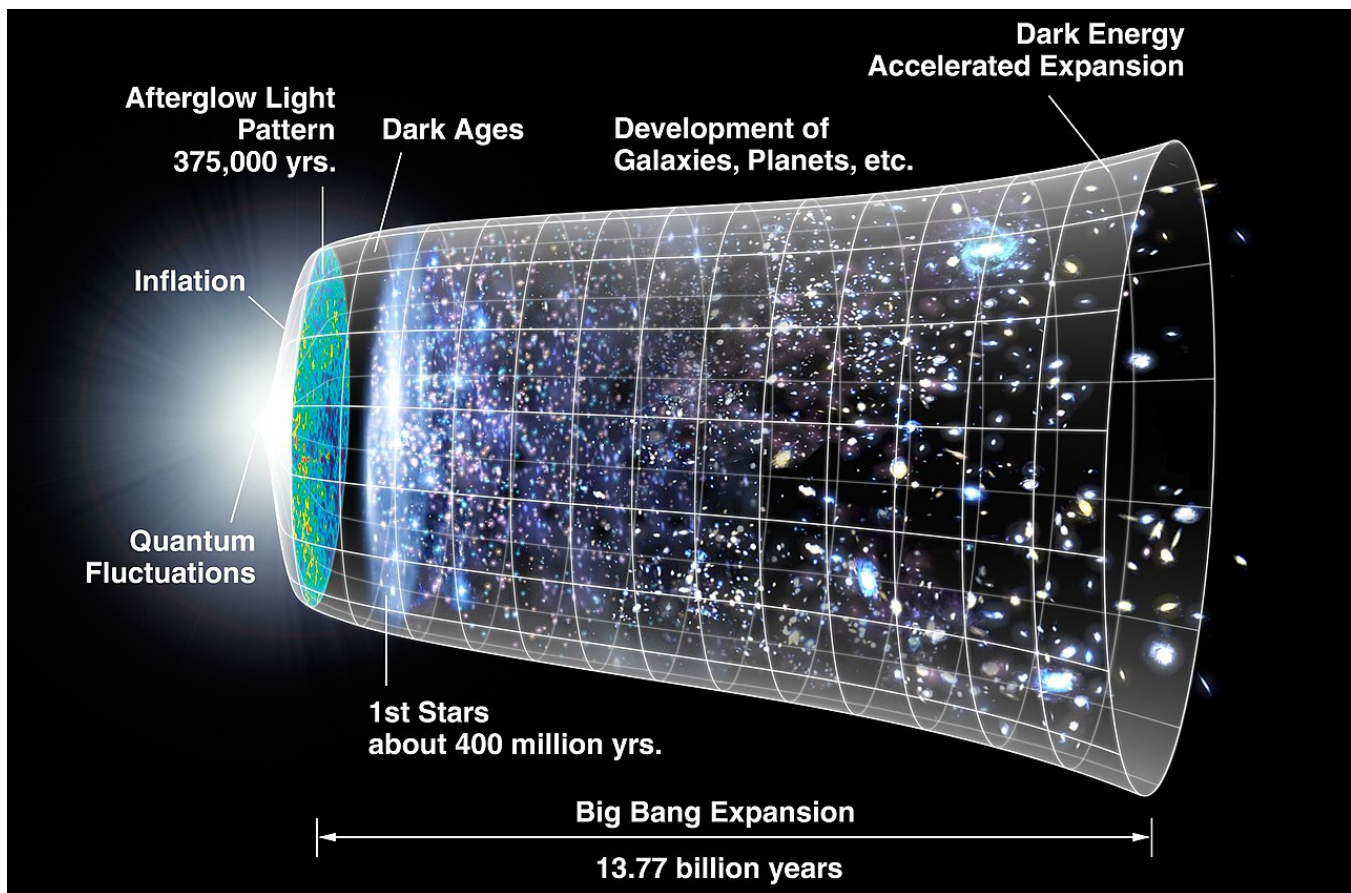


Figure 1.4: *Illustration of the history of the Universe as observed by looking out to greater distances. This is presented in relation to the age of the Universe. This figure is taken from Ref [28].*

1.1.4 Cosmic Microwave Background

It is worth noting that all evidence found so far for the existence of dark matter is gravitational, since dark matter does not interact with radiation. All of the evidence has also been relatively small scale on the overall scale of the universe, but larger scale observations have also been made that imply that there must be some form of matter that does not interact with radiation. An example of a large scale observation is that of the cosmic microwave background (CMB).

The CMB is the relic radiation, thought to be left over from the Big Bang, that fills all of the observable universe [29]. Initially, the Universe is thought to have consisted of an extremely hot and dense plasma of subatomic particles that was also opaque, since Thomson scattering of the photons off the free electrons in the dense medium meant that the photons were not able to travel freely. As expansion occurred and this plasma cooled, light elements were formed from the combination of the subatomic particles (see section 1.1.5) on the scale of minutes after the Big Bang. After several hundred thousand years of further cooling and expansion, photons were free to dissipate across space. It is these photons that are referred to as the CMB, and they represent

the limit to what can be observed of the early Universe. Because of the finite speed of light, looking further away in space also corresponds to looking backwards in time, and the CMB from the surface of last scattering of the photons at the point of decoupling (when photons and particles were no longer in thermal equilibrium) is the furthest back in time that can be observed. The timeline of the Universe is illustrated in Figure 1.4, which shows the notable milestones in the formation of structures that are observable today as the Universe aged and the CMB cooled [29].

Although CMB radiation is largely uniform when mapped across the sky, it has been found to display some anisotropy when observed on certain spatial scales, as is shown by Figure 1.5, which was created by the Planck Telescope [30]. The figure specifically shows data for the Stokes parameter³ I using ‘Commander’, one of four algorithms used in Ref [30] to map the CMB. Anisotropies in the CMB represent regions of compression and rarefaction during the epoch of last scattering of the CMB photons, combined with the gravitational redshift of the photons from escaping the potential wells. The combination of these effects is known as the Sachs-Wolfe effect [31].

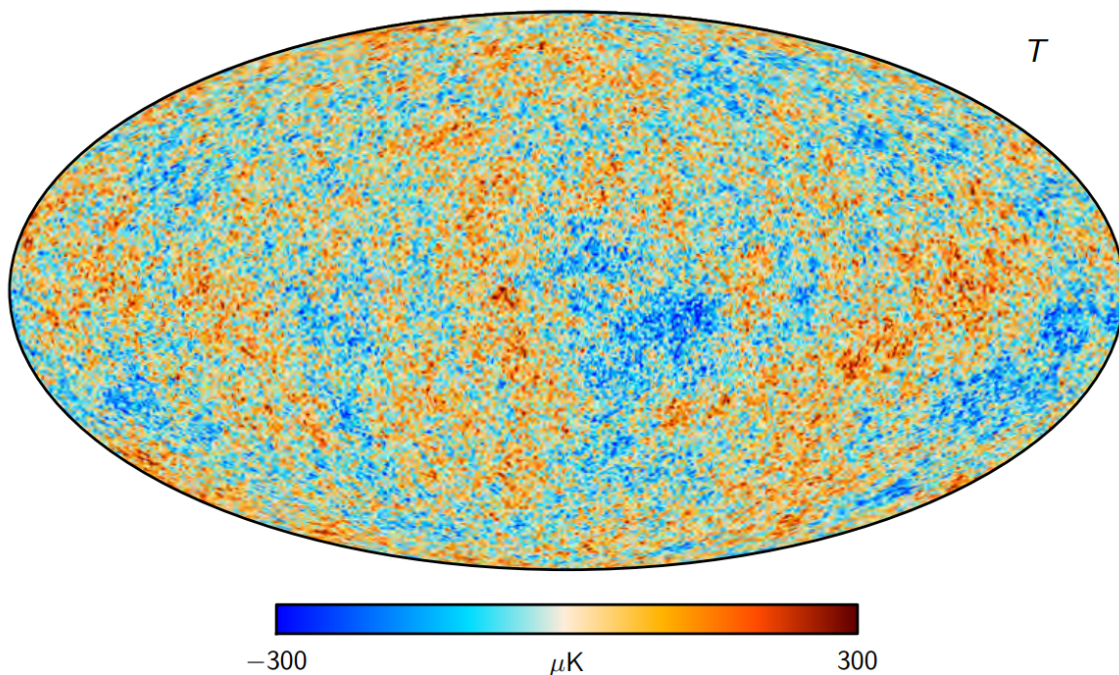


Figure 1.5: Mapping of the temperature anisotropy of the CMB across the sky by the Planck telescope, specifically using the ‘Commander’ algorithm for reconstruction, discussed in Ref [30]. This plot maps the temperature difference for the Stokes parameter I . Plot taken from Ref [30].

This non-uniformity during the epoch of last scattering is due to acoustic oscillations of the plasma in the early universe [32]. Small perturbations in the plasma would have led to regions with a higher density, and consequently more particles would be gravitationally attracted to these

³The Stokes parameters are used in electromagnetic theory to describe the state of polarization.

areas. Simultaneously, heat from the photon-matter interactions created an outward pressure driving baryons away from these high density regions, and it is these two competing processes that led to the formation of baryonic pressure waves. However, dark matter does not interact with photons and hence would not have felt this outward pressure, and would have simply collapsed into the gravitational wells created by these over-dense regions. As the Universe expanded and cooled past the threshold for neutral hydrogen to form, photons were able to diffuse away, meaning there was no longer an outward pressure driving these oscillations, and shells of baryonic matter were left behind. These shells are observable as the temperature anisotropies in the CMB. From the previous description, it is clear that the structure of these anisotropies will be dictated by the relative quantities of baryonic matter and dark matter in the early Universe, as well as by the curvature of the Universe. After decoupling, these over-dense regions were able to gravitationally attract more matter which led to the formation of stars and galaxies, and ultimately the overall structure of the Universe that can be seen today.

In order to fully understand how these anisotropies are studied, spherical harmonics need to be considered to represent the CMB in terms of an orthonormal basis on the surface of a sphere. Generally, any field on a sphere can be written as a sum of the spherical harmonics $Y_{\ell m}(\theta, \phi)$ [33], as is shown in:

$$T(\theta, \phi) = \sum_{\ell, m} a_{\ell m} Y_{\ell m}(\theta, \phi), \quad (1.9)$$

with coefficients $a_{\ell m}$. $Y_{\ell m}(\theta, \phi)$ undergoes ℓ oscillations around the sphere, hence ℓ can be used to determine the wavelength of the oscillations, and is summed from 0 to infinity. m runs from $-\ell$ to ℓ .

D_ℓ is a way of representing the variance, or power spectrum, of the coefficients $a_{\ell m}$, and it is this variable that is plotted in Figure 1.6. This figure shows the temperature fluctuations, D_ℓ , plotted against the angular scale, ℓ , and allows a peak structure of the oscillations to be seen. In this figure, odd peaks represent the compression phase, where the temperature of the CMB peaks, and even peaks represent the rarefaction phase, corresponding to a trough in the temperature.

The positions of these different peaks indicate characteristic qualities of the Universe [34]. Specifically, the first peak can be used to obtain the curvature of the Universe. This process involves comparing the physical features on the surface of last scattering, such as those produced by acoustic peaks, to the angular features on the sky. The second peak is particularly sensitive to the baryon density. This is because baryons have mass and will be attracted into gravitational potential wells. This will increase the compression in high density regions and therefore amplify the odd peaks with respect to the even peaks. The third peak is particularly sensitive to the dark matter density. A greater density of dark matter increases the gravitational potential well that baryons will fall back into after a period of rarefaction, which means the density during these periods is even further reduced and hence the even peaks are amplified with respect to the odd

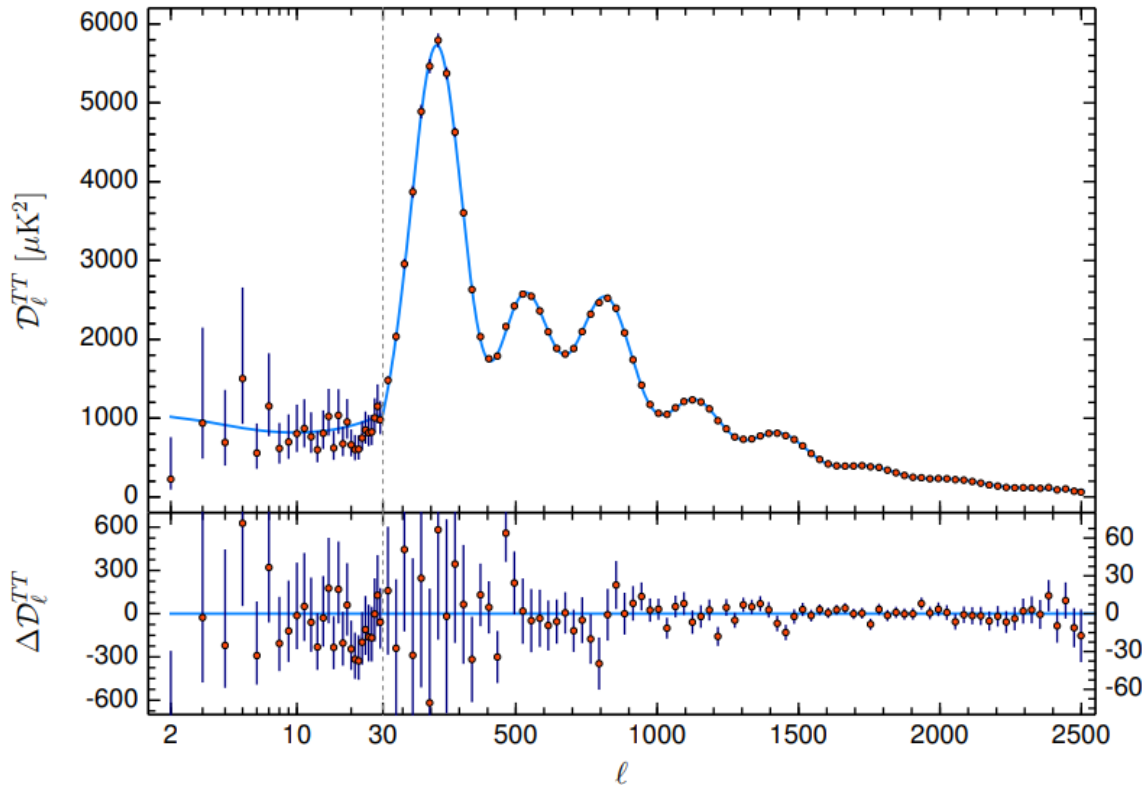


Figure 1.6: CMB anisotropy shown by temperature fluctuations as a function of angular scale. The data shown was collected by the Planck satellite. The solid blue line shows the best fit assuming the Λ CDM cosmology. This figure was produced by the Planck collaboration and taken from Ref [1].

peaks. Therefore, the results shown in Figure 1.6 not only imply that dark matter must indeed exist, but also allow for measurement of the quantities in which it would be expected. Specifically, fitting the anisotropy distribution can give a cold dark matter density of $\Omega_c h^2 = 0.1200 \pm 0.0012$ [1] (h being a redefinition of Hubble's constant, H_0 , defined as $h = H_0 / (100 \text{ km s}^{-1} \text{ Mpc}^{-1})$), but this value depends on the specifics of the fitting.

1.1.5 Big Bang Nucleosynthesis

Big Bang Nucleosynthesis (BBN) is the process by which isotopes heavier than H-1 were created in the early Universe following the Big Bang [35], in the first few minutes of the lifetime of the Universe. While not a comprehensive list of all interactions that could have occurred, the following are some of the most important [36, 37]:





Following this chain of interactions from just free protons and neutrons, light elements up to the mass of lithium can be created.

The relative quantities in which these light elements were created by BBN depend on the lifetime of the free neutron as well as the properties of the early Universe, such as the ratio of baryons to photons, η . The primordial abundances of light elements can be calculated for a given value of η and this is what is shown in Figure 1.7, with the widths of the curves for He-4, H-2 (alternatively referred to as deuterium, D), He-3, and Li-7 representing the 2σ uncertainties [40]. The figure also shows the abundances in relation to the baryon density, written as $\Omega_b h^2$. Yellow boxes on the figure show constraints on η set by observations. Also shown is the value of η , again with a 2σ uncertainty band, as given by studies of BBN and the CMB.

The figure shows that observations are generally in good agreement with the values calculated based on BBN and the CMB, except in the case of lithium, for which there is a discrepancy. This is known as the ‘lithium problem’ [37], but recent studies suggest that the measured primordial Li-7 abundance should be viewed as a lower bound rather than a measure [41]. This would resolve the conflict of the lithium problem. From the deuterium result however, the baryon density of the universe can be heavily constrained as $0.021 \leq \Omega_b h^2 \leq 0.024$ to a 95% confidence limit (CL) [40]. Going further, the density of luminous matter in the Universe has been measured to be $\Omega_{stars} = 0.0027 \pm 0.0005$ [42], so this means that most baryons must not be luminous, and are likely part of some diffuse intergalactic medium. Given that the mass density of the Universe is $\Omega_m \approx 0.3$ [40], this implies that the majority of mass consists of non-baryonic matter that is also non-luminous. This is further evidence of the existence of dark matter.

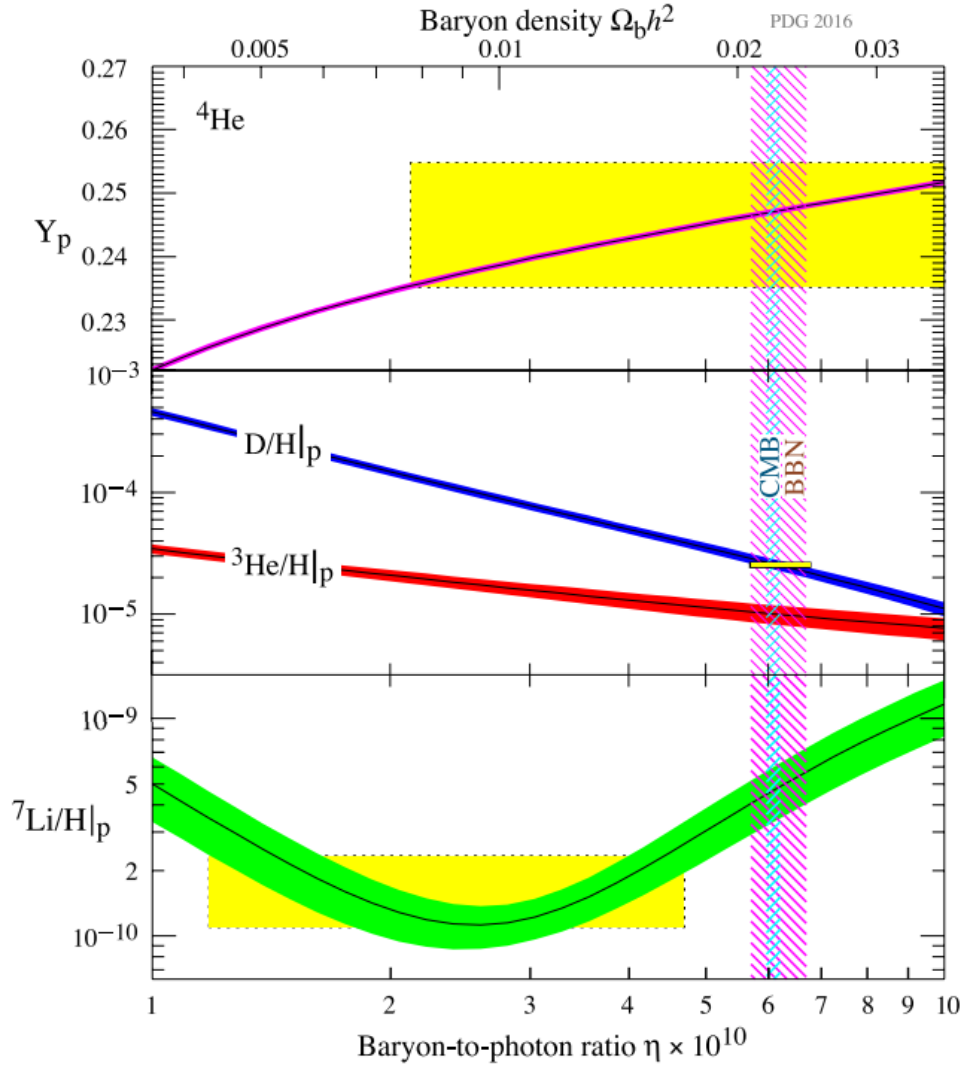


Figure 1.7: Primordial abundance with respect to baryon-photon ratio η , (or equally the baryon density, $\Omega_b h^2$) for ${}^4_2\text{He}$, ${}^2_1\text{H}$ (alternatively referred to as deuterium, D), ${}^3_2\text{He}$, and ${}^7_3\text{Li}$, calculated using and updated version [38] of the Wagoner code [39]. The width of these curves represents the 95% confidence limit (CL) uncertainty on these calculations. Also shown are the best-fit values of η and $\Omega_b h^2$ from observations of BBN and the CMB, both with a 95% CL uncertainty. Yellow boxes indicate the constraints placed by observations (absorption features of quasars, emission lines in compact galaxies, absorption lines of metal-poor stars [40]). Figure taken from Ref [40].

A summary of the cosmological parameters, as measured by the Planck collaboration, is given in Table 1.1 [1], in which it is clear that the total matter density of the Universe ($\Omega_m = \Omega_c + \Omega_b$) is dominated by dark matter. Here, Ω_c represents the density of cold dark matter (‘cold’ here meaning non-relativistic in the early Universe at the time when structures started to form. See section 1.2).

Parameter	Symbol	Value
Hubble Constant	H_0	$67.36 \pm 0.54 \text{ km s}^{-1} \text{ Mpc}^{-1}$
Baryon Density	$\Omega_b h^2$	0.02237 ± 0.00015
Cold Dark Matter Density	$\Omega_c h^2$	0.1200 ± 0.0012
Dark Energy Density	Ω_Λ	0.6847 ± 0.0073

Table 1.1: Summary of the parameters in the standard cosmological model using the marginalised mean and 68% error using the ‘Plik’ likelihood [1].

1.2 Properties of Dark Matter

With all of these different observations suggesting the presence of some missing matter in the Universe, the evidence in favour of dark matter is compelling. From all of these findings, there are some properties of dark matter that can be inferred, whatever it may be [43].

Firstly, it is clear that dark matter must be electrically neutral, since it is not detected by most conventional methods and therefore does not appear to interact via the electromagnetic force. There were suggestions of an electrically charged dark matter candidate known as a CHAMP [44], but this has all but been ruled out as a dark matter candidate [43].

Crucially, any dark matter candidate must have a non-zero mass, such that it is able to account for the missing mass in galaxies that the introduction of dark matter is trying to solve. Candidates could have a very small mass, and this would simply require them to be present in very large quantities to account for all of the dark matter.

Dark matter is known to have been present in the early Universe in the same quantity as is seen by observations today due to measurements of the CMB. Specifically, it is thought that the current density is the same as the density at the point of ‘freeze-out’. Initially, dark matter would have been in thermal equilibrium with the baryonic matter in the Universe, which would in turn have been in thermal equilibrium with the photons. As expansion and cooling occurred, there would have been less energy available for the dark matter production mechanism, and once the energy dropped below the dark matter mass threshold the production would have been kinematically forbidden. This is what is known as the freeze-out point. Self-annihilation of dark matter (another condition required of many dark matter candidates) would have continued, however, but at a decreasing rate as expansion continued and the dark matter density decreased. Eventually, the probability of annihilation would have become sufficiently small as to cause the dark matter density to maintain a constant value, known as the relic density. This is illustrated by Figure 1.8 [45].

It can be seen from the figure that the number density of dark matter particles, n (scaled by the temperature, T , cubed), decreases as temperature decreases due to expansion. The point of freeze-out occurs when the rate of interactions, Γ , is approximately equal to the rate of expansion, H . After this point, the number density decreases at a slower rate than when in equilibrium, but

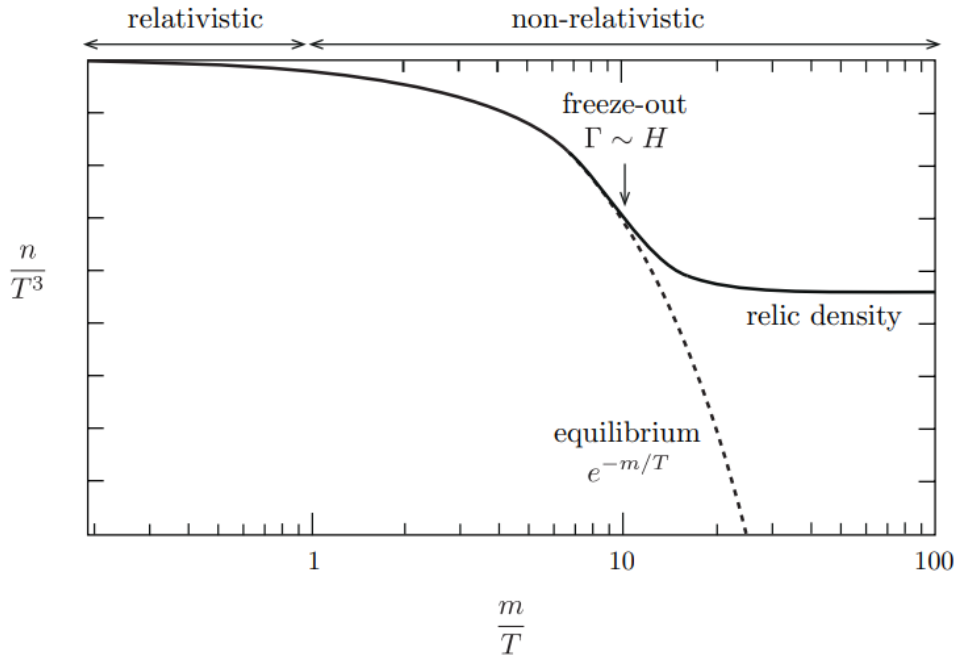


Figure 1.8: Diagram illustrating the freeze-out process in the early Universe. Number density of particles, n , scaled by the temperature, T , cubed, is plotted against the particle mass, m , scaled by the temperature. Freeze-out occurs when the rate of interactions, Γ , is approximately equal to the rate of expansion, H . This figure is taken from [45].

continues to decrease due to annihilation before levelling out at the relic density. Since the current dark matter density is equal to the relic density, it is necessary that dark matter must be stable, or at least have an extremely long lifetime, greater than the age of the Universe.

If dark matter had been relativistic in the period prior to freeze-out, it would not have been gravitationally bound, and would therefore not have formed the structures that we see today in the CMB. Therefore, another property of dark matter is that it must have been non-relativistic prior to freeze-out. Dark matter with such a property is usually referred to as cold dark matter (CDM).

So far, evidence has been shown that implies that dark matter exists, and the required properties of this missing matter have been considered. However, the question remains as to what constitutes dark matter, and this question is the focus of section 1.3.

1.3 Dark Matter Candidates

In section 1.1 the evidence for the existence of dark matter was presented, but no suggestion was made as to what constituted this missing matter. In sections 1.3.1-1.3.3 a few potential candidates for dark matter will be discussed.

1.3.1 MACHOs

One proposed dark matter candidate is massive compact halo object (MACHO) dark matter [46], which consists of astronomical objects that emit minimal radiation, such as black holes or neutron stars [47]. These bodies cannot be imaged directly, but can be searched for by use of microlensing when they come between a light source and the observer [21].

Several different experiments, such as the MACHO project [48], the Optical Gravitational Lensing Experiment (OGLE) [49], and the Expérience pour la Recherche D'Objets Sombres (EROS) [50], searched for MACHOs in the Milky Way by this method. The combined data from all three of these experiments is reported on in Ref [51]. They found that there was not a sufficient number of MACHOs to account for the missing mass in the galaxy, and were able to rule out MACHOs with masses $10^{-7} - 30 M_{\odot}$.

For larger MACHOs, with masses larger than 100 solar masses, the timescale required for observations using gravitational lensing increases to a few years [47], which becomes a limiting factor in the surveys that can be conducted. One method to study such MACHOs is to observe binary star systems on which these massive objects, if present, would be expected to have an effect [52]. Some such studies conservatively showed that MACHOs with masses $\sim 10-10^7 M_{\odot}$ make up no more than around 50% of the galactic halo [47]. For even larger MACHOs, a strong constraint can be placed based on the velocity dispersion of the galactic disc [53].

Therefore, the window of MACHO masses for a viable dark matter candidate has all but been shut, with only the $< 10^{-7} M_{\odot}$ region left to probe for hypothesised primordial black holes⁴ [54]. MACHOs will contribute a small amount to the missing mass inferred by the observations in section 1.1, but not enough for them to be the sole explanation for dark matter.

1.3.2 WIMPs

A popular candidate to explain the missing matter in the Universe is a new hypothesised elementary particle known as a weakly interacting massive particle (WIMP) [46]. This is, in itself, a sub-category of dark matter candidates that describes particles with mass, such that its gravitational effects are observable, but that otherwise only interacts with normal, baryonic matter via the weak force.

If such a particle existed in the very early Universe, during the time when the Universe was at a very high temperature, a state of thermal equilibrium between particles (including WIMPs) and photons would have been present, with the two number densities having been approximately equal [46]. Following the freeze-out process discussed previously in this chapter, the comoving density of WIMPs would have reached a constant value (the actual density continues to decrease

⁴Primordial black holes are black holes that formed very soon after the Big Bang when dense pockets of subatomic particles could have collapsed into black holes without the need for supernova compression. This would mean that they had a much less limited mass range than stellar black holes.

due to the continued expansion of the universe) at the relic density (assuming that they are stable particles, which is a requirement for a dark matter candidate).

By use of the Boltzmann equation [55], the relic density of a particle can be related to its interaction strength, and given that the density of dark matter in the Universe is known, it can be calculated that the interaction strength required for a dark matter candidate, with dimensionless couplings $\mathcal{O}(1)$ [56], is on the electro-weak scale. Therefore, if these hypothetical WIMPs were to exist then they would solve the dark matter problem. This is sometimes referred to as the ‘WIMP miracle’ [57]. This provides further weight to the WIMP dark matter hypothesis, if it is assumed that essentially all of the dark matter in the Universe is explained by a single candidate (although the relic density does have a strong dependence on the exact nature of the lightest neutralino [58] when considering that particular candidate).

WIMPs are themselves a sub-category of dark matter candidates, and there are a number of WIMP candidates [59]. One of the most attractive WIMP candidates is the lightest neutralino of supersymmetry. Supersymmetry [60] is a theory that proposes that every fermion in the standard model has a boson partner, and vice versa. In the simplest theories, these supersymmetric partners share all the same properties (mass and quantum numbers) with the exception of spin, for which they differ by a half-integer value. It cannot be true that superpartners have the same mass due to the differing masses of fermions and bosons that have so far been observed, and hence a more complicated theory of supersymmetry, with spontaneous symmetry breaking allowing superpartners to differ in mass, is required. However, there is so far no experimental evidence of supersymmetry despite many years of searching [61].

Supersymmetry, if proven to be correct, would solve a problem in physics known as the ‘naturalness problem’ [62]. This problem is that the Higgs boson provides the mechanism which generates the mass of all particles [63], and therefore acquires its own mass by interaction with itself. However, if interactions beyond first-order are considered, and loops are introduced, this interaction can theoretically involve any other particle, and with any momentum (since the only requirement is that the momenta of the two particles created in the loop cancel). To obtain the Higgs mass in this instance, an infinite range of momenta must be integrated over, and hence the Higgs mass would go to infinity, but experimental measurement has shown that the Higgs has a finite mass of approximately 125 GeV [64]. Since supersymmetry predicts that all fermions have a boson superpartner, and all bosons have a fermion superpartner, this would lead to every loop term in the integral to calculate the Higgs mass having an equivalent term with the opposite sign, and hence all of these loop terms would cancel [65]. Therefore, supersymmetry would solve the ‘naturalness problem’.

According to supersymmetry there are five Higgs bosons (two neutral, two charged, and one CP-odd neutral), all of which have superpartners known as Higgsinos [65]. The lightest supersymmetric particle (a superposition of B and W^0 gauginos and the two neutral higgsinos) is a particularly

attractive WIMP candidate due to the fact that its calculated relic density can be in agreement with what is required for dark matter [66], although this is not true over most of the parameter space of supersymmetry [67]. Additionally, in supersymmetric models in which ‘R-parity’ is conserved, then the lightest supersymmetric particle would be stable, which is a requirement for any WIMP candidate. Therefore, if supersymmetry is correct, then it would solve the dark matter problem.

1.3.3 Further Dark Matter Candidates

Beyond WIMPs and MACHOs there are many other proposed dark matter candidates that have the potential to solve the dark matter problem, some of which will be mentioned briefly here. Two general classes of non-WIMP dark matter are referred to as Feebly Interacting Massive Particles (FIMPs) [68], that are produced by ‘thermal freeze-in’ as opposed to the conventional thermal freeze-out, and super-WIMPs [69], that interact ‘superweakly’ (even more weakly than WIMPs) and were created by decays of the freeze-out produced state. The thermal freeze-in mechanism involves a dark matter candidate with a negligible abundance in the early Universe and that has sufficiently weak interactions with the early Universe particles that it is thermally decoupled from the plasma. Despite being weak, these interactions with the plasma lead to more dark matter production, and the abundance ‘freezes in’ when the temperature drops below the mass of the FIMP. Both of these classifications, FIMPs and super-WIMPs, will have interaction cross-sections with the Standard Model particles that are much smaller than the weak scale, meaning that such particles would evade detection by all direct detection experiments proposed to date. The following two candidates have interactions on these energy scales.

Firstly, axions [70] are becoming an increasingly popular candidate as WIMP searches limit further and further the parameter space in which a potential WIMP could exist. A proposed solution to the so-called ‘strong CP problem’ [71], where charge and parity symmetries are not necessarily obeyed in quantum chromodynamics (QCD), an otherwise extremely successful theory, is the introduction of a new scalar field. This new field has a corresponding pseudo-Goldstone boson: the axion. The axion proposed by current theories would be extremely light and very long lived. This means that, in large enough quantities, the axion could fulfil the dark matter candidate requirements of making up the missing mass in the Universe, and being stable on the timescale of the age of the Universe.

Secondly, dark photons (more properly known as dark Z' vector bosons) [72] are another possible candidate, if they are stable over the required timescale. As well as production by the usual freeze-out or freeze-in mechanisms, dark photons could also be produced by universal inflationary fluctuations [73].

This is by no means a comprehensive list of all other candidates, but illustrates that there are in fact a number of different options as to what could constitute dark matter. Further candidates are discussed in Ref [74].

1.4 Searching for Dark Matter

In the previous section, hypotheses for potential dark matter candidates were presented. Due to the very different nature of many of the dark matter candidates that have been proposed, any experiment that aims to detect dark matter must, in most cases, be confined to searching for a single candidate. For the work presented in this thesis, the class of candidates in question is WIMP dark matter.

Although different dark matter candidates require different detection methods, there is also more than one way to approach trying to detect a specific candidate, and WIMPs are a good example of this. WIMP searches can be broadly divided into three categories: collider searches, indirect detection, and direct detection. Figure 1.9 illustrates these different approaches. Reading the figure from left to right, a dark matter particle, χ , interacts with a standard model particle, p , usually in the form of a nuclear recoil (NR). When evidence of such an interaction is seen within a detector, this is known as direct detection. Reading from top to bottom, two dark matter particles annihilate with each other and produce two standard model products. Detection of these products is known as indirect detection of dark matter. Finally, reading from bottom to top, two standard model particles annihilate, usually in the context of a particle collider, and produce two dark matter particles that cannot be detected, but would be seen as missing transverse momentum. In this section, these three approaches to WIMP dark matter searches will be covered, and examples of experiments using these methods will be provided.

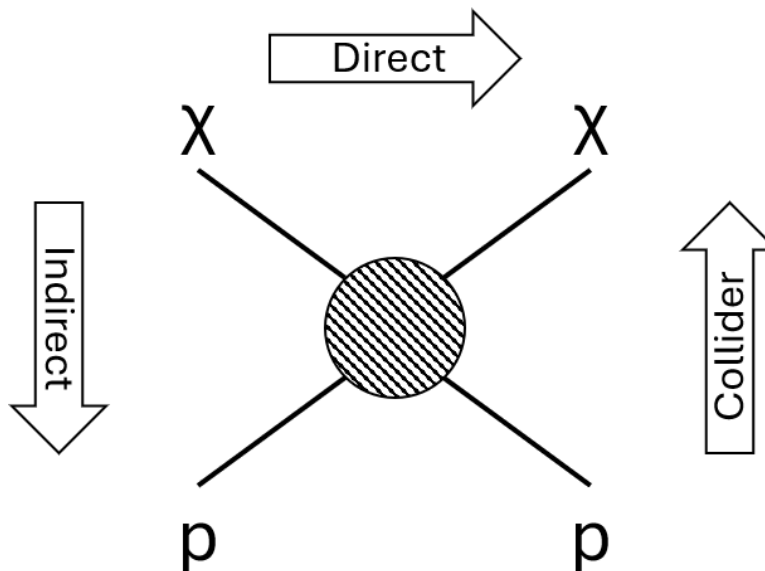


Figure 1.9: Illustration of the different approaches to detecting dark matter. χ represents a dark matter particle and p represents a standard model particle. Reading the diagram from left to right (or equally right to left) shows direct detection, top to bottom shows indirect detection, and bottom to top shows the approach of collider searches.

1.4.1 Collider Searches

One approach to searching for WIMPs is to use a particle collider, such as the Large Hadron Collider (LHC) at CERN [75]. The high energy collisions between particles observed at such an experiment provide the energy to create new particles, which could potentially include WIMPs. Experiments such as ATLAS [76], CMS [77], and LHCb [78] at the LHC rely on a particle detector surrounding the collision point. The detector is split into different detecting subsystems to detect as many different particles, and their various characteristics, as possible. However, as has been discussed in previous sections, the key characteristic of a WIMP, or of any dark matter candidate, is that it does not interact via the electromagnetic force, and is therefore very difficult to detect.

This means that rather than looking for a WIMP signal at a particle collider, the search is for missing transverse momentum from the initial collision that cannot be accounted for among the observed products. WIMPs are not the only particle that could take energy away, unseen, from a particle collision however, as neutrinos also escape without leaving a signature in the detectors. It is also not possible to say, in the case of some missing transverse momentum being noted, that it is definitely due to a dark matter candidate and not some other currently unknown particle that also cannot be detected by current detectors. For this reason, in collider searches, rather than directly calling these undetected particles dark matter, they tend to be referred to as invisible particles [75]. This ultimately means that, although particle colliders could provide a hint as to the mass of a potential WIMP, this would then have to be confirmed by a direct or indirect detection of a WIMP with that mass.

1.4.2 Indirect Detection

The remaining two methods of WIMP dark matter detection that will be considered here both aim to detect dark matter that already exists in the Universe, rather than trying to create it. Indirect dark matter searches rely on detecting the products of interactions that WIMPs undergo elsewhere in the Universe. There are a few different methods of indirect detection.

It was discussed in section 1.1.2 that galaxies are expected to have a roughly spherical dark matter halo, and in section 1.3.2 that the relic density of WIMPs is low enough that the probability of two WIMPs meeting and annihilating is small. However, a large mass, such as the sun, would create a sufficiently large gravitational potential well as to cause the accumulation of WIMPs in greater numbers than the usual relic density [79] after their interactions with the solar material. This would in turn increase the probability of self-annihilation. The products of annihilation can vary depending on the mass and energy of the annihilating particles, but the products more commonly searched for in this type of experiment are gamma photons or neutrinos. H.E.S.S [80] and VERITAS [81] are examples of telescopes that detect gamma photons, and IceCube [82] and Super-Kamiokande [83] are examples of neutrino observatories. However, an issue with search-

ing for signals coming from the galactic centre is the abundance of additional gamma photons emanating from this bright region.

1.4.3 Direct Detection

The final approach to WIMP detection, and the one that is used for the work in this thesis, is the direct detection of WIMP dark matter. This involves observing interactions between WIMPs and regular matter in the form of a detector. The aim is to detect WIMPs, in the halo of the Milky Way, that the Earth will pass through as the galaxy rotates.

The differential rate of WIMP events detected by a direct detection dark matter experiment is usually written in terms of counts/kg/day/keV. For a WIMP with mass m_χ and a detector medium nucleus of mass m_N , this rate can be written as [84, 85]:

$$\frac{dR}{dE_R} = \frac{\rho_0}{m_N m_\chi} \int_{v_{min}}^{\infty} v f(v) \frac{d\sigma_{\chi N}}{dE_R}(v, E_R) dv, \quad (1.19)$$

where ρ_0 is the local density of WIMPs, $\frac{d\sigma_{\chi N}}{dE_R}(v, E_R)$ is the differential cross-section for WIMP-nucleus elastic scattering, and $f(v)$ is the velocity distribution of the WIMPs (normalised to unity). The speed of a WIMP relative to a target nucleus is $\sim 100 \text{ km s}^{-1}$, so the elastic scatter occurs in the extreme non-relativistic limit, and hence the recoil energy, E_R , can be calculated in the centre of mass frame as:

$$E_R = \frac{\mu_N^2 v^2 (1 - \cos \theta)}{m_N}, \quad (1.20)$$

where θ is the scattering angle in the centre of mass frame and $\mu_N = m_\chi m_N / (m_\chi + m_N)$ is the WIMP-nucleus reduced mass. v_{min} is the minimum velocity of a WIMP required to produce an NR with energy E_R , and can now be expressed as:

$$v_{min} = \sqrt{\frac{m_N E_R}{2\mu_N^2}}. \quad (1.21)$$

The upper limit of the velocity distribution in Equation 1.19 is formally written as infinity, but in reality is limited by the escape velocity for a WIMP in the galactic rest frame, v_{esc} , since a greater velocity would mean that it was no longer gravitationally bound to the Milky Way [84].

The WIMP-nucleus differential cross-section, $\frac{d\sigma_{WN}}{dE_R}(v, E_R)$, encapsulates all of the physics describing how the hypothesised WIMPs would interact with the detector. By considering the interaction of WIMPs with specific nucleons within the nucleus, this overall differential cross-section can be broken down into a sum of the spin-dependent [86] (SD, described by an axial-vector Lagrangian coupling the WIMP to the quarks [85]) and spin-independent (SI, described by a scalar or vector Lagrangian coupling the WIMP to the quarks) components, as is shown in:

$$\begin{aligned} \frac{d\sigma_{WN}}{dE_R} &= \left(\frac{d\sigma_{WN}}{dE_R} \right)_{SD} + \left(\frac{d\sigma_{WN}}{dE_R} \right)_{SI}, \\ \frac{d\sigma_{WN}}{dE_R} &= \frac{m_N}{2\mu_N^2 v^2} (I^{SI} \sigma_0^{SI} F_{SI}^2(E_R) + I^{SD} \sigma_0^{SD} F_{SD}^2(E_R)). \end{aligned} \quad (1.22)$$

In this equation, σ_0^{SI} and σ_0^{SD} are the spin independent and spin dependent cross-sections, at zero momentum transfer, for scattering on the nucleons of the nucleus. I^{SI} and I^{SD} are nuclear enhancement factors that allow the cross-section for the nucleus as a whole to be calculated for, rather than just individual nucleons. This is known as coherent scattering. In the simplest case of spin-independent interactions with sufficiently low momentum transfer, this enhancement factor is given by $I^{SI} = A^2$, where A is the mass number of the target element. This means that the mass number of an element increases the coherent scattering cross-section according to A^2 , which is one of the reasons why xenon is selected by LZ as a suitable target, since it has a high mass number. This enhancement factor can be more complex in some cases, such as for neutrino scattering, for which $I^{SI} \approx (A - Z)^2$, where Z is the atomic number of the target element.

The dependence on momentum transfer is encoded in the form factors, $F_{SI}^2(E_R)$ and $F_{SD}^2(E_R)$. It is important to note, however, that this treatment is less accurate when dealing with large mass nuclei in the case of spin-dependent interactions, as it corresponds to consideration of only the unpaired nucleon ('single-particle' model) or nucleons with the same spin as the unpaired nucleon ('odd-group' model). In the plane wave approximation, the form factor is the Fourier transform of the density distribution of the 'scattering centres' [87].

The total differential rate of WIMPs for a given experiment, in units of counts/keV, is obtained by multiplying the differential rate of Equation 1.19 by the mass of the detector target and the total run time of the experiment. This is why it is favourable for direct dark matter experiments to have larger detectors and run for long periods of time, so that this total rate is as high as possible to maximise the probability of detecting a signal.

The velocity distribution, $f(v)$, used in Equation 1.19 is assumed to follow the Maxwell-Boltzmann form of the Standard Halo Model (SHM) [88]. The Gaussian form of this distribution in the galactic rest frame is given by [89]:

$$f(v) = \frac{1}{(\pi v_0^2)^{3/2} N_{esc}} e^{-\frac{v^2}{v_0^2}} \Theta(v_{esc} - |v|). \quad (1.23)$$

Here, v_0 is the rotational speed of the sun around the centre of the galaxy, and v_{esc} is again the galactic escape velocity. For the Milky Way, these values are measured to be $v_0 = 220 \text{ km s}^{-1}$ and $v_{esc} = 544 \text{ km s}^{-1}$. $\Theta(v_{esc} - |v|)$ is the Heaviside function that truncates the velocity distribution at the escape velocity, and N_{esc} renormalises the distribution after this truncation.

The integral in Equation 1.19 can be solved between zero and infinity to give [87]:

$$\frac{dR(0, \infty)}{dE_R} = \frac{R_0}{E_0 r} e^{-E_r/E_0 r}, \quad (1.24)$$

where R_0 is a constant, $E_0 = \frac{1}{2}m_\chi v_0^2$, and $r = 4m_\chi m_N / (m_\chi + m_N)^2$.

The velocity of the Earth relative to the dark matter distribution, v_E , must also be taken into account. This value varies as the Earth orbits the sun, but is given approximately by $v_E \approx 244 \pm 15 \sin(2\pi y)$ km s^{-1} , where y is the elapsed time from approximately the 2nd March, in years [87]. If a finite v_{esc} and a non-zero v_E are taken as limits to the integral in Equation 1.19, it can be shown that [87]:

$$\frac{dR(0, v_{esc})}{dE_R} = \frac{k_0}{k_1} \left(\frac{dR(0, \infty)}{dE_R} - \frac{R_0}{E_0 r} e^{-v_{esc}^2/v_0^2} \right), \quad (1.25)$$

$$\frac{dR(v_E, \infty)}{dE_R} = \frac{R_0}{E_0 r} \frac{\pi^{1/2} v_0}{4v_E} \left(\text{erf} \left[\frac{v_{min} + v_E}{v_0} \right] - \text{erf} \left[\frac{v_{min} - v_E}{v_0} \right] \right), \quad (1.26)$$

$$\frac{dR(v_E, v_{esc})}{dE_R} = \frac{k_0}{k_1} \left(\frac{dR(v_E, \infty)}{dE_R} - \frac{R_0}{E_0 r} e^{-v_{esc}^2/v_0^2} \right), \quad (1.27)$$

where k_0 and k_1 are normalisation constants.

There are different approaches that have been taken for the construction of direct detectors for WIMP dark matter. Some use crystals cooled to very low temperatures, such as the Cryogenic Rare Event Search with Superconducting Thermometers (CRESST) [90], where an incoming WIMP would cause excitation of the crystal lattice. Another approach is to fill the detector with a liquid noble element. These are excellent scintillators so give a high electron and light yield when an incoming particle interacts with them [91], which is ideal for signal detection. They are also relatively unreactive due to their completely filled outer valence shells, which allows for the target material to be kept as pure as possible, although high purity can also be achieved in detectors that do not use noble elements.

Some experiments opt for argon as the target material in such a detector, such as DarkSide [92, 93], but a more common choice is xenon, as was used for the LUX [94, 95, 96], ZEPLIN [97, 98], XENON10 [99], XENON100 [100, 101], XENON1T [102], and PandaX-4T [103] experiments, and is currently being used for XENONnT [104], and LZ [4]. For a 1000 day exposure using a 5.6 tonne fiducial mass of liquid xenon, it was projected that LZ would exclude, at a 90% CL, spin-independent WIMP-nucleon cross-sections of 1.4×10^{-48} cm^2 and above for a 40 GeV/c^2 WIMP [105]. A next generation dark matter experiment is planned to expand on the work of the XENON and LZ collaborations, along with the DARWIN consortium [106], and this future detector is XLZD [107, 108].

Xenon is a particularly good element to use in a WIMP search due to its high mass number that enhances the coherent scattering cross-section, as previously discussed. In addition to this, xenon nuclei are of comparable mass to the hypothesised WIMPs, and therefore the nuclear recoil signal will be kinematically maximised [109]. The high atomic number of xenon and its density in liquid form give it the advantage of very effective self-shielding against external gamma ray backgrounds,

making the centre of the detector relatively background-free, provided that the detector radius is on the scale of ~ 0.5 m or greater.

Because a WIMP interaction with matter would be a very rare event, it is necessary to shield direct dark matter detectors from cosmogenic backgrounds, such as muons produced by cosmic rays interacting with the atmosphere. For this reason, most detectors of this type are shielded under a substantial overburden of rock. This can be achieved by creating a cavern in which to house the detector, either inside a mountain, as is the case for Gran Sasso National Laboratory [110] which houses both the DarkSide and XENONnT experiments, or deep underground, such as at SURF that houses LZ. Both approaches have their benefits and disadvantages. A mountain laboratory allows for much easier detector construction, as components can be simply driven in via tunnels, whereas for an underground laboratory, the size of component that can be transported underground is limited by the size of the vertical shafts that provide access to the facility. However, the minimum overburden for an underground laboratory corresponds to normal incidence of the cosmogenic backgrounds, which will generally not be the case for a mountain overburden. This means that cosmogenic backgrounds with large incident angles (relative to normal incidence) will likely travel through less rock (relative to the vertical overburden) before reaching the detector in the case of a mountain overburden, although this depends on the specific mountain.

Chapter 2

The LUX-ZEPLIN (LZ) Detector

In section 1.4, the different possible approaches that can be taken in a WIMP dark matter search were discussed. While the LUX [95] and ZEPLIN-III [97] experiments were dual-phase TPCs like LZ, the earlier predecessor ZEPLIN-I [111] used a single-phase scintillation detector rather than a TPC. As will be explained in detail later in this chapter, a TPC requires an electric field to drift electrons, that are liberated by an incoming particle, into the gas region where they can produce a secondary signal. The primary signal is due to excitation of the xenon atoms by the incoming particle. In a scintillation detector however, the electric field is not required. This means that ionised target atoms in the detector can recombine and produce an additional photon signal in these types of detector.

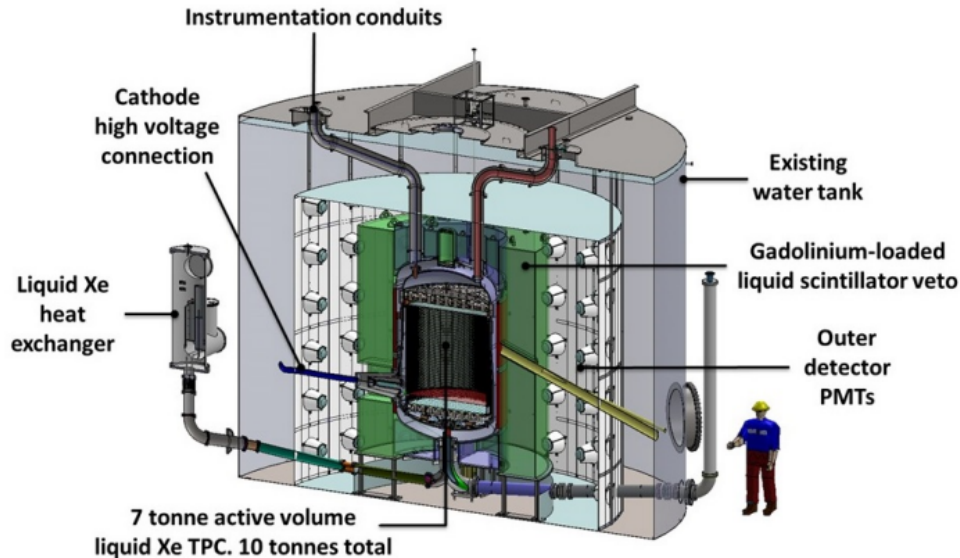


Figure 2.1: *Diagram of the LZ detectors. This figure is taken from Ref [112].*

The work presented in this thesis builds on, and contributes to, the WIMP search of the LZ collaboration [4], which is a direct detection experiment. The LZ detector is a dual-phase xenon TPC containing 7 tonnes of active liquid xenon, located ~ 1.5 km underground at the 4850 ft level

of SURF [113]. This gives an overburden of approximately 4300 mwe [113] to shield the detector from cosmogenic background signals caused by high energy particles undergoing interactions with the atmosphere.

The TPC of LZ is surrounded by two veto detectors. Moving out from the TPC, the first is the 2 tonne liquid xenon ‘Skin’, which is primarily designed to tag gamma photons. The next is the Outer Detector (OD), which contains 17 tonnes of gadolinium-loaded liquid scintillator (GdLS), designed to tag neutrons. All of this is contained within a water tank of 238 tonnes of ultra-pure water [114] to shield the TPC from radioactive backgrounds in the rock surrounding the detector cavern. This detector arrangement is shown in Figure 2.1 [112].

2.1 The Time Projection Chamber (TPC)

The dual-phase TPC of LZ contains 7 tonnes of purified liquid xenon, with a small (8 mm [112]) region of gaseous xenon at the top of the detector. It is mounted in a double-walled titanium cryostat, and it was ensured that this vessel was made out of titanium with minimal radioactive impurities, so as to limit the background signals seen by the detector [115]. Across two arrays at the top and bottom of the TPC are 494 photomultiplier tubes (PMTs) to collect light, and the detector is lined with reflective polytetrafluoroethylene (PTFE), so that minimal light is lost. This setup is shown in Figure 2.2, along with a representation of the typical signals that the PMTs would output. This figure also shows the electrode grids used to apply electric fields across the detector. Between the cathode and gate grids a field is applied to drift electrons up to the top of the TPC. At the top of the liquid phase, between the gate and anode grids, a stronger electric field is applied to extract electrons from the liquid surface. More details of the grids and electric fields in LZ will be provided in section 2.4.

When an incoming particle enters the TPC, if it interacts with the liquid xenon it can do so in one of two primary ways: it can interact with the nucleus of a xenon atom causing a nuclear recoil (NR), or it can interact with the electrons causing an electron recoil (ER). In both cases, the recoiling xenon atom will cause surrounding atoms to be excited into a higher energy state, and also be ionised. As the xenon de-excites it emits photons, referred to as the S1 signal, that are picked up by the PMTs at the top and bottom of the detector. The efficiency for the detection of these photons is written as g_1 , and is maximised by lining the inside of the TPC in reflective PTFE. The electrons released by the ionisation are drifted to the top of the detector and extracted into the gaseous region. This is achieved by the application of electric fields in the detector, and these are described in section 2.4. In the gaseous region the electrons produce electroluminescence photons, referred to as the S2 signal. This signal is primarily picked up by the top PMTs due to their proximity to the gaseous region. It is the thickness of this region at the top of the detector that dictates the width of the S2 signals. The gain of the S2 channel, or the number of photons detected

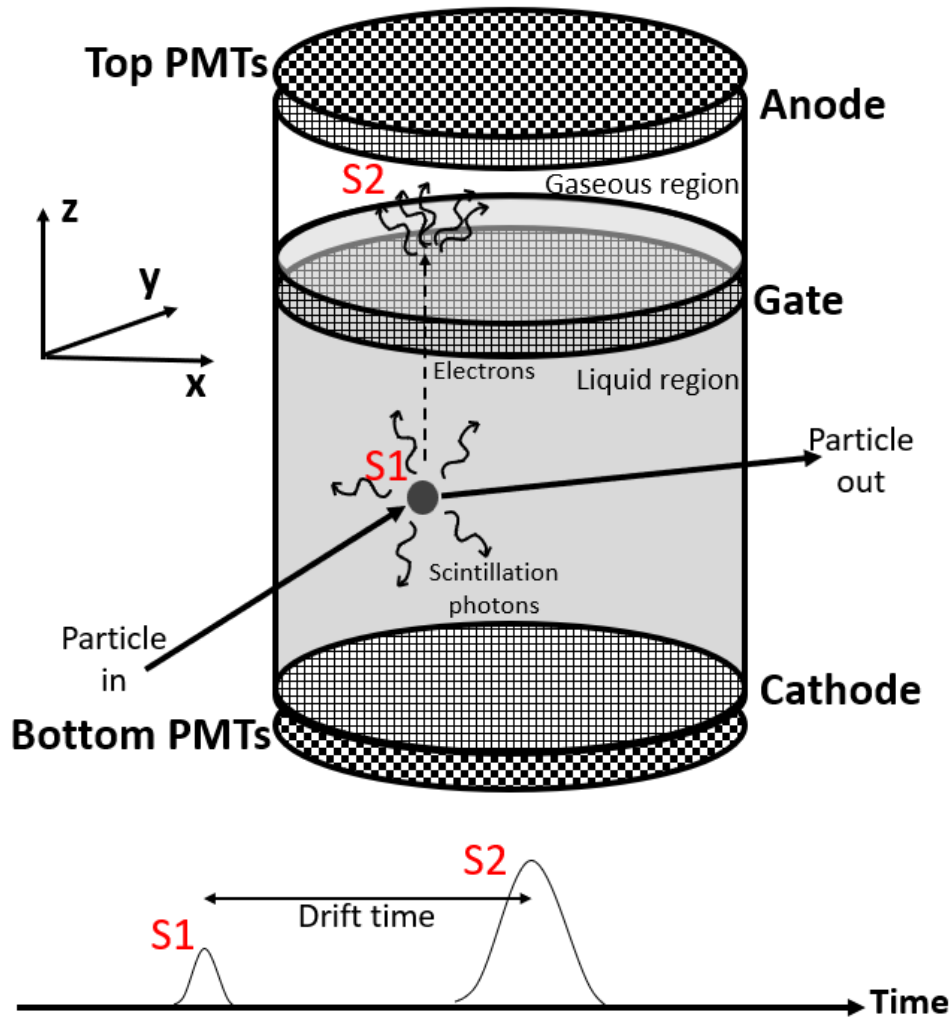


Figure 2.2: Diagram illustrating how signals are generated in a dual-phase noble element time projection chamber. Also shown at the bottom of the figure is an example waveform produced by the PMTs, with an illustration of how drift time is calculated.

per ionisation electron, is written as g_2 . Both the S1 and S2 signals are measured in terms of the number of photons detected by the PMTs (phd). This differs from the units of photoelectrons produced (phe), used by some other experiments such as notably LUX [96], in that it accounts for double photoelectron emission [116].

Since the S1 signal travels at the speed of light in liquid xenon, on the scale of the TPC it can be assumed that the S1 signal is received by the PMTs instantaneously. The time before the PMTs register the S2 signal is governed by the drift time of the electrons, which depends on the depth in the detector at which the interaction occurred. The photon portion of S2 propagation can also be assumed to be instantaneous. Therefore, the time between the S1 and S2 signals gives the drift time of the electrons, and can be used to calculate the depth, or z position, of the event in the TPC. The hit pattern of light on the top PMT array from the S2 signal can be used to establish the xy location from analysis of the probability distributions of PMT output signals (using the

Mercury algorithm [117]), and hence three-dimensional reconstruction of event position is possible in a dual-phase TPC. For ZEPLIN-III for which the Mercury algorithm was developed, spatial resolutions were measured to be 13 mm and 1.6 mm FWHM (full width half maximum) for S1 and S2 signals respectively [117].

There is some positional dependence in the size of the S1 and S2 signals due to factors such as non-uniform electric field and non-operational PMTs. Therefore, S1 and S2 signals are normalised to a central position in the TPC, and these corrected signals are referred to as S1c and S2c respectively. The relative sizes of the S1c and S2c signals from an event allow for discrimination between NR and ER events. This is because scintillation is quenched for NRs, meaning that energy is lost to heat. Additionally, NRs leave denser tracks in the detector, and are assumed to have a higher rate of electron-ion recombination. This makes the collection of ionisation electrons more difficult [118]. Events are plotted in the parameter space of $\log(S2c)$ vs. $S1c$, in which NR and ER events form clear bands, as shown in Figure 2.3. The specific location of an event in this parameter space can indicate the type of particle that interacted with the liquid xenon. This figure is taken from the first LZ WIMP search paper [114] analysing the 2022 LZ WIMP search (WS2022) dataset, and uses deuterium-deuterium (DD) and tritium calibration sources for the NR and ER bands respectively.

The S1c and S2c signals can also be used to reconstruct the recoil energy of the interaction. The so-called ‘Doke formula’ [119] used to calculate this energy is given by:

$$E = N_q \frac{W}{L(E)} = (N_{ph} + N_{e^-}) \frac{W}{L(E)} = \left(\frac{S1c}{g_1} + \frac{S2c}{g_2} \right) \frac{W}{L(E)}, \quad (2.1)$$

where $N_{ph} = \frac{S1c}{g_1}$ is the number of photons generated at the interaction site, and $N_{e^-} = \frac{S2c}{g_2}$ is the number of electrons. N_q is the total number of quanta, and so is the sum of N_{ph} and N_{e^-} . W is the work function of the liquid xenon, taken to be 13.5 eV [120], and $L(E)$ is the Lindhard factor [121], which describes the energy lost as heat rather than as observable excitation and ionisation. This factor is assumed to be 1.0 for ERs, not because no energy is lost to heat, but because the energy loss to heat is approximately constant, and hence can be incorporated into the definition of W . However, for NRs the Lindhard factor is dependent on energy, and so must be included separately in the Doke formula.

2.2 The Skin

It is desirable to utilise additional radiation detectors outside of the TPC because non-WIMP backgrounds, such as gamma rays and neutrons, are likely to undergo multiple interactions with matter in the vicinity of the detector, as well as in the TPC itself. Therefore if this surrounding area can also produce detectable signals for any interactions that occur, a greater understanding of detector backgrounds, and a greater ability to identify them, can be obtained. This also allows for

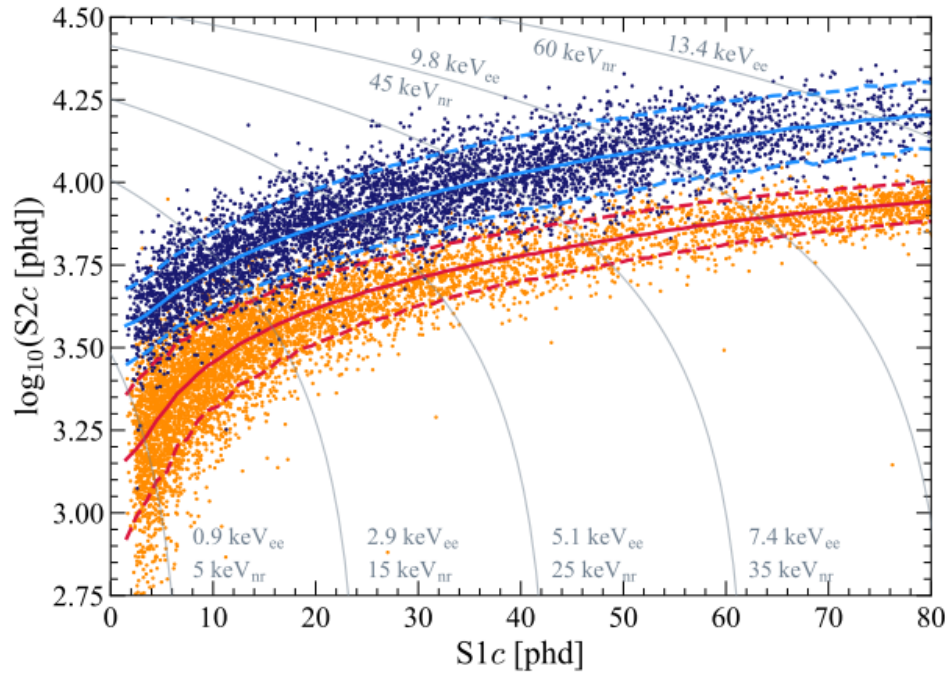


Figure 2.3: NR (orange) and ER (blue) calibration data events illustrating the power to differentiate events by their position in $\log(S2c)$ vs. $S1c$ space. Specifically, this uses WS2022 DD and tritium calibration data for the NR and ER band calibrations respectively. 90-10 CL Gaussian NR (red) and ER (light blue) bands are shown, calculated from simulations. Grey lines indicate the energy contours and are given in both electron-equivalent energy and nuclear recoil energy. This plot was taken from Ref [114].

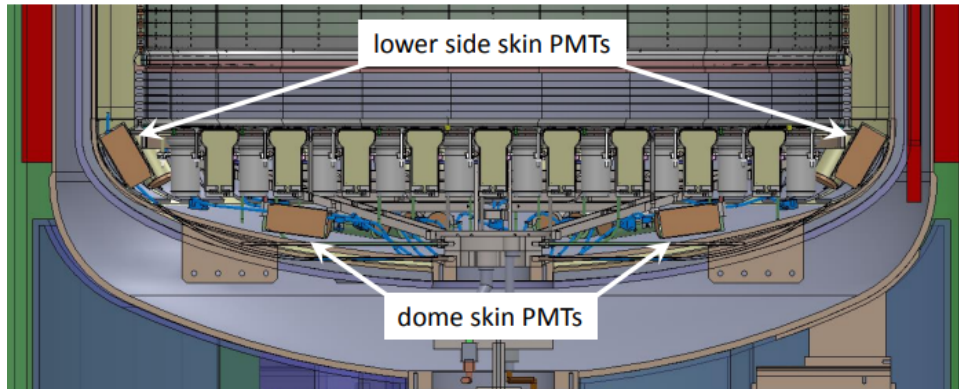


Figure 2.4: Visualisation of the dome and lower side sections of the Skin veto detector, along with the mounting of the Skin PMTs in these regions. This figure is taken from Ref [112].

a better comprehension of backgrounds that may not interact in the TPC at all, and are largely, if not fully, attenuated by the surrounding material.

The first of the two veto detectors used in LZ is known as the Skin, which is an additional volume filled with liquid xenon. Around the sides of the TPC, this constitutes a volume ranging

between 4 cm to 8 cm in thickness [112] that is unavoidable for an incoming particle. There is also a skin volume below the bottom PMT array, known as the dome skin, which contains a greater thickness of liquid xenon. A visualisation of the lower part of the Skin detector is shown in Figure 2.4 [112]. One of the primary uses of the Skin is to veto gamma rays that may leak into the TPC from external interactions. The skin has a total of 180 PMTs around the sides (half looking upwards, half looking downwards), and a further 12 viewing the dome skin.

2.3 The Outer Detector (OD)

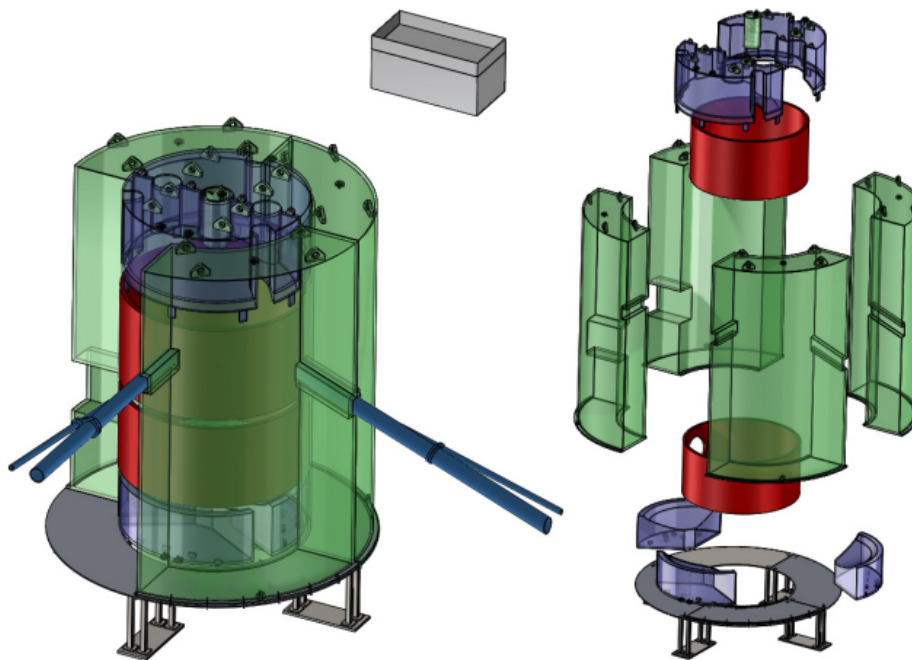


Figure 2.5: *Layout of the outer detector system used in LZ, shown both as assembled (left) and exploded (right). The ten acrylic tanks filled with GdLS are shown in green and blue, the water displacers are shown in red, the stand is shown at the bottom of the detector, and the grey box is the liquid scintillator reservoir. This figure is taken from Ref [112].*

Outside of the Skin is the second veto detector, the Outer Detector (OD), which comprises a large (61 cm thickness of scintillator [112]), clear, acrylic tank containing GdLS. The structure of the OD is shown in Figure 2.5 [112]. A radioassay of this liquid scintillator for use in LZ was carried out in a small detector *ex-situ* [122], finding radioactive contaminants to be sufficiently low for use in LZ. The reason for the gadolinium doping of the liquid scintillator is to increase the neutron capture cross-section, since the primary objective of this detector is to provide veto signals for neutrons. The OD aims to capture neutrons after they have interacted in the TPC so

that they can be tagged, especially if the neutron only interacts once in the TPC and produces a WIMP-like signal. The typical capture time for a neutron in GdLS is $\sim 30 \mu\text{s}$ [112], which is relatively short compared to the maximum drift time of the TPC (which is field dependent and so differs between WS2022 and the 2024 LZ WIMP search (WS2024), but is approximately $1000 \mu\text{s}$). The energy release, of approximately 8 MeV [112], in the form of gamma photons after neutron capture on gadolinium gives a distinctive signal for this type of interaction.

Outside of the OD are 120 PMTs that view the GdLS volume to collect light from the interactions that occur there, hence the need for the outer walls of the OD to be transparent. The OD PMTs are located in a tank containing ultra pure water, with a sufficient distance between the PMTs and the OD such that any gamma rays resulting from radioactivity in the PMTs will be attenuated by the water. The OD PMTs undergo regular calibration by use of the Optical Calibration System (OCS) [123] that shines light into the OD and measures the response. The majority of signals that are seen in the OD are due to the background of gamma rays emitted from the rock of the surrounding cavern. The radioactive contamination levels leading to this were measured to be $220 \pm 60 \text{ Bq kg}^{-1}$ from K-40, $29 \pm 15 \text{ Bq kg}^{-1}$ from U-238, and $13 \pm 3 \text{ Bq kg}^{-1}$ from Th-232, which is consistent with the shotcrete material that was used to coat the cavern walls [124].

In order to understand how many neutrons are evading being tagged by the OD, it is essential to be able to quantify the efficiency of this detector. This was primarily done by LZ for both WS2022 and WS2024 using an AmLi neutron source, but AmBe was also studied [114].

It is important to consider that these sources have a relatively high rate of gamma production, which can artificially elevate the neutron tagging efficiency if it is not properly accounted for. The selection for these studies applied most analysis cuts, and only took events within 1σ of the NR band mean. The number of events in this selection formed the denominator of the efficiency. For an event to be counted in the numerator it was required that it have an OD pulse with a coincidence greater than 5 PMTs within 300 ns of the TPC S1 signal. Failing this, an event was also vetoed if the largest OD pulse in a given time window from the S1 was above a certain threshold. The values for this time window and threshold can be varied, but for WS2022 were set at $1200 \mu\text{s}$ and 200 keV/ 37.5 phe respectively. When calculating the overall veto efficiency for LZ, events with a veto signal in the Skin were also included in the numerator of the efficiency.

2.4 Electric Fields in LZ

It has already been mentioned that it is necessary to apply electric fields across the TPC in order to drift electrons in the liquid towards the surface, and also to extract them from the liquid surface and into the gaseous region. This is achieved by the use of four electrode grids [125] and a field cage embedded in the PTFE panels, which line the inside of the TPC, that shapes the electric field.

Each of the electrode grids consists of a fine wire mesh to optimise optical transparency, and the four grids are (in descending order from the top of the detector) the anode, the gate, the cathode, and the bottom PMT shield grid. These electrode grids divide the TPC into three distinct regions: the electroluminescence region, the drift region, and the reverse field region (RFR). A diagram of these regions is shown in Figure 2.6.

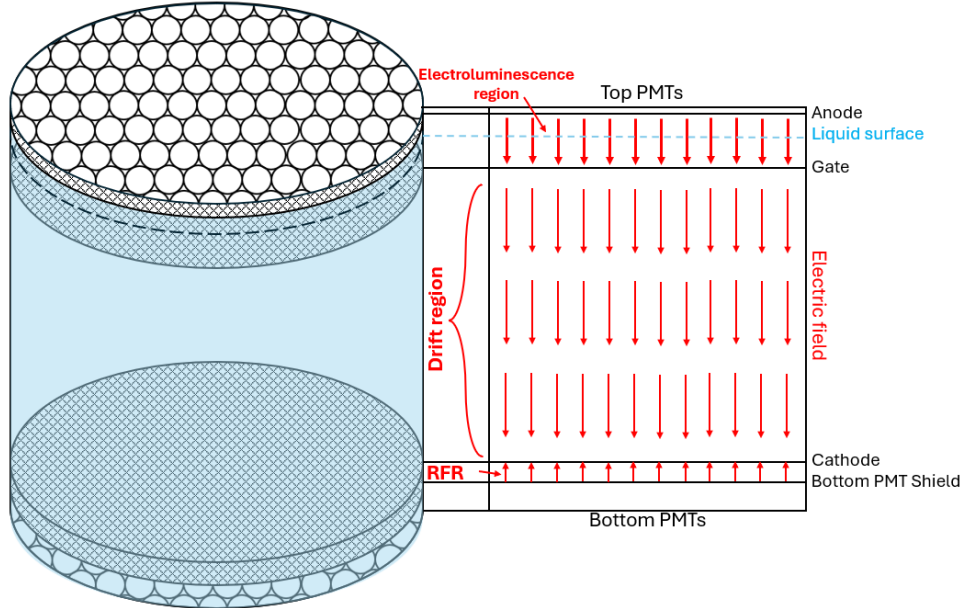


Figure 2.6: Diagram illustrating the position of the electrode grids in LZ and the resultant regions of electric field.

The electroluminescence region is between the gate and the anode, which create an electric field that is significantly stronger than the drift field. This is the field that extracts electrons from the liquid surface and causes the electroluminescence that gives rise to the S2 signal as the electrons travel towards the anode, where they are collected. This field is stronger by a factor of approximately two in the gas phase than in the liquid phase due to the relative permittivity. For WS2022, this field strength was 7.3 kV cm^{-1} in the gas phase at radial position $r = 0$ [114]. For WS2024 the field strength below the liquid surface, again at $r = 0$, was 3.4 kV cm^{-1} [126]. The separation between the gate and anode electrodes is 13 mm, with the liquid surface 5 mm above the gate [112].

The drift region between the cathode and the gate contains the active volume of liquid xenon that is used as the target in the WIMP search, and is therefore the most important region of the TPC. For WS2022, the drift field was 193 V cm^{-1} [114], and for WS2024 the field was lowered to 97 V cm^{-1} [126] due to the presence of persistent light emission localised to the Skin region below the cathode. It is essential that the electric field in this region is as uniform as possible, with field lines running parallel to the walls. This is so that the drift of electrons produced during interactions can be well understood, and the electrons will travel vertically upwards to the liquid surface, and

therefore always produce an S2 electroluminescence signal for an event. Non-uniformities in the field could lead to charge loss at the walls of the detector, and lead to difficulties relating an S2 to the corresponding S1.

Finally, the RFR is the region located between the bottom PMT shield and cathode grids. This region was constructed to be as small as possible so as to limit the number of events occurring in this area, since an event with a scatter in the RFR and in the active volume can mimic a WIMP signal (although such events are easily removed by a fiducial volume (FV) cut that requires events to be in some central volume of the detector). Minimising the volume of the RFR region also reduces the quantity of liquid xenon it contains, which is expensive to acquire and is much better utilised in the active volume. Electrons in this region are drifted downwards such that they do not produce an S2 signal.

2.5 Xenon Circulation System

To minimise backgrounds and to maximise the quality of signal generation and propagation in the TPC, it is important that the purity of the xenon target is kept as high as possible. This purification is carried out by an inline radon reduction system, utilising charcoal [127] and a heated zirconium getter [128]. The getter is filled with pellets of zirconium alloy, through which the gaseous xenon is passed. Zirconium is very reactive and bonds with nearly all non-noble gases that pass over the surface of the pellets [129]. The high temperatures encourage the impurities at the surface of the pellets to diffuse further into the bulk, thus leaving the surface available for further bonding.

Crucially, the getter requires the xenon to be gaseous, and so the liquid xenon from the TPC must be heated and evaporated into the appropriate state for purification. When being re-introduced into the TPC, the xenon must be back in liquid phase, and so must be cooled and condensed. These two requirements are tackled simultaneously by use of a two-phase heat exchanger [112].

In order to facilitate the circulation of xenon in LZ, after being condensed the liquid xenon is channelled into the bottom of the TPC. Xenon is removed from the top of the TPC for purification by use of a weir system, located between the gate and anode grids, over which the liquid xenon can flow as more is introduced from below. This is illustrated by Figure 2.7 [112]. Circulation is driven for the gaseous xenon by up to two gas compressors [112], which reduce the volume and hence increase the pressure of the xenon.

There are, broadly speaking, two circulation states in which the LZ TPC can operate, and these are referred to as ‘high-mixing’ and ‘low-mixing’ due to the effect that they have on the movement of radioisotopes within the TPC. The choice of state is controlled by the cryogenics and circulation systems. In the high-mixing state, radioisotopes and calibration sources are distributed uniformly

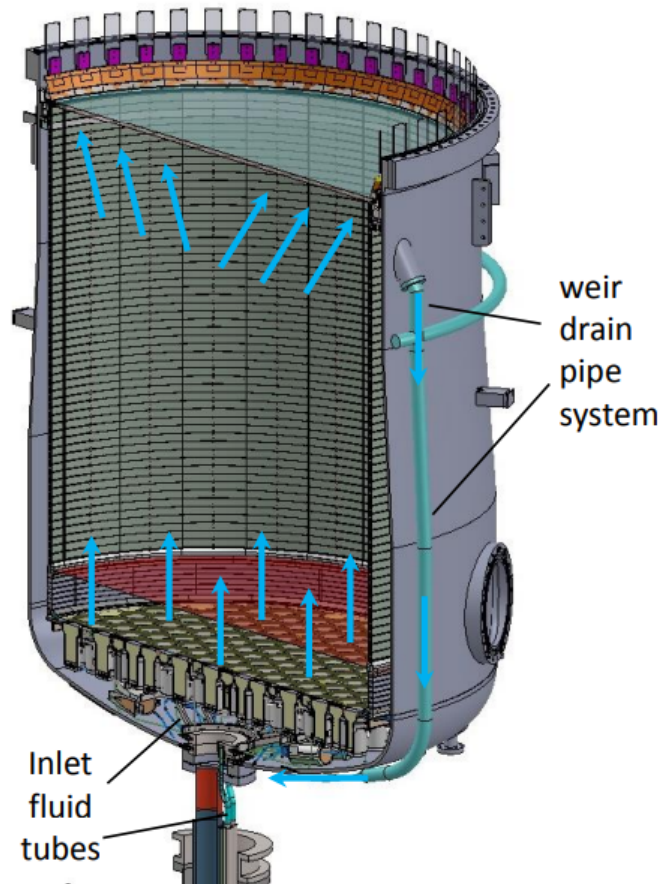


Figure 2.7: *Cutaway of the LZ TPC, with the flow paths and circulation system elements indicated. The flow of xenon over the weir can be seen towards the top of the figure. This figure is taken from Ref [112].*

throughout the TPC volume, whereas in the low-mixing state distinct regions of laminar flow can be seen. The understanding of the flow in this state is used for the development of a cut to remove the prominent Pb-214 ER background that occurs in the radon decay chain [126].

2.6 Cryogenics and Vacuum Systems

Liquid xenon is preferable over gaseous xenon as a detector medium due to its higher density (3 g cm^{-3} [112]), high scintillation yield, and due to the fact that the charge quenching of NRs in liquid xenon leads to better NR ER discrimination. At atmospheric pressure, xenon has a relatively small range of temperatures over which it will be in its liquid phase (around 162-165 K) [119]. Compared to other noble gases, the boiling point of xenon is relatively high [130], which is another advantage of choosing xenon as a detector medium. However, in order to keep the xenon in the detector in its liquid phase, a cryogenics system is still required to provide cooling, and for LZ this is done using nitrogen in liquid and gaseous phases [112].

To keep the xenon gas as pure as possible, surrounding volumes are continuously pumped to a vacuum and monitored for any change in pressure that could indicate a leak, either of xenon gas or of outside air into the vacuum space.

2.7 Electronics

Even with the all of the shielding and background minimisation, LZ still collects large amounts of data that have to be processed by a data acquisition (DAQ) system [131]. Much of this was developed from the data acquisition system of the predecessor to LZ, LUX, that was also housed in the Davis cavern of SURF [132].

It is of critical importance to LZ that the PMTs are monitored and well looked after, since replacement before decommissioning of the experiment is not possible. PMT trips can cause the loss of WIMP search live time as detector conditions are not stable while PMTs are being re-biased, and hence data collected in this time is not usable science data. A schematic of the signal processing chain for the TPC PMTs is shown in Figure 2.8 [112], which utilises dual-gain signal processing. Digital filters of various lengths are used to distinguish S1 and S2 pulses, information which can be used for the purposes of triggering (see section 2.9.1).

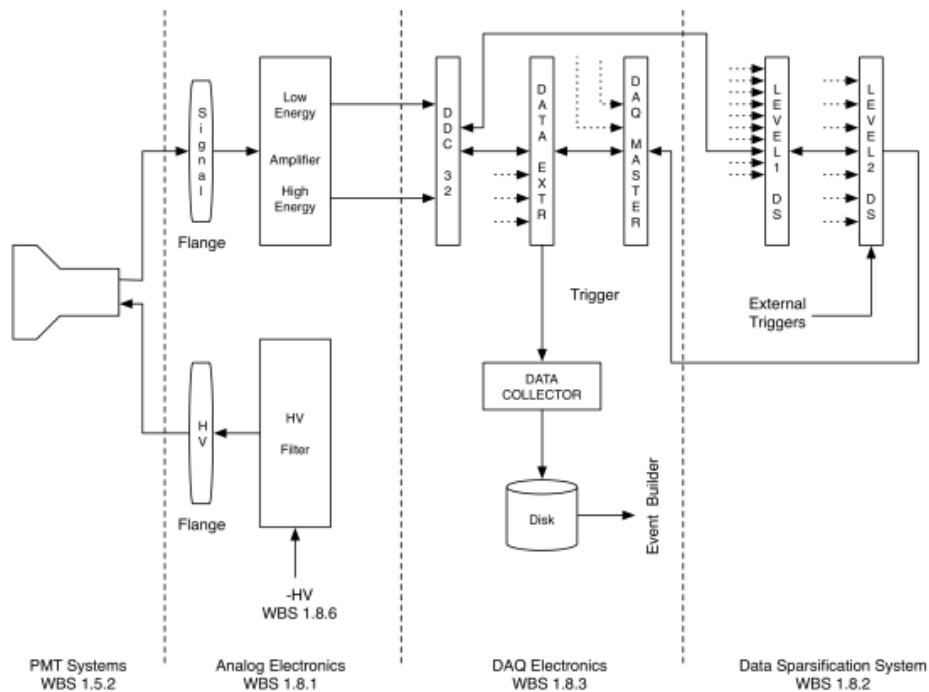


Figure 2.8: Diagram of the signal processing for the TPC PMTs. These PMTs use dual-gain signal processing. This figure is taken from Ref [112].

2.8 Calibrations

Calibration of the detector is a critical part of any experiment as it allows understanding of the detector response to a range of different incoming particles to be developed. This is done by exposing the detector to a source of particles that are produced by a well understood process and at a well understood rate. In the case of LZ, the sources used in calibration can be broadly separated into NR sources and ER sources, and the signals produced by these calibrations in $\log(S2c)$ vs. $S1c$ space can be used to create Gaussian bands in which the majority of NR and ER events would be expected to lie. For LZ, the NR and ER bands are usually produced using simulations of the calibration sources, then verified with calibration data. Full details of the LZ calibration systems can be found in Ref [133].

In order to expose the detector to a large enough number of events from a calibration source, it needs to be ensured that the incoming particles are able to penetrate into the TPC. There are three methods of doing this for the LZ detector. The first method is to use the calibration source deployments (CSDs), three tubes at the top of the detector that extend down next to the TPC, down which radioactive sources can be lowered. The details of this system will be covered in section 2.8.1. The second approach to exposing the TPC to a calibration source is to inject the source into the xenon flowing into the TPC. This procedure is detailed in section 2.8.3. The final method is the use of a DD neutron generator for NR calibrations, where the neutron beam is allowed to travel down a conduit and into the TPC. Discussion of this process will be in section 2.8.4.

2.8.1 CSDs

The CSDs, as previously mentioned, are three tubes that protrude from the top of the LZ water tank and allow for radioactive sources to be lowered down into a position next to the TPC, from which high signal rates can be produced [112]. Motors are in place at the top of the CSD units to lower the sources down to the desired z position, relative to the detector, using a deployment filament of strong, thin, nylon composite. The position of the source is determined using a laser based position monitoring system. The design of the CSD system is illustrated in Figure 2.9 [112].

When calibrations are carried out using the CSDs, the xy signature in the detector is distinctive, as the rate of interactions is greatest next to the CSD(s) where the source is located. Similarly, the highest rates in drift time, or z , would be expected at the height to which the source had been lowered. An example of the positional distribution of events for a CSD deployed source, specifically an AmLi neutron source, is shown in Figure 2.10, for reference. The positional features seen in the figure are purely due to the calibrations infrastructure of the detector, and there is no physics reason why certain areas of the detector see higher rates here. The events in the figure are shown relative to the FV and active volume, where the FV is defined such that only a small percentage of

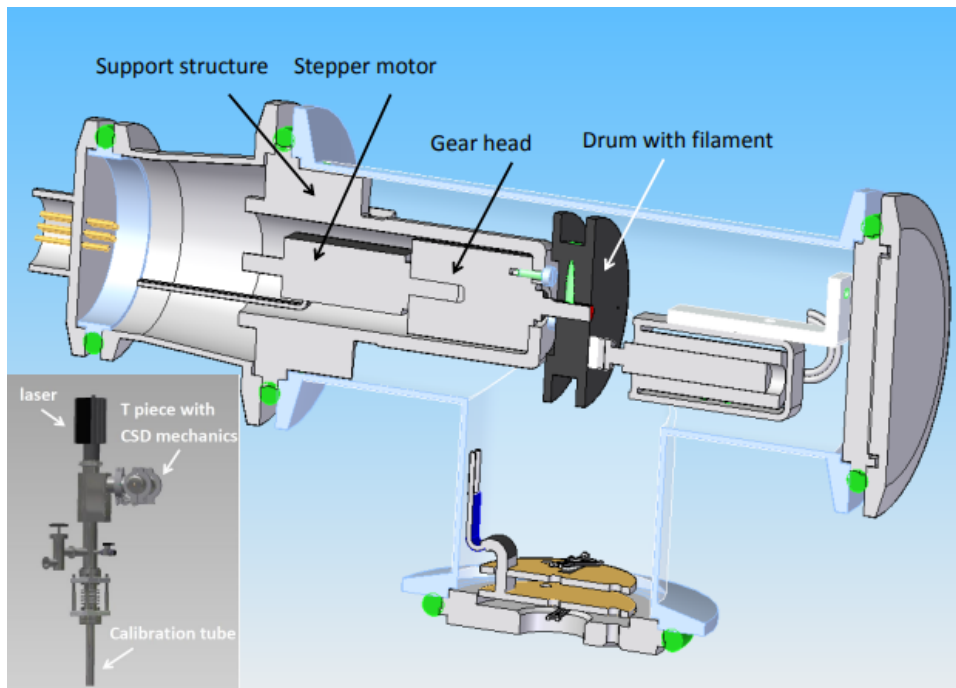


Figure 2.9: *Design of the CSD system. The figure shows the internal components of the T piece, along with how this component fits within the overall CSD system, in the bottom left of the figure. This figure is taken from Ref [112].*

the high rate of events occurring near the TPC walls is allowed inside the FV. The FV is discussed further in section 4.2.1 and section 6.2.1 for WS2022 and WS2024 respectively.

In the first of the two plots included in this figure, the positions of the three CSD tubes are clear at approximately the 7 o'clock, 11 o'clock, and 3 o'clock positions. In the second plot, events can be seen clustered around a drift time of $\sim 550 \mu\text{s}$, which corresponds to the height of 700 mm to which the source was deployed.

2.8.2 Alpha Neutron Sources

For the work presented in this thesis, two of the most important calibration sources that utilise the CSDs are the AmBe and AmLi neutron sources. The AmBe source can provide recoil energies in excess of 300 keV [112], whereas AmLi gives a distinct endpoint at around 40 keV due to a maximum neutron energy of 1.5 MeV [134]. These sources combine an alpha emitter (americium) with a target material (beryllium and lithium respectively). The emitted alpha particles are absorbed by the target, which is transmuted into a different nuclide that is usually in an excited state. This excited nuclide will primarily decay by the emission of neutrons, or be produced alongside a neutron, making these combinations of elements very effective neutron sources. However, the excited nuclide can also decay from the excited state by the emission of gamma photons, which can present an additional background during calibrations that use these sources. An example decay

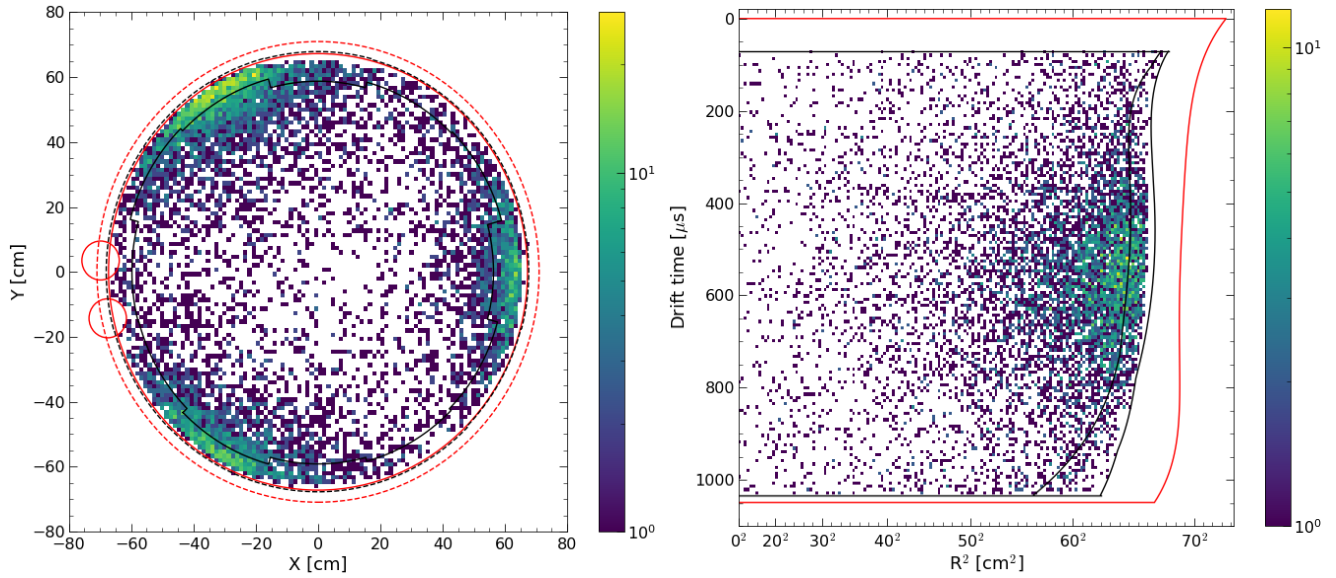
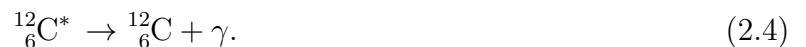
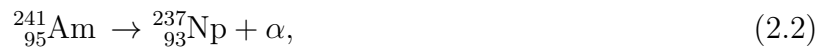


Figure 2.10: *The spatial distribution, after analysis cuts, of WS2024 SS AmLi calibration data, with the source lowered to 700 mm in the CSDs. This data is the combination of three calibration datasets, during each of which the source was lowered down one of the three CSDs to the target height. Shown here is the distribution of events in the xy plane (left), where the red lines show the ϕ -averaged active volume edges at the top (dashed) and bottom (solid) of the active volume. Similarly, the black lines show the ϕ -varying fiducial edges at the top (dashed) and bottom (solid) of the fiducial volume (FV). The smaller circular regions at the 9 o'clock position indicate areas that are cut due to higher rates that are seen because of the field cage resistors. Also shown in this figure is the distribution in R^2 vs. drift time space (right), where the red line indicates the boundary of the active volume of the detector. The black lines show the minimum and maximum squared radii of the FV as radius varies with ϕ , for each value of drift time.*

chain for AmBe, that produces a neutron and a gamma photon, is [135]:



2.8.3 Source Injection

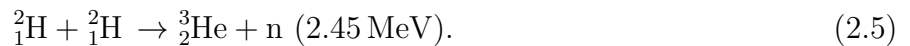
Another way to introduce a calibration source into the TPC is to inject controlled amounts of activity into the flow path of xenon circulation (described in section 2.5). Once the required

amount of radioactive gas has built up inside an emanation source that is installed in the circulation system, a small flow of xenon gas is allowed to pass through it. This xenon is then re-introduced into the main circulation. Examples of sources that are injected into the detector in this way are Kr-83m and Xe-131m. Kr-83m decays at an energy of 41 keV with a half-life of 1.8 hours, whereas Xe-131m decays at an energy of 164 keV and with a half-life of 11.9 days [112]. Once injected into the xenon flow, elevated rates will be seen in the TPC until a sufficient amount of time has passed for the radioactive source to have decayed away. Due to the much higher half-life, this period is much longer for Xe-131m than it is for Kr-83m. The end time for calibrations carried out in this way occurs when the activity drops low enough such that usual background rates dominate. This is distinct from the sharp cut off seen when other types of source are removed, such as for calibrations that use the CSDs.

Tritiated methane (CH3T) is also injected in a similar fashion, but is stored externally in a pressurised bottle that fills an evacuated dosing region, through which the xenon carrier gas is allowed to flow [112]. The energy spectrum for CH3T beta decay is broad, with an endpoint at 18.6 keV. It also has a long half-life of 12.3 years [112], so the use of it in calibrations relies heavily on the fact that it can be effectively removed by the getter during xenon circulation, otherwise the detector would be contaminated with a dominating gamma background.

2.8.4 DD Neutron Generation

For the work presented in this thesis, there is a strong argument that the most important calibration source is the DD neutron generator [136, 137]. This differs from the previous neutron sources discussed, namely AmLi and AmBe, as DD does not rely on radioactive decay, but rather a fusion reaction, to create neutrons. Specifically, 2.45 MeV neutrons are produced by the fusion of two deuterium nuclei, according to the process described in:



The DD generator exploits this interaction by accelerating deuterium ions in a plasma towards a target using an electric field [138]. The ions are implanted in the target and are then present to undergo fusion with subsequent incoming deuterium ions. This means that neutron production initially increases up to the point at which the target is saturated, after which a constant rate of neutrons is produced.

The nuclear recoil energy deposited by these neutrons in the detector can be calculated under the assumption that the collisions are elastic, with the maximum nuclear recoil energy occurring for a head-on collision. For a neutron of mass m_n colliding head on with a nucleus of mass m_{Xe} under these assumptions, both kinetic energy and linear momentum will be conserved in the interaction, hence it can be shown that [15]:

$$u_n - u_{Xe} = v_{Xe} - v_n, \quad (2.6)$$

where u represents the velocities before the collision and v represents the velocities after the collision. Since the mass of the xenon nucleus is very large compared that of the neutron, in the centre-of-mass (COM) reference frame $u_{Xe} \approx 0$. Using this, along with the conservation of momentum once more, it follows that:

$$v_{Xe} = \frac{2m_n u_n}{m_n + m_{Xe}}, \quad (2.7)$$

and subsequently that:

$$E_{Xe} = E_n \frac{4m_n m_{Xe}}{(m_n + m_{Xe})^2}, \quad (2.8)$$

where E_{Xe} is the recoil energy of the xenon nucleus, and E_n is the energy of the incoming neutron. For neutrons of energy 2.45 MeV, this corresponds to an endpoint of the DD energy spectrum at 74 keV. Equation 2.8 can be generalised for cases where the scattering angle in the COM frame, θ_{COM} , is not π radians (as it is for a head-on collision), and this generalisation is given by[139]:

$$E_{Xe} = E_n \frac{4m_n m_{Xe}}{(m_n + m_{Xe})^2} \frac{(1 - \cos(\theta_{COM}))}{2}. \quad (2.9)$$

For LZ, the DD generator is positioned outside of the water tank, and can produce up to 10^9 neutrons per second released over a full 4π spherical solid angle [112]. These neutrons are then channelled through the water tank and outer detector to reach the internal xenon volume by dedicated conduits. This means that when DD calibration data is looked at in terms of the reconstructed three-dimensional position of events, there is a higher rate of events at the closest point to the end of the conduit in the TPC, and then continuing along the beam line. This is illustrated in Figure 2.11. In both of the plots shown in this figure, the position of the DD conduit is clear and is located at around the 9 o'clock position, at the top of the TPC.

This is an extremely useful NR calibration source as it provides a source of monoenergetic neutrons (albeit smeared into a Gaussian energy distribution). True neutron interactions can also be further identified in the case of DD calibrations by relating the time of the event to the pulsing of the neutron beam. Overall, this provides a source of neutrons with considerably fewer background signals than either the AmLi or the AmBe neutron sources, which is why DD is the main NR calibration source that was utilised in the work described over the coming chapters.

2.9 Interpreting Signals

It was discussed in section 2.1 how S1 and S2 signals are produced by an incident particle interacting with the liquid xenon in the TPC, and how these signals are detected by two arrays of PMTs,

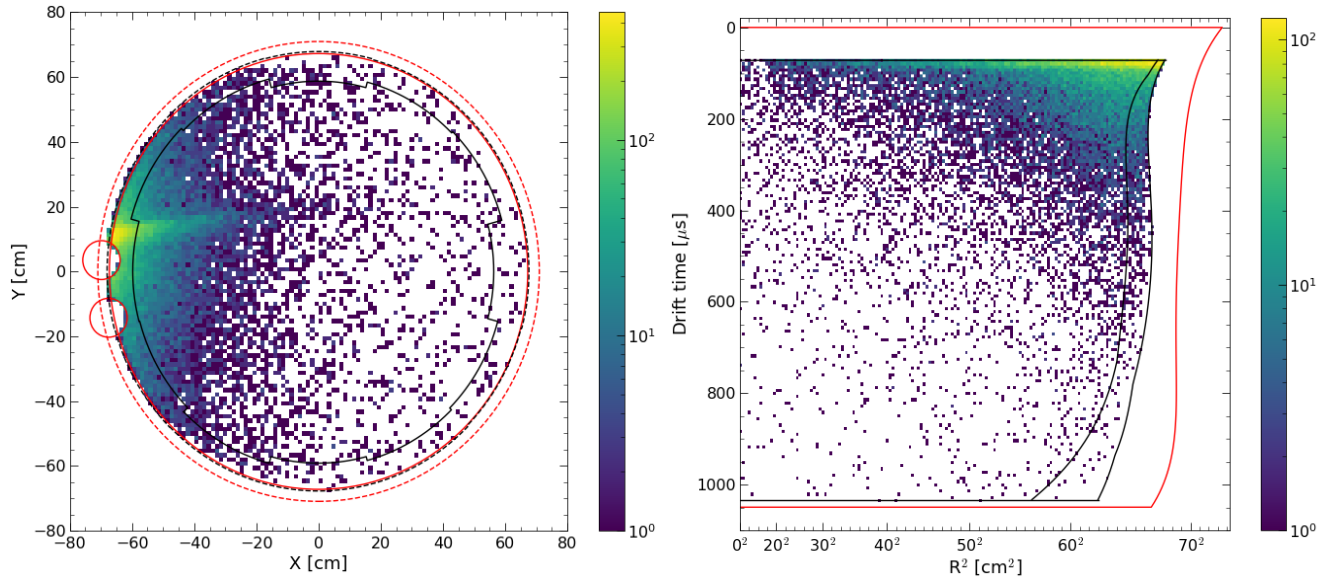


Figure 2.11: *The spatial distribution of WS2024 SS DD calibration data, after analysis cuts. Shown here is the distribution of events in the xy plane (left), where the red lines show the ϕ -averaged active volume edges at the top (dashed) and bottom (solid) of the active volume. Similarly, the black lines show the ϕ -varying fiducial edges at the top (dashed) and bottom (solid) of the FV. The smaller circular regions at the 9 o'clock position indicate areas that are cut due to higher rates that are seen because of the field cage resistors. Also shown in this figure is the distribution in R^2 vs. drift time space (right), where the red line indicates the boundary of the active volume of the detector. The black lines show the minimum and maximum squared radii of the FV as radius varies with ϕ , for each value of drift time.*

at the top and bottom of the detector. In this section, the process following that measurement will be discussed in order to explain how the analysis methods presented in this thesis can be carried out on the data. To do this, the interpretation of the waveform output of the PMTs must first be considered. In addition, the triggers for a waveform to be saved must be established. Following this, this section will cover the classification of different pulse types and event types by the LZ Analysis Package (LZAP) software. Finally, the useful reduced quantities (RQs) that can be extracted from these waveforms and used for analysis will be discussed.

2.9.1 Waveforms and Triggering

Each individual PMT in the TPC produces an output waveform showing how voltage varies over time. The amplitude of the voltage output from the PMTs is proportional to the number of photons detected. All of these waveforms can be summed to give the total signal output of LZ. When a sufficiently large pulse of light is seen, this triggers the saving of a window of time 2.0 ms before and 2.5 ms after the pulse (in WS2022 [114]). The triggering requirements can be fine

tuned such that there is the requirement of an S2 signal, or it can be a global trigger that can be triggered by any type of pulse. The trigger can be set to look for pulses in any of the TPC, Skin, or OD, and waveforms in the event window will be saved for all three of these detectors in any case.

S2 pulses can be distinguished from S1 pulses by their distinctive shapes, shown in Figure 2.12. S2 pulses consist of a build up of numerous single electron (SE) pulses, and S1s likewise consist of a build up of single photoelectron (SPE) pulses. The shapes of these constituent pulses are also shown in Figure 2.12.

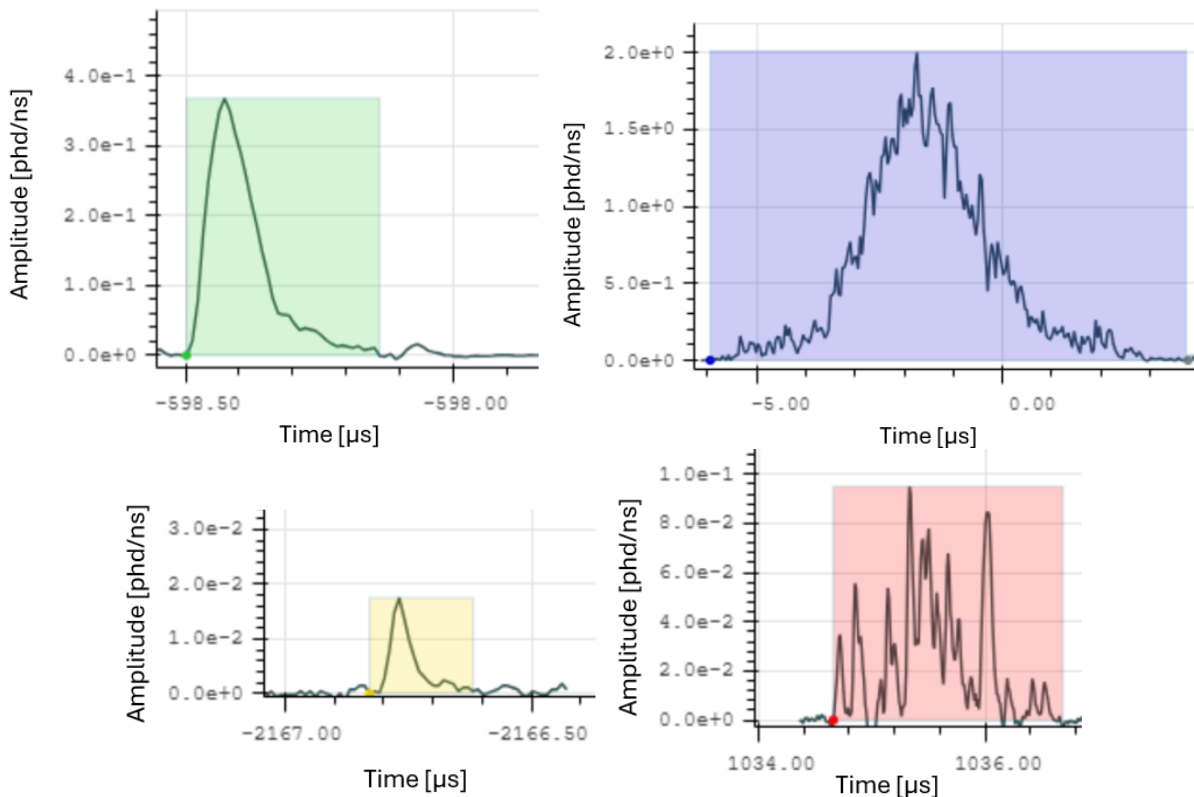


Figure 2.12: Examples of the typical shapes of S1 (top left), S2 (top right), SPE (bottom left), and SE (bottom right) pulses in a dual-phase TPC. Times are relative to the pulse on which the event triggered.

SE pulses have a longer, more jagged shape relative to SPE pulses. This is because they represent a single electron being extracted from the liquid surface then undergoing electroluminescence, during which multiple interactions in the gas occur. Therefore, some S2 light is emitted by each of these interactions. Conversely, SPEs represent a single photon of S1 light reaching the PMTs, and so have a much sharper shape. SEs and SPEs are detected regularly on their own due to a variety of background processes, such as radiation from the detector surroundings and components, or

spontaneous emission of electrons from the electrode grids. However, it is only when a sufficient number of SEs or SPEs occur at once that a signal constitutes an S1 or S2.

An example of an event waveform is shown in Figure 2.13, and examples of the four types of pulse mentioned above can be seen here, with S1s in green, S2s in blue, SEs in red, and SPEs in yellow. Pulses that did not look like any of the above are classified as ‘other’, in grey. This classification of pulses in the waveform is performed by LZAP.

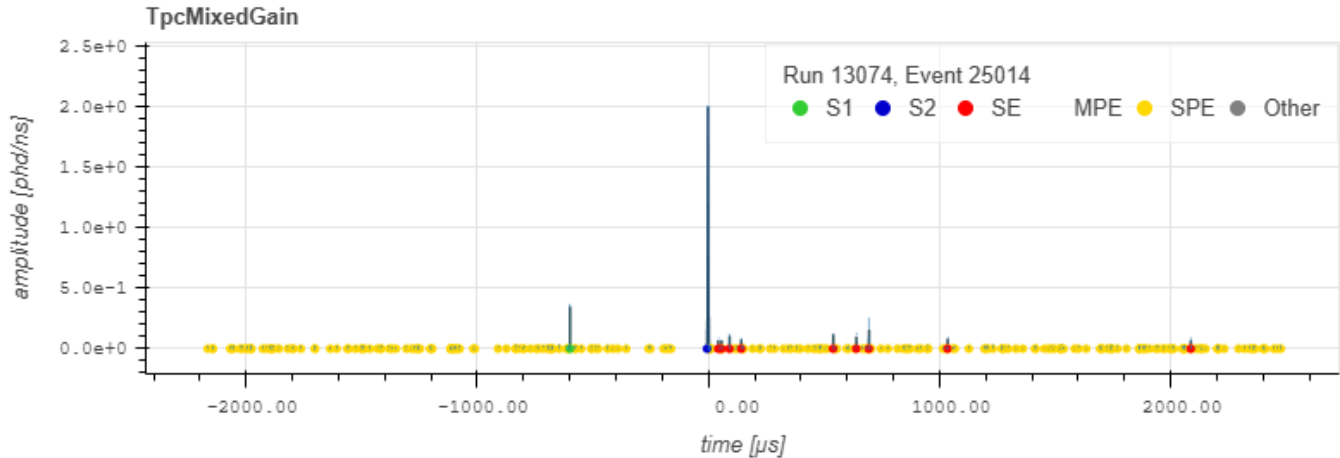


Figure 2.13: An example waveform for an SS event containing an S1, an S2, and multiple SEs and SPEs. Different pulse types, as identified by LZAP, are colour-coded, with S1s in green, S2s in blue, SEs in red, SPEs in yellow, and ‘other’ pulses in grey. This waveform displays the pulse amplitude against time from the pulse on which the event triggered. In this case this is the S2, as detected by the TPC PMTs.

2.9.2 LZAP

LZAP is a software package used for the identification of different pulse types [112]. To do this, it looks for the distinctive sharp shapes of the S1 and SPE pulses, and the jagged multiple pulses of an SE, or the Gaussian-like shape of an S2. Pulse classification is achieved using a threshold based algorithm that looks at four parameters: coincidence, prompt fraction, height-to-width ratio, and pulse area. To establish when multiple SEs or SPEs become an S2 or S1 respectively, a threshold is set as to the minimum number of PMT channels in which a simultaneous signal is required, and this variable is referred to as the coincidence. The prompt fraction variable looks at the total area of the pulse, in a given time window from its start time, relative to the total size of the pulse. This essentially quantifies how much of the signal is at the beginning of the pulse. The different pulses are further distinguished by the height-to-width ratio and the pulse area, since it was shown in Figure 2.12 that the different pulses have notably different shapes and sizes.

Once all pulses have been classified, LZAP also performs event classification. This is a crucial step as this is where events are classified as single scatter (SS), multiple scatter (MS), pile-up, or

‘other’. An SS event has one S1 followed by one S2. There will likely also be SEs and SPEs in the event, and potentially smaller S1s or S2s that LZAP has deemed unlikely to be correlated with the event. An MS event will have one S1 pulse followed by multiple S2s. The reasons for this are covered in detail in section 3.2, but it is due to S1 light from the individual scatters arriving essentially simultaneously, whereas the S2 pulses are separated in time. A pile-up event will have multiple valid S1s and S2s, but it is not possible to identify for certain which S1 correlates with which S2(s), hence this type of event is usually difficult to use for any meaningful analysis. The final classification possibility is ‘other’, which is a class reserved for events that don’t fit into any of the previous categories, such as events with multiple S1s but only one S2, for example. For the majority of the work presented in this thesis, MS events are selected exclusively based on their LZAP classification, but the MS NR selection from data in chapter 5 also considered some ‘other’ type events that had veto detector signals and were seen by eye to be potential MS events. In most cases however, the loss of MS events that are classified as ‘other’ forms part of the systematic uncertainty due to LZAP classification.

The classification efficiencies of LZAP for the version used in WS2024 were found by P. Brás *et al.*, utilising ‘handscanning’ campaigns. This entails analysts manually looking at a selection of event waveforms to identify pulse and event classifications, and comparing these classifications with those produced by LZAP. For SS events, the LZAP identification efficiency of S1 and S2 pulses was studied as a function of S1 and S2 area respectively. A study has not yet been carried out to evaluate the efficiency for identifying MS events, but this is planned for the future and would quantify a systematic error that has an impact on the work presented in this thesis.

There are numerous reasons that could lead to misclassification of an event, but the crucial area of interest for this work is misclassifications involving MS events. This could be either a true MS event being classified as something else, or a non-MS event being classified as MS. One example of the former would be a true MS event with two S2s that occur too close in time and/or space to be resolvable by LZAP as two pulses, and the event would therefore be classified as SS.

The work presented in chapter 3 onwards mostly relies on the LZAP classification of MS events. Therefore, there will be an additional background of MS-classified non-MS events, and MS events that are not classified as MS will be lost from the analysis. This is thought to have a relatively small effect on the overall analysis due to a high LZAP identification efficiency, but future work is aiming to quantify this for MS events.

2.9.3 Reduced Quantities (RQs)

Once LZAP has classified pulses, and subsequently classified events, meaningful variables can then be extracted from the saved waveforms, and these are referred to as reduced quantities (RQs). There are many of these, but only some of those most relevant to this work will be discussed here.

Firstly, all LZ data is divided into runs, each of which contains a set number of events. This

allows WIMP search runs to be distinguished from calibration runs (see section 2.8), or any other run that should not be included in the WIMP search, for example if work in the detector cavern was producing additional background noise during a particular run. Therefore, to identify individual events, each run is allocated a run number and each event within that run is allocated an event number.

Two crucial RQs that are extracted are the S1 and the S2 (subsequently corrected to S1c and S2c). These are obtained from the area of the relevant pulses in the waveform. This depends on where the start and end points of the pulses are set, and this is again something that is managed by LZAP. This means that pulse start and end times are also accessible RQs. For an MS event, as previously mentioned, there is one observed S1 signal and multiple S2s. This means that the S1 RQ is a scalar, but the S2 RQ is a vector of size N , if N is the number of scatters in the event. However, the spatial correction depends on the drift time (or equivalently the z depth in the detector), and there are N different drift times between the S1 and the S2s. Consequently, when the spatial correction is applied, the S1 is corrected separately for each of the different drift times, and so S1c is a vector of size N . The drift time selection for the S2s is trivial, so S2c remains a vector of size N . When S1c is used in the work presented in this thesis, it will be an S2c-weighted average value of the entries in the S1c vector, so that there is only one value of S1c, as is observed for the S1.

As was covered in section 2.1, LZ is able to produce spatial reconstruction of events. This means that x , y , and drift time can be found for an event, and these are important RQs for position reconstruction as well as for the aforementioned spatial corrections to the S1 and S2 signals. x and y are obtained from the hit pattern of PMTs on the top array using the Mercury reconstruction algorithm [117]. With knowledge of the electron drift field, drift time can be directly converted to z position in the TPC. For an MS event, there will be N x positions, y positions, and drift times, so the RQs for all of these will be vectors of size N .

RQs are also available containing information from the waveform outputs of the Skin and OD. As will be covered in section 3.1.1, there are a few of these RQs that are particularly relevant for this analysis. Firstly, as with the S1 and S2 areas in the TPC, the area, in phd, of a pulse in the veto detectors can be found, as can the start and end points of any pulses. Start times of pulses in the veto detectors are particularly useful to compare to the start time of the S1 pulse in the TPC to establish if there is correlation between a veto signal and a TPC signal. Another useful RQ is the coincidence of a veto signal, which indicates how many PMTs detected it. That is obtained by looking for a signal at that specific time across the individual PMT waveforms, rather than just looking at the total summed waveform.

2.10 Simulations

An essential part of any rare event search, or indeed of most modern physics experiments, is the ability to simulate the data that is expected to be observed. With an accurate simulation of all of the known backgrounds that will produce signals in the TPC it becomes very clear, when comparing simulation to data, when new, not yet understood features arise. Therefore, it is crucial that the simulation is well tuned to the data so that the two are comparable. LZ uses several different simulation packages, that are described in this section, to simulate backgrounds as well as calibration data, and even WIMP signals. The full simulation framework used in LZ is discussed in Ref [140].

Broadly speaking, there are two primary approaches that are taken by LZ to simulating events: full-chain and fast-chain. Full-chain simulations exclusively use the ‘Basically A Component-Centric Analogue Response to AnyThing’ (BACCARAT) software (based on Geant4) to fully simulate all the RQs that would normally be measured for an event. This comes with a heavy computing requirement and demands long run times. Alternatively, BACCARAT can be used to just give the energy depositions of the incident particles, which can then be passed to the ‘LZ Light Analysis Montecarlo Application’ (LZLAMA) software that formulates RQs based on these energy depositions. This is much faster to run, but gives a limited set of RQs. In either case, it is essential that the response of the liquid xenon target to incoming particles is properly modelled, and for this the Noble Element Simulation Technique (NEST) is used [141, 142, 143]. Some further details on these three simulation packages are given in the rest of this section, and summarised in Table 2.1 are the simulations that are used throughout this thesis. As can be seen from the table, this work exclusively uses LZLAMA simulations.

Simulated Source	Simulation Type	Campaign
DD	LZLAMA	WS2022 & WS2024
AmLi	LZLAMA	WS2024
Neutron Background	LZLAMA	WS2022 & WS2024
Th-232	LZLAMA	WS2022
Na-22	LZLAMA	WS2024
Th-228	LZLAMA	WS2024

Table 2.1: *Simulated datasets used throughout the work presented in this thesis.*

2.10.1 NEST

The NEST software [141, 142, 143] is an experiment-independent simulation of the noble element microphysics that leads to the production of charge and light when an incoming particle interacts

with a noble liquid. It is also able to simulate the corresponding S1 and S2 signals that would be seen by a specific detector. NEST has been tuned and verified by a number of different experiments and over a range of different calibration techniques [120].

For the work that is the focus of this thesis, the use of NEST was limited to its simulations of charge and light yield, as a function of recoil energy, for liquid xenon. These distributions are different in the cases of NRs and ERs (specifically ERs caused by beta particles), and all four of these distributions are shown in Figure 2.14.

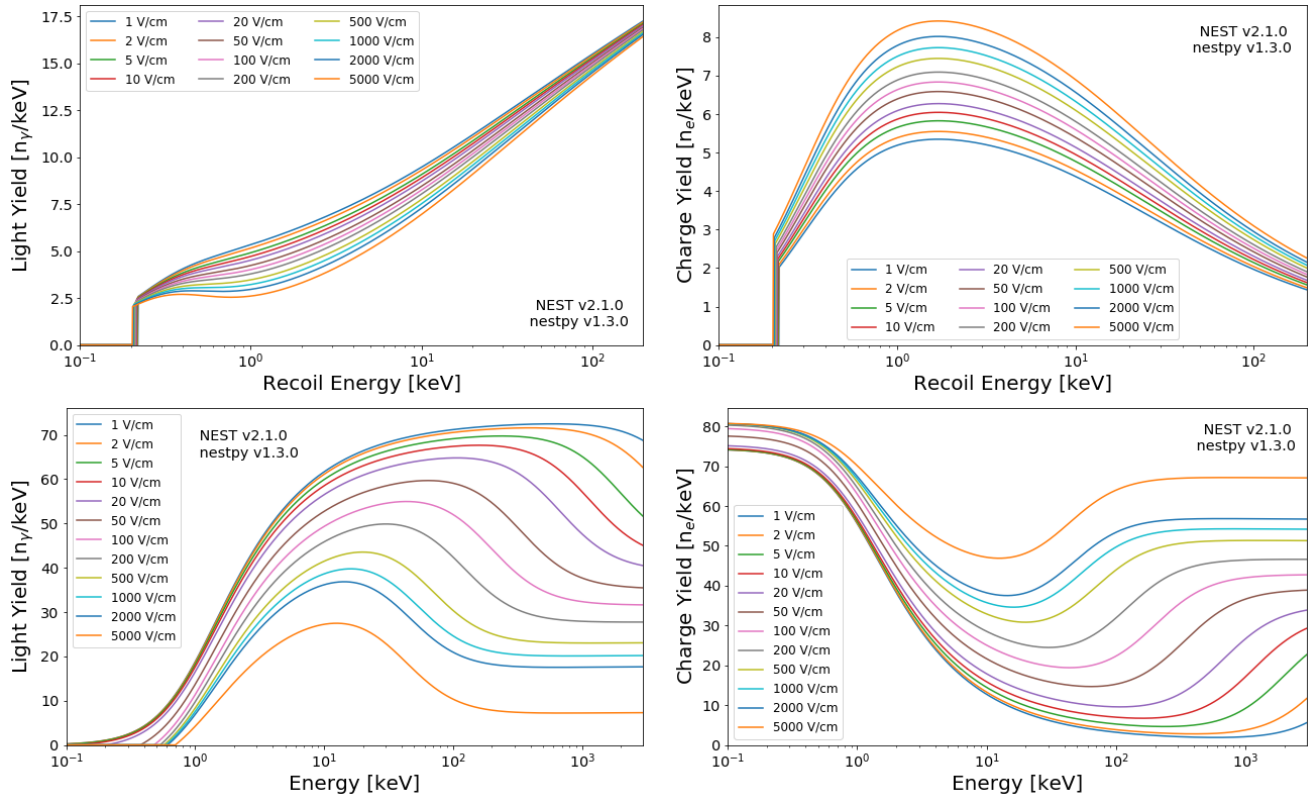


Figure 2.14: *The light (left) and charge (right) yields, as functions of recoil energy, produced by NEST for both NRs (top) and beta ERs (bottom). These curves are shown for a variety of drift fields. These plots were obtained from Ref [144].*

2.10.2 BACCARAT

Full-chain simulations use BACCARAT [140], a Geant4 [145, 146] framework, to propagate incident particles through the detector, modelling all of the interactions that they undergo along with all of the interactions of subsequently created particles. As previously mentioned, BACCARAT can be used to fully simulate events, and it does this by working in conjunction with NEST, which produces light and charge yields for an interaction. Ray tracing of the resultant S1 and S2 photons (once the electron drift and electroluminescence has been simulated) then determines what PMTs are hit.

Alternatively, BACCARAT can just save out energy depositions, which can be handed to LZLAMA for the quicker fast-chain simulation.

2.10.3 LZLAMA

LZLAMA [140] can either run using energy depositions produced by BACCARAT, or by sampling pre-simulated probability density functions (PDFs). LZLAMA does not simulate the full propagation of particles in the detector, including ray tracing, and so has a limited range of RQs that it can produce, but it is able to run much faster than the full-chain simulation. Specifically, the RQs that are lost when this method is used are those that concern pulse shape, and coincident signals between PMTs.

It is LZLAMA using BACCARAT energy depositions that was used to produce the neutron background simulations used for WS2022 and WS2024 that are discussed respectively in sections 4.5 and 6.4.

2.11 Background Signals

In order to be able to accurately identify a potential WIMP signal, it is essential to have a comprehensive understanding of all of the other signals that will be seen in the detector, referred to as the background signals. Several approaches are taken to minimise the background in LZ, such as constructing the detector underground with a rock overburden to shield from cosmogenic backgrounds, and mounting the detector inside a tank of ultra-pure water to shield from radiation in the rock surrounding the detector cavern. It was also ensured that all of the materials from which the detector was constructed were as pure as possible to minimise radioactive impurities, and that the construction of LZ was carried out under the cleanest possible conditions, to avoid contamination from materials that could undergo radioactive decay [147]. Nevertheless, there are still non-WIMP particles that are able to penetrate the TPC and generate signals. In this section, some of the backgrounds of LZ will be explored, and it will be explained how they can be differentiated from a dark matter signal. A detailed review of the backgrounds expected to be seen by LZ can be found in Ref [148].

2.11.1 Electron Recoil Events

The majority of the background in LZ consists of ER events, mostly due to gamma photons and beta particles that are produced by radioactivity in the detector components and the surrounding cavern. These can usually be easily distinguished from a potential WIMP signal by the discrimination between ER and NR events that can be obtained in the $\log(S2c)$ vs. $S1c$ parameter space.

However, at low energies, where discrimination between NR and ER events is more difficult, it is essential to have a good understanding of these backgrounds.

There are a number of different ways in which an ER event could be produced, and the main radioactive contaminants responsible for these are listed in Table 2.2 [149, 150]. The first ER background is gamma photons emitted by radioactive elements contained within the rock surrounding the detector cavern [124], specifically from decays of Th-232, U-238, and K-40 [150]. This background is reduced by the water tank in which LZ is placed, and also by the use of an FV selection for WIMP search data that only uses events from a central volume of the TPC, and hence exploits the self-shielding properties of liquid xenon.

Radioisotope	Type	Energy [keV]	Half-life	TPC Rate [nBq kg ⁻¹]
Th-232	γ	63.8 and 140.9	1.41×10^{10} y	-
U-238	γ	49.6 and 113.5	4.47×10^9 y	-
K-40	γ	1460.8	1.28×10^9 y	-
Co-60	γ	primarily 1173.2 and 1332.5	5.27 y	-
Kr-85	β	687.1 (highest endpoint)	10.8 y	42.3 (no error given)
Ar-39	β	565.0 (endpoint)	269 y	0.876 (no error given)
Pb-210	β	63.5 (highest endpoint)	22.3 y	-
Pb-212	β	573.8 (highest endpoint)	10.6 h	$(0.137 \pm 0.019) \times 10^3$
Pb-214	β	1024.0 (highest endpoint)	26.8 mins	$(3.10 \pm 0.10) \times 10^3$

Table 2.2: Summary of the main radioactive contaminants contributing to the ER background of LZ. Note that the TPC rate was not measured for cavern and detector gamma sources. In the WS2022 ROI it was estimated that these accounted for 1.4 ± 0.4 events. The Pb-210 activity from plate out on the TPC walls was measured to be (2.32 ± 0.15) mBq. Measurements in this table were obtained from Refs [149, 150].

Radioactivity from trace amounts of Th-232, U-238, K-40, and Co-60 in detector components also contributes to the gamma background seen in a WIMP search [150]. Extensive efforts were made to minimise these impurities as well as to minimise the introduction of any contaminants during construction [147], but a small amount remains nevertheless. Since this source of background signals is inside the TPC itself, the shielding afforded by the water tank outside of the TPC cannot help with this background, but fiducialisation of the liquid xenon again provides some shielding against it. Extensive simulations are run to understand and model the background produced by all of the components of the detector and the traces of radioactive elements that they contain. The combination of detector and cavern gamma backgrounds were estimated to have contributed 1.4 ± 0.4 events to the WS2022 region of interest (ROI) [150], the area of $\log(S2c)$ vs. $S1c$ parameter space on which the WIMP search focuses.

The beta particle background is largely present due to beta-emitting radioisotopes in the liquid

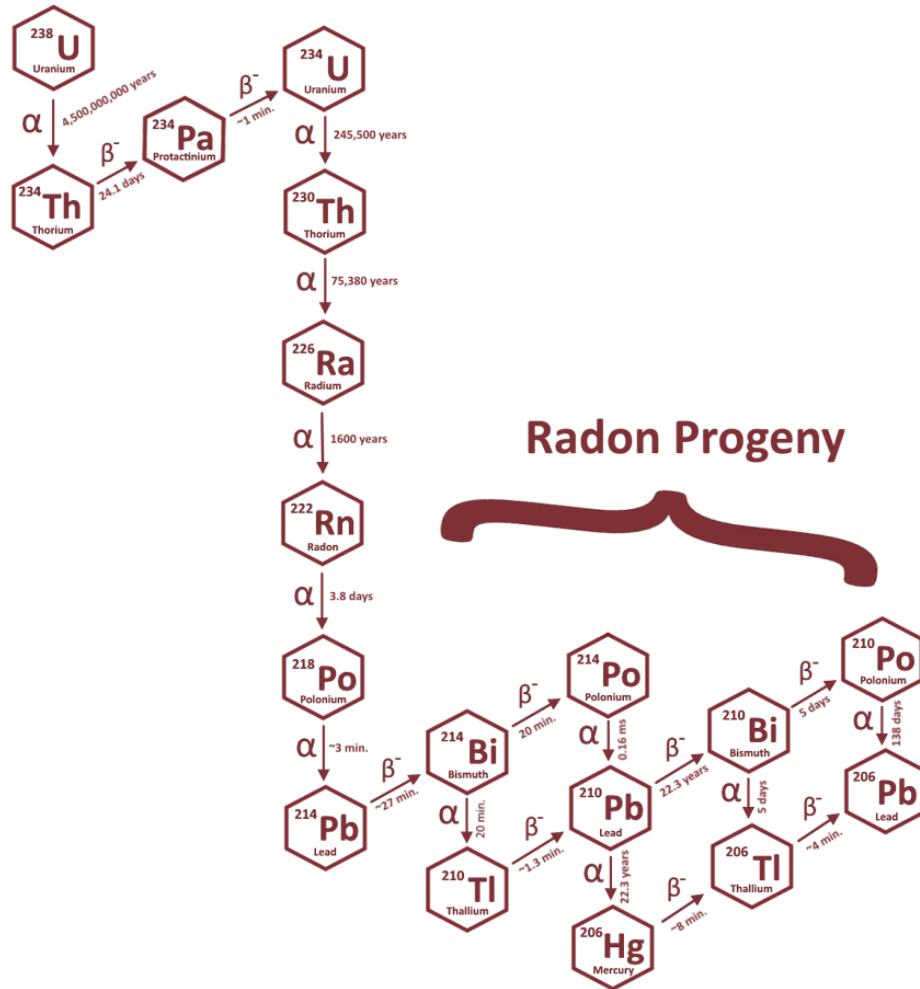


Figure 2.15: *U-238 decay chain that produces Rn-222, along with subsequent decays. Figure taken from Ref [151].*

xenon. Specifically, Kr-85 and Ar-39 occur in trace amounts in natural xenon. Also, the decay chains of Rn-222 and Rn-220 contain beta-emitting radioisotopes that can generate low-energy ERs in the WIMP ROI [150]. The decay chain of U-238 that produces Rn-222, and the subsequent decays of Rn-222, are shown in Figure 2.15 [151], where these beta-emitting isotopes can be seen. In this decay chain, Bi-214 is not a concern since it is followed promptly by the decay of Po-214 with a half-life of $164 \mu\text{s}$ [150]. This gives a distinctive event topology that can be identified, and would likely appear as a ‘pile-up’ event. The half-life of Pb-210 is 22 years, and so it will be removed from the liquid xenon before it decays. However, Pb-210 can plate out onto surfaces, such as the TPC wall, and cause a beta background with an activity of $(2.32 \pm 0.15) \text{ mBq}$ [150]. Another beta emitting radioisotope in the Rn-222 decay chain is Pb-214, information on which is given in Table 2.2.

The concentration of Rn-220 is expected to be much lower than that of Rn-222, due to a shorter half-life limiting the emanation time before decay. The decay chain is analogous to that of Rn-222,

with Bi-212 and Po-212 always appearing together in an event, so not being problematic for the WIMP search. Tl-208 does not have naked beta decay modes, and so only Pb-212 is considered as an ER background for this decay chain, and is therefore included in Table 2.2.

2.11.2 Accidental Coincidences

Another background that should be considered is that of accidental coincidences between uncorrelated lone S1 and lone S2 signals, that are erroneously interpreted as an SS, or even an MS, event. There are a number of reasons that these lone pulses can be created. Lone S1s can be created in charge-insensitive regions of the TPC, where electrons will not be successfully drifted to the gaseous region to create an S2 signal. They could also be caused by Cherenkov radiation from charged particles emitted by the PMTs or PTFE walls, or by light leaks from outside of the TPC. Lone S2s can be created by events that have S1s smaller than the threshold for LZAP to identify them as S1s, as was discussed in section 2.9. They could also be events that take place very near to the liquid surface, where the S1 is lost, merged with the S2, or mis-classified. Alternatively, events that occur in the gas above the anode, or electron emission from the grids [152] are also among the potential causes of lone S2s.

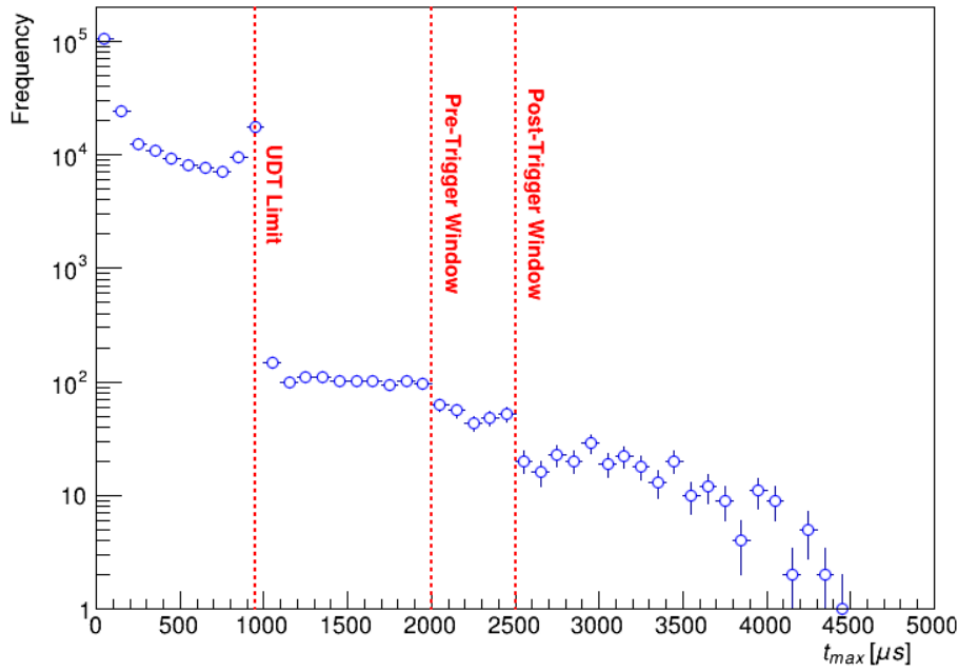


Figure 2.16: Maximum drift time of 10 runs of WS2022 MS data with no analysis cuts applied, shown with respect to the unphysical drift time (UDT) limit, the pre-trigger window, and the post-trigger window.

There is a maximum possible drift time for the electrons of an event in LZ, which is defined by the strength of the drift field and the depth of the TPC, between the anode and the cathode.

If an accidental coincidence of a lone S1 and a lone S2 occurs with less than this maximum drift time between the pulses, it will likely be interpreted as a valid event. However, since the S1 and S2 in this case are not correlated, the drift time between them is arbitrary, and so it is equally as probable that it has any value. This includes drift time values that are larger than the maximum drift time possible in the TPC. This is shown for MS events in Figure 2.16, where it can indeed be seen that there are events with a drift time that is beyond the unphysical drift time (UDT) limit. Defining a UDT MS event, however, is not trivial as it is in the case of SS events, since the event contains N drift times. Therefore, the decision was made that an MS physical drift time (PDT) event would require all scatters to have a PDT, and hence the maximum drift time, t_{max} , of the event must be physical:

$$t_{max} = \max(d_1, d_2, \dots, d_N), \quad (2.10)$$

for an N scatter event with drift time d_i in between the S1 and the i^{th} S2. An alternative definition of the MS drift time that could be used to identify UDT events is the S2c-weighted average drift time. However, this definition would allow events with unphysical scatters to be defined as PDT events, provided that the other scatters in the event had sufficiently short drift times, and sufficiently large S2c pulses, as to make the overall average drift time physical. It was decided that events such as these should not be considered PDT events, and hence t_{max} was chosen as the MS drift time.

The distribution of maximum drift times for MS events from ten runs of WS2022 data, with no cuts applied, is shown in Figure 2.16. It can be seen from the figure that the majority of the events occur entirely within the TPC, and hence have a maximum drift time less than the UDT limit. Furthermore, there is an increased rate of events toward the top and bottom of the TPC as proximity to the electrode grids increases, and hence the background event rate is elevated (when no cuts are applied). Between these regions at the top and bottom of the TPC, a steady decrease in the rate of events can be seen. This is likely largely due to the fact that the Skin detector that surrounds the TPC is thinner at the top than it is at the bottom, so provides more shielding towards the bottom of the detector. Moving beyond the UDT limit, it is seen that the rate of events drops significantly, but does not go to zero. This is evidence of the MS accidental coincidence events. Beyond the UDT limit, two further points of interest have been marked on the figure: the pre-trigger and post-trigger window lengths. The rate of events decreases further at both of these points since the trigger windows restrict the amount of time in which the pulses contributing to an accidental coincidence event can occur. This also explains why no events are seen with a maximum drift time greater than $4500 \mu s$, as this is the full width of the event window. The relatively flat rate of events in between the UDT limit and the pre-trigger window threshold can be used to evaluate the number of accidental coincidence events expected in the TPC, which in this sample would be ~ 100 .

Therefore, one method of quantifying the expected rate of the accidental coincidence events is to look at the rate of events detected with a UDT, as this rate would be expected to be constant for all drift times, regardless of whether they are higher or lower than the maximum possible PDT.

Accidental coincidences are usually thought of in terms of the SS WIMP search dataset, where one lone S1 is accidentally correlated with one lone S2. However, it has been shown that MS accidental coincidences can also occur, and in this case the situation is more complicated. This is because there are multiple options for how an MS accidental coincidence can occur. Since ‘MS events’ is a broad, overarching term that describes any event with more than one scatter, an accidental coincidence could consist of a lone S1 and any number of lone S2s. As the number of S2s in an accidental coincidence event increases, the probability of such an event occurring decreases, as it requires the coincidence of many S2s, but there are more ways in which an MS accidental coincidence can be constructed. If an SS event is correlated with a lone S2, this would lead to a falsely interpreted double scatter event. Similarly, a true double scatter and a lone S2 could be seen as an accidental coincidence triple scatter event, but this could equally consist of a true single scatter and two lone S2s. As the number of scatters, N , increases, the number of ways of constructing an accidental coincidence event increases as N as well. For example, an event with two scatters has two potential formations for an accidental coincidence event: lone S1 + lone S2 + lone S2, or SS + lone S2.

SS accidental coincidence events are tackled broadly by two approaches. The first is to develop cuts that remove them where possible, and the second, where this is not possible, is to develop a model of them for the WIMP search ROI where a dark matter signal would be found, so that any signal can be compared to this model.

When developing accidental coincidence cuts, specific populations caused by specific physics processes can be targeted since some of these produce pulses with unique shapes that can be identified. When developing these cuts, it is important that a high signal acceptance is maintained, so that these cuts would remove minimal WIMP candidate events. The specifics of these cuts will be discussed further in chapters 4 and 6. It is important to note that these accidental coincidence cuts were tuned using SS data, since that was the focus of the WIMP searches, and during chapter 4 it will become apparent that in many cases the tuning does not map to MS events. There is not yet a set of accidental coincidence cuts developed specifically for MS events, but this is one of the focuses of future work. In WS2022, discussed in chapter 4, the SS accidental coincidence cuts are directly adapted for MS events, but as will be discussed in that chapter, this is seen to potentially be an overly harsh set of cuts. For WS2024, the approach taken is not to apply any accidental coincidence cuts to MS events, but rather to assess by eye the waveforms of all NR candidates to select neutron-like events. This will be discussed further in chapters 5 and 6.

A problem is encountered when using the UDT accidental coincidence events to model the PDT events, in that very few UDT events survive all of the data cuts. A greater number of

events is needed to effectively study the effect of cuts on accidental coincidence events. This is modelled for SS events using the so-called ‘chopstitch’ method [150], in which lone S1 events are artificially overlaid with lone S2 events to create a manufactured population of accidental coincidence events. This gives a dataset with high enough statistics to study the effect of all cuts on accidental coincidences.

2.11.3 Neutrinos

Signals can be produced in LZ by neutrinos interacting with the detector, and hence they are a background that has to be considered in the WIMP search. Neutrinos can come from several different sources, such as from the sun or from interactions occurring in the atmosphere. They can also interact in the detector in different ways: either as ER or NR events.

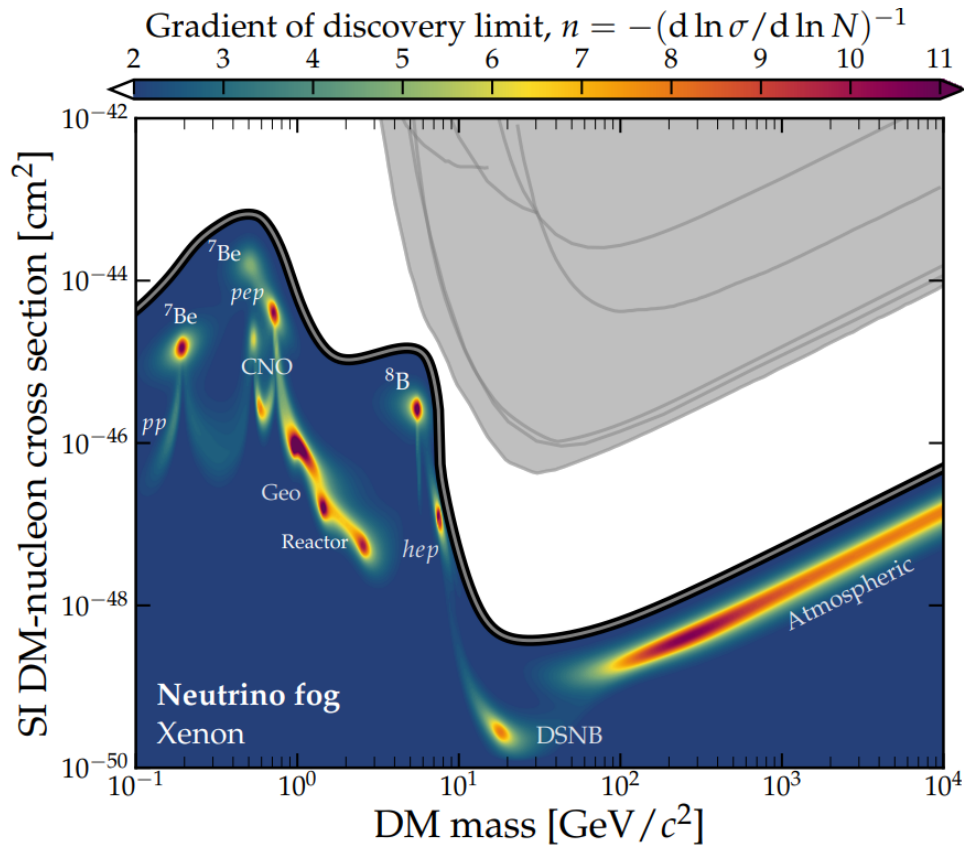


Figure 2.17: Visualisation of the neutrino fog relative to exclusion limits set by experiments preceding LZ (grey). Within the neutrino fog the different sources of neutrinos are labelled, and the opacity of the neutrino fog (the extent to which CE ν NS impedes a dark matter discovery), n , is shown by the colourbar. $n < 2$ is the approximately background-free regime. This figure is taken from Ref [153].

As may be expected from what has been discussed so far in this thesis, the more problematic neutrino background is when they produce WIMP-like NRs via coherent elastic neutrino-nucleus

scattering (CE ν NS) [154]. Depending on the source of the neutrinos, they can produce recoils of varying energies, but a neutrino signal will have a relatively low interaction cross-section with respect to the region of mass vs. interaction cross-section parameter space that has so far been ruled out in the search for WIMPs, as can be seen in Figure 2.17. Because of solar neutrinos, the neutrino interaction rate is highest at low energies, and therefore this is where the effect on WIMP limits is the strongest. This region corresponds to the maximum recoil energy for relatively low WIMP masses, as was shown by Equation 2.8.

However, as direct WIMP dark matter searches progress, with currently no signal to suggest discovery, detectors are probing further into the low mass, low cross-section regions of the WIMP parameter space, and are approaching the point at which these CE ν NS interactions will become a concern. For LZ, the expected rate of CE ν NS neutrinos was calculated using Refs [155, 156, 157, 158].

CE ν NS neutrinos can be produced by a number of different sources, for example they can be solar neutrinos from the decay of B-8 [159]:



These nuclear recoils tend to have relatively low energies, of order ~ 1 keV and below. Neutrinos can also be produced by cosmic ray interactions with the atmosphere. This produces pions, which then decay to muons (or antimuons, depending on the charge of the pion) along with muon antineutrinos (or muon neutrinos). The muons (or antimuons) can then subsequently decay to produce electrons (or positrons), electron antineutrinos (or electron neutrinos), and muon neutrinos (or muon antineutrinos). These atmospheric neutrinos can cause recoils of up to ~ 80 keV [159].

The region of parameter space that these neutrino interactions occupy is referred to as the ‘neutrino fog’, since any potential WIMP signal in this region would be, with current detector technologies, indistinguishable from the neutrino background. An illustration of this neutrino-dominated region of the parameter space is shown in Figure 2.17 [153]. The limits produced by LZ in WS2022 and WS2024 (shown later in Figures 4.1 and 5.1), in the years following the production of this plot, serve to further push the area of explored WIMP parameter space towards the neutrino fog. There are plans for future detectors, such as the proposed CYGNUS detector [160], to use directional information about interactions to be able to distinguish neutrino signals in this region [161].

2.11.4 Neutrons

Neutrons provide problematic background signals in LZ due to the fact that they are indistinguishable from the expected signal from a WIMP interaction [162]. This is because neutrons are massive and have no charge, so when they interact with xenon atoms they will most likely cause NRs, just as a WIMP would. They also tend to cause the nucleus to recoil at around the energies

that would be expected for WIMP dark matter. The skin and OD veto detectors are used by LZ to tag the majority of neutrons that cause a signal in the TPC. The skin detector utilises liquid xenon, as in the liquid phase of the TPC, as a source of scintillation light to detect interactions with neutrons, whereas the OD uses GdLS, as was discussed in sections 2.2 and 2.3 respectively.

There are a number of different processes that can produce neutrons that could contribute to the neutron background, and these could occur in the rock surrounding the detector cavern, or in the components of the detector themselves [163]. The two most prominent processes (and hence those included in the neutron background simulation discussed in sections 4.5 and 6.4) are (α, n) interactions (from decays of Th-232 and U-238) and spontaneous fission, specifically fission of U-238.

In (α, n) interactions, the decay chain of the parent isotope produces alpha particles that can in turn interact with other materials to produce neutrons [164]. This process is important for materials with low to medium atomic numbers, as they will have a lower potential barrier for the alpha-nucleus interaction to take place, so require less energetic alpha particles. Spontaneous fission of U-238 is another neutron production mechanism that has a lower probability than (α, n) , but is the dominant background in materials with high atomic numbers, since the Coulomb barrier suppresses (α, n) reactions [164].

U-238 chain alpha decays can be referred to as ‘early’ or ‘late’, and this is in reference to the position in the U-238 decay chain where they occur. In all of the Th-232 and U-238 decay chains, the system is initially assumed to be in secular equilibrium¹. However, secular equilibrium can be broken if a long half-life occurs in the chain, if an isotope emanates away after production, or if the produced isotope undergoes chemical processing. For the U-238 chain there is a significant breaking of the secular equilibrium at Ra-226 (see figure 2.15), due to produced radon gas emanating away. This splits the chain into two sections, each with their own secular equilibrium, that are referred to as ‘early’ and ‘late’.

Neutrons can also be produced by energetic muons, that are themselves produced by atmospheric interactions of cosmic rays. The large rock overburden under which LZ is built helps to reduce the number of these muon-induced neutrons, and the remaining rate of such events is estimated to be at least three orders of magnitude lower than the rate of production of radiogenic neutrons in the surrounding rock [163].

¹Secular equilibrium means that all isotopes in the chain are decaying at the same rate. This requires the half-life of the daughter isotopes to be much shorter than that of the parent isotopes, and that the system has had enough time to reach equilibrium.

2.12 Statistics

In this section, the statistical methods that are relevant to the work presented in this thesis, and to setting a dark matter limit in general (or potentially making a discovery) will be explored. A statistical test that will be shown to be central to this analysis is the χ^2 test, and therefore the details of this area of statistics will be covered in section 2.12.1. The statistical approach to WIMP searches, or rare event searches more generally, will be covered in section 2.12.2. Specifically, this will look at profile likelihood ratios (PLRs) and how LZ results are compared to the expected background and signal PDFs to assess the likelihood that a discovery has been made, or quantify the limit that can be set.

2.12.1 χ^2 Tests

A statistical method that will prove crucial to the work presented in the thesis, is the χ^2 statistical test [165]. This test can be used to establish whether or not there is a statistically significant difference between a dataset and a model, and whether that dataset could have feasibly been produced by the model. The null-hypothesis for such a test is that the data follows the expected model, and this is the hypothesis that the test will try to disprove. The standard formula for the χ^2 test statistic is:

$$\chi^2 = \sum_i \frac{(O_i - E_i)^2}{\sigma_i^2}, \quad (2.12)$$

where O_i is a set of values obtained from a model and E_i are the experimentally observed values to which the obtained values are being compared. σ_i^2 here is the variance of the observed values. As will be discussed in chapter 3, in the context of the work presented in this thesis, the ‘expected’ values correspond to the measured S1c and S2c quantities and the obtained values that are being compared to them are from NEST NR and ER models.

In many cases the χ^2 statistic is used to compare two distributions, with the i^{th} entry being a comparison for a given bin of the two histograms. In this case, assuming the entries in each bin are Poisson distributed [165], it can be stated that $\sigma_i = \sqrt{E_i}$, which when substituted in to Equation 2.12, gives a more commonly seen form of the χ^2 statistic:

$$\chi^2 = \sum_i \frac{(O_i - E_i)^2}{E_i}. \quad (2.13)$$

The value of χ^2 indicates how well the data fits the expectation, with smaller values indicating a better fit. What constitutes a good fit, however, depends on the number of degrees of freedom, k , in the test. This can be calculated as the number of observations minus the number of fitted parameters.

The χ^2 statistical test requires comparison of the result to the χ^2 distribution, the PDF of which is given by:

$$p(x, k) = \frac{x^{(k/2)-1} e^{-x/2}}{2^{k/2} \Gamma(\frac{k}{2})}, \quad (2.14)$$

for $x > 0$, where x is the value of the χ^2 statistic [165]. For $x < 0$, this distribution is defined as zero for all values. Note that this distribution assumes Gaussian errors, which was deemed to be a reasonable assumption for the work presented in this thesis. This equation uses the gamma function, Γ [166], that is defined as:

$$\Gamma(z) = \int_0^{\infty} t^{z-1} e^{-t} dt. \quad (2.15)$$

It is clear from Equation 2.14 that the χ^2 distribution is dependent on the number of degrees of freedom, k , and this is further illustrated by Figure 2.18, which shows how this distribution varies with different values of k . By integrating this distribution between zero and the χ^2 test statistic found for a given study, the probability of obtaining such a value of χ^2 , given the expected values of the variables, is obtained. This new integrated distribution is known as the cumulative distribution function (CDF).

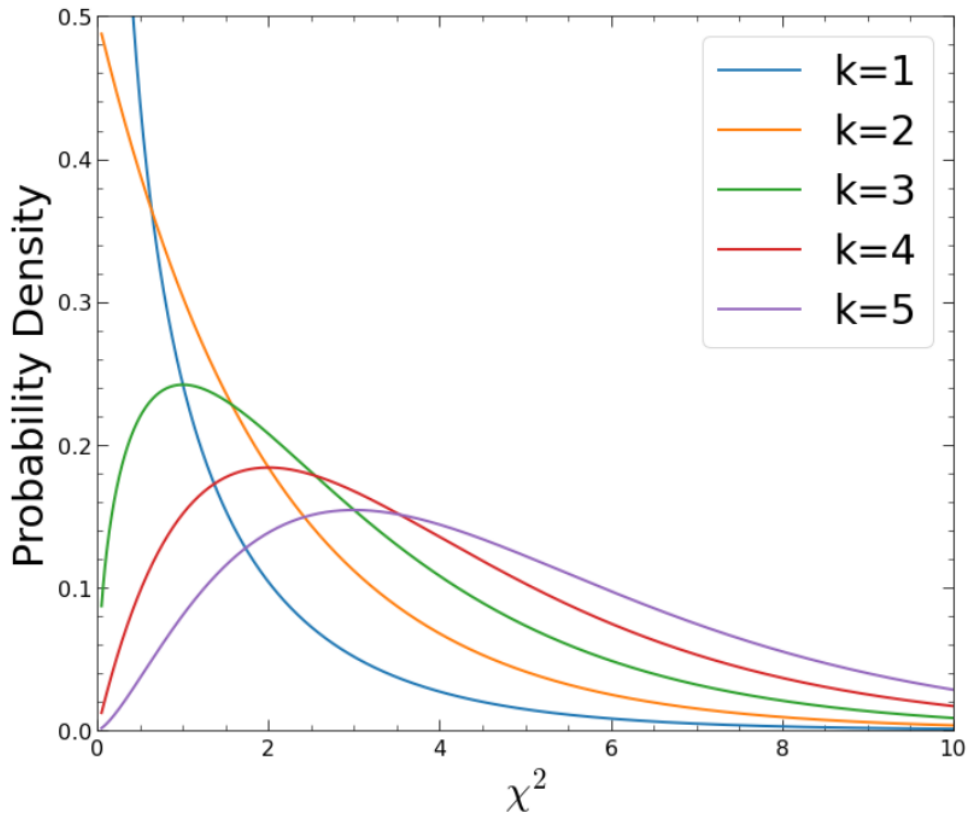


Figure 2.18: The χ^2 distribution for different numbers of degrees of freedom, k .

The p-value of the test is defined as being the probability of obtaining a χ^2 value that is at

least as large as the observed test statistic. The value of the CDF at a set point is the inverse of this requirement (it describes the probability of obtaining a value up to a maximum), so the CDF value must be subtracted from 1 to get the p-value. A p-value that is below some pre-defined threshold (the significance of the test) means that the result is statistically significant, and that the null hypothesis can be rejected. This would mean that the observed data does not follow the model, and would be the case for larger values of χ^2 .

2.12.2 PLR Tests

A PLR test is another statistical method that enables a model to be compared to the data collected and therefore, given two models, can be used to select the most likely model for having produced that data. Specifically, in the case of rare event searches, such as a WIMP search, the two models being tested are the background only hypothesis, and the background plus signal hypothesis. Essentially, this can be used to evaluate whether the data collected is consistent with what would be expected for a WIMP signal, in addition to all the backgrounds that would also be expected.

The statistical test in a counting experiment, like a rare event detector, is more complex than the χ^2 test considered in the previous section, since it is no longer a binary distinction between whether or not the data fits the model. The background plus signal hypothesis is not just a single model, and can include any number of signal events, μ , detected, provided there is at least one. For this reason, a range of different values of μ have to be considered in this test. The use of PLR tests rather than χ^2 tests also allows for errors to be non-Gaussian, which is a required assumption for χ^2 tests.

All background plus signal models, as well as the background only $\mu = 0$ model, are just PDFs against which data can be compared. As in the case of the χ^2 test, which used χ^2 , this comparison requires the use of a test statistic. In this instance, the test statistic, t_μ , is defined by:

$$t_\mu = \begin{cases} -2 \ln \frac{L(\mu, \hat{\theta}(\mu))}{L(0, \hat{\theta}(0))}, & \text{if } \hat{\mu} < 0 \\ -2 \ln \frac{L(\mu, \hat{\theta}(\mu))}{L(\hat{\mu}, \hat{\theta})}, & \text{if } \hat{\mu} \geq 0 \end{cases}. \quad (2.16)$$

This equation contains a number of different elements to consider. Firstly, the likelihood function L is similar to a PDF, but with a key difference. A PDF, $P(x)$, has fixed arguments, such as μ and σ in the case of a Gaussian distribution, but x is variable. A likelihood function, $L(x)$, is evaluated at a fixed value of x , but with variable arguments.

$\hat{\mu}$ indicates the value of μ for which L is maximised. There are numerous other parameters aside from the number of WIMP events detected, μ , that are utilised in this statistical test, but since these are not the parameter of interest they are referred to as nuisance parameters, and are all included under the notation of θ . Similarly, $\hat{\theta}$ indicates the value of θ for which the likelihood is maximised. $\hat{\theta}(\mu)$ refers to the value of θ for which the likelihood is maximised for a given value

of μ , rather than globally. It is by the use of this term that profiles $\hat{\theta}$ in μ that this becomes a profile likelihood ratio, rather than simply a likelihood ratio.

For a given background plus signal model, for each value of μ , Monte Carlo simulations can be run to establish a PDF as a function of the test statistic, t_μ . From this, p-values can be calculated for that hypothesis, and the upper limit of μ can be calculated according to a specified confidence level. By varying the background plus signal models used, this method can set limits for different WIMP masses and interaction cross-sections, as is presented in the LZ WIMP search papers [114, 126], and is shown in Figures 4.1 and 5.1.

2.13 LZ Performance Parameters

A number of different parameters that describe the performance of the LZ detector across both WS2022 and WS2024 are shown in Table 2.3. It can be seen from the table that the higher drift and extraction fields used in WS2022 lead to improved detector performance. However, the extraction field was lowered for WS2024 to reduce spurious electron and photon emission from the electrode grids, and the cathode voltage, and hence the drift field, was reduced due to the emergence of persistent light emission located in the Skin region below the cathode.

Parameter	WS2022	WS2024
Drift Field [V cm ⁻¹]	193	97
g_1 [phd/photon]	0.114	0.112
g_1^{gas} [phd/photon]	0.092	0.076
Single Electron Size [phd]	58.5	46.9
Extraction Efficiency [%]	80.5	72.5
g_2 [phd/electron]	47.1	34.0

Table 2.3: LZ detector parameters for WS2022 and WS2024. The parameters in the bottom half of the table are from NEST calculations. Values in this table are taken from Refs [114, 126].

Chapter 3

Multiple Scatter Neutrons

The tendency of neutrons to scatter multiple times in the target medium is exploited for the work presented in the following chapters to produce an estimate of the number of single scatter neutron events, and thus learn crucial information about an important background to direct dark matter searches.

In this section the neutron background will be reintroduced, and the main approaches that can be taken to addressing it will be discussed. The work presented in this thesis focuses on an MS-driven method of estimating the neutron background, and the issues encountered with this approach will be explained. Following this will be the introduction of a novel method of tackling these problems. This new method, referred to as the $\Delta\chi^2$ method, will then be explained in detail to conclude the chapter.

3.1 Neutrons

As was discussed in section 2.11.4, neutrons are a crucial background to understand since they produce an NR signal that is indistinguishable from that of a WIMP. There are two main ways in which LZ tackles this issue: the use of additional veto detectors to tag neutrons that enter the TPC, and using MS neutron events in the TPC to infer the rate of WIMP-like SS neutron events. As will be seen later in this thesis, these two methods can also be used in combination to help understand the neutron background to the greatest possible extent.

3.1.1 Outer Detector and Skin Vetoes

As was discussed in sections 2.2 and 2.3 respectively, surrounding the TPC of LZ are the Skin and OD veto detectors. These are used primarily to tag neutrons and gamma photons that could cause signals in the TPC, so that these signals can be ruled out as WIMPs. These veto detectors can produce two types of signal that are referred to as prompt and delayed.

A prompt veto signal is due to a gamma or fast neutron scatter in one of the veto detectors, within a certain time of the S1 in the TPC. Since the incoming particle could scatter in a veto detector either before or after interacting in the TPC, this time window extends both before and after the S1. In order for an event with a prompt veto signal in either the Skin or the OD to be tagged (and therefore removed by a veto cut from the WIMP search dataset), there are a few requirements that have to be met. The specifics of these requirements are tuned individually for each WIMP search, so for WS2022 and WS2024 they are presented in Table 3.1, and will be discussed further in sections 4.2.4 and 6.2.4 respectively. The thresholds of these requirements will also be different for the Skin and OD detectors. The first of the checks for a veto signal is the aforementioned requirement that the prompt veto signal is within a certain time before or after the S1. This aims to ensure that the veto and S1 signal are indeed due to interactions from the same particle, and from a fast scatter. The next condition to be met is based on the size of the veto signal in phd, so that it is clear that the signal is distinct from background noise. This requires the pulse in the veto detector to be above a certain threshold. Finally, there is the requirement that the signal is registered across a certain minimum number of PMTs, to avoid any signals due to anomalous behaviour of just one, or a couple of PMTs. This threshold is set by the background rate of events for that veto detector.

	WS2022	WS2024
Skin Prompt	-500 ns < Δt < 500 ns coincidence > 2 PMTs (data) pulse area > 2.5 phd	-250 ns < Δt < 250 ns coincidence > 2 PMTs (data) pulse area > 2.5 phd
Skin Delayed	500 ns < Δt < 1200 μ s coincidence > 55 PMTs (data) pulse area > 50 phd	250 ns < Δt < 600 μ s coincidence > 2 PMTs (data) pulse area > 46 phd
OD Prompt	-300 ns < Δt < 300 ns coincidence > 5 PMTs (data) pulse area > 4.5 phd (sim)	-300 ns < Δt < 300 ns coincidence > 5 PMTs (data) pulse area > 4.5 phd
OD Delayed	300 ns < Δt < 400 μ s coincidence > 5 PMTs (data) pulse area > 17.6 phd	300 ns < Δt < 600 μ s coincidence > 5 PMTs (data) pulse area > 32 phd

Table 3.1: Comparison of WS2022 and WS2024 prompt and delayed veto cuts for the Skin and OD veto detectors. Δt here represents the time between the veto pulse and the S1 in the TPC.

A delayed veto signal largely targets neutrons that take time to thermalise and get captured, typically by the gadolinium in the OD, after scattering in the TPC. As with the prompt veto, there are certain requirements that a delayed veto signal must meet in order to tag an event. The

temporal requirement is that the veto signal occurs in a delayed time window after the S1. The signal needs to be close enough to the S1 in time that the two can be correlated, but long enough afterwards that the signal can still be classified as ‘delayed’, allowing for the thermalisation time of the neutron (can take up to times of $\mathcal{O}(100 \mu\text{s})$) and neutron capture ($\sim 30 \mu\text{s}$ for gadolinium [112]). The logic behind the other two requirements of pulse size and PMT coincidence is identical to the case of prompt signals, but the particular thresholds used vary in the two cases. Note that the high coincidence threshold of 55 PMTs for the Skin delayed veto in WS2022 is due high noise levels in the Skin during this period.

3.1.2 Multiple Scatters to Estimate Single Scatters

Since WIMPs have a very low nucleon interaction cross-section by definition, it can be assumed that they will interact at most once in the TPC. Conversely, neutrons have a much larger interaction cross-section, and therefore often interact more than once in the TPC, in the form of an MS event. If it is assumed that the ratio of SS neutron events to MS neutron events is the same in both data and simulation, then the rate of SS neutron events expected to appear in the WIMP search ROI can be estimated. This means that any WIMP-like signal that may be detected could be compared to this expected number of neutrons in the dataset in order to establish whether the signal is consistent with the neutron background, or rather suggests the presence of WIMP events.

To achieve this, the SS/MS ratio of neutrons needs to be well understood. Since this ratio cannot be measured directly from WIMP search data (the converse problem that an SS neutron-like signal could theoretically be a WIMP), the calculation is performed using a combined simulation of all of the expected neutron backgrounds in the detector. Neutron calibration data is used to verify that the SS/MS ratio is consistent between data and simulation. A detailed breakdown of this process will be covered in sections 4.5 and 6.4 for WS2022 and WS2024 respectively. The SS/MS ratio from simulation, $N_{SS}^{sim}/N_{MS}^{sim}$, is used to estimate the number of SS neutrons in WIMP search data, N_{SS}^{data} , from the number of MS neutrons in WIMP search data, N_{MS}^{data} , according to:

$$N_{SS}^{data} = \frac{N_{SS}^{sim}}{N_{MS}^{sim}} N_{MS}^{data}. \quad (3.1)$$

This, however, assumes that the SS/MS ratio is constant with nuclear recoil energy, E_{nr} , which is not necessarily (and indeed will later be shown not to be) the case. Therefore, Equation 3.1 can be generalised to:

$$N_{SS}^{data} = \sum_j^{N_{MS}^{data}} \left(\frac{N_{SS}^{sim}(E_{nr})}{N_{MS}^{sim}(E_{nr})} \right)_j, \quad (3.2)$$

where the the sum is over the energies of the N_{MS}^{data} neutron candidates found in MS data. Here, the value of the SS/MS ratio is added for the specific energy value of the j^{th} event. This introduces

a new assumption that the energies of the MS events are representative of the energies of the SS events, but the energy dependence of the SS/MS ratio is relatively small, and in the instance of an energy independent SS/MS ratio Equation 3.2 reduces back to Equation 3.1. Therefore it was decided that the assumption inherent in Equation 3.2 is preferable over that of no energy dependence.

The final measurement required for the estimate described by Equation 3.1, and equally by Equation 3.2, is that of the number of MS neutrons in the WIMP search dataset, N_{MS}^{data} . Dealing with MS events rather than the usual WIMP search SS events, however, presents some unique issues that will be addressed in the following sections of this thesis.

3.2 The Multiple Scatter Problem

Each of the scatters in an MS event produces its own scintillation (S1) and ionisation (S2) signal. The signals are separated by the flight time of the neutron (or whatever particle causes the MS event) in between scatters, plus the difference in time taken for the signal to reach the PMTs due to different z positions of the scatters. For an S2, the signal propagation speed to the PMTs is mostly dependent on the speed at which the electrons drift towards the extraction region, and is therefore strongly dependent on the drift field applied. For an S1, the propagation speed of the signal to the PMTs is just the speed of light in liquid xenon, and so, over the relatively small dimensions of the detector with respect to this speed, S1 signals can be considered to be received instantaneously.

Because the S1 signals from separate scatters of a given event all arrive instantaneously, the result is that the waveform obtained for an MS event appears to contain only one S1. This is due to the fact that the individual S1s are only temporally separated by the flight time in between scatters, which is of $\mathcal{O}(\text{ns})$ for a neutron (based on the mean free path of 10 cm [150] for a 2.45 MeV neutron), and is too short to be resolved by the LZ TPC. This single visible S1 is then the sum of all of the S1 light across all of the scatters. Since the S2 signals propagate at the drift speed of electrons in the TPC, the waveform will show S2 signals from all scatters, provided that they are sufficiently separated in z position as to be resolved (they also need to be sufficiently separated in the xy plane as to be resolved if the drift times are similar, but this is not an issue of signal transmission time). The result of this is that for an MS event with N scatters, one S1 and N S2 signals are observed.

As was described in section 2.1, NR ER discrimination can be performed for an SS event by plotting it in $\log(\text{S2c})$ vs. S1c space, and seeing where it is located with respect to the NR and ER bands. For an MS event though, the question immediately arises as to how it can be represented in this space when multiple S2c values and one total S1c value are present. The simplest approach, and indeed the approach that was used before the studies presented in this thesis were carried out,

is to sum the S2c signals for the event to give a total S2c value. This means that each event has only one S1c and total S2c value, and hence can be plotted in $\log(S2c)$ vs. S1c space.

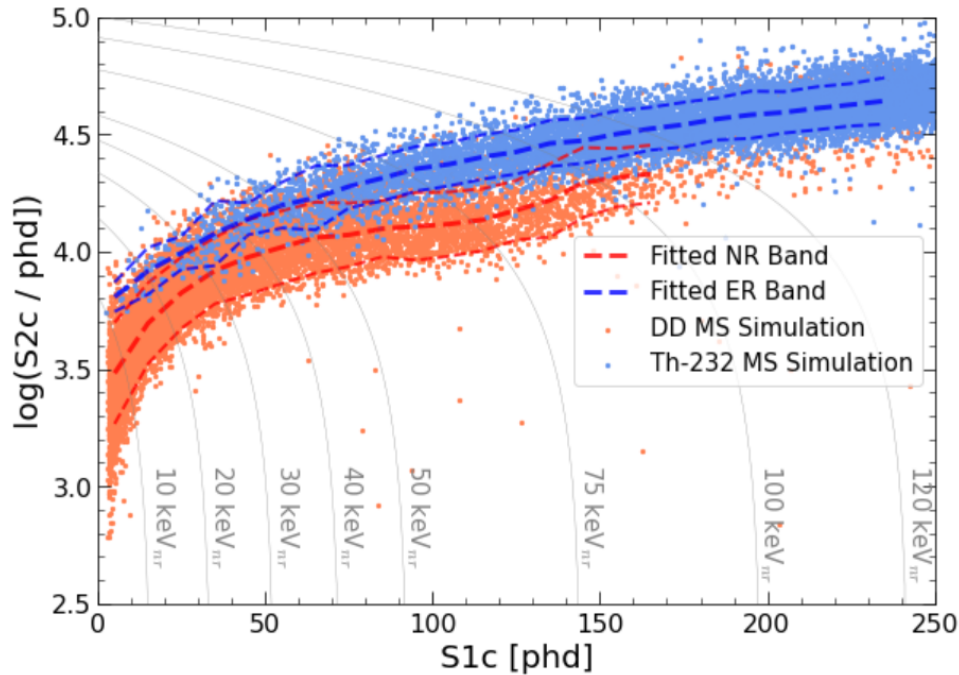


Figure 3.1: DD (light red) and Th-232 (light blue) simulated MS data illustrating the overlapping of the MS NR and ER bands in $\log(S2c)$ vs. S1c space. Total S1c and S2c signals are used to represent MS events in this space. Also shown here are the fitted NR (red) and ER (blue) Gaussian 90-10 CL bands for these datasets. The DD data has a strict FV cut (see section 4.2.1), and cathode, gate and field cage resistor cuts applied. An ROI cut ($S1c < 250$ phd, $2.5 < \log(S2c / \text{phd}) < 5.0$) is applied to both datasets.

However, this leads to a problem. For SS events, when ER and NR events are plotted using calibration data, as was shown in Figure 2.3, there is a clear separation between the two populations. With MS events though, the NR and ER bands overlap, as is shown in Figure 3.1. The NR band is higher and wider in $\log(S2c)$ than it is for SS events. Note that a larger ROI is used for this figure than will be applied for most of the rest of the work in this thesis in order to see the position of MS NR and ER events at higher energies. Due to the maximum DD SS neutron energy of 74 keV, the SS NR band cannot be defined beyond S1c values of around 100 phd using DD simulation, which limits the ROI that can be used in many cases.

If the total MS calibration dataset is broken down into the individual scatter multiplicities, it can be seen that the NR band rises with each additional scatter. This is illustrated by Figure 3.2, which shows how the average $\log(S2c)$ value (left plot, red lines) and average S1c value (right plot, red lines) vary with the number of scatters. Both distributions show a rising average value with the number of scatters, but this is most prominent and noticeable in $\log(S2c)$, and is what causes the MS NR band to collide with the MS ER band.

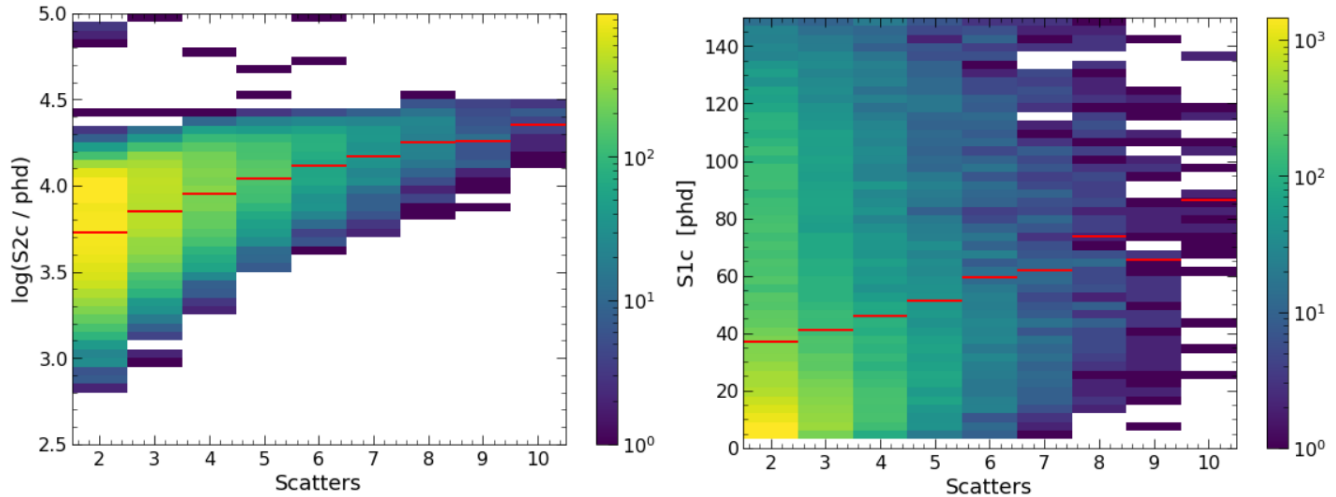


Figure 3.2: Total $\log(S2c)$ value (left) and $S1c$ value (right) as a function of the number of scatters for WS2022 MS DD NR calibration data, with the mean value for each number of scatters indicated (red line). The data has a strict FV cut (see section 4.2.1), an ROI cut ($S1c < 150$ phd, $2.5 < \log(S2c / \text{phd}) < 5.0$), and cathode, gate and field cage resistor cuts applied.

Further investigation found that the reason for this effect is the non-linear relationship between the recoil energy of a scatter and the resultant charge and light yield. NEST simulations (discussed in section 2.10.1) show this to be the case, and the charge and light yield distributions, as a function of recoil energy, for NRs and beta ERs were shown in Figure 2.14. This means that for a given total recoil energy, the total charge and light yields are different if the energy is deposited all at once (SS), or deposited in smaller quantities over a number of recoils (MS). The net effect of this is what is observed in Figure 3.1, that the total MS S2c (and S1c to a lesser extent) increases, relative to an equivalent energy SS event, when the S2c pulses are simply summed.

Consequently, in $\log(S2c)$ vs. $S1c$ space, NR ER discrimination for MS events is relatively poor, as is illustrated by Figure 3.3 that shows the leakage of simulated Th-232 MS ER events into the NR band in this space as a function of $S1c$. It can be seen that this leakage is most prominent around 150 phd where the NR band is seen to rise in Figure 3.1 due to higher numbers of scatters being more common at these energies. This poor discrimination is problematic for the calculation of the SS neutron estimate since, in order to use Equation 3.2, the number of MS neutrons (NR events) in the WIMP search data is required. If the NR and ER MS events cannot be distinguished, then this number cannot be measured.

Therefore, a new parameter space is required in which better discrimination between NR and ER MS events can be achieved. The existence of such a parameter space is motivated by the fact that in using just the total S2c value, information regarding the individual pulse sizes has been disregarded. This suggests that an analysis that utilises this knowledge of the S2c of each of the scatters could potentially provide better discrimination.

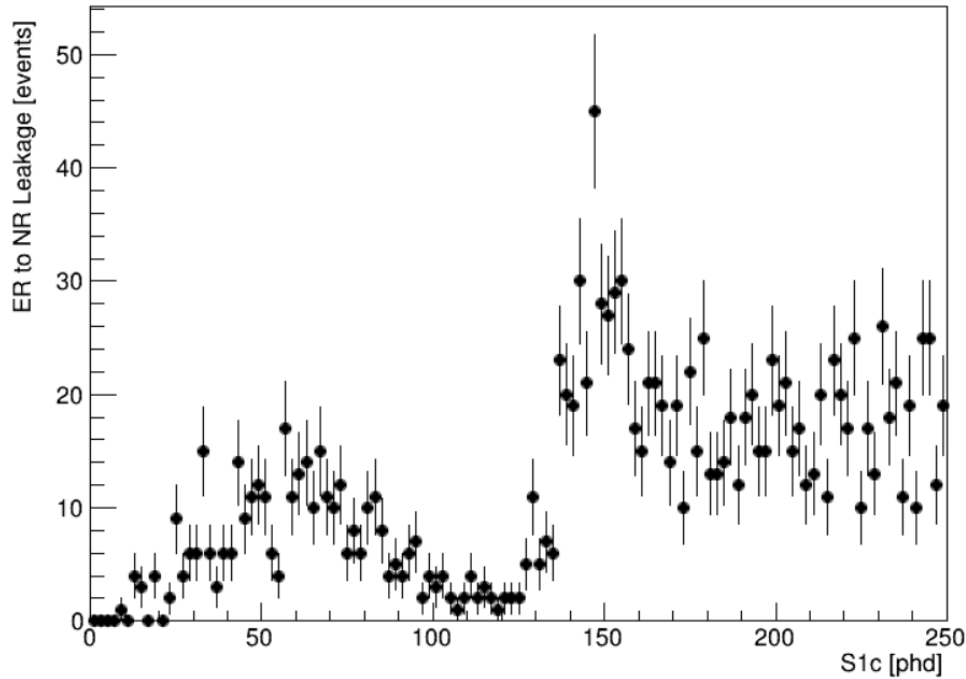


Figure 3.3: Leakage of simulated *Th-232* MS ER events into the MS NR band in $\log(S2c)$ vs. $S1c$ space as a function of $S1c$. The NR band is extrapolated to 250 phd in $S1c$.

3.3 The $\Delta\chi^2$ Method

The following MS analysis method was developed in order to create a parameter space with better NR ER MS discrimination power than the traditional $\log(S2c)$ vs. $S1c$ space, thus addressing the problem highlighted in the previous section. The following will describe how this method treats a single MS event with one total $S1c$ pulse and N $S2c$ pulses, where N is the number of scatters in the event.

In order to create this new parameter space, a new variable, $\Delta\chi^2$, is defined according to:

$$\Delta\chi^2 \equiv \chi_{NR}^2 - \chi_{ER}^2. \quad (3.3)$$

This parameter evaluates how NR-like or ER-like a given MS event is by comparing χ^2 fits of the event data to both the NR and ER models for charge and light production, as defined by NEST. Since these are χ^2 tests, a larger value indicates a worse fit of the model to the data. This means that NR events should have a negative value of $\Delta\chi^2$, and ER events should have a positive value, since the parameter is driven by the worse of the two fits. The various steps of this analysis method are presented as a flowchart in Figure 3.4, the details of which will now be explained chronologically.

Firstly, since only the total $S1c$ is known, an estimate for the individual $S1c$ pulses from each of the N scatters is required. To obtain this, the $S1$ light is estimated to be apportioned across

the scatters in the same proportions as the S2 light, shown by:

$$S1c_i = \left(\frac{S2c_i}{S2c^{tot}} \right) S1c^{tot}, \quad (3.4)$$

for the i^{th} scatter of the event. In this equation the ‘tot’ superscript indicates the total of all summed pulses of that type for an event.

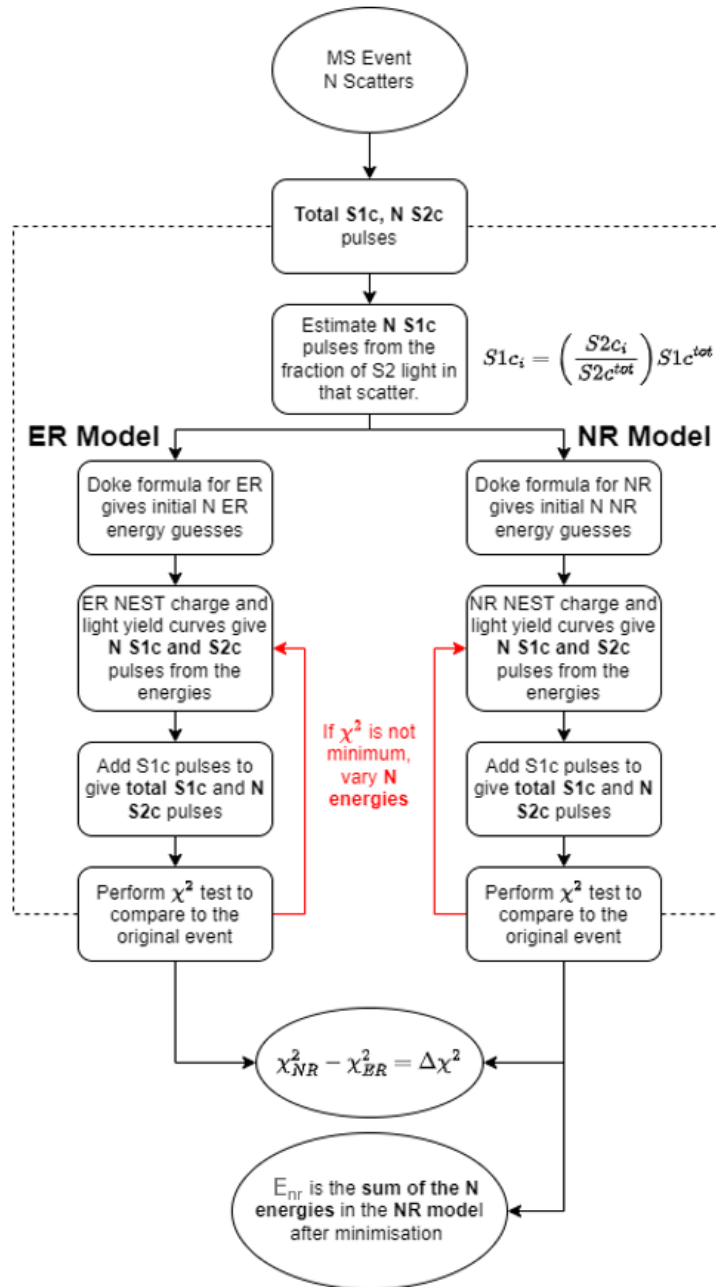


Figure 3.4: Flowchart illustrating the $\Delta\chi^2$ analysis method. Note that the loops shown in red are handled within the minimisation of χ^2 for each of the NR and ER branches.

From this point, the method splits into two simultaneous branches, as is illustrated in Figure 3.4.

The two branches model the MS event as having all NR scatters, or all ER scatters. Investigation into the number of MS events with mixed NR and ER scatters found the occurrence of such events to be minimal (except in the case of inelastic NRs, as will be discussed in section 4.3). From the initial estimate of the S1c and S2c for each of the scatters, the Doke formula [119]:

$$E = N_q \frac{W}{L(E)} = \left(\frac{S1c}{g_1} + \frac{S2c}{g_2} \right) \frac{W}{L(E)},$$

can be used to calculate the recoil energy of the scatter. This formula was discussed previously in section 2.1, and was expressed in Equation 2.1.

N_q can also be expressed as the power law $N_q = \alpha E^\beta$, where α and β can be found from fitting E vs. N_q across NRs from numerous different experiments with different drift fields [120]. The previously discussed Lindhard factor, $L(E)$, and the work function, W , are accounted for by the constants α and β in this case. Therefore, for NRs, Equation 2.1 can be expressed in the form of:

$$E = \left(\frac{N_q}{\alpha} \right)^{1/\beta} = \left(\frac{1}{\alpha} \left[\frac{S1c}{g_1} + \frac{S2c}{g_2} \right] \right)^{1/\beta}. \quad (3.5)$$

Therefore, using Equation 2.1 for the ER model and Equation 3.5 for the NR model, an initial estimate of the N scatter energies can be made in both the NR and ER cases. From these energies, the NEST charge and light yield distributions, shown in Figure 2.14, are used to obtain the charge and light yields (Q_y and L_y) under both of the two recoil hypotheses, and therefore S1c and S2c (the NEST distributions will give the average spatially corrected values provided the correct g_1 and g_2 are used) are calculated according to:

$$S1c = g_1 L_y E, \quad (3.6)$$

$$S2c = g_2 Q_y E. \quad (3.7)$$

It is primarily for this reason that it is important that up to date, accurate values of the gains g_1 and g_2 are used. The use of incorrect values will lead to shifts in the location of an event in $\Delta\chi^2$ space, potentially causing it to enter or leave a band.

Following this step, the S1c pulses are summed to give a total S1c and N S2cs, comparable with the original measured event quantities. χ^2 tests are then performed on the two models with respect to the original measured quantities, and χ^2 is minimised for each hypothesis by varying the individual scatter energies. Initially, the fractional errors on S1c and S2c that are used in the definition of the χ^2 test statistic (discussed in section 2.12.1) were assumed to be equal to the inverse of the square root of the number of S1 photons detected and electrons extracted from the liquid surface, n_{ex} , respectively, based on Poisson statistics. This is the assumption made for the version of the $\Delta\chi^2$ method that is used for WS2022, which is covered in chapter 4. This means that the errors on the total S1c pulse and the S2c pulses for a given event were of the forms shown in:

$$\sigma(S1c) = \sqrt{S1c}, \quad (3.8)$$

$$\sigma(S2c) = \frac{S2c}{\sqrt{n_{ex}}} = \frac{S2c}{\sqrt{\frac{S2c}{SE}}} = \sqrt{S2c \times SE}, \quad (3.9)$$

respectively. Here, SE is the pulse area produced by a single electron being extracted from the liquid surface, and causing electroluminescence while travelling to the anode. This type of pulse is what constitutes an S2 when many occur at the same time, as was previously discussed in section 2.9.2.

The definition of χ^2 in each of the NR and ER branches of this method is given by:

$$\chi_{model}^2 = \frac{(S1c_{event}^{tot} - S1c_{model}^{tot})^2}{\sigma^2(S1c_{event}^{tot})} + \sum_i^N \frac{(S2c_{i,event} - S2c_{i,model})^2}{\sigma^2(S2c_{i,event})}, \quad (3.10)$$

for an N scatter event. Here, ‘model’ represents either NR or ER depending on which branch of the algorithm is being calculated for. ‘Event’ refers to the initial measured quantities of the MS event, and therefore will be the same for both of the two branches. The error assumption expressed by Equations 3.8 and 3.9 is removed for WS2024, and the description of the updated approach is discussed at length in section 3.3.1.

Once the minimised values of χ^2 are obtained for both the NR and ER models, then the difference between the two is found, and $\Delta\chi^2$ is defined according to Equation 3.3. To get a two-dimensional parameter space comparable to the traditional $\log(S2c)$ vs. $S1c$ space, $\Delta\chi^2$ is plotted against the sum of the fitted scatter energies in the NR model, E_{nr} . For conciseness, this parameter space will henceforth be referred to as $\Delta\chi^2$ space, unless any changes to the x axis variable need to be specified. Gaussian NR and ER bands can be defined in this space, using calibration source simulations, that can be used to identify NR and ER MS events. Full technical details of the implementation of this method can be found in Appendix A.

Prior to the update to the $\Delta\chi^2$ method, during the work done for WS2022, it was investigated whether a loosening of the assumptions presented in Equations 3.8 and 3.9 could lead to an improved discrimination between NRs and ERs for MS events. This constituted assuming that the fractional errors were proportional to the minimum number of information carriers (S1 photons and extracted electrons for S1 and S2 signals respectively), rather than the direct equalities shown in these equations. The constants of proportionality were referred to as a for S1 and b for S2. This investigation did not yield meaningful results, and the subsequent, more rigorous, update to the methodology of the $\Delta\chi^2$ method meant that this avenue of investigation was not pursued further. Nonetheless, a brief overview of this study follows.

Data was acquired for the widths of several photopeaks of different energies and a linear best fit of energy peak width against the square root of the energy was calculated. For the energies

at which data was acquired, a and b were varied, and the expected energy widths were calculated from the Doke formula for the different error values. The values of the constants of proportionality that followed the best fit line calculated from the data the most closely were $a = 1.03$ and $b = 2.70$. However, when applied to the error calculation in the $\Delta\chi^2$ method, these tuned values were not found to give improved discrimination, and so these two constants were set to unity for the WS2022 analysis. It is not yet fully understood why this attempted improvement did not lead to better discrimination power.

3.3.1 Incorporating S1 S2 Correlations into the $\Delta\chi^2$ Parameter

The initial assumption in the calculation of χ^2 , for each of the two recoil hypotheses, was that the fractional error on the S1 and S2 signals was equal to the reciprocal of the square root of the minimum number of information carriers. However, this does not account for the inherent anti-correlation between S1 and S2 signals, due to recombination fluctuations after ionisation of the xenon by an incident particle. Recombination is when electrons liberated from the xenon atom are re-captured by the ion before they are drifted away by the electric field. De-excitation that occurs during recombination means that additional photons are released, and hence the S1 signal is increased. However, since there are fewer electrons to be extracted into the electroluminescence region, the S2 signal is reduced. This is why recombination fluctuations lead to an anti-correlation between S1 and S2 signals. This can be seen by the shape of the ER photopeaks in $\log(S2c)$ vs. $S1c$ space, shown in Figure 3.5. For these peaks, as $S1c$ increases, $S2c$ decreases.

Consequently, the definition of χ^2 that is minimised for both the NR and ER models needs to be updated to allow for these correlations, which requires the matrix equation described by:

$$\chi^2 = \underline{x}^T \underline{\underline{\Omega}}^{-1} \underline{x}, \quad (3.11)$$

with, for an N scatter event:

$$\underline{x} = \begin{pmatrix} S1c_{event}^{tot} - S1c_{model}^{tot} \\ S2c_{1,event} - S2c_{1,model} \\ S2c_{2,event} - S2c_{2,model} \\ \dots \\ S2c_{N,event} - S2c_{N,model} \end{pmatrix}.$$

Let $\sigma_{ci}^2 = \sigma_c^2(S2c_i)$ and $\sigma_{mi}^2 = \sigma_m^2(S2c_i)$ for $(i=1, \dots, N)$, then:

$$\underline{\underline{\Omega}} = \begin{pmatrix} \sigma_m^2(S1c^{tot}) + \sum_{i=1}^N \sigma_{ci}^2 & -\sigma_{c1}^2 & -\sigma_{c2}^2 & \dots & -\sigma_{cN}^2 \\ -\sigma_{c1}^2 & \sigma_{m1}^2 + \sigma_{c1}^2 & 0 & \dots & 0 \\ -\sigma_{c2}^2 & 0 & \sigma_{m2}^2 + \sigma_{c2}^2 & \dots & 0 \\ \dots & \dots & \dots & \dots & \dots \\ -\sigma_{cN}^2 & 0 & 0 & \dots & \sigma_{mN}^2 + \sigma_{cN}^2 \end{pmatrix}.$$

Note that in this definition of the covariance matrix $\underline{\underline{\Omega}}$, all S1c and S2c values are the measured quantities in the original event. The terms $\sigma_m(S1c)$, and $\sigma_m(S2c)$ refer to the uncertainty arising from fluctuations in the measurement of S1 and S2 respectively. This is a detector dependent effect. σ_c refers to the experiment independent anti-correlation between S1 and S2 due to recombination fluctuations. For both S1 and S2, the total uncertainty includes components due to measurement and recombination fluctuations. In the NR model, the anti-correlation terms, $-\sigma_c^2(S2c)$, are assumed to be zero, since this effect is much more prominent for ERs. This is because NR interactions involve quenching, and this means that a third possible channel (heat) is added to the ionisation and scintillation signals. Therefore, the anti-correlation between ionisation and scintillation is less strong, since energy can be lost to heat. Note that in the case where these anti-correlation terms go to zero, Equation 3.11 reduces back to Equation 3.10. The energy values for the respective widths of S1c and S2c can then be calculated from:

$$\sigma(E_1) = \frac{W}{g_1} \sigma(S1c), \quad (3.12)$$

$$\sigma(E_2) = \frac{W}{g_2} \sigma(S2c). \quad (3.13)$$

Finally, the terms needed for the covariance matrix can be found using:

$$\sigma_m^2(E_1) = \frac{1}{2}(\sigma^2(E) + \sigma^2(E_1) - \sigma^2(E_2)), \quad (3.14)$$

$$\sigma_m^2(E_2) = \frac{1}{2}(\sigma^2(E) - \sigma^2(E_1) + \sigma^2(E_2)), \quad (3.15)$$

$$\sigma_c^2 = \frac{1}{2}(\sigma^2(E_1) + \sigma^2(E_2) - \sigma^2(E)). \quad (3.16)$$

The full derivations of these equations are confined to Appendix B for brevity, but they come from the assumption that each of the $\sigma(E_1)$ and $\sigma(E_2)$ widths comprises a component due to measurement (m) and a component due to S1 S2 anti-correlations (c), first discussed in Ref [167].

To characterise the energy distributions of these parameters, a study was carried out using ER photopeaks from the WS2024 SS dataset, for which the electron equivalent energy (E_{ee}) (using the Doke formula of Equation 2.1 with the Lindhard factor set to 1), S1c, and S2c, along with $\sigma(E_{ee})$, $\sigma(S1c)$, and $\sigma(S2c)$ were measured. This data was provided by G. Pereira. 13 peaks were used

for this, and these measurements are laid out in Table 3.2. In this table, the superscript μ refers to the mean value. This data was taken using only the bottom PMT readings for S2c, and hence uses the notation of S2_bc. This choice was made in order to reduce the chances of saturation of PMTs in this study, since the bottom PMTs will see less S2 light from the peak events, some of which were relatively high energy. The use of S2_bc leads to a lower g_2 value of $g_{2b} = 11.98$. This difference would require a correction when used on S2c rather than S2_bc pulses in the calculation of $\sigma_m(S2c)$ for a given MS event.

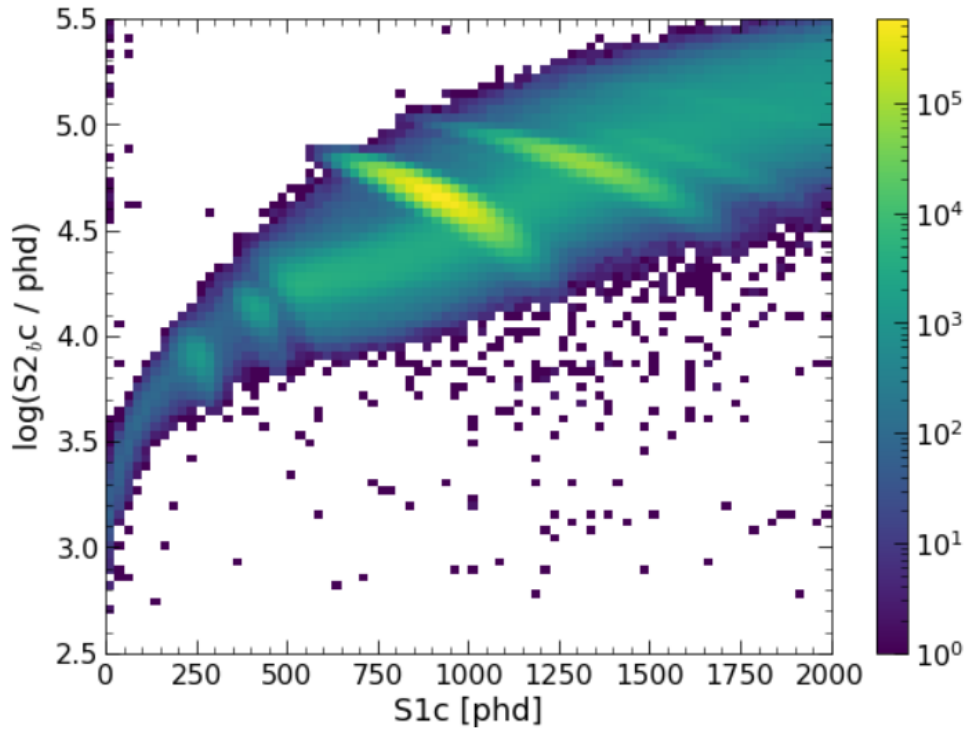


Figure 3.5: *WS2024 photoppeak data within the range of $0 \text{ phd} < S1c < 2000 \text{ phd}$, $2.5 < \log(S2_{b,c} / \text{phd}) < 5.5$. $S2_{b,c}$ here indicates that data was taken using only the bottom PMT array for S2s. Dataset provided by G. Pereira.*

Figure 3.5 shows some of the peaks used for this study in the S1c vs. $\log(S2_{b,c})$ parameter space, specifically those with an S1c value less than 2000 phd. One peak from this dataset was not measured and listed in Table 3.2. This was the 63 keV peak associated with the neutron activation of xenon, and it was not included as it was not present during the initial energy resolution study conducted by G. Pereira.

The mean values and widths of S1c, S2_bc, and electron equivalent energy that are reported in Table 3.2 were verified, since this data was not produced by the author of this thesis. Some rough peak selections were applied in S1c vs. $\log(S2_{b,c})$ space, and the peaks were fitted with Gaussian distributions for the three aforementioned variables. It is recognised that this verification process was less thorough than that which was followed for the creation of the data in Table 3.2, and therefore, in the case of any minor discrepancies, the data produced by G. Pereira was assumed to

Peak	E_{ee}^{μ} [keV]	$S1c^{\mu}$ [phd]	$S2bc^{\mu}$ [$\times 10^5$ phd]	$\sigma(E_{ee})$ [keV]	$\sigma(S1c)$ [phd]	$\sigma(S2bc)$ [phd]
^{127}Xe	28.9 ± 0.4	195 ± 2	0.054 ± 0.001	2.5 ± 0.6	26 ± 2	1200 ± 100
^{83m}Kr	40.95 ± 0.05	283 ± 1	0.0775 ± 0.0005	2.29 ± 0.05	23 ± 2	1140 ± 70
^{131m}Xe	163.780 ± 0.008	991.5 ± 0.2	0.4488 ± 0.0004	4.305 ± 0.008	84.4 ± 0.3	7080 ± 50
^{127}Xe + ^{129m}Xe	236.192 ± 0.008	1425.8 ± 0.3	0.6517 ± 0.0004	5.228 ± 0.008	107.6 ± 0.4	9230 ± 50
^{214}Bi	609.1 ± 0.2	3081 ± 6	2.258 ± 0.005	7.9 ± 0.2	208 ± 7	19700 ± 700
^{214}Bi	911.6 ± 0.4	4289 ± 5	3.711 ± 0.004	11.1 ± 0.5	329 ± 6	31200 ± 600
^{228}Ac	967.6 ± 0.3	4506 ± 6	3.988 ± 0.005	10.1 ± 0.4	347 ± 8	32000 ± 600
^{214}Bi	1120.2 ± 0.2	5105 ± 5	4.725 ± 0.007	11.6 ± 0.3	398 ± 7	38600 ± 900
^{60}Co	1169.8 ± 0.4	5297 ± 9	4.993 ± 0.008	12.3 ± 0.5	390 ± 10	38000 ± 1000
^{40}K	1460.7 ± 0.1	6478 ± 6	6.350 ± 0.006	12.0 ± 0.1	455 ± 8	44100 ± 900
^{214}Bi	1764.5 ± 0.7	7650 ± 10	7.828 ± 0.007	14 ± 1	560 ± 20	53000 ± 900
^{214}Bi	2206.1 ± 0.4	9390 ± 30	9.98 ± 0.03	16.8 ± 0.4	400 ± 40	40000 ± 5000
^{208}Tl	2618.2 ± 0.3	10950 ± 20	12.03 ± 0.02	16.9 ± 0.3	570 ± 30	55000 ± 3000

Table 3.2: *WS2024 photopeak data used for the study of the distributions of $\sigma_m^2(E_1)$, $\sigma_m^2(E_2)$, and σ_c^2 , provided by G. Pereira.*

be correct.

The first peak that was studied in more detail was the Kr-83m peak at 40.95 keV, and the verification of the measurements for this peak is shown in Figure 3.6. Firstly, the top left plot of the figure shows the rough selection applied in $S1c$ vs. $\log(S2bc)$ space to select this peak from the total photopeak dataset. The top right plot of the figure shows the distribution of the events in this selection in $S1c$, and this is fitted with a Gaussian distribution, a process which gave the best-fit values for the mean and standard deviation of $S1c^{\mu} = (258.6 \pm 0.4)$ phd and $\sigma(S1c) = (24.6 \pm 0.5)$ phd. The values measured for this verification and those recorded in Table 3.2 for this peak can be compared. While these measurements do not match exactly, given the rough nature of the verification process with respect to the more thorough measurement process conducted by G. Pereira, it was deemed that the agreement was sufficient to give confidence in the values that had been supplied.

The same process was followed for the bottom left plot of the figure which shows the $S2bc$ distribution. The fitting yielded results of $S2bc^{\mu} = (7860 \pm 20)$ phd, and $\sigma(S2bc) = (1050 \pm 20)$ phd. Finally, for the bottom right plot, in which energy is plotted, it was found that (38.61 ± 0.03) keV, and $\sigma(E_{ee}) = (2.50 \pm 0.04)$ keV. Agreement in both of these cases with the measured values in Table 3.2 was again sufficient to verify the numbers provided.

The next peak for which measurements were verified was the Xe-131m peak at 163.780 keV, and the verification plots are shown in Figure 3.7. As for the Kr-83m peak, the figure shows the rough peak selection in $S1c$ vs. $\log(S2bc)$ space (top left plot of the figure), along with Gaussian fits to the distribution of events in the peak for $S1c$, $S2bc$, and electron equivalent energy. The values

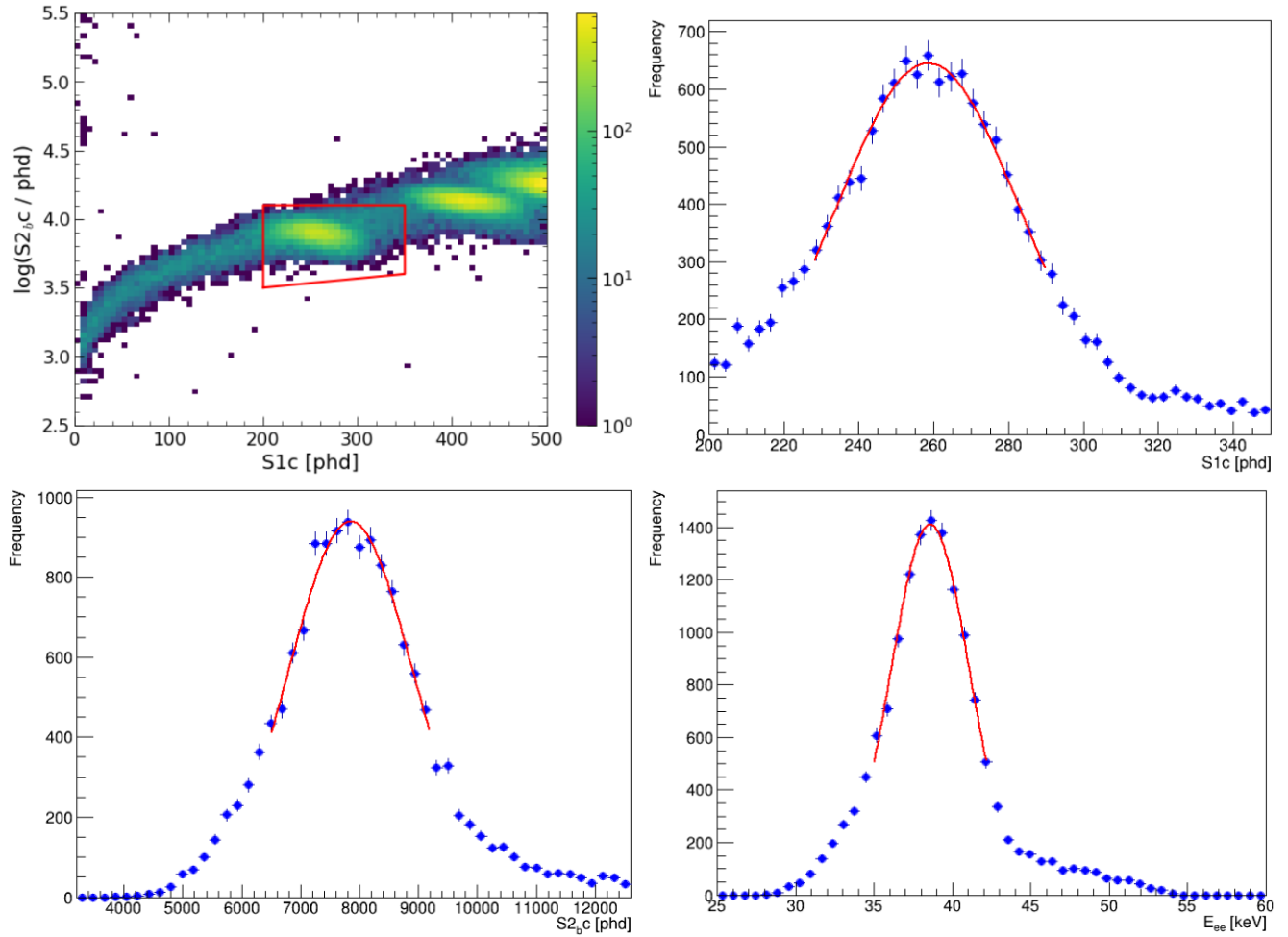


Figure 3.6: Verification of the $S1c$, $S2_b,c$, and electron equivalent energy measurements of the 40.95 keV Kr-83m photopeak from WS2024 data. The peak selection is shown in $S1c$ vs. $\log(S2_b,c)$ space (top left), along with the distribution of these events in $S1c$ (top right), $S2_b,c$ (bottom left), and electron equivalent energy (bottom right). The following values for the means and standard deviations of the Gaussian fit curves shown (red) for these distributions were obtained: $S1c^\mu = (258.6 \pm 0.4)$ phd, $\sigma(S1c) = (24.6 \pm 0.5)$ phd, $S2_b,c^\mu = (7860 \pm 20)$ phd, $\sigma(S2_b,c) = (1050 \pm 20)$ phd, $E_{ee}^\mu = (38.61 \pm 0.03)$ keV, and $\sigma(E_{ee}) = (2.50 \pm 0.04)$ keV.

obtained from these fits were as follows: $S1c^\mu = (924.00 \pm 0.03)$ phd, $\sigma(S1c) = (79.26 \pm 0.04)$ phd, $S2_b,c^\mu = (44.770 \pm 0.003) \times 10^3$ phd, $\sigma(S2_b,c) = (7.135 \pm 0.004) \times 10^3$ phd, $E_{ee}^\mu = (156.992 \pm 0.002)$ keV, and $\sigma(E_{ee}) = (4.117 \pm 0.002)$ keV. These values can again be compared to the measurements provided in Table 3.2.

Generally, it is seen that the measurements made for the verification of the Xe-131m peak are in better agreement with the measurements provided than was the case for the Kr-83m peak. This is likely largely due to the fact that the Gaussian fits in Figure 3.7 match the data considerably better than those in Figure 3.6. This could be because the Xe-131m photopeak is a better match

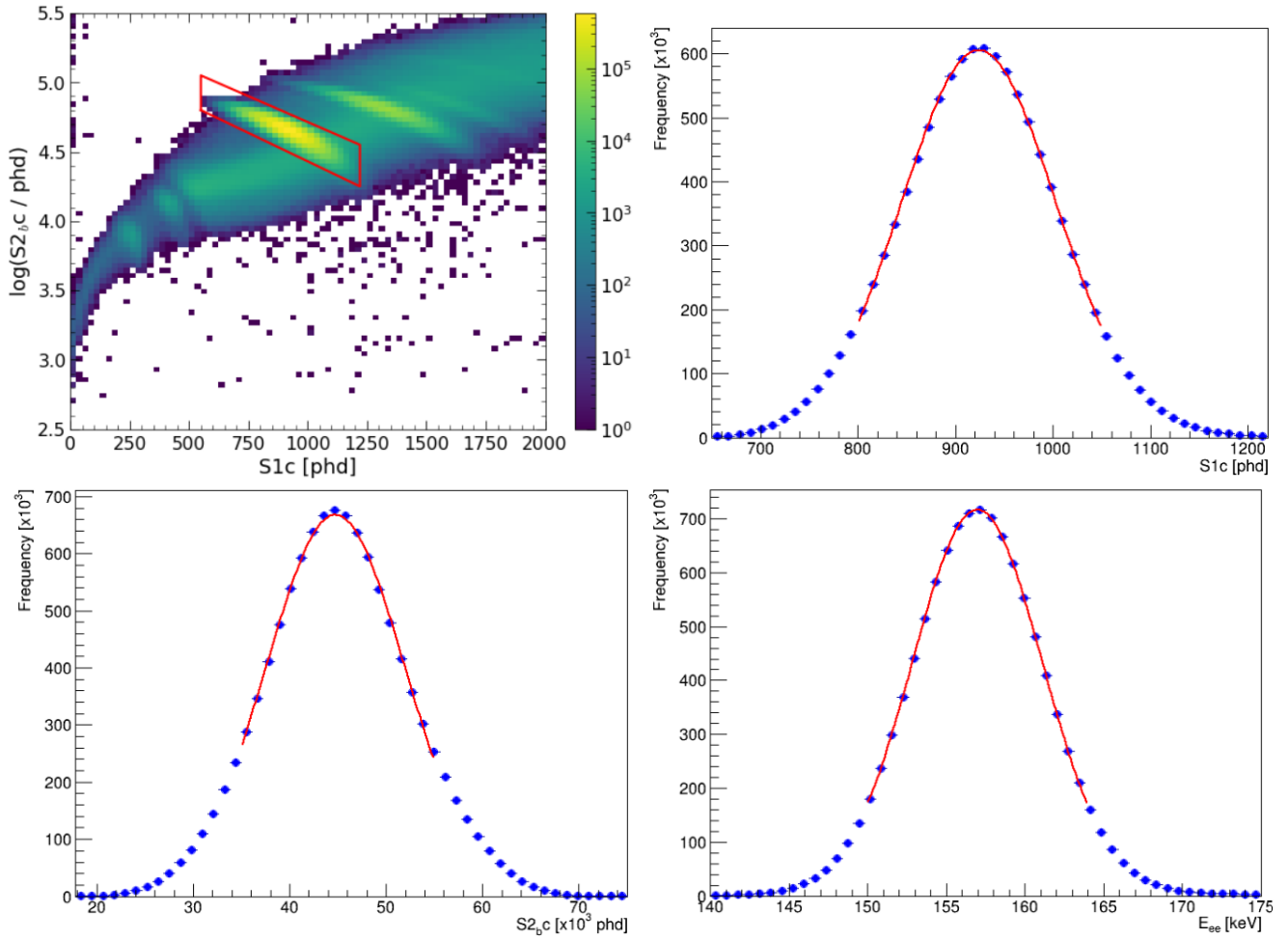


Figure 3.7: Verification of the $S1c$, $S2_b c$, and electron equivalent energy measurements of the 163.780 keV Xe-131m photopeak from WS2024 data. The peak selection is shown in $S1c$ vs. $\log(S2_b c)$ space (top left), along with the distribution of these events in $S1c$ (top right), $S2_b c$ (bottom left), and electron equivalent energy (bottom right). The following values for the means and standard deviations of the Gaussian fit curves shown (red) for these distributions were obtained: $S1c^\mu = (924.00 \pm 0.03) \text{ phd}$, $\sigma(S1c) = (79.26 \pm 0.04) \text{ phd}$, $S2_b c^\mu = (44.770 \pm 0.003) \times 10^3 \text{ phd}$, $\sigma(S2_b c) = (7.135 \pm 0.004) \times 10^3 \text{ phd}$, $E_{ee}^\mu = (156.992 \pm 0.002) \text{ keV}$, and $\sigma(E_{ee}) = (4.117 \pm 0.002) \text{ keV}$.

to a simple Gaussian distribution, as was used for the verification, whereas the Kr-83m peak could be more complex, potentially involving some skew. It is important to note that the verification measurements do not perfectly agree with the more comprehensive measurements made for this peak, but this level of agreement was deemed sufficient to verify the measurements provided.

The final peak that was studied as part of this verification process was the 236.192 keV peak from the combination of Xe-127 and Xe-129m photoemission, the selection and Gaussian fits for which are shown in Figure 3.8. As for the previous peaks, the figure shows the rough peak selection in $S1c$ vs. $\log(S2_b c)$ space (top left), along with Gaussian fits to the distribution of peak events in

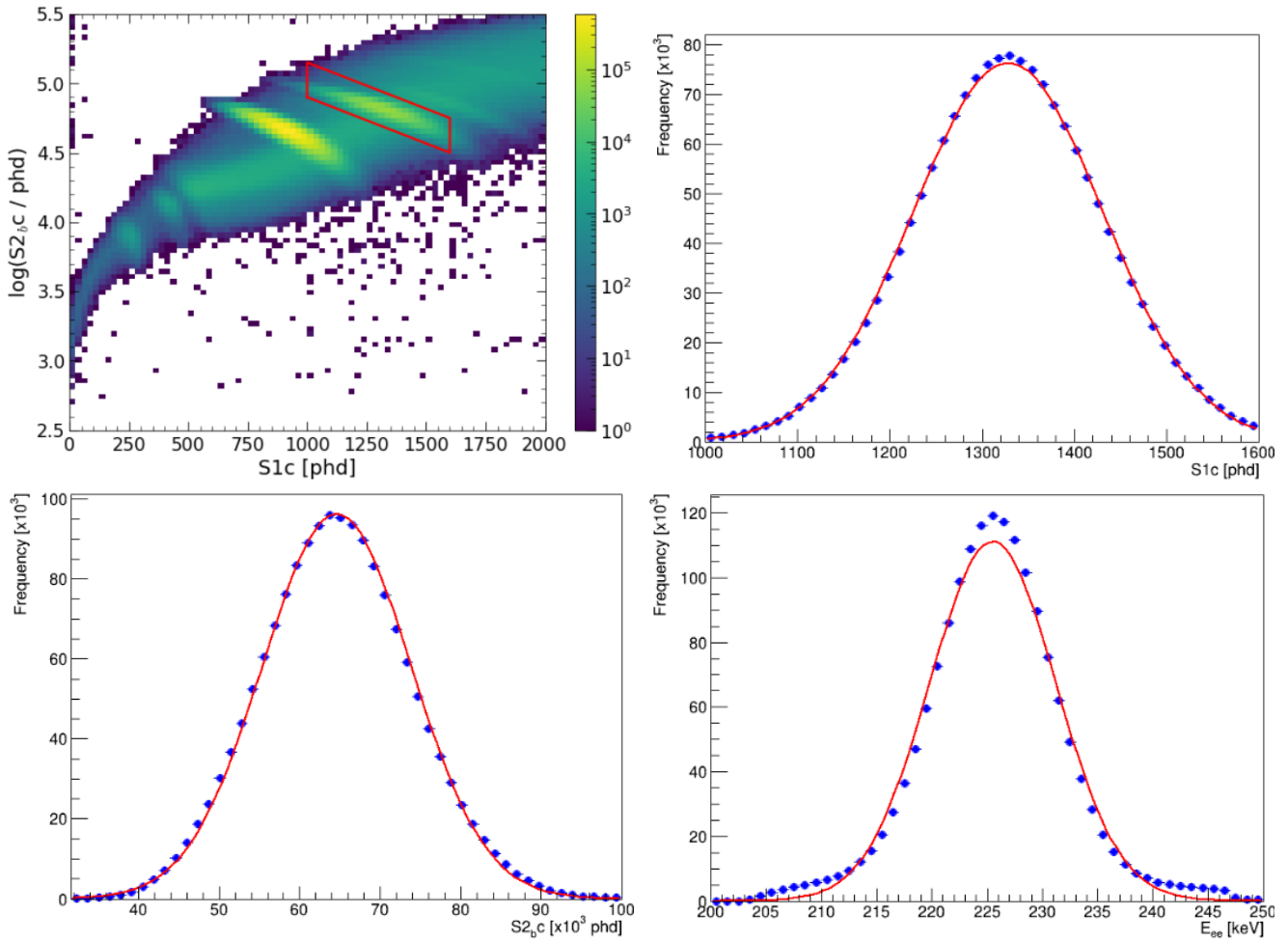


Figure 3.8: Verification of the $S1c$, $S2_{b,c}$, and electron equivalent energy measurements of the 236.192 keV Xe-127 + Xe-129m photopeak from WS2024 data. The peak selection is shown in $S1c$ vs. $\log(S2_{b,c})$ space (top left), along with the distribution of these events in $S1c$ (top right), $S2_{b,c}$ (bottom left), and electron equivalent energy (bottom right). The following values for the means and standard deviations of the Gaussian fit curves shown (red) for these distributions were obtained: $S1c^\mu = (1328.4 \pm 0.1)$ phd, $\sigma(S1c) = (101.0 \pm 0.1)$ phd, $S2_{b,c}^\mu = (64.35 \pm 0.01) \times 10^3$ phd, $\sigma(S2_{b,c}) = (9.31 \pm 0.01) \times 10^3$ phd, $E_{ee}^\mu = (225.600 \pm 0.006)$ keV, and $\sigma(E_{ee}) = (5.213 \pm 0.007)$ keV.

$S1c$, $S2_{b,c}$, and electron equivalent energy. Once more the verification values can be compared to the measurements provided, the verification values being as follows: $S1c^\mu = (1328.4 \pm 0.1)$ phd, $\sigma(S1c) = (101.0 \pm 0.1)$ phd, $S2_{b,c}^\mu = (64.35 \pm 0.01) \times 10^3$ phd, $\sigma(S2_{b,c}) = (9.31 \pm 0.01) \times 10^3$ phd, $E_{ee}^\mu = (225.600 \pm 0.006)$ keV, and $\sigma(E_{ee}) = (5.213 \pm 0.007)$ keV.

As was found for the Xe-131m peak, the agreement and fits for the Xe-127 + Xe-129m peak were found to be better than for the Kr-83m peak, but not in complete agreement with the more comprehensively measured values. Nevertheless, the agreement was sufficient to accept the provided values for this peak. A comparison between the values measured in this verification

and the values measured by G. Pereira is shown in Table 3.3. Going further, having verified the measured values for the three peaks for which this process is easiest (some peaks are difficult to measure due to being very faint, for example), it was decided that the measurement process was sufficiently well understood and verifiable that the values provided by G. Pereira for electron equivalent energy (E_{ee}), S1c, and S2_bc, along with $\sigma(E_{ee})$, $\sigma(S1c)$, and $\sigma(S2_{bc})$, could be accepted.

Kr-83m				
Variable	Provided Mean	Verification Mean	Provided σ	Verification σ
S1c [phd]	283 ± 1	258.6 ± 0.4	23 ± 2	24.6 ± 0.5
S2c [phd]	7750 ± 50	7860 ± 20	1140 ± 70	1050 ± 20
E_{ee} [keV]	40.95 ± 0.05	38.61 ± 0.03	2.29 ± 0.05	2.50 ± 0.04
Xe-131m				
Variable	Provided Mean	Verification Mean	Provided σ	Verification σ
S1c [phd]	991.5 ± 0.2	924.00 ± 0.03	84.4 ± 0.3	79.26 ± 0.04
S2c [phd]	44 880 ± 40	44 770 ± 30	7080 ± 50	7135 ± 4
E_{ee} [keV]	163.780 ± 0.008	156.992 ± 0.002	4.305 ± 0.008	4.117 ± 0.002
Xe-127 + Xe-129m				
Variable	Provided Mean	Verification Mean	Provided σ	Verification σ
S1c [phd]	1425.8 ± 0.3	1328.4 ± 0.1	107.6 ± 0.4	101.0 ± 0.1
S2c [phd]	65 170 ± 40	64 350 ± 10	9230 ± 50	9310 ± 10
E_{ee} [keV]	236.192 ± 0.008	225.600 ± 0.006	5.228 ± 0.008	5.213 ± 0.007

Table 3.3: Comparison of WS2024 photopeak measurements made by G. Pereira with the verification measurements made by the author of this thesis.

By feeding these values into Equations 3.14-3.16, $\sigma_m^2(E_1)$, $\sigma_m^2(E_2)$, and σ_c^2 can be found for each of the peaks. In Figure 3.9, $\sigma_m(S1c)/S1c$ is plotted as a function of the mean S1c of the peak. Note that this conversion between S1c and E_1 is just the inverse of what was used in Equation 3.12. This data is fitted with the standard calorimeter resolution function, which is given by:

$$\frac{\sigma_m(S1c)}{S1c} = \sqrt{\left(\frac{a}{\sqrt{S1c}}\right)^2 + \left(\frac{b}{S1c}\right)^2 + c^2}. \quad (3.17)$$

From this, for a given value of S1c, $\sigma_m(S1c)$ can be obtained. Note that the errors on a , b , and c given in Figure 3.9 are not propagated further in the current version of this analysis. The figure shows that the calorimeter resolution function is a good fit to the data and can provide a representative distribution when the fitted parameters are used.

Similarly, Figure 3.10 shows $\sigma_m^2(S2_{bc})/S2_{bc}^2$ plotted as a function of mean S2_bc. Note the persistence of the power of two from Equation 3.15 here, since the values of $\sigma_m^2(S2_{bc})$ are negative

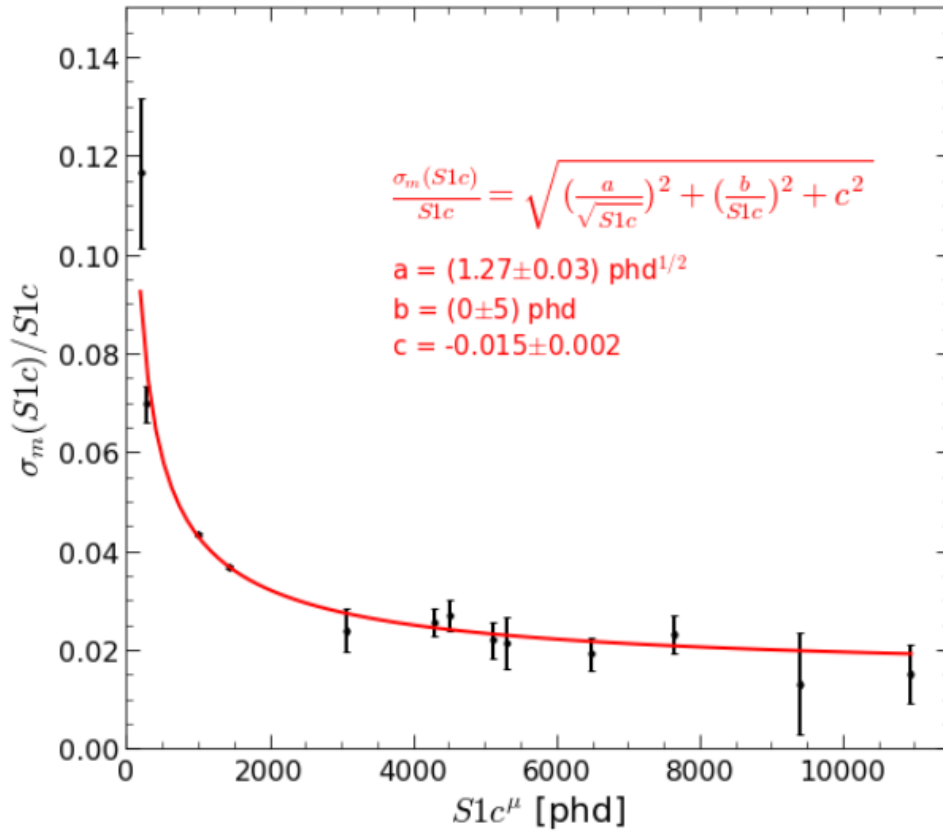


Figure 3.9: Distribution of the resolution of $\sigma_m(S1c)$ as a function of the mean $S1c$ value for WS2024 photopeaks, fitted with the standard calorimeter resolution function, shown by Equation 3.17. This fit has $\chi^2 / ndf = 11.2 / 10$.

for some of the peaks, and hence obtaining a meaningful result from taking the square root is not possible. However, it can be seen that, within errors, the component of the $S2_{bc}$ width due to the measurement of the signal is largely consistent with zero. This data is fitted with the square of the standard calorimeter resolution function, and indeed that fit yields the result that the data is most consistent with a constant value of zero, although this is due to the fit being forced to zero because of the negative data points with small errors. Therefore, $\sigma_m(S2c)$ was set to zero for this work, and the aforementioned correction to $\sigma_m(S2c)$ to account for the difference between $S2c$ and $S2_{bc}$ is no longer necessary. This means that the $S2c$ width is dominated by the uncertainty introduced by the recombination fluctuations, σ_c . It is worth noting in Figure 3.10 that the third and fourth lowest energy points sit below zero, and do not have error bars sufficiently large as to include zero in their range. It is not currently known why the measurements made for these specific photopeaks are not completely in agreement with the rest.

Finally, Figure 3.11 shows σ_c plotted against the number of ions, obtained as $N_{ion} = S2_b c^\mu / g_{2b}$. This was fitted to a polynomial with non-zero coefficients for powers of 1/2 and 1, as shown by:

$$\sigma_c = a\sqrt{N_{ion}} + bN_{ion}. \quad (3.18)$$

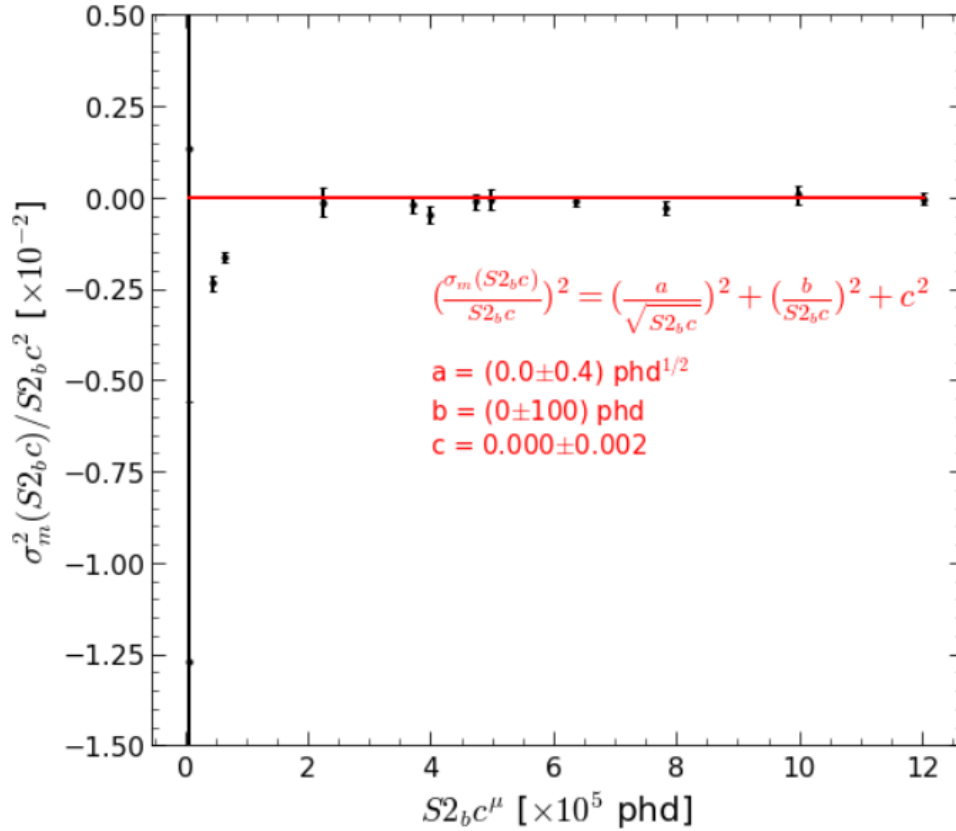


Figure 3.10: Distribution of the resolution of $\sigma_m^2(S2_b c)$ as a function of the mean $S2_b c$ value for WS2024 photopeaks, fitted with the square of the standard calorimeter resolution function that is shown by Equation 3.17. Note that the error bars on the first two points extend beyond the scope of this plot. This fit has $\chi^2 / ndf = 266.6 / 10$.

This parametrisation was chosen simply because it is seen to have a good fit to the data below $N_{ion} \approx 6 \times 10^4$.

The two points with the largest numbers of ions were outliers from this trend, and were therefore not included in the fit. A potential explanation for this discrepancy is saturation effects of PMTs at larger S2c values. This could have occurred despite efforts to mitigate this by the use of only the bottom PMTs, which see less S2 light. This means that this fit cannot be not shown to be valid above $\sim 6 \times 10^4$ ions. However, this is not a concern for this work since both WS2022 and WS2024 have an upper limit cut of $S2c < 10^5$ phd with respective g_2 values of 47.1 phd/electron and 34.0 phd/electron, giving maximum numbers of ions of 2123 and 2941 respectively, and these values are significantly below the region where the fit is no longer valid. A second fit was performed on the data, including the two points with the highest numbers of ions, to the function $\sigma_c = a \tanh(b\sqrt{N_{ion}} + cN_{ion})$, shown in blue in the figure, but this fit is not used for the work presented in this thesis. From Figure 3.11, for a given value of S2c, with a known g_2 , σ_c can be obtained.

Therefore, for a given event, the covariance matrix, $\underline{\underline{\Omega}}$, is filled using the S2c values and the average S1c value measured for the event, before fitting with either the NR or the ER model. In

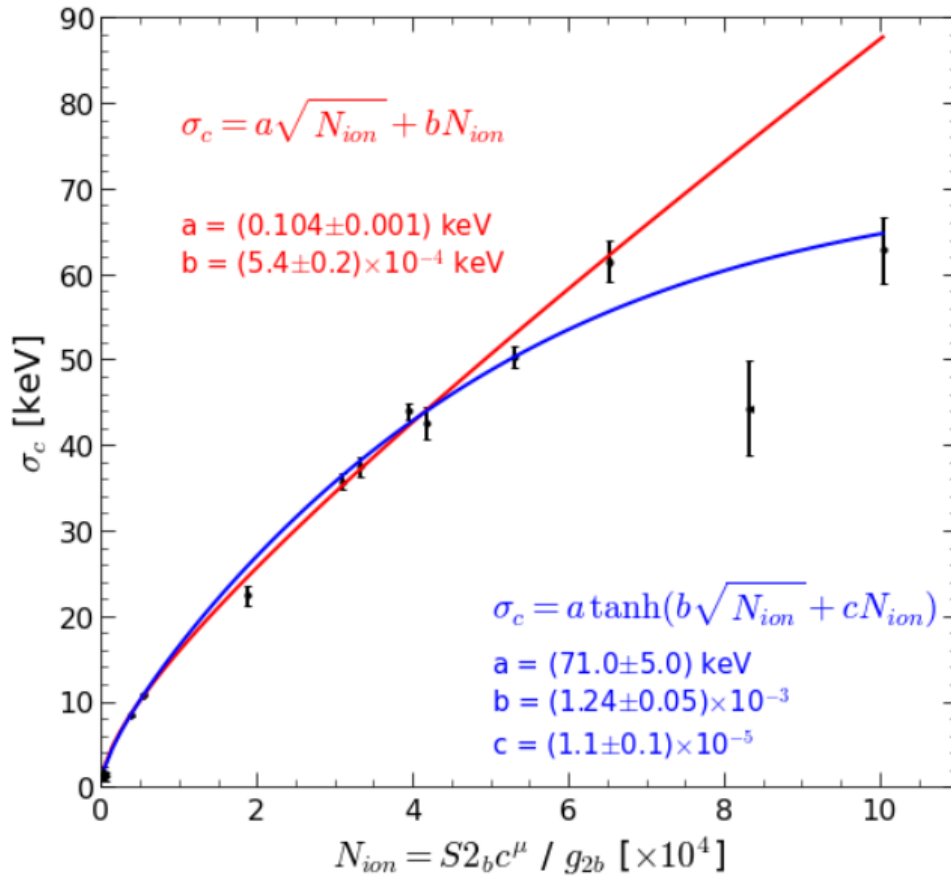


Figure 3.11: Distribution of σ_c as a function of the number of ions (defined by $N_{ion} = S2_b c^\mu / g2b$) for WS2024 photopeaks, fitted with a polynomial with non-zero coefficients for powers of 1/2 and 1 (red), as shown by Equation 3.18, and with a tanh function of that polynomial (blue). The two peaks with the highest numbers of ions were not included in this fit. This fit has $\chi^2 / ndf = 37.4 / 9$.

the case of the NR model, a version of this matrix with only the diagonal elements is used, as was previously discussed.

This new definition of χ^2 is minimised for both of the two branches of the method, as it was previously, and $\Delta\chi^2$ is calculated in the same way, but for a given event it will now have a different, more meaningful value, that encodes the inherent anti-correlation between S1 and S2 signals due to recombination fluctuations.

3.4 Multiplicity of MS Events

So far, MS events have largely been discussed as a single group, distinct only from SS events. However, for an event to be classed as having ‘multiple’ scatters, it need only have more than one, and hence this classification of events contains within it many subsets of events for the specific numbers of scatters that they contain. Therefore, it is worth considering the multiplicity of MS

events to better understand the makeup of the MS classification as a whole.

Figure 3.12 shows the number of scatters across all events in the WS2024 DD calibration dataset, after the application of data quality cuts. This includes both MS events and SS events, to put the proportion of each multiplicity in context. It can be seen from this figure that around 39% of DD events have only one interaction in the TPC, and are therefore classified as SS. One scatter is the single most probable number of scatters for a DD neutron to undergo, but because of the fact that the MS classification encompasses all events with more than one scatter, it is more probable that a DD neutron event will be an MS event rather than an SS event, with 61% of the events shown in Figure 3.12 being MS events.

The proportion of events with each subsequent number of scatters is seen to decrease exponentially, as shown by the fit displayed in the figure. It follows that if only the MS events are considered, the largest subset of events is the double scatters, which comprise around 25% of the DD events, and therefore approximately 41% of MS events. Triple scatters then account for $\sim 23\%$ of MS events, and quadruple scatters account for $\sim 9\%$. The largest number of scatters seen in this dataset was 30, but such high scatter events are uncommon, with MS events with more than 12 scatters making up only around 0.5% of the DD dataset studied here.

Events with a large number of scatters also pose an issue for the $\Delta\chi^2$ analysis method, since they drastically increase the computation time. This is due to the fact that in each of the two χ^2 minimisations there is a large number of free parameters (equal to the number of scatters) to vary in order to find the best fit. For this reason, in the $\Delta\chi^2$ analysis, a cut is imposed to remove events with greater than 20 scatters. This removes a very small subset of events from the analysis, but these events would have a dramatic impact on the computation time.

3.5 Previous Recombination Fluctuation Studies

Recombination fluctuations have been studied previously for liquid xenon, notably by the LUX collaboration [167]. Figure 3.13 shows a result from this investigation, where the recombination fluctuations were measured, here referred to as σ_r ($\sigma_r = \sigma_c$), as a function of the number of ions, as was done for LZ in section 3.3.1. The figure also compares this distribution to NEST simulations with different values of ω , a constant that parameterises the size of the fluctuations relative to a typical Poisson distribution [167]. Note that σ_r is plotted here in units of quanta, rather than keV, and these two representations differ only by a factor of W .

In order to compare the LUX results to those found in section 3.3.1, the LUX results for σ_c were converted into units of keV. Note that the LUX result covers a smaller range of N_{ion} than is used for this work. The comparison of the results presented in Figure 3.11 with the LUX best-fit results is shown in Figure 3.14. While the magnitude of these results are the same, there is a noticeable difference between the LUX and LZ datasets. The reasons for this discrepancy are

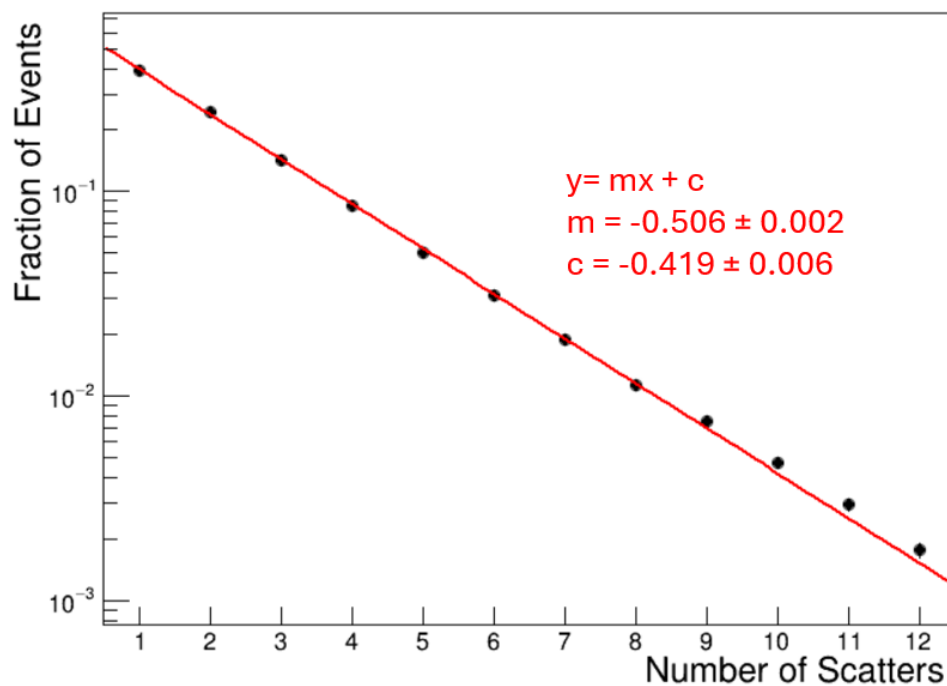


Figure 3.12: Multiplicity of DD calibration events in WS2024 after data quality cuts, shown as a fraction of the total number of events. Y error bars are too small to be seen. A log scale is used on the y axis and the data is fitted with a linear function of the form $y = mx + c$. This fit has $\chi^2 / \text{ndf} = 53.4 / 10$.

currently unclear.

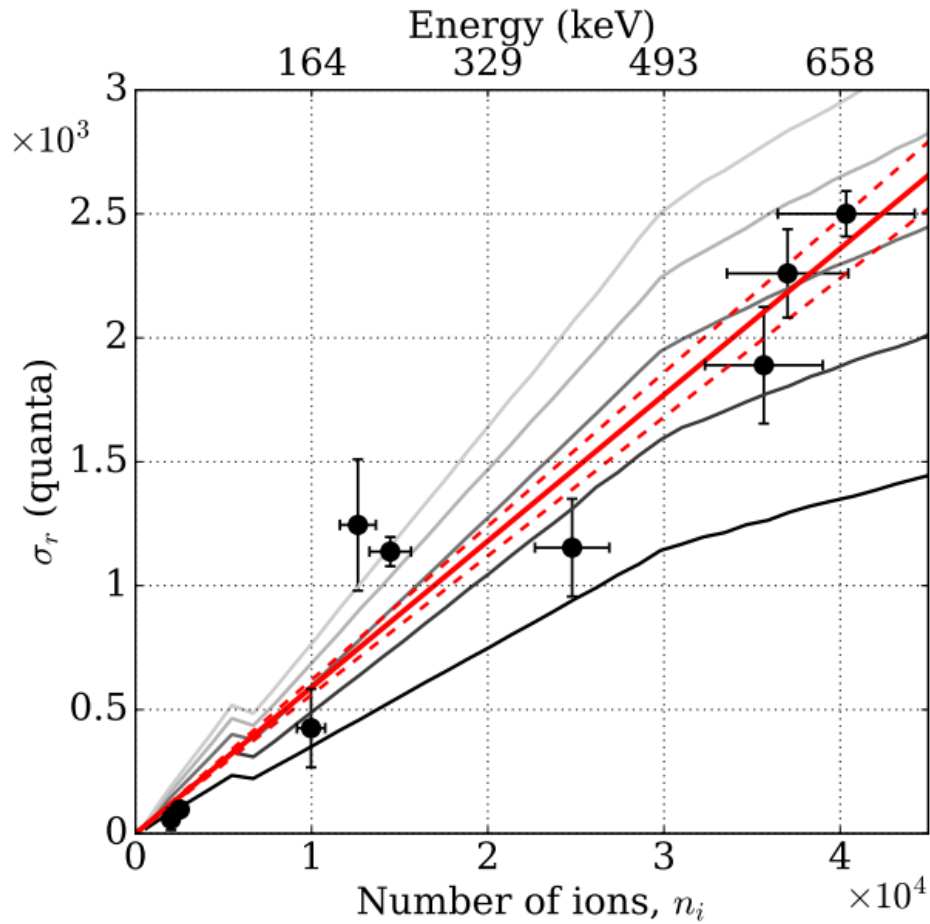


Figure 3.13: Recombination fluctuations, σ_r , plotted as a function of the number of ions, as measured by the LUX collaboration. The solid red line shows the linear best fit, with the dashed red lines showing the 1σ uncertainty on the fit. The solid grey and black lines show the distribution for NEST simulations that use different values of ω , a constant that parameterises the size of the fluctuations relative to a typical Poisson distribution. This figure is taken from Ref [167].

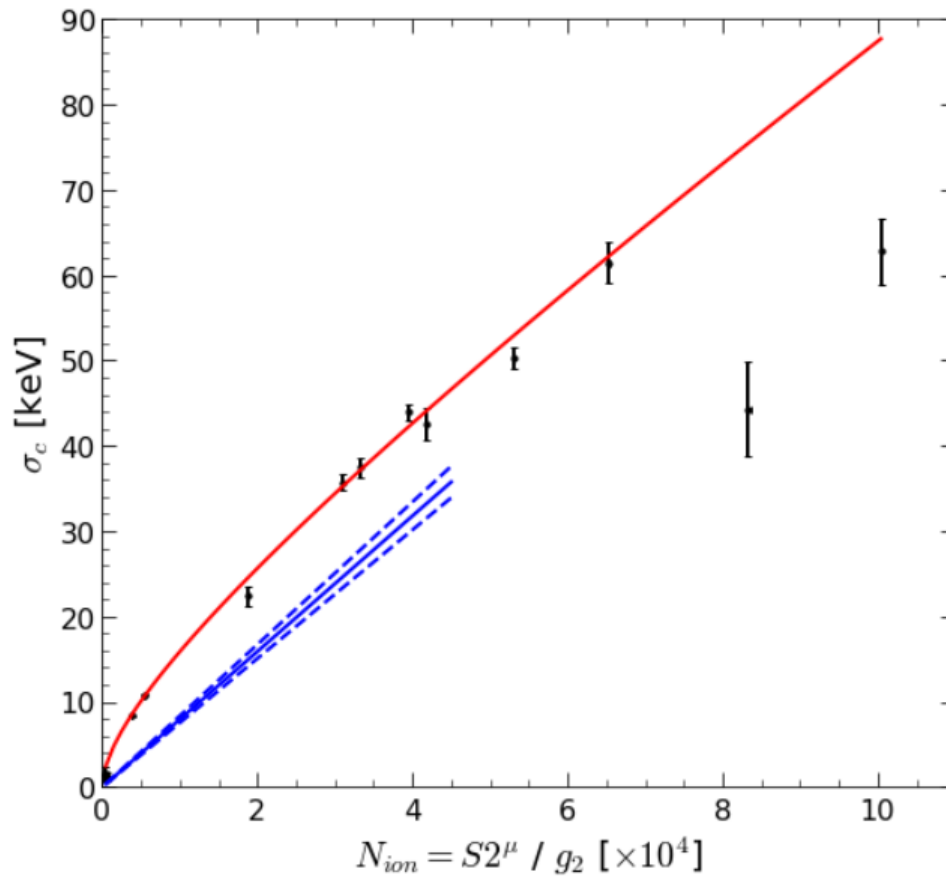


Figure 3.14: Re-plotting of the number of ions vs. σ_c (shown in Figure 3.11) to compare to the LUX result for measurement of the same parameter. As previously, data points from this work are shown along with the best-fit line (red) of a polynomial with non-zero coefficients only for $1/2$ and 1 . The LUX result linear best fit line (solid blue), along with the 1σ uncertainty (dashed blue) are plotted for comparison.

Chapter 4

WIMP Search 2022 Neutron Single Scatter Estimate

In 2022 LZ completed its first period of data collection [114]. During this time, the detector was running with a drift field of 193 V cm^{-1} (with a 4% variation over the detector volume used in the analysis, established by simulation) and a gas extraction field of 7.3 kV cm^{-1} at the centre of the detector. Taking all analysis cuts into consideration, the total live time of this WIMP search was 60 ± 1 days. The results of this WIMP search are given in section 4.1.

The methods presented in chapter 3, but without the recombination fluctuation update to the analysis, are applied to this data in order to produce an SS neutron estimate for the WIMP search ROI, and the results of this are presented across sections 4.2-4.9. It was during the WS2022 campaign that the $\Delta\chi^2$ analysis was initially developed.

4.1 LZ WS2022

The first WIMP search of the LZ detector [114] comprised 89 days of data (excluding calibration periods, DAQ system dead time, periods of anomalous trigger rates, and any detector maintenance periods), which is reduced to 60 ± 1 days after the live time loss of certain analysis cuts. Specifically, these cuts removed events in the wake of very large S2s or muons, after which the rates in the detector would be temporarily elevated. Details of the analysis cuts used in WS2022 will be given in section 4.2.

Using this data, LZ was able to set a new limit on spin-independent WIMP-nucleon cross-section, the limit curve for which is shown in Figure 4.1. This was calculated according to the statistical methods described in section 2.12.2.

As has been covered in previous chapters, it is essential that the number of SS neutrons is understood for a WIMP search. For WS2022, two estimates were made for this number, and they are described in Ref [150]. These results were released before the development of the $\Delta\chi^2$ method,

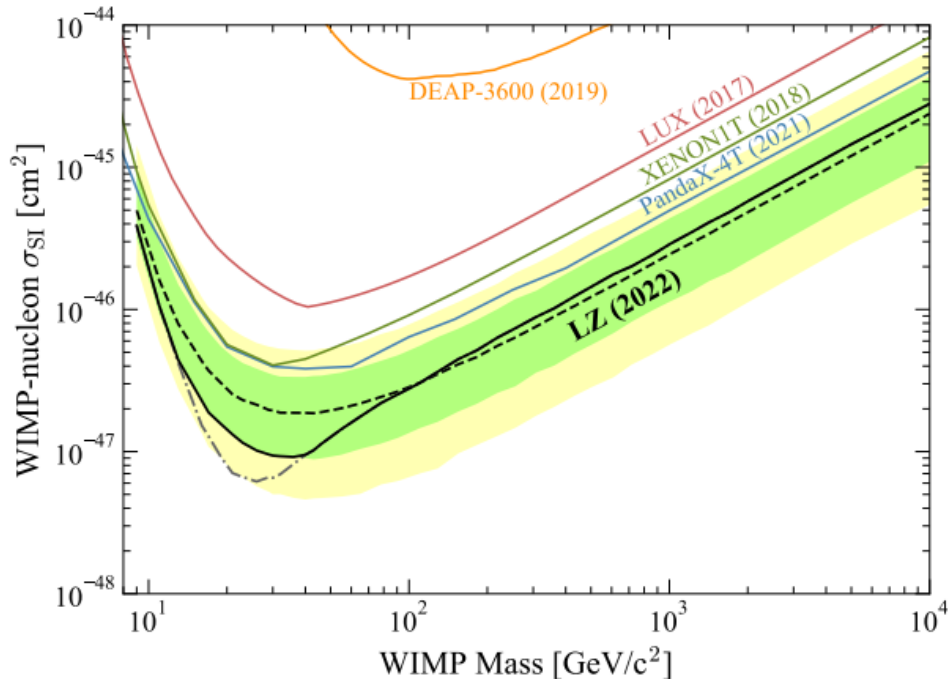


Figure 4.1: The WS2022 LZ spin-independent limit in WIMP cross section vs. WIMP mass space. The 90% confidence limit is shown by the black line, with the grey dot-dashed line showing this limit before power constraint. The green and yellow bands represent the 1σ and 2σ sensitivity bands respectively. Included in this figure for comparison are limits from PandaX-4T [103], XENON1T [102], LUX [95], and DEAP-3600 [168]. This figure is taken from Ref [114].

so this method was not used for the estimates that are described in Ref [150]. The first method used involved the study of SS events that had an OD veto signal, but otherwise passed all WIMP search cuts. The best fit number of neutrons in this sample was found to be $0^{+0.8}$, which led to an estimate of SS neutrons with no OD veto signal of $0^{+0.2}$ in the WIMP search ROI, with the uncertainty calculated as the standard deviation of the Gaussian constraints.

The second method was more comparable to the work in this thesis, and used the number of MS NR events to estimate the number of SS neutron events. This study found 10 MS neutrons in the WS2022 dataset, after selection of events with an OD veto signal and manual verification of candidate waveforms (‘handscanning’), and produced an estimate of 0.29 (no uncertainty provided in the reference) SS neutron events in the ROI with no veto signal [150].

4.2 Analysis Cuts for the $\Delta\chi^2$ SS Neutron Estimate

In order to calculate the MS-driven SS neutron estimate, before any analysis can be carried out on the data, a selection of data cuts are applied. This is to minimise unwanted backgrounds, such as accidental coincidences (see section 2.11.2). For the MS-focused work presented here, the cuts

applied are intended to match the WS2022 WIMP search cuts as closely as possible, since it is for this dataset that the estimate of SS neutrons is being made. An obvious distinction that must immediately be made between the dataset used for this study, and that used for the WIMP search, is that the WIMP search applies an SS selection, as defined by LZAP (see section 2.9.2), whereas for this MS study an MS selection is required.

It is also important to note that for LZLAMA simulated events, considerably fewer cuts are imposed. This is largely due to the fact that many of the cuts listed in this section, particularly the accidental coincidence cuts, rely on information about pulse shape that is not present in LZLAMA RQs. Accidental coincidences pose less of an issue in simulated data however, so these cuts are not required. For simulations, the cuts applied are the ROI cut, the strict FV cut, and the field cage resistor cut. In some cases, cuts are also applied for gate and cathode events.

4.2.1 Fiducial Volume

A crucial cut that is applied to the data is the FV cut that requires that events occur within a certain volume of the liquid xenon in the centre of the TPC. This means that there is effective self-shielding by the liquid xenon against particles, such as gammas and neutrons, most of which are expected to interact relatively close to the walls of the TPC. Near the walls, there are also localised field effects that can cause S2 charge loss. Also, embedded sources, such as radon, can plate out on the PTFE of the walls. Collectively, the build up of background events near the wall is referred to as ‘wall events’. The FV is much quieter, and therefore preferable for rare event searches, such as for WIMPs. The FV is defined such that there is a set small amount of leakage of wall events into the FV at each value of drift time. Therefore, a comprehensive model of wall events is required in order to define the FV. For WS2022, the definition of the FV can be seen in red in Figure 4.2. It is important to note that the FV cut is defined in terms of the uncorrected positions of scatters in the TPC, and all tuning of this cut was done using those RQs.

For SS events, whether or not they pass the FV cut (and are kept in the dataset) is trivial, as they occur at a single defined position that can be measured. However, for MS events this becomes non-trivial, since there are multiple interaction points. Initially, this was handled by using the S2c-weighted average value for x and y positions, as well as the drift time, as is done for the S1c values described in section 2.9.3. This meant that only the average position of the MS event needed to be in the FV. However, issues were discovered with this approach as it allowed certain events with failed position reconstruction to be included in the final dataset. For example, a double scatter event that had interactions incorrectly reconstructed as being outside of the TPC, but on opposite sides, could have the average position of the scatters being inside the FV, and therefore be included in the dataset.

A more common problematic event topology was seen while using the weighted average definition of the MS FV cut though, and this is shown in Figure 4.2. These are primarily double scatter

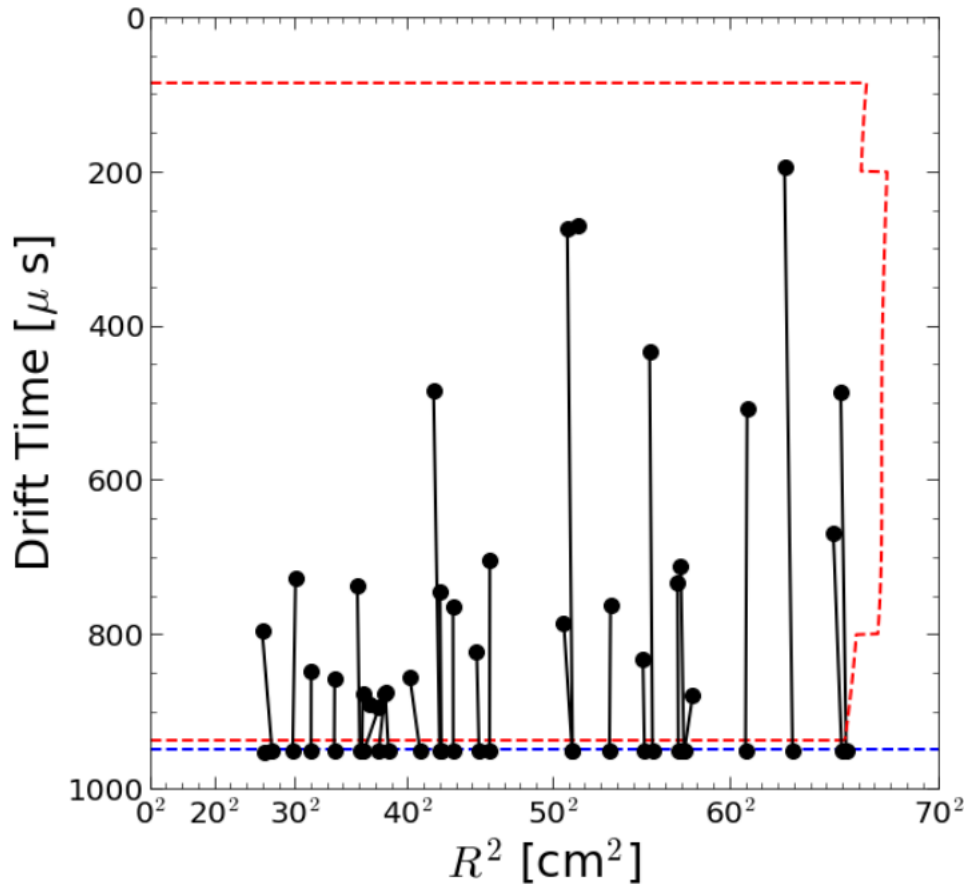


Figure 4.2: R^2 vs. drift time spatial distribution for a sample of WS2022 MS events passing the data quality cuts that have a UDT scatter on the cathode. All scatters are shown for a given event, connected by a line in an arbitrary order. Also shown in this figure is the FV boundary (red) and the UDT limit (blue).

events that have one scatter just beyond the UDT limit, sitting on the cathode. The other scatter (or scatters) is always nearly directly above the first. These are clearly not events that should be kept for analysis in this study, since they have a scatter that has an unphysical drift time, and therefore cannot be an NR interaction in the TPC. Note that the lines connecting the scatters of a given event in this figure just connect the scatters in order of drift time, since the order in which they occurred is not known.

By looking at the waveforms of these individual events, as is shown in Figure 4.3, it is seen that many of them have an additional, clear S1 pulse that LZAP had not considered to be part of the event. It is likely that for the events where this is not seen to be the case, that the additional S1 is just too small to be visible. Therefore, these events are in fact misclassified pile-up events. Since the first S1 of these events has been missed, both S2s are correlated with the second S1. This means that one of the scatters is falsely reconstructed as having a much smaller drift time (and therefore a higher position in the TPC), despite the drift times for the two events being, in reality, very similar. This is illustrated in Figure 4.3.

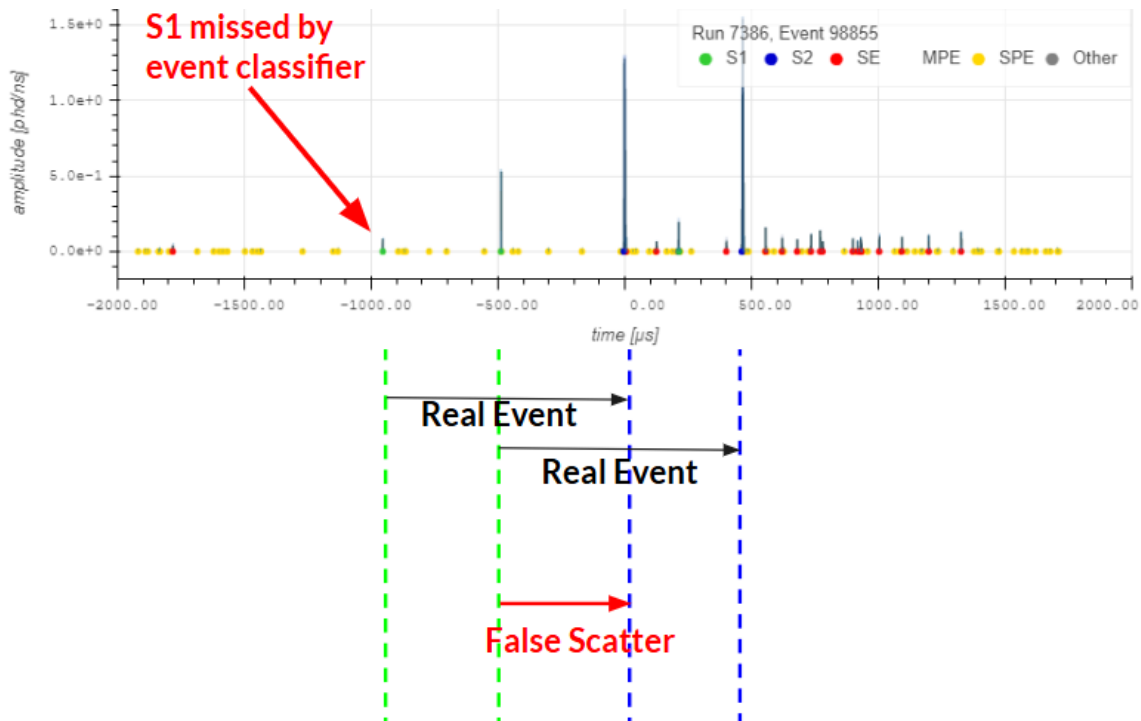


Figure 4.3: Illustration of how a mis-classified pile-up event can be interpreted as a vertical MS event. This event contains two S1 pulses (one of which is missed by the event classifier) and two S2 pulses. Below the waveform for an example event, the pulse matching that leads to the false MS event is illustrated.

Therefore, both of the events involved in the pile-up actually take place on the cathode. It was hypothesised that these could be decays of Bi-214 and Po-214 in the decay chain of U-238. This would be a beta decay of Bi-214 to Po-214, followed by an alpha decay of Po-214 to Pb-210. The S1 from the alpha decay would likely be more prominent than that from the beta decay, which could explain why the smaller S1 is overlooked. If this hypothesis is correct, the time between the two pile-up events (measured by the time between S2s) would have a half-life equal to that of Po-214: $164 \mu\text{s}$. The results of this study are shown in Figure 4.4.

In the few instances where three scatters are present, two values are contributed to this plot, since there are two times between the S2 reconstructed on the cathode and the two S2s reconstructed above the cathode. As can be seen from Figure 4.4, the half-life is indeed consistent with that of Po-214, since the value extracted from an exponential fit to the data is $180 \pm 40 \mu\text{s}$. The relatively small number of events in this study leads to a large error on this value for the half-life, and the need for relatively wide binning in Figure 4.4, but nevertheless the result is close to that expected for Po-214, which is also well within the error.

MS events such as these should not be included in the studies presented in this thesis, and therefore a new version of the MS FV cut was developed, which will henceforth be referred to as the strict FV cut. This cut is described as ‘strict’ because, rather than just requiring the average

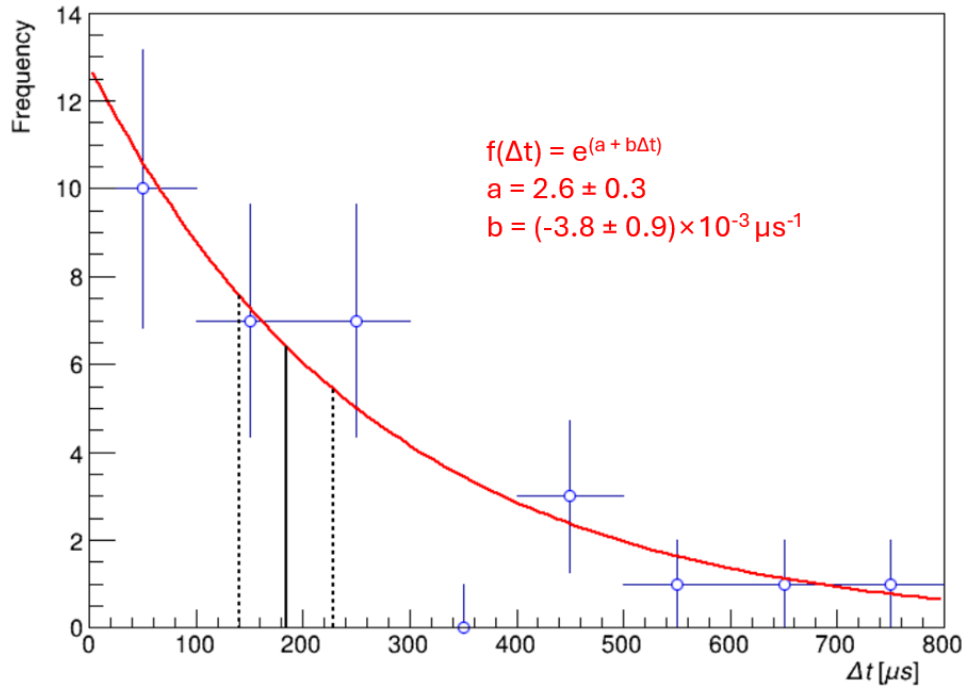


Figure 4.4: The time difference between $S2$ pulse starts (Δt) for MS events that have a scatter on the cathode, fitted with an exponential decay of function $f(\Delta t) = e^{(a+b\Delta t)}$ (red line). The bin at $350 \mu\text{s}$ is excluded from the fit due to zero events being recorded in that bin. The corresponding half-life of the function and the range of the error on the value are shown by the black solid and dashed lines respectively, $t_{1/2} = (180 \pm 40) \mu\text{s}$. $\chi^2 / \text{ndf} = 1.208 / 5$ for the exponential fit to the data.

scatter position of an MS event to be within the FV, it requires each individual scatter to be inside the FV. This makes logical sense as events with even one unphysical scatter will be excluded.

4.2.2 Field Cage Resistor Cut

The field cage that surrounds the TPC in order to shape the electric field, and minimise non-uniformity, was described in section 2.4. There are resistors that make up a part of this field cage [4] that have an elevated rate of radioactivity, and hence a relatively high rate of events is seen in their vicinity. For these regions, events within a certain radius of the field cage resistors are removed from the WIMP search dataset, and so the same requirement is applied to MS events. Again, a strict requirement, as with the FV, is enforced on MS events here, where they fail the cut and are removed if any of their scatters occur within the field cage resistor region. The radius around the resistors that was removed (from the full height of the detector, since it is a chain of resistors running up the field cage) is 6.0 cm.

4.2.3 Region of Interest

For WIMP searches, only a certain region of the $\log(S2c)$ vs. $S1c$ parameter space is of interest, and this is because it is in this region that WIMPs would be expected to create a signal. For this MS-driven SS neutron estimate, the ROI used, unless specified otherwise for additional studies, is $2.5 < \log(S2c / \text{phd}) < 5.0$, $S1c < 500$ phd. For MS events, this cut is applied to the $S1c$ and total $S2c$.

4.2.4 OD and Skin Veto Cuts

As has already been discussed at length in section 3.1.1, the Skin and OD veto detectors can detect a signal that is correlated with a signal in the TPC, and use that to eliminate an event as a WIMP candidate. For that reason, in WS2022 any SS event with a signal in either the Skin or OD is cut from the dataset. However, when studying neutrons it must be considered that the OD and Skin were designed to tag neutrons, and have an $(89 \pm 3)\%$ efficiency [114]. Therefore, the number of neutrons that are removed by a veto signal cut is relatively high by design. This means that, to increase statistics, the study presented in this chapter is also carried out using the requirement of a veto signal (the contrary to the usual requirement of no veto signal), and with a veto detector agnostic approach.

The specific requirements for the OD and Skin veto cuts in WS2022 are as follows. For the OD prompt veto, an event is tagged if there is a pulse within 300 ns (before or after) the $S1$ pulse, and with a coincidence threshold of 6 PMTs. For LZLAMA simulations, such as the neutron background simulation, where coincidence is not an applicable RQ, a minimum pulse area threshold of 4.5 phd is enforced instead. For the delayed veto, an event is tagged if the OD pulse is between 300 ns and 400 μs after the $S1$, and if it has a coincidence of at least 6 PMTs (not imposed for simulation). There is also a pulse area threshold of 17.6 phd.

For the prompt skin veto, a pulse is required within 500 ns (before or after) of the $S1$. A pulse area of 2.5 phd is required, and for non-simulation there is also the requirement of a coincidence of at least 3 PMTs. The delayed veto tags an event if the pulse is between 500 ns and 1200 μs after the $S1$, has an area of at least 50 phd, and, for non-simulation, requires a coincidence of at least 56 PMTs, based on high background rates observed.

4.2.5 Accidental Coincidence Cuts

As was discussed in section 2.11.2, a number of cuts were developed to try to target the population of accidental coincidences. A crucial caveat relevant for this analysis however, is that the accidental coincidence cuts were tuned on SS data for the purpose of being used on SS data. These cuts usually target specific topologies of $S1$ and $S2$ pulses that are seen in lone $S1$ s and $S2$ s, and therefore can be included in accidental coincidence events. The majority of these cuts were also not only tuned

on SS cuts, but constructed in such a way that they cannot be applied to MS events without alterations being made (for example, a cut would expect only one S2, as would be found in an SS event, and would break if multiple were presented). Therefore, MS versions of the accidentals cuts were made, where necessary, and the general approach taken to this was to apply the cuts to each of the individual pulses in the MS events, and require that all pulses passed the cuts. The accidental coincidence cuts that required alteration, along with the MS alterations made, are shown in Table 4.1. While not strictly an accidental coincidence focused cut, the valid xy reconstruction cut also required MS alteration, and is therefore also listed in this table.

Some further accidental coincidence cuts required no adaptation to be used for MS events. The S1 top-bottom asymmetry cut, as in the case of the S2 top-bottom asymmetry cut, requires that the top-bottom asymmetry of an S1 pulse (how light from the S1 signal is split across the PMT arrays) is reasonable given the known relationship with drift time. The S1 channel timing cut targets isolated S1s and S1s from hot PMTs. The spread in time over which different PMT channels peak for these types of event is seen to be distinct from usual S1s, and hence these populations can be targeted in this way.

Another accidental coincidence focused cut is the so-called ‘stinger’ cut. Since the electrode grids in LZ are not solid sheets, but rather metallic meshes, this means that it is possible for electrons travelling through the gaseous electroluminescence region of the TPC to pass through the anode grid and enter a region of lower electric field on the other side. At this point, the electrons will stop emitting electroluminescence. Once above the anode, however, they will turn and accelerate back towards it, and as they enter a region of higher electric field once more they will emit electroluminescence again before hitting the anode.

This leads to a characteristic waveform topology that contains an SE pulse, followed by a gap, followed by a small S1-like pulse. The S1 from this process is referred to as a ‘stinger’ S1, and is an isolated S1 pulse that can lead to an increased rate of accidental coincidences. A stinger S1 can also follow multiple electrons undergoing electroluminescence, and therefore can be preceded by an S2 pulse rather than an SE. It could also be preceded by a pulse that LZAP has identified as an ‘other’ pulse, but is in fact an SE or an S2, so this cut also checks for that event topology. Any events in which these sequences of pulses are seen are removed by this cut.

In this analysis, events with energies less than $12 \text{ keV}_{\text{nr}}$ are not considered in order to minimise the impact of accidental coincidence events as well as other low energy background signals.

4.2.6 Electron Train Veto

Electron trains (e-trains) and photon trains (ph-trains) occur in the aftermath of a particularly large S2 pulse in the TPC, known as a ‘progenitor’ S2. This large pulse causes further ionisation and excitation, and hence is followed by an increased rate of SEs. This is thought to be due to thermalisation and trapping of electrons at the surface of the liquid phase before they can be

Cut	Description	MS Alterations
Excess Area	Targets events with a significant total area of additional pulses before the S1, or between the S1 and S2.	Checks the area before the S1, and between the S1 and the first S2, relative to the first S2 area.
S1 Prominence	For events with multiple S1 pulses, ensures that at least one is within a physical drift time of the S2.	Checks physical drift times of S1s relative to the first S2.
High Single Channel	Targets events with an abnormally large amount of light in a single channel.	This cut is drift time dependent, so uses the weighted drift time for MS events.
S2 Top-Bottom Asymmetry	Verifies that the top-bottom asymmetry of an S2 pulse (how light from the S2 signal is split across the PMT arrays) is reasonable given the known relationship with drift time.	Checks that every S2 passes the cut.
Narrow S2	Removes abnormally narrow S2 events.	Checks that every S2 passes the cut.
Early Peak S2	Removes events with a characteristic spike early in the S2.	Checks that every S2 passes the cut.
S2 Rise Time	Removes events with an abnormally flat topped S2.	Checks that every S2 passes the cut.
Valid xy Reconstruction	This cut verifies that Mercury has output a valid reconstruction of the xy position for a given event.	Checks the first S2 of the event.

Table 4.1: LZ WS2022 accidental coincidence cuts that required MS adaptation, and how they were adapted for application to MS events. The valid xy reconstruction cut is also included since this required MS adaptation.

extracted into the gaseous electroluminescence region [169]. This phenomenon was also investigated for the LUX experiment [152]. When many of these pulses occur at once, as was discussed in section 2.9.2, SEs can be interpreted as S2s. As well as the SEs following a large progenitor S2, there are

also SPEs, which can be interpreted as an S1 pulse when many occur at once. All of this means that it is difficult to be sure that any pulses detected in the TPC in a given time window following a large S2 are in fact due to a separate interaction in the detector. It is for this reason that the e-train veto cut is used to remove a small amount of live time after every progenitor S2, so that there is no uncertainty over events in these windows.

4.2.7 Muon Cut

Another phenomenon that can cause temporary, localised, increased rates in the TPC is a muon passing through. This generally produces a much longer region of high rates across the detector as the highly energetic muon causes ionisation all along its path. The flux of muons is reduced by a factor of 3×10^6 , compared to the surface, by the 4300 mwe rock overburden [112], but muons still constitute a notable background to LZ. This muon flux is created by cosmic ray interactions with the atmosphere.

Like with a large progenitor S2, in the aftermath of a muon event there is an increased rate of SEs, SPEs, S2s, and S1s. Therefore, the muon cut searches for muon events and removes them from the WIMP-search dataset, along with any events that occur within the 20 s window following the event, during which the detector is blinded by the high rates.

Fortunately, since muons interact so clearly, they can be relatively easily spotted in the data by the signature hotspots that they produce. They are also very likely to interact with both the Skin and the OD, as well as the TPC, and can therefore additionally be identified by their veto signals.

4.2.8 Exclusion Periods

During the running of the detector, there are certain times when it is not possible to take meaningful WIMP search data due to an elevated rate of background noise. Runs in these exclusion periods are removed from the WIMP search dataset.

Firstly, the hotspot cut removes events from any runs that were recorded when there were localised elevated rates in the detector. During standard running, there were occasional periods of spurious electron emission from the electrode grids. Generally, these were transient phenomena, but could be seen as a localised ‘hotspot’ of increased rates in the xy plane of the TPC.

As data was collected, event rates were continuously monitored, and any run that contained one of these hotspots was flagged. The data quality in these flagged runs was later assessed and, if necessary, the run is removed from the dataset by the hotspot cut, which refers to a list of runs to exclude.

The S1 rate spike exclusion period removes events from periods during which elevated rates of S1s were detected.

4.2.9 OD Burst Cut

The OD burst noise cut aims to remove events that have erratic, continuous pulses in the OD, where usually clear sharp peaks are seen. The suggested origin of such pulses is mechanical sources exterior to the LZ water tank that affect only the OD. Overly noisy events are removed from the dataset.

4.2.10 Additional Cuts

In the interest of completeness, the final WS2022 cuts will be briefly mentioned here. Firstly, the sustained rate cut was designed to remove events with an excessively high SPE rate. Next, the buffer cut ensures there is a ‘buffer’ present at the end of TPC, OD, and Skin waveforms, where no pulses of note occur, in order to make sure that no part of the event is being missed. Lastly, the SS window cut enforces that events are not included from the final maximum drift time from the end of the event window.

4.3 NR and ER Band Definitions

To be able to differentiate between NR and ER MS events, an understanding of where these events are located in $\Delta\chi^2$ space is needed. To achieve this, reliable sources of MS NR and ER events are required. Initially, simulated data is used to generate the high statistics necessary to create the NR and ER bands in which these populations of events would be expected to sit, then these bands are verified using calibration data.

The 90-10 CL Gaussian bands for WS2022 are shown in Figure 4.5. Here, the simulations used for the NR and ER bands are DD and Th-232 respectively. Aside from the ROI cut, no cuts are applied to the Th-232 dataset, but the DD dataset has a strict FV cut applied, along with cuts for events around the gate, cathode, and field cage resistors. This is because statistics are much lower for MS ER events, so cuts have to be limited. Visible in the DD plot (left) of this figure, is a population of NR events, sitting closer to the ER band, at around ~ 170 keV_{nr} (note that this unit indicates the energy under the nuclear recoil model). This is thought to be a collection of inelastic NR events where kinetic energy is not conserved in some, or all, of the scatters. This means that the nucleus recoils as normal, but is also excited. As the nucleus de-excites, it emits photons which cause ERs. This means that an inelastic NR event can actually produce both NRs and ERs. Because of energy quenching in NRs, where energy is lost to heat rather than the observable scintillation or ionisation channels, it is the ER interactions that dominate in an inelastic NR event. It is for this reason that they appear more ER-like.

The right plot of Figure 4.5 shows the simulated Th-232 data used to create the ER band. Production of this dataset required the simulation of many more events, since low energy MS ERs

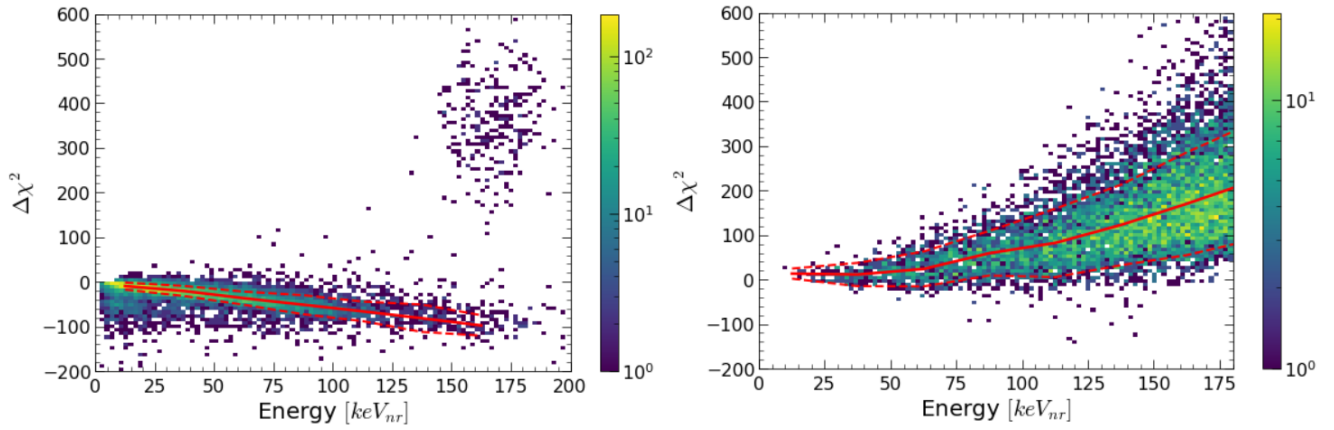


Figure 4.5: The 90-10 CL Gaussian NR (left) and ER (right) bands in $\Delta\chi^2$ vs. total fitted NR energy space (shown in red) used for the $\Delta\chi^2$ WS2022 analysis, overlaid on the respective DD and Th-232 simulations used to create them. The DD simulation has a strict FV cut applied, along with cuts for the gate, cathode, and field cage resistors. The NR band fitting is limited to $S1c < 120$ phd to avoid effects on the band from the inelastic scatter population (top right of the plot). A pre-fit ROI cut of $S1c < 250$ phd and $2.5 < \log(S2c / \text{phd}) < 5.0$ is applied to both datasets. The energy range of the left plot is extended to show the inelastic population.

are much less common than low energy MS NRs.

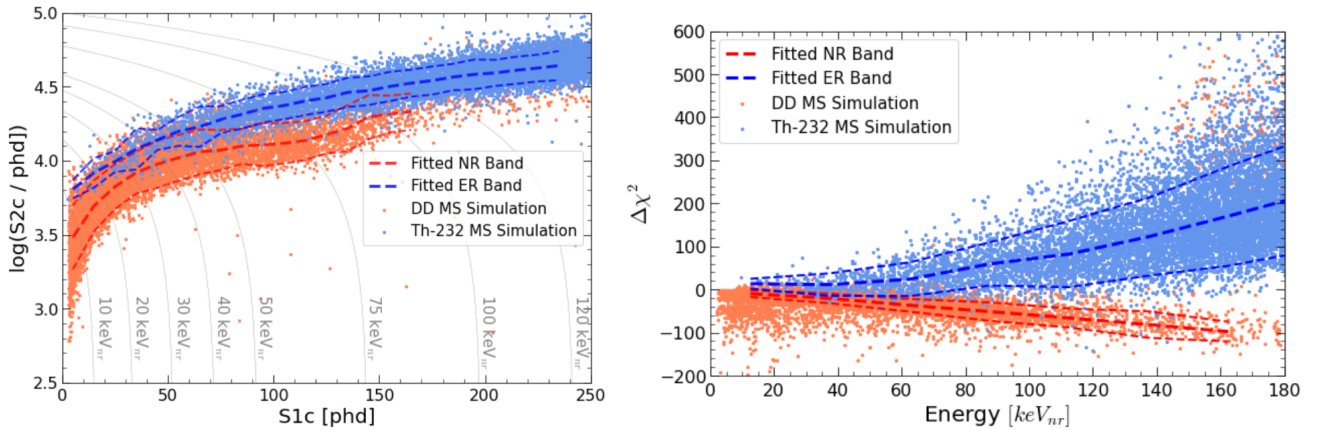


Figure 4.6: A demonstration of the difference in MS NR ER discrimination between the $\log(S2c)$ vs. $S1c$ parameter space (left), and the $\Delta\chi^2$ vs. total fitted nuclear recoil energy parameter space (right) using NR (DD, shown in light red) and ER (Th-232, shown in light blue) simulated data for WS2022. Also shown are fitted 90-10 CL Gaussian bands (red and blue respectively) for each of these two datasets, in each of the two parameter spaces. NR energy contours are shown in $\log(S2c)$ vs. $S1c$ space. A pre-fit ROI cut of $S1c < 250$ phd and $2.5 < \log(S2c / \text{phd}) < 5.0$ has been applied to both datasets and the DD simulation has a strict FV cut applied, along with cuts for the gate, cathode, and field cage resistors.

Figure 4.6 shows these two simulated datasets overlaid with each other, along with the fitted bands, in both $\log(S2c)$ vs. $S1c$ space and in $\Delta\chi^2$ space. NR energy contours are shown in $\log(S2c)$ vs. $S1c$ space for reference, but it should be noted that these energies are not directly comparable to those in the post-fitting $\Delta\chi^2$ space due to the non-linearity of charge and light production with recoil energy (discussed in section 3.2), as well as the effects of the fitting itself. It can be clearly seen that the discrimination between NR and ER events is markedly improved in the latter parameter space with respect to the former, as is shown by the comparison of ER leakage into the NR band in the two parameter spaces, as is presented in Figure 4.7.

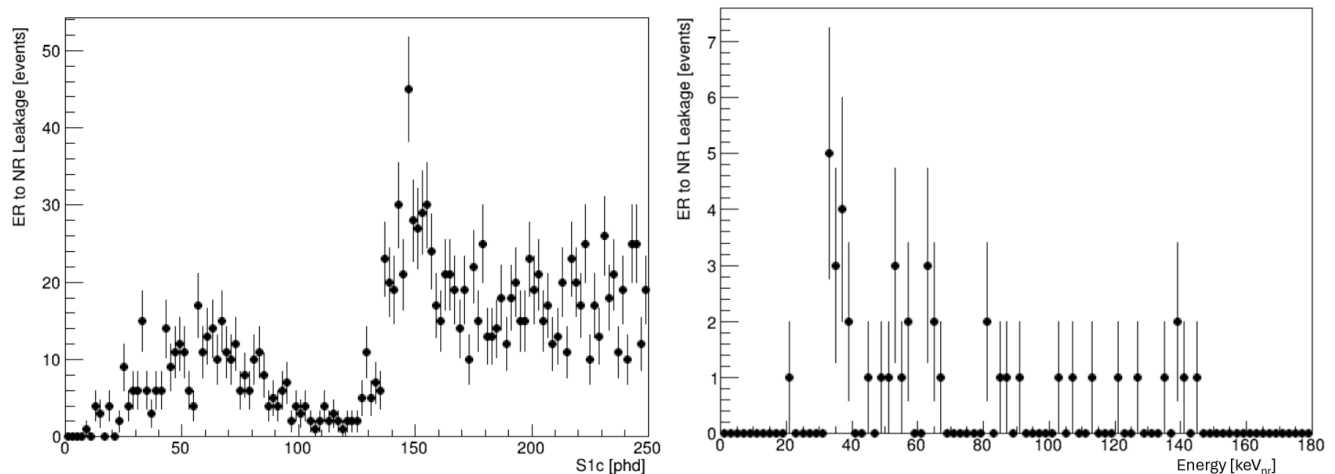


Figure 4.7: A comparison of the leakage of ER events into the NR band in $\log(S2c)$ vs. $S1c$ space (left) and $\Delta\chi^2$ vs. total fitted NR energy space (right) for WS2022. For values beyond the end of the NR band (in $S1c$ or energy), the NR band is extrapolated.

Validation of the NR band is relatively straightforward, since the DD calibration data (see section 2.8.4) provides a good source of MS neutrons. The verification of the NR band using the DD calibration data is shown in the top plot of Figure 4.8, and demonstrates that the distribution of simulated NR events in $\Delta\chi^2$ space is comparable to that seen in calibration data. In addition to this, the population of inelastic scatter events, seen at around 170 keV_{nr} in this figure, can also be used as a partial verification of the ER band, as previously discussed.

The NR validation is also repeated using a different source of neutrons, specifically AmLi, to assess the effect of different neutron sources on the NR band. In principle, NRs from any source, be it different neutron sources or WIMPs, should sit in the NR band, and so the band should not be source specific. However, statistical errors and backgrounds remaining in the datasets could lead to slightly different bands for different neutron sources. The bottom plot of Figure 4.8 shows the AmLi calibration data with the overlaid DD and Th-232 simulation bands. From this figure it can indeed be seen that the NR band represents the AmLi data well, and hence is verified for different neutron sources. Once again, this figure shows that the inelastic NR population of AmLi events lines up well with the ER band calculated from the Th-232 simulation. Any further verification of

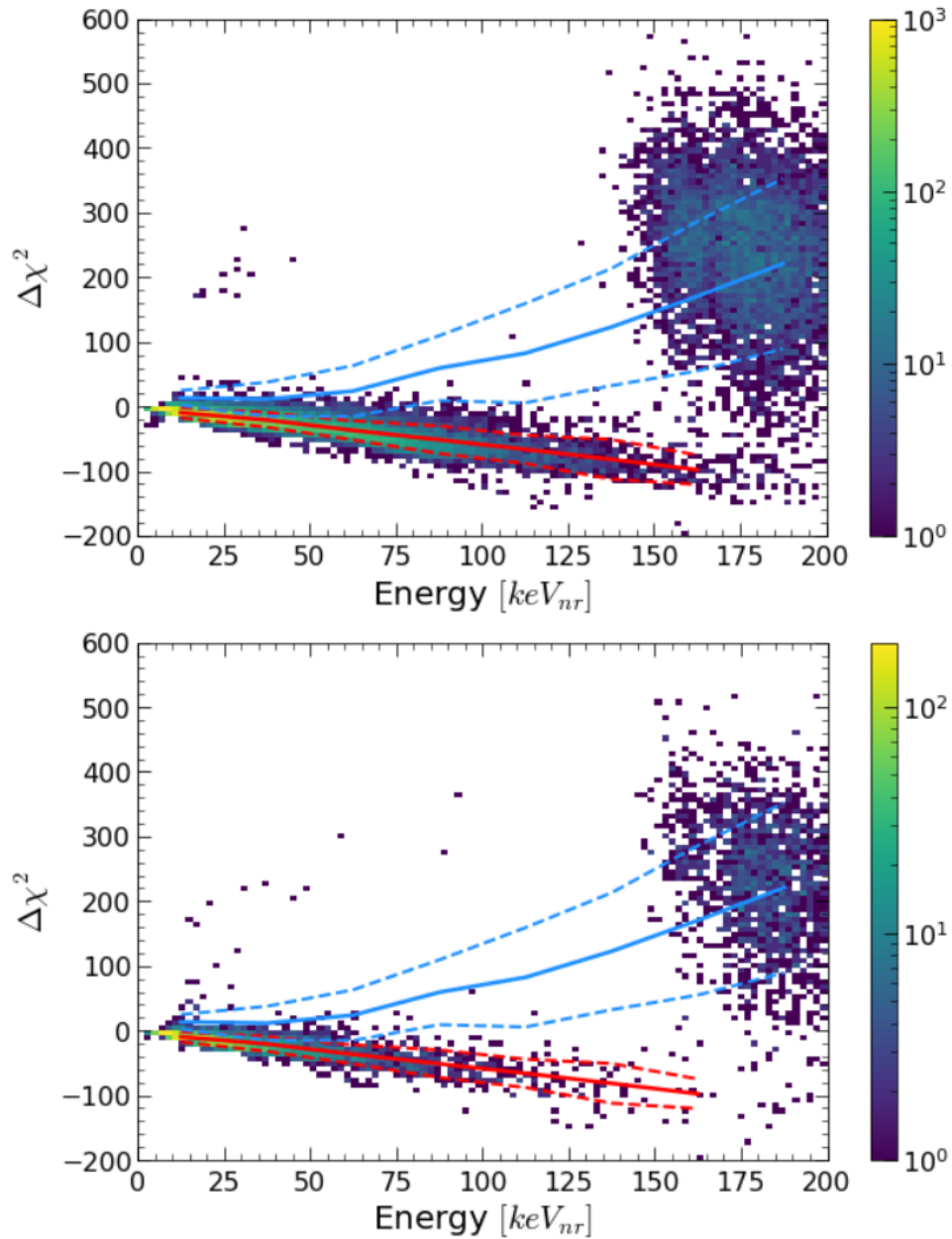


Figure 4.8: *WS2022 $\Delta\chi^2$ space NR band verification using DD (top) and AmLi (bottom) MS calibration data, with calibration data quality cuts applied. Shown here are the NR (red) and ER (blue) bands that were produced using the DD and Th-232 simulations respectively.*

the ER band is difficult, as it is hard to find a source of relatively low energy MS ER events with sufficiently high statistics.

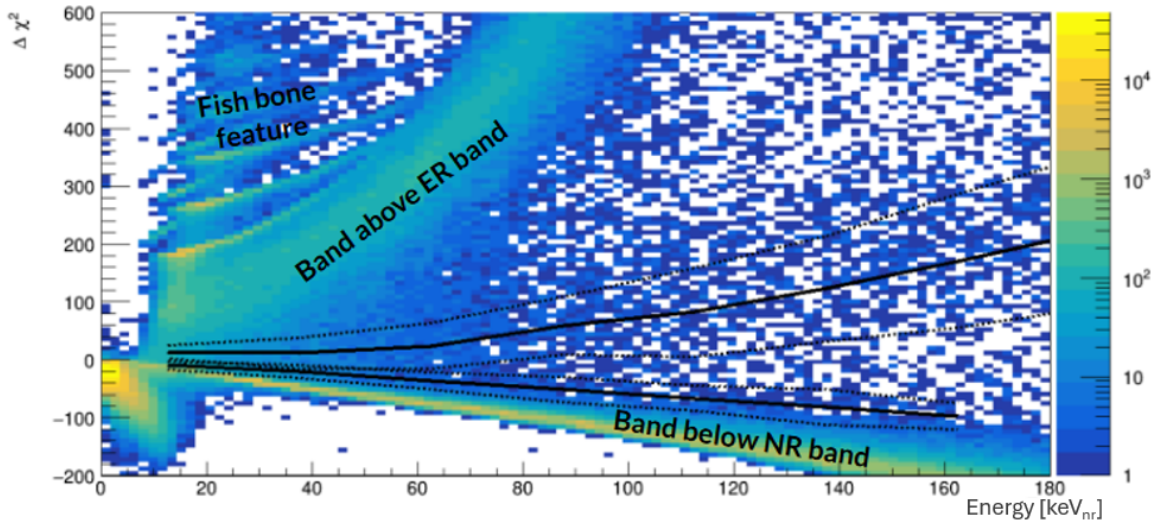


Figure 4.9: All WS2022 events in $\Delta\chi^2$ vs. total fitted nuclear recoil energy space. The NR (lower) and ER (upper) bands are both shown in black here for reference, with some other features of note annotated on the figure.

4.4 Exploring $\Delta\chi^2$ Space

In addition to the ER and NR bands seen in $\Delta\chi^2$ space, some additional features are also visible. In order to study the different structures that can be seen in this space in more detail, the analysis is run over the entire WS2022 MS dataset with no analysis cuts. The resultant distribution of events from this is shown in Figure 4.9. The notable features seen here are a band below the NR band, a band above the ER band, a low energy, low $\Delta\chi^2$ cluster of events, and a ‘fish bone’ type of structure at low energies, for $\Delta\chi^2$ values above ~ 180 . Each of these features is investigated individually, using a smaller sample of $\sim 23\,000$ events (selected using an ROI of $S1c < 500$ phd and $2.5 < \log(S2c/\text{phd}) < 5.0$), in which all structures except the ‘fish bones’ are visible. To study this final structure, a much larger dataset of approximately a third of all WS2022 runs is used. The smaller sample of events is shown in Figure 4.10, with the three features to be studied highlighted.

4.4.1 The Band Above the ER Band

A selection is made of events that sit in the band seen to lie above the ER band in Figure 4.10, corresponding to region ‘A’ in the figure. These events have been classified as ‘more ER-like’ than true ER events by the $\Delta\chi^2$ analysis, although it may be more accurate to describe the evaluation as ‘less NR-like’, since it is the worse of the ER and NR fits (hence a larger χ^2 value) that dominates the $\Delta\chi^2$ value. The selection of these events in $\Delta\chi^2$ space (top left) is shown in Figure 4.11, along with where they are found in the parameter space of $\log(S2c)$ vs. $S1c$ (top right), the xy position of all scatters (bottom left), and R^2 vs. drift time for all scatters (bottom right).

When the xy positions of all scatters of these events are plotted, a clear ring structure can be

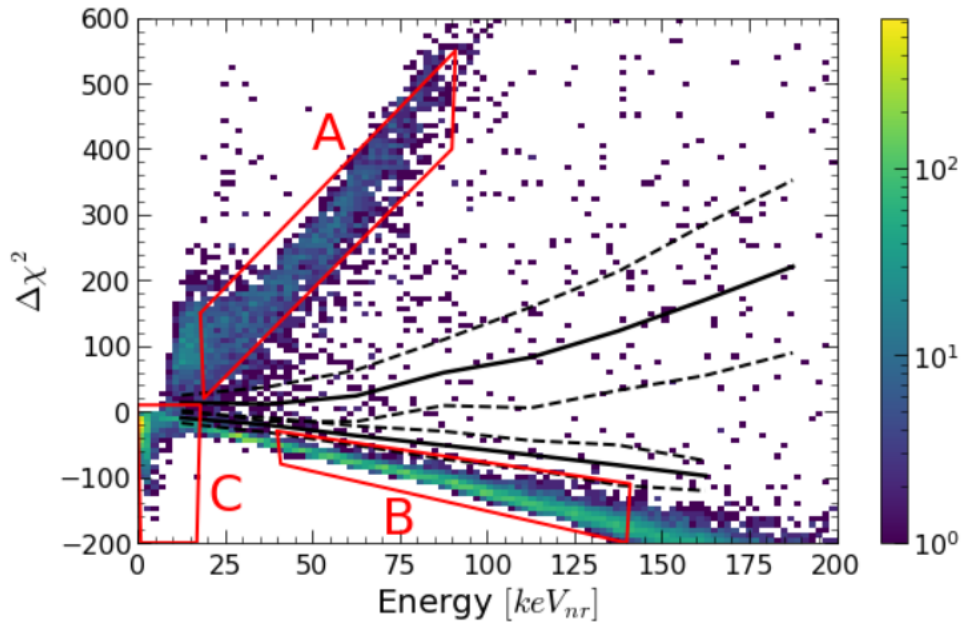


Figure 4.10: The sample of $\sim 23,000$ WS2022 events, with only an ROI cut applied ($S1c < 500$ phd and $2.5 < \log(S2c/phd) < 5.0$), used for further study of features in $\Delta\chi^2$ space. The three features highlighted are the band above the ER band (A), the band below the NR band (B), and the low energy cluster of events (C). The NR (lower) and ER (upper) bands are shown here in black for reference.

seen. The majority of the scatters that do not contribute to this ring formation are located outside of the TPC, and hence are most likely due to an error in reconstruction by Mercury. Mercury reconstruction typically fails in the areas around deactivated PMTs. This ring structure is thought to be due to the so-called ‘glue ring’ that secures the grid wires [125]. Specifically, in this case, the glue ring of the anode. This also explains why nearly all of these events are seen at approximately a drift time of $0 \mu\text{s}$, on the detector anode, in the plot of R^2 vs. drift time. In $\log(S2c)$ vs. $S1c$ space, these events also form a clear population above the ER band and at low energies. Due to their position at the very top of the detector, nearly all of these events should be removed by the FV cut.

4.4.2 The Band Below the NR Band

The next selection made on the sample of WS2022 data with no cuts is on the band structure seen below the NR band, corresponding to region ‘B’ in Figure 4.10. As for the previous selection, the events of interest are shown in the same four parameter spaces, displayed in Figure 4.12. This selection is made at higher energies to avoid contamination from the low energy collection of events in $\Delta\chi^2$ space.

As the distribution in the xy plane shows (bottom left plot of the figure), unlike for the structure above the ER band, here there is a relatively uniform distribution of events across different radii.

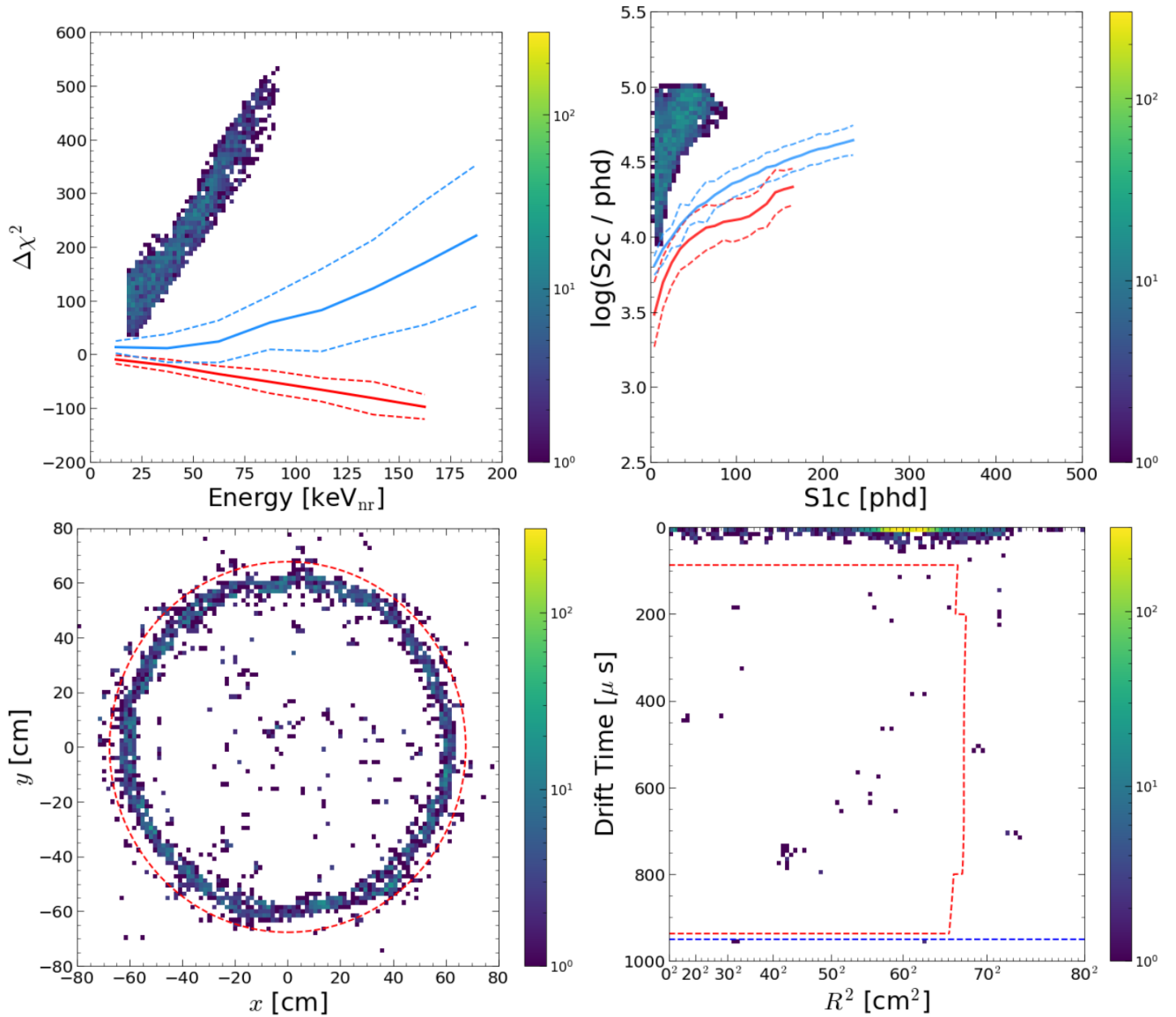


Figure 4.11: The band feature above the ER band in $\Delta\chi^2$ space, shown in a range of parameter spaces. Events in $\Delta\chi^2$ space, where the selection is made, are shown (top left) with the NR (red) and ER (blue) Gaussian 90-10 CL bands, generated using DD and Th-232 simulations respectively. Events in $\log(S2c)$ vs. $S1c$ space are shown (top right) alongside Gaussian 90-10 CL bands generated from the NR (red) and ER (blue) simulations. The xy distribution of all scatters of the events is shown (bottom left), where the red line indicates the maximum extent of the FV. The distribution of all scatters of the events in drift time vs. R^2 is shown (bottom right), where the red line indicates the FV boundary. The blue line indicates the UDT limit. The reason for the cluster of events at around $R^2 = 42^2$ cm², drift time = 750 μ s is currently unknown.

Again, there are some events that are outside of the TPC in this space, and they are again assumed to be events that have not had their xy position reconstructed correctly. Looking at the drift times

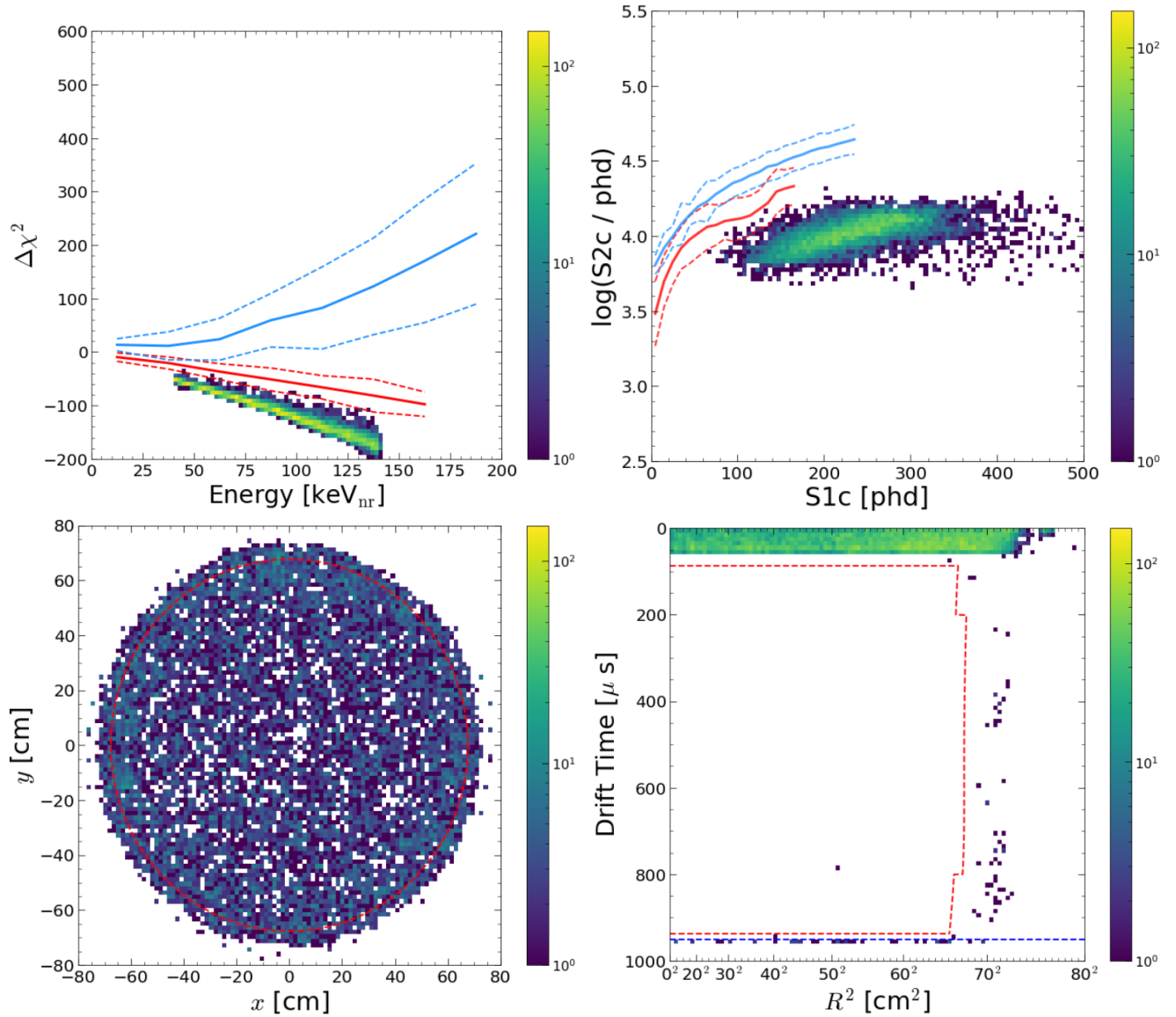


Figure 4.12: The band feature below the NR band in $\Delta\chi^2$ space, shown in a range of parameter spaces. Events in $\Delta\chi^2$ space, where the selection is made, are shown (top left) with the NR (red) and ER (blue) Gaussian 90-10 CL bands, generated using DD and Th-232 simulations respectively. Events in $\log(S2c)$ vs. $S1c$ space are shown (top right) alongside Gaussian 90-10 CL bands generated from the NR (red) and ER (blue) simulations. The xy distribution of all scatters of the events is shown (bottom left), where the red line indicates the maximum extent of the FV. The distribution of all scatters of the events in drift time vs. R^2 is shown (bottom right), where the red line indicates the FV boundary. The blue line indicates the UDT limit.

of the events in this selection (bottom right plot of the figure), they are nearly all located in the gas region at the top of the detector, above 60 μ s. In $\log(S2c)$ vs. $S1c$ space (top right plot of the figure), the selected events also appear in a region below the NR band. Since all of these events

are above the FV, they would also be expected to be removed by the FV cut.

4.4.3 Low Energy Cluster of Events

There is a cluster of events at low energy, tending to be slightly more NR-like, with $\Delta\chi^2$ values less than zero. As before, these events are selected, corresponding to region ‘C’ in Figure 4.10, and plotted across the same four parameter spaces as for previous selections. This is shown in Figure 4.13.

As in both of the previous selections, there is a population of events in this group that have incorrectly reconstructed xy positions, but here the proportion of these events is much larger. The remainder of the events have xy positions largely focused on a few hotspots in the detector (see the bottom left plot of the figure). These could be due to emission from the electrode grids which result in an increased number of lone S2s, and hence an increased number of accidental coincidences, in these regions. A significant number of these events have an unphysical drift time, and hence must be accidental coincidences (see section 2.11.2). These UDT scatters sit below the range shown in the bottom right plot of Figure 4.13. The deduction that these events are accidental coincidences is further supported by the fact that they sit in the region of $\log(\text{S2c})$ vs. S1c space (top right plot of the figure) in which accidental coincidences are typically found.

The events that have UDT scatters would be removed by a strict FV cut, and given that these events are thought to be accidental coincidences they would ideally be removed by MS accidental coincidence cuts. However, there is not currently a set of dedicated MS accidental coincidence cuts and so the approaches taken to removing these events are discussed in sections 4.2.5 and 6.2.9 for WS2022 and WS2024 respectively, and were also outlined in section 2.11.2.

4.4.4 ‘Fish Bone’ Structure

Unlike for the other selections, the $\sim 23\,000$ event sample is not sufficiently large as to make the ‘fish bone’ feature visible, so a selection on a larger dataset of approximately a third of all WS2022 runs is made. Here, four separate subgroup selections are made to distinguish the individual ‘fish bones’ of the structure. The selection and the distributions across $\Delta\chi^2$ space (top left) and $\log(\text{S2c})$ vs. S1c space (top right) are shown in Figure 4.14. For the xy (bottom left) and R^2 vs. drift time (bottom right) plots shown in this figure, the S2c-weighted average value is used for each event to avoid overcrowding of the plots.

The top left plot of the figure shows the four samples taken from the different ‘bones’ of the structure in $\Delta\chi^2$ space, and illustrates the colour-coding convention that will be used throughout the figure for the four subgroups of events. The top right plot of the figure shows these events in $\log(\text{S2c})$ vs. S1c space, and it can be seen that all selected events have a relatively low S1c value and a high S2c value. This is another region in which accidental coincidence events would be

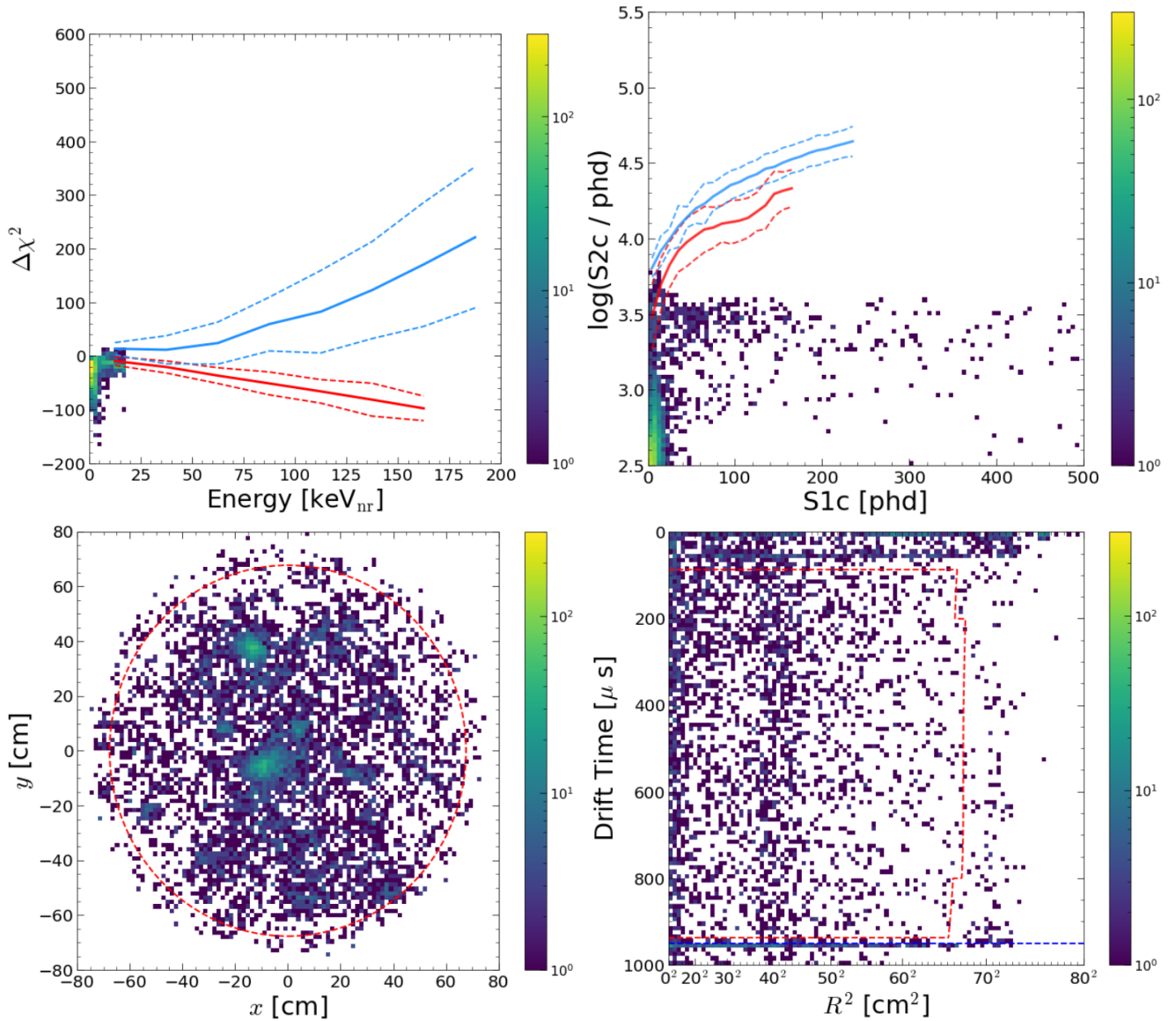


Figure 4.13: The low energy cluster of events in $\Delta\chi^2$ space, shown in a range of parameter spaces. Events in $\Delta\chi^2$ space, where the selection is made, are shown (top left) with the NR (red) and ER (blue) Gaussian 90-10 CL bands, generated using DD and Th-232 simulations respectively. Events in $\log(S2c)$ vs. $S1c$ space are shown (top right) alongside Gaussian 90-10 CL bands generated from the NR (red) and ER (blue) simulations. The xy distribution of all scatters of the events is shown (bottom left), where the red line indicates the maximum extent of the FV. The distribution of all scatters of the events in drift time vs. R^2 is shown (bottom right), where the red line indicates the FV boundary. The blue line indicates the UDT limit.

expected to be found, and therefore that is likely the source of these events. There is no discernable difference between the different subgroups in this parameter space.

Looking at the S2c-weighted average xy distribution of events in the bottom left plot of Figure

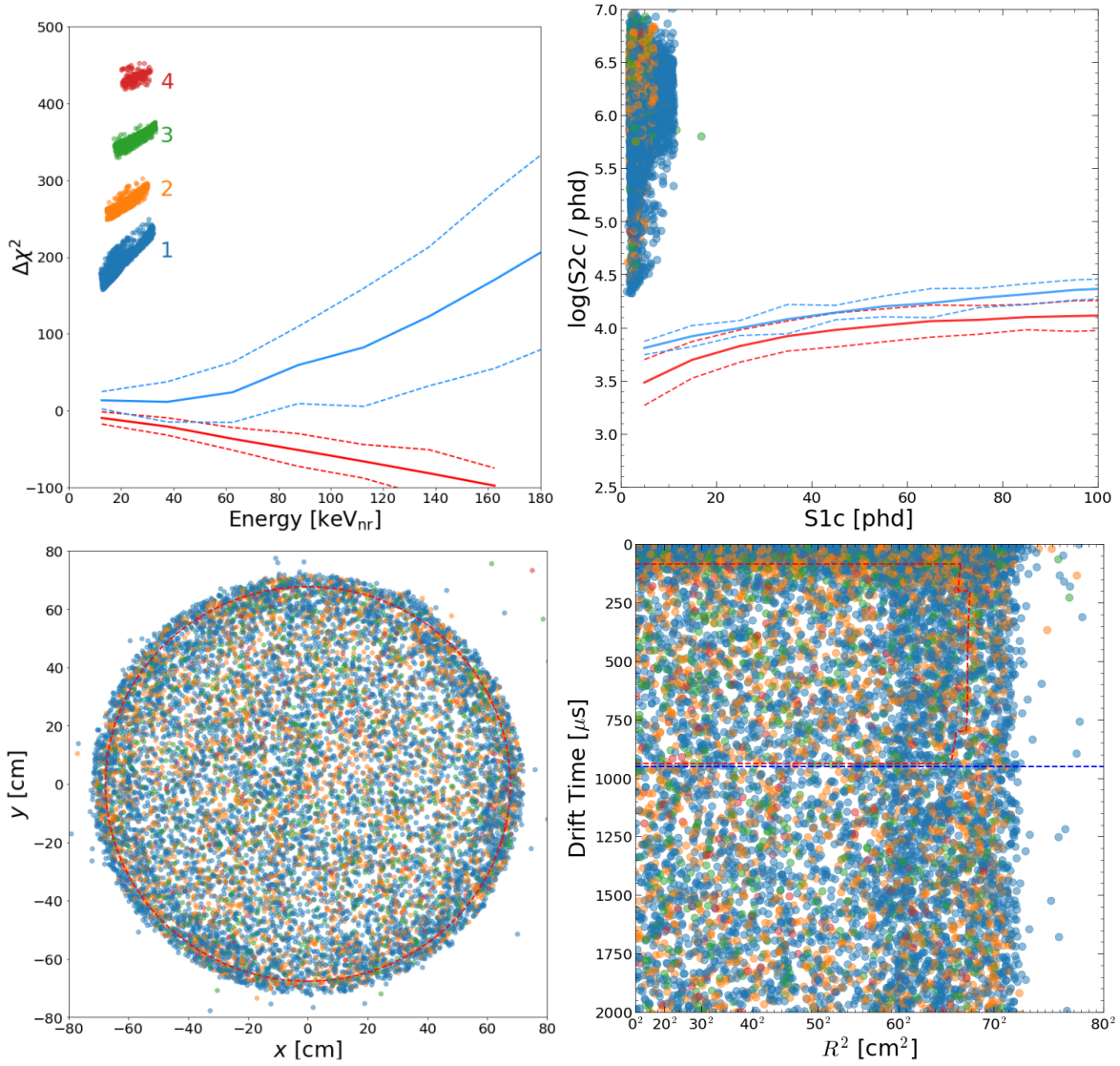


Figure 4.14: Samples of the ‘fish bone’ structure of events in $\Delta\chi^2$ space, shown in a range of parameter spaces. Events in $\Delta\chi^2$ space, where the selection is made, are shown (top left) with the NR (red) and ER (blue) Gaussian 90-10 CL bands, generated using DD and Th-232 simulations respectively. The selection is subdivided into four groups for each of the ‘bones’ of the structure, and these are numbered and colour-coded. Events in $\log(S2c)$ vs. $S1c$ space are shown (top right) alongside Gaussian 90-10 CL bands generated from the NR (red) and ER (blue) simulations. The colour-coding of events from the top left plot continues here. The average $S2c$ -weighted xy distribution of the events is shown (bottom left), where the red line indicates the maximum extent of the FV. The average $S2c$ -weighted distribution of the events in R^2 vs. drift time is shown (bottom right), where the blue line indicates the UDT limit, and the red line indicates the FV boundary.

4.14, the events appear to be concentrated towards the edge of the TPC (potentially related to wall

events), but there is no noticeable difference for the different subgroups. It should be noted that some events sit far outside of the TPC in this parameter space, indicating failed xy reconstruction.

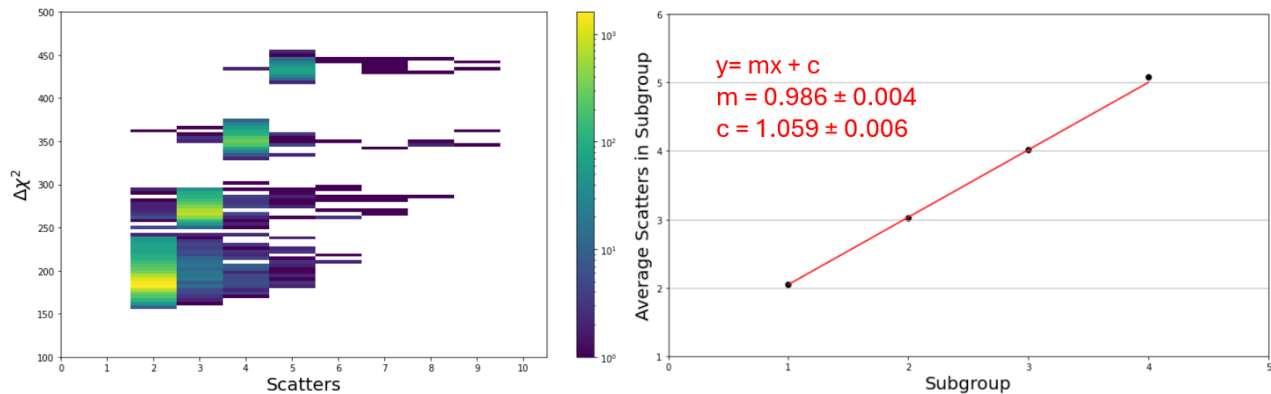


Figure 4.15: $\Delta\chi^2$ values of events in the ‘fish bone’ structure, as a function of the number of scatters in the event. Also shown is the average number of scatters in each subgroup of the selection. Error bars are the standard error on the mean for each subgroup, but are too small to be seen. This distribution is linearly fitted to $y = mx + c$, with $\chi^2 / \text{ndf} = 12.9 / 2$.

Interestingly, the bottom right plot of the figure shows that many events have an S2c-weighted average drift time that is greater than the UDT limit (note that this limit now appears towards the middle of this plot), with average drift times up to around $4100 \mu\text{s}$. This means that many of these events would be removed by any sort of FV cut, and they are all most probably accidental coincidence events that would be removed by accidental coincidence cuts. Once more, however, there is no indication of what distinguishes the different sub-structures that can be seen in $\Delta\chi^2$ space.

A hypothesis proposed to explain these sub-structures is that they could be related to the number of scatters in the event. To investigate this, the $\Delta\chi^2$ value is plotted for events in the ‘fish bone’ structure as a function of the number of scatters in the event, and the results of this are shown in the left plot of Figure 4.15. These results suggest that there is indeed a correlation between the number of scatters in an MS event in this structure and its location in $\Delta\chi^2$ space. To test this theory further, for each of the four selected subgroups the average number of scatters is calculated, and the results of this are shown in the right plot of Figure 4.15. This shows a clear linear increase in the average number of scatters in each of the subgroups for increasing values of $\Delta\chi^2$, with the average number of scatters increasing by approximately one for each subgroup higher in $\Delta\chi^2$.

Further investigation reveals that events that sit in the ‘fish bones’ have scatters that are fitted with approximately the same energy. These events have high values of S2c, and hence the initial energy estimates used in the fitting are very high. For WS2022, the $\Delta\chi^2$ analysis implements a limit on the fitted scatter energies according to the upper limit of the NEST distributions (shown

in Figure 2.14). This results in events with very high energy initial energy estimates immediately hitting this parameter limit in the fitting, and hence beginning the fitting with scatters of all the same energy (the upper energy limit). This results in the scatters maintaining very similar energies throughout the fitting process, and this is what forms the ‘fish bone’ structure. Very few of these events pass data quality cuts, particularly the ROI selection, and any that do are distinct in $\Delta\chi^2$ space from the NR and ER bands, so are not a concern for the work presented in this thesis.

4.5 Neutron Background Simulation SS/MS Ratio

The approach of using the rate of MS neutron events to estimate the rate of SS neutron events, described by Equation 3.2, is reliant upon knowing the expected SS/MS ratio of neutrons, which can only be obtained from simulation. Specifically, 644 separate simulations are used, comprising 4 different neutron producing processes, occurring in 28 different materials, found in 77 different detector components. Not all materials and processes occur in all components. The 4 processes included in the simulations are (α, n) due to the decay chains of Th-232, ‘late’ U-238, and ‘early’ U-238, as well as the spontaneous fission of U-238.

The $\Delta\chi^2$ analysis is run over all of the MS events in the simulations, after cuts, in order to evaluate the positions of all events in $\Delta\chi^2$ space, so that events in the NR band can be selected. The SS events have cuts applied, but do not require the $\Delta\chi^2$ analysis. For an SS event, unlike an MS event, there is not any additional information beyond S1c and S2c (used in the usual $\log(\text{S2c})$ vs. S1c space) that can be utilised to provide a better discrimination. An NR band selection is applied for the SS events in $\log(\text{S2c})$ vs. S1c space. All events have a cut applied to require energies greater than $12 \text{ keV}_{\text{nr}}$, to remove accidental coincidence events (less likely to be present in simulations but the cut is applied for consistency with cuts applied to data).

The energy distributions of MS and SS events are shown in Figure 4.16. The distributions are weighted for each simulation separately to account for the activity of the process, the size of the simulation, and the number of live days of run time in the final WS2022 dataset. Weighted distributions are shown for all three configurations of the veto requirement discussed in section 4.2.4 for the MS events, namely requiring no veto signal (red), requiring a veto signal (blue), and no veto requirement (green). The SS veto requirement is always that the event does not have a veto tag, as is required for a WIMP candidate. Note that the energy in the case of SS events is simply calculated using the NR version of the Doke formula, described in Equation 3.5, whereas for the MS events the energy is the sum of the fitted energies in the NR model, as previously.

Following this, the energy dependent SS/MS ratio is calculated for each of the three MS veto requirements, and the results of this are shown in Figure 4.17. The distributions shown in the figure are all relatively flat with energy, so the use of a constant value for each of the three ratios, especially over a more restricted energy range afforded by a less conservative ROI, would

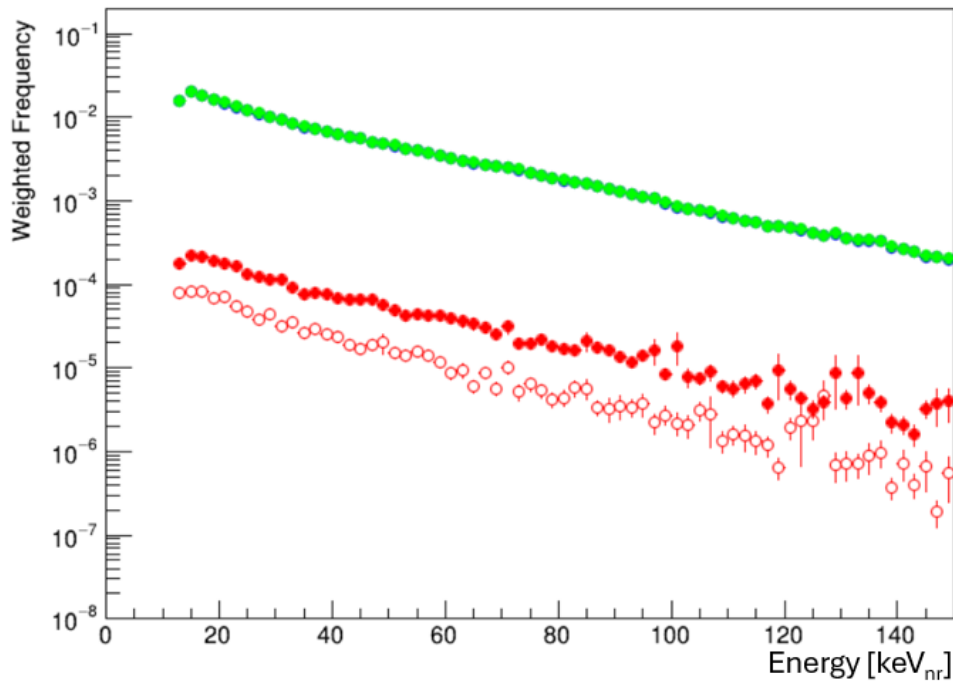


Figure 4.16: *Weighted energy distributions of SS and MS events in the WS2022 neutron background simulation. Simulation cuts are applied to this data, including a post-fitting accidental coincidence cut requiring energies greater than 12 keV_{nr} . The weighting is calculated as the product of the activity of the source simulated, the inverse of the number of events simulated for that source, and the number of WS2022 live days. Open circles indicate SS events and filled circles indicate MS events. The three different veto requirements included are requiring no veto signal (red), requiring a veto signal (blue), and veto agnostic (green). Note that blue data points are largely hidden behind the green points.*

be reasonable. In the figure a peak can be seen at around 120 keV_{nr} in all three distributions, and this is due to the peak seen at this value for SS events in Figure 4.16. The specific cause of this peak in the neutron background simulation SS energy spectrum is not currently known, however,

4.6 Correcting SS/MS Ratio Differences in Simulation and Data

Equation 3.2 inherently assumes that the SS/MS ratio is the same in simulation as it is in data, but that is not guaranteed to be the case. To investigate this assumption, simulation and calibration data can be studied, for particular neutron calibration sources, to compare the data and simulated SS/MS ratios in isolation from the WIMP search data and neutron background simulations. Let a variable, r_{cal} , be defined, such that it is the ratio of SS/MS ratios in data and simulation, as

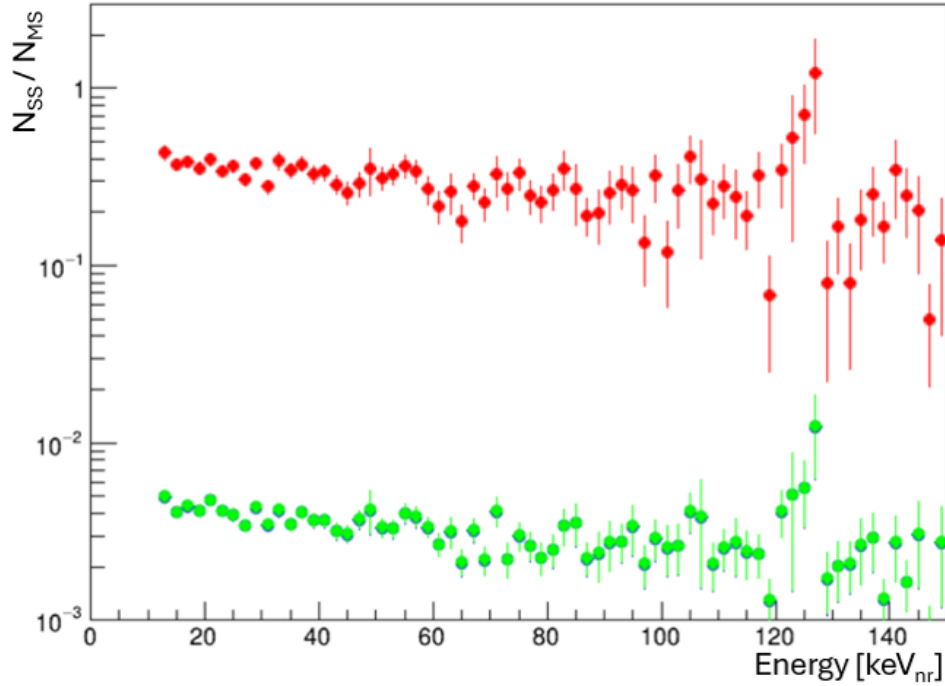


Figure 4.17: *SS/MS ratio as a function of energy, as calculated for the WS2022 neutron background simulation after cuts. The three different MS veto requirements included are requiring no veto signal (red), requiring a veto signal (blue), and veto agnostic (green). The SS veto requirement is the same in all cases and requires that there is no veto signal. Note that blue data points are largely hidden behind the green points.*

described by:

$$r_{cal} = \frac{\left(\frac{N_{SS}^{cal,data}}{N_{MS}^{cal,data}} \right)}{\left(\frac{N_{SS}^{cal,sim}}{N_{MS}^{cal,sim}} \right)}. \quad (4.1)$$

The subscript ‘cal’ here refers to an individual neutron calibration source. Those considered for this study were AmLi, AmBe, and DD. For r_{cal} to be accurate, it is required that the calibration source chosen is able to provide clean neutron data, with minimal contamination from other backgrounds. When the data for these sources is studied with calibration data quality cuts applied (a subset of the WS2022 cuts that were selected for calibration data), it is seen that the data for the DD source contains significantly fewer background signals than the data for either AmLi or AmBe, so it was decided that the DD source would be used for this study, hence $r_{cal} = r_{DD}$. The SS and MS datasets for the DD calibration data and DD simulation are compared in Figure 4.18.

To correct for any difference in the SS/MS ratio between the data and the simulation, Equation 3.2 is adapted to allow r_{DD} to be used as a correction factor. This is expressed in:

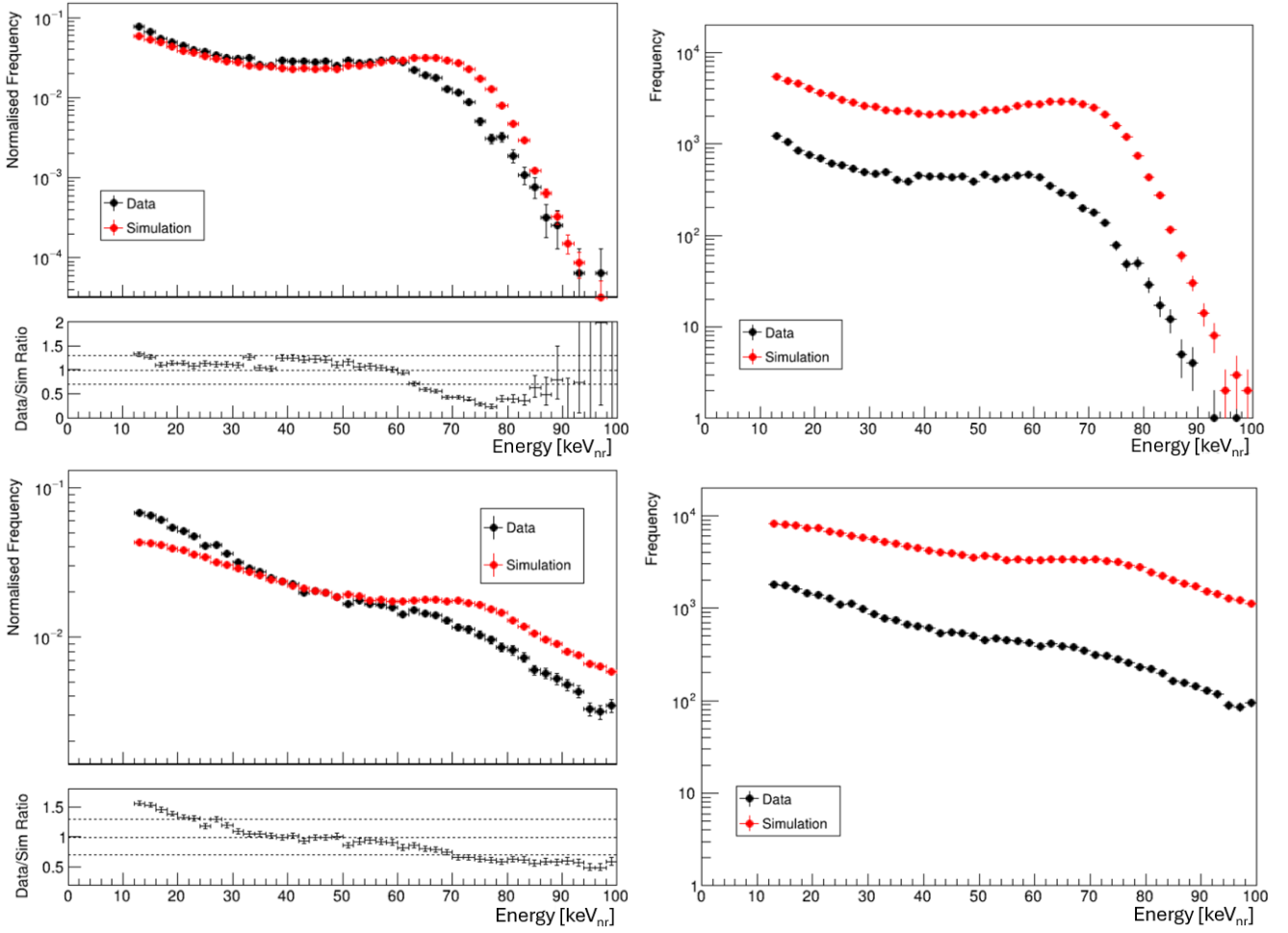


Figure 4.18: Energy distributions of WS2022 DD SS and MS events for data and simulation after analysis cuts. Comparisons between data and simulation are shown for SS events (top) and MS events (bottom), both with normalisation (left) and without (right). Where normalisation is applied, this enforces that the distributions integrate to unity. In these normalised plots, the ratio of the distributions is also shown, with dashed lines at 1.25, 1.00, and 0.75 as a guide to the eye. Across all subplots, data is shown in black and simulation is in red.

$$N_{SS}^{data} = \sum_j^{N_{MS}^{sim}} \left(\frac{N_{SS}^{sim}(E_{nr})}{N_{MS}^{sim}(E_{nr})} \right)_j r_{DD}(E_{nr}), \quad (4.2)$$

where r_{DD} is also represented as having an energy dependence. The ratio of SS/MS, for both DD simulation and DD calibration data, is shown in Figure 4.19, along with the ratio of these two distributions, r_{DD} . SS events from a 2.45 MeV DD source are expected to have an end point at 74 keV_{nr} due to the maximum energy that they could deposit in a single scatter. However, the SS distributions for both the data and the simulation here are seen to extend beyond this energy. This is most likely due to the energy resolution of the detector. r_{DD} is seen to vary with energy,

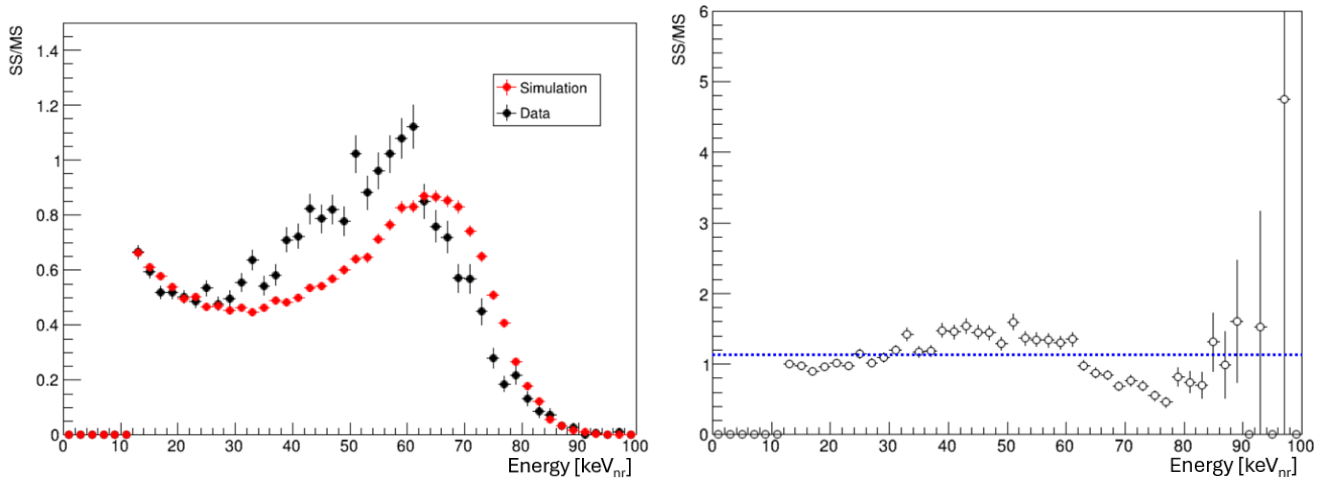


Figure 4.19: *WS2022 energy distributions of the SS/MS ratio for DD data and simulation (left) and r_{DD} (right), after analysis cuts. The SS/MS ratio plot follows the convention of Figure 4.18 where simulation is shown in red and calibration data is shown in black. On the r_{DD} plot, the average value across the bins is shown by the blue dashed line, and is 1.13 ± 0.01 .*

but it was deemed appropriate to remove the energy dependence of the correction factor and to take it as a constant value. For WS2022 this is found to be 1.13 ± 0.01 . The distributions shown in the left plot of Figure 4.19 have clearly different shapes, which leads to this energy variation of r_{DD} . These different shapes are potentially due to the use of an outdated version of GEANT4 for producing the simulations. The corresponding plot for WS2024 (Figure 6.10) shows a much better agreement between the shapes of the data and simulation distributions, suggesting that the simulation is more accurate in that case. By taking r_{DD} as constant for WS2022, the difference in shape between the data and simulation distributions does not impact the result, but this does introduce another potential source of systematic error.

4.7 Multiple Scatter Neutron Candidates in Data

The final element required for this analysis is the selection of MS neutron candidates from the WS2022 data. After the application of all of the aforementioned analysis cuts, including the strict FV cut, there are no MS events remaining, regardless of the veto signal requirement imposed. As was discussed in section 4.2.1, it was this dataset that prompted the realisation of the necessity of the strict FV cut. All MS events from the WS2022 dataset that pass the data quality cuts (with the exception of the accidental coincidence cut requiring an energy greater than 12 keV_{nr}) with a weighted FV are shown in Figure 4.20, across multiple parameter spaces. This dataset illustrates further why the strict FV cut is required. Not only can the suspected Bi-Po events, investigated in section 4.2.1, be seen as both NR band events (red) and non-NR band events (black) in the

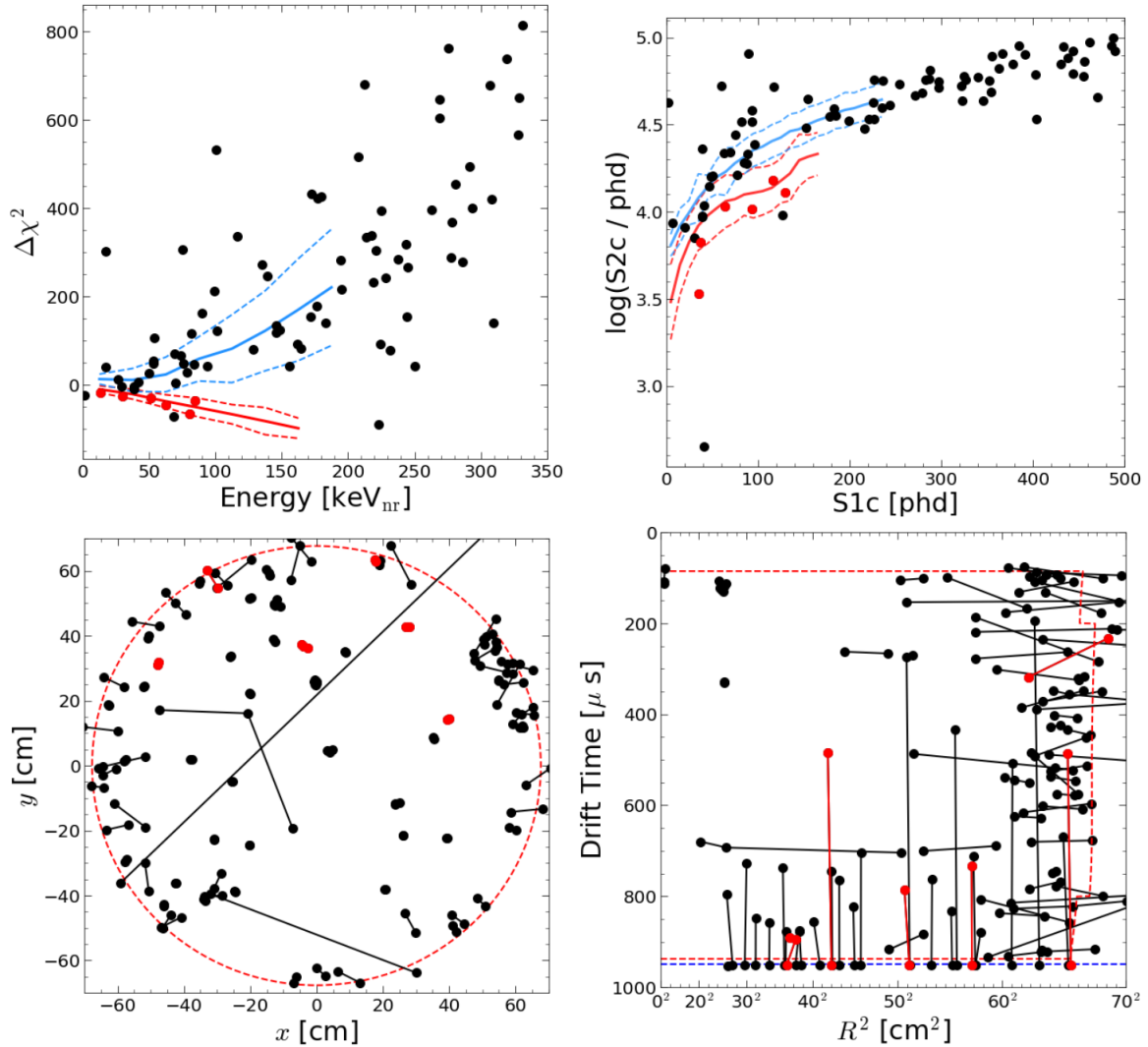


Figure 4.20: *WS2022 MS events passing all data quality cuts with a weighted FV, with events in the $\Delta\chi^2$ NR band highlighted (shown in red). Events in $\Delta\chi^2$ space are shown (top left) alongside the NR (red) and ER (blue) Gaussian 90-10 CL bands in this space, generated using DD and Th-232 simulations respectively. The distribution in $\log(S2c)$ vs. $S1c$ space is likewise shown (top right) alongside Gaussian 90-10 CL bands generated from the NR (red) and ER (blue) simulations. The xy distribution of all scatters of the events is shown (bottom left), where the red dashed line indicates the maximum radius of the FV. Connecting lines between the scatters of a given event are arbitrary. The distribution of all scatters of the events in drift time vs. R^2 is shown (bottom right), where the red line indicates the boundary of the FV. The blue line indicates the UDT limit at the cathode. Connecting lines between the scatters of a given event are again arbitrary.*

bottom right plot of this figure (distinguishable by their vertical scatter topology, with a scatter on the cathode), but further events that should be removed also appear. For example, the bottom left

plot of Figure 4.20 shows the xy distribution of the MS events passing the analysis cuts, and one event in particular can be seen to have its scatters on opposite sides of the detector. Furthermore, the rightmost scatter, that extends beyond the limits of this plot, is reconstructed as having an x and y position of ~ 1000 cm, which is clearly unphysical. In addition to this event, which is an extreme example, it can be seen in both of the bottom two plots of the figure that the use of the weighted FV, rather than the strict FV, increases the number of events around the boundary of the FV. This makes sense due to the self-shielding nature of xenon, which is what motivates the use of an FV, but by using the strict FV it helps to limit this background of primarily gamma events as much as possible.

Figure 4.20 also crucially shows (in red) the 6 events that sit in the NR band in $\Delta\chi^2$ space. It is these events that would be the MS neutron candidates used in the final estimate were it not for the fact that all 6 fail the strict FV cut that is clearly necessary for this data, hence the final result of 0 MS NR events. 5 of the 6 events appear to be Bi-Po events, with the tell-tale vertical topology with a scatter on the cathode. The final event looks to be a good neutron candidate, but with one of its two scatters just beyond the limit of the FV (as can be seen in the lower right plot of Figure 4.20 at around $R^2 \approx 65^2$ cm² and ~ 200 μ s). It is events such as this that prompted the use of a wider strict FV for some of the studies in WS2024 (see chapter 5).

This result of 0 events is likely, at least in part, due to the way in which the accidental coincidence cuts are applied to the MS data, since the cuts are just adapted to work for MS events, but retain their initial tuning, which was for SS events. Because of this, it is probable that the MS versions of the accidental coincidence cuts are overly harsh.

Given that the MS analysis mentioned in section 4.1 found 10 MS neutron events in this dataset, it would be informative to know where these events sit in $\Delta\chi^2$ space. The selection of these events was completely independent from their position in this space, and depended only on an OD veto signal and manual selection of neutron-like events based on the event waveforms. As can be seen in Figure 4.21, 7 out of 10 of these events are found to be within the NR band, which further validates the $\Delta\chi^2$ analysis method. For the events that do not sit in the NR band, the reasons why this is the case will now be addressed.

One of the 10 events is mis-classified by LZAP as an SS event, so does not pass the MS selection cut for the $\Delta\chi^2$ analysis work. One event is found to be just below the boundary of the NR band in $\Delta\chi^2$ space, and is also below the MS NR band in $\log(S2c)$ vs. $S1c$ space. With a looser band selection, this event could be caught. The third event that is not in the NR band sits in the ER band in $\Delta\chi^2$ space. This event is thought to be an inelastic neutron event, causing the signal to appear more ER-like. Studies are ongoing into the inelastic NR populations, and these could lead to the development of defined inelastic regions in $\Delta\chi^2$ space that would allow inelastic NR events to be more easily identified. The main barrier to this currently is the disagreement between simulation and data for these events, due to the way in which inelastic scatters are treated by the

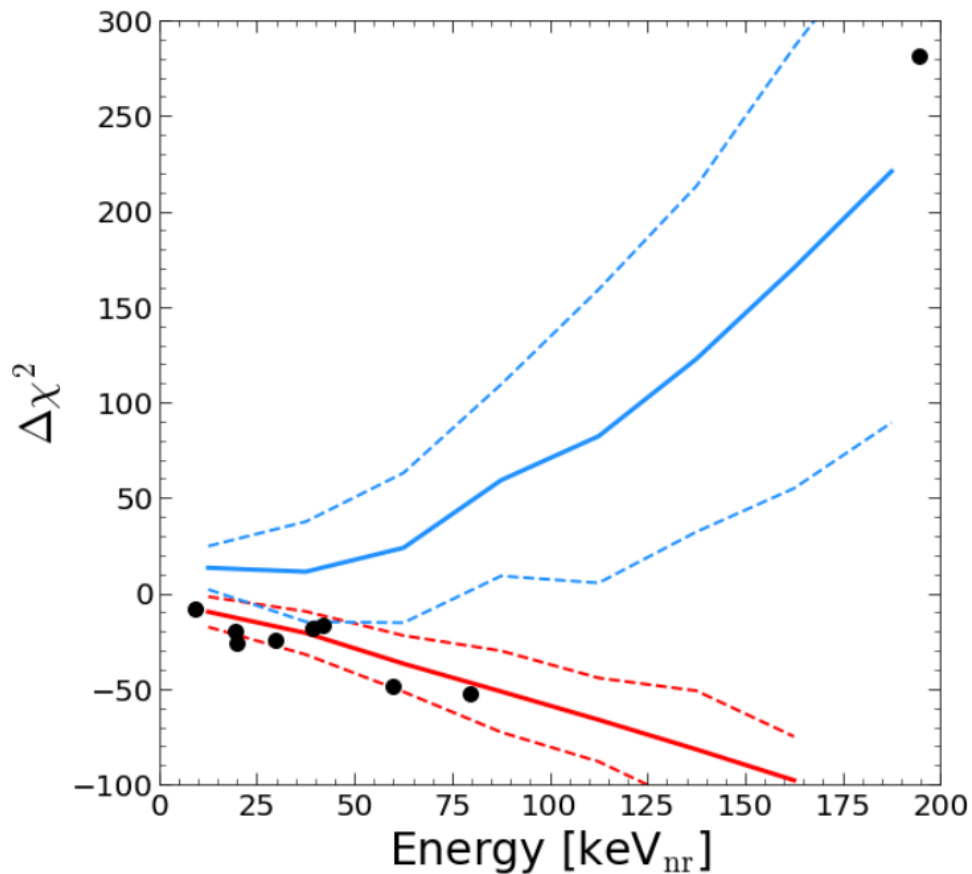


Figure 4.21: *The MS neutron candidates (1 is identified as SS by LZAP and so is not shown here) identified by the independent, OD-based LZ WS2022 neutron study, shown in $\Delta\chi^2$ space. Also shown are the NR (red) and ER (blue) Gaussian 90-10 CL bands in this space, generated using DD and Th-232 simulations respectively.*

GEANT4 simulations.

The next question that follows is why the remaining NR band events are not found in the $\Delta\chi^2$ SS neutron estimate work, and again the answers for these events will be systematically looked at. The reasons are presented graphically in Figure 4.22, where it is shown whether each of the 9 MS-classified events passes or fails various analysis cuts. Only cuts that at least one event fails are shown in this figure, with the exception of the weighted FV cut, which is included for reference to compare with the strict FV cut. 3 events are removed because they have a scatter outside of the FV, and hence fail the strict FV cut, but would be kept if the weighted FV cut was used (before further cuts are applied). 2 events fail the narrow S2 cut, 2 events fail the S1 shape cut, 3 events fail the S2 early peak cut, 2 events fail the sustained rate cut, and finally 1 event fails the e-train veto. As can be seen from Figure 4.22, only 2 of the 9 events pass all analysis cuts, and these are the events that sit in the ER band (7569 109866) and just below the NR band (7894 83432), and hence are not selected as NR events. This is further evidence that the accidental coincidence cuts used for MS events in the $\Delta\chi^2$ study are likely overly harsh in the number of events that they

cut. For this reason, in the absence of dedicated MS accidental coincidence cuts, it was decided for WS2024 that no accidental coincidence cuts would be applied to MS data, and instead suitable neutron candidates would be selected by manual verification of event waveforms.

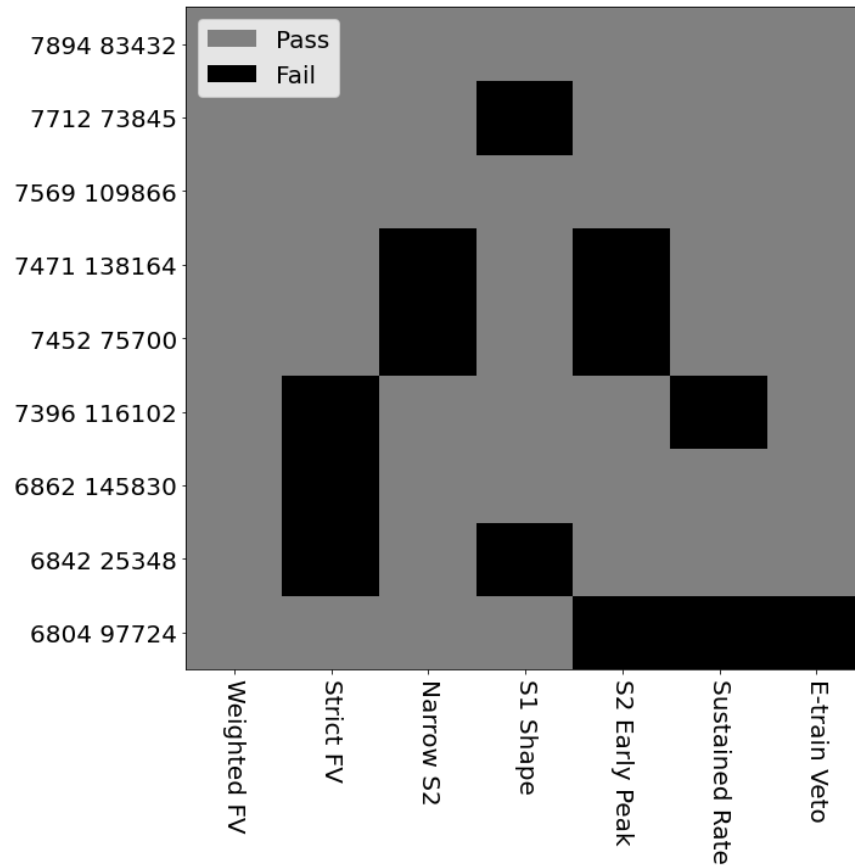


Figure 4.22: Visualisation of the cuts failed by the MS neutron candidates identified by the independent, OD-based LZ WS2022 neutron study. Only cuts failed by an event are shown, along with the weighted FV. 7569 109866 is the event in the ER band and 7894 83432 is the event just below the NR band.

4.8 WS2022 $\Delta\chi^2$ SS Neutron Estimate

The final results, combining the contributions of sections 4.5-4.7 using Equation 4.2, are shown in Table 4.2. This gives the estimate for the number of SS neutrons in the WIMP search dataset that pass all analysis cuts, and have no corresponding veto signal, which would make them indistinguishable from WIMP signals.

These results are presented for three different veto signal requirements on the MS data and simulations used in this study, as has been the case throughout this chapter. Ideally, the requirement of no veto signal would be applied to MS events (since this is what is being applied to SS events, so any systematic errors due to cuts should cancel), but because of the high neutron tagging

efficiency of the veto detectors, this requirement leads to relatively small MS datasets. To tackle this issue, the requirement is inverted to instead require a veto signal for the second version of the result, and for the third version all veto requirements are removed to maximise the size of the dataset. Since the vast majority of neutron events will have a veto signal, the results for the veto signal and veto agnostic requirements are very similar, as has been seen throughout this chapter, and is shown in the final results in Table 4.2. Quoted in this table are the 90% CL upper limits on the estimates. Due to the lower statistics of the result with the requirement of no veto signal, it can be seen in this table that the statistical error on the result is notably larger.

Because no MS neutrons are found to pass all analysis cuts, all three versions of the WS2022 SS estimate are limits rather than estimates. With the higher statistics afforded by the ‘veto signal’ and ‘veto agnostic’ conditions, a better constraint is able to be placed on the result. These results are consistent with the LZ WS2022 SS neutron background estimate, stated in Ref [150], of $0^{+0.2}$ neutrons.

	No Veto Signal	Veto Signal	Veto Agnostic
SS Neutron Estimate	$0^{+0.9}$	$0^{+0.01}$	$0^{+0.01}$

Table 4.2: Results of the $\Delta\chi^2$ SS neutron estimate for WS2022. Errors are the 90% CL upper limits on the estimates.

4.9 Choice of Neutron Interaction Cross-Section Library

There is an additional systematic error on the distributions shown in section 4.5 that should be considered. At the stage of the BACCARAT simulation of the energy deposition that is required as an input for LZLAMA, the choice of neutron interaction cross-section library can be specified. If it is not specified, the default is the G4NDL-4.5 library. Different libraries have slightly different values for nuclear data of various elements, and the neutron interaction cross-section is one of these properties.

In order to quantify the magnitude of the systematic error introduced by this choice, a different cross-section library, JEFF-3.3, is selected to compare to the default G4NDL-4.5. Due to the heavy computing burden, it is not practical to reproduce the entire neutron background simulation with the new library, so it was decided that this study would only investigate the effects of a different library on the process-material-component simulation that is the largest contributor of SS neutrons to the analysis after FV, ROI, and veto cuts, and after weighting. Figure 4.23 shows the 20 largest contributors of neutrons after these requirements were imposed, of which Th-232 (α, n) interactions with the ceramic in the forward field resistors is seen to be the largest contributor.

In order to compare the two different versions of the simulation, the full analysis as outlined in sections 4.6 - 4.8 is run, with the SS/MS ratio obtained exclusively from the two different library

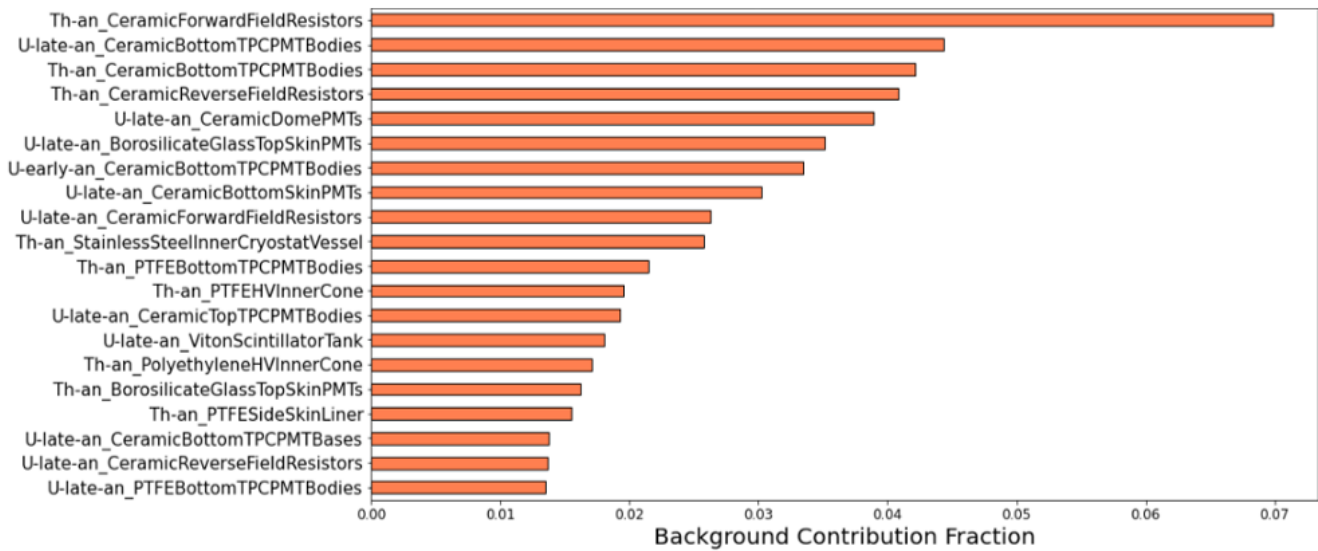


Figure 4.23: The 20 process-material-component simulations that contribute the most to the WS2022 SS neutron background, after weighting and cuts are applied.

versions of the same simulation, so that the final result in the two cases can be compared. The results of this are presented in Table 4.3. It can therefore be concluded that the systematic error present due to the choice of a different neutron interaction cross-section library is approximately ten times smaller than the statistical error on the result, when the JEFF-3.3 and default G4NDL-4.5 libraries are compared. Therefore the systematic error here can be considered to be negligible.

	No Veto Signal	Veto Signal	Veto Agnostic
G4NDL-4.5	$0^{+0.637}$	$0^{+0.0090}$	$0^{+0.0089}$
JEFF-3.3	$0^{+0.714}$	$0^{+0.0100}$	$0^{+0.0099}$
Fractional Error ((JEFF-G4NDL)/G4NDL)	0.121	0.111	0.112
WS2022 Result (Syst. Error)	$0^{+0.1}$	$0^{+0.001}$	$0^{+0.001}$
WS2022 Result (Stat. Error)	$0^{+0.9}$	$0^{+0.01}$	$0^{+0.01}$

Table 4.3: Results of the WS2022 neutron simulation cross-section library study, and final $\Delta\chi^2$ SS neutron estimates for WS2022, including both systematic and statistical errors. Errors are the 90% CL upper limits on the estimates.

Chapter 5

LZ WIMP Search 2024 Single Scatter Neutron Estimate

Between the 27th March 2023 and the 1st April 2024, LZ accrued 220.0 live days of WIMP search data during a campaign referred to as WS2024. This was combined with the data already taken during the WS2022 campaign and produced a world-leading limit on the possible masses and cross-sections of a WIMP dark matter candidate [126], shown in Figure 5.1. This gave a total of 280 live days of data that were used to produce this result. The WS2024 total live time consisted of 40.9 days in the high-mixing state, due to recently injected calibration sources, and 179.1 days in the low-mixing state. Bias mitigation was carried out for WS2024 by the method of ‘salting’ the data, which entails introducing an unknown number of artificial WIMP-like events into the dataset that are removed at the end of the analysis campaign. These salt events were generated using a combination of individual S1 and S2 pulses from tritium and AmLi calibration datasets that had been sequestered [126].

As for WS2022, for WS2024 it was necessary to quantify the expected number of SS neutrons in the WIMP search dataset, and this was primarily done for LZ by using the neutron tagging capability of the OD and Skin. This estimate was verified by a TPC-only MS-based SS neutron estimate that utilised the $\Delta\chi^2$ method for the selection of MS data events. The details of this estimate are presented in this chapter. In addition to this LZ WS2024 SS neutron estimate, a secondary estimate was produced by the author of this thesis, for which the $\Delta\chi^2$ analysis is used in every step, as is the case for the WS2022 estimate discussed in chapter 4. To distinguish between the two WS2024 estimates, this will henceforth be referred to as the $\Delta\chi^2$ WS2024 SS neutron estimate, and will be discussed in detail in chapter 6.

The general principle of using Equation 3.1 to construct an SS neutron estimate, that was used to produce the WS2022 neutron estimate results, is the same for the LZ and $\Delta\chi^2$ WS2024 SS neutron estimates. There are a few differences between the two WS2024 analyses, and these differences will be highlighted in section 5.1. It should be noted here that the SS/MS ratio work

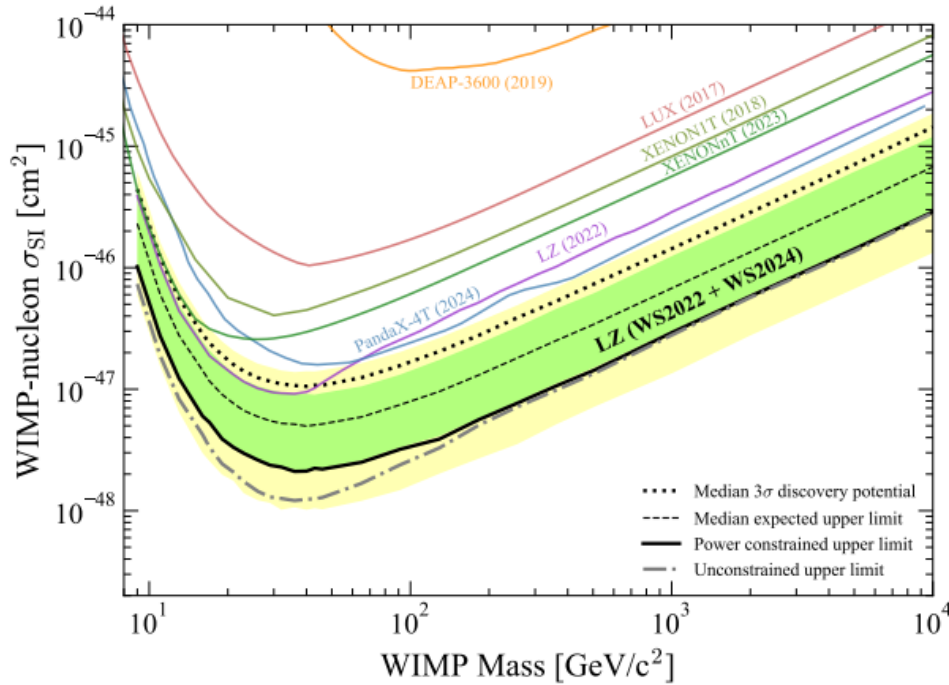


Figure 5.1: The LZ WS2024 and WS2022 combined spin independent WIMP-nucleon cross-section 90% CL upper limit as a function of WIMP mass, shown as the solid black line (-1σ power constraint applied). The limit without this power constraint is shown by the grey dot-dashed line. The green and yellow bands represent the 1σ and 2σ sensitivity bands respectively. The black dashed line shows the median expectation, and was calculated using post-fit background estimates. The dotted black line shows the median 3σ observation potential from the post-fit model. For context, the previous LZ limit from WS2022 [114] is shown, along with limits from PandaX-4T [103], LUX [95] (all power constrained to -1σ), XENONnT [104] (reinterpreted with a power constraint of -1σ), XENON1T [102], and DEAP-3600 [168]. This figure is taken from Ref [126].

mentioned in this chapter was carried out by A. Usón, and the remainder of the work for the LZ WS2024 SS neutron estimate was carried out by the author of this thesis in conjunction with E. Fraser.

5.1 Differences Between the LZ and $\Delta\chi^2$ Single Scatter Neutron Estimates

Firstly, it was decided for the LZ WS2024 SS neutron estimate that the FV should be increased, since many neutrons are expected to interact closer to the walls of the detector and not reach the FV due to the self-shielding properties of the liquid xenon in the TPC. With this in mind, two separate estimates are made with different FV definitions. The first expands the FV to be 2 cm in

from the ideal wall of the TPC, and the second expands the FV all the way up to the ideal wall (0 cm from the ideal wall). In both of these cases, the strict FV requirement is maintained, so that all scatters are physical and within the FV. In the latter of these two requirements, the amount of backgrounds seen in WIMP search data becomes very high, and the $\Delta\chi^2$ parameter space (along with all other studied parameter spaces) become a lot more noisy. This is illustrated by Figure 5.2, which shows $\Delta\chi^2$ space for the strict FV (top left), the strict FV 2 cm from the ideal wall (top right), and the strict FV 0 cm from the ideal wall (bottom)¹. The FV selections in this work also increase the upper drift time limit of the FV from 1034 μs in the high-mixing state (1030 μs in the low-mixing state) to 1046.5 μs in the high-mixing state (1042.4 μs in the low-mixing state), compared to the main WIMP search.

In all three plots of Figure 5.2, a population of events, that are most likely accidental coincidences, can be seen to form a steep band above the ER band. These events are likely equivalent to the events seen in WS2022, discussed in section 4.4, that corresponded to low-S1c, (relatively) high-S2c accidental coincidence events in the ROI. As the FV is expanded, it can also be seen from the figure that a second steep structure of events can be seen below the NR band. Investigation of this population shows that many of these events are spatially correlated with the resistors at the nine o'clock position in the detector that are known to cause higher rates of events, hence the usual implementation of a cut for these regions. This cut is described in section 6.2.2, but is not applied to this dataset in order to boost statistics. In a $\Delta\chi^2$ MS analysis however, this type of event can be easily distinguished from NR events at all but the lowest of energies.

A final piece of information that can be extracted from these plots is the reassuring position of the ER events that appear in higher numbers as the FV is expanded towards the wall. The appearance of these events is due to the fact that the liquid xenon is very effective at self-shielding against gamma rays, and hence the majority of these photons will interact at the edges of the detector. The position of these events in $\Delta\chi^2$ space can be seen to track the ER band that was produced using Na-22 simulated data, and this helps to verify the ER band. The production of the NR and ER MS bands shown in Figure 5.2 followed exactly as in section 6.3, except that the bands shown in that section are slightly more up-to-date than those which were used for this estimate due to this analysis being carried out first.

Because of the noisy parameter space that is seen for the FV that extends to 0 cm from the ideal wall, an additional requirement is enforced that events in this selection must have an OD delayed veto tag (pulse area > 32 phd, 300 ns < time from S1 pulse < 600 μs). Aside from this, the LZ WS2024 SS neutron estimate is veto agnostic, although any veto signals for candidate events are noted.

Additionally, a pre-fitting ROI that is notably larger than the usual WS2024 SS ROI is used

¹Note that the $\Delta\chi^2$ method now has the S1 S2 anti-correlations implemented, and so $\Delta\chi^2$ generally has much smaller, more meaningful values. This is discussed further in section 6.1.

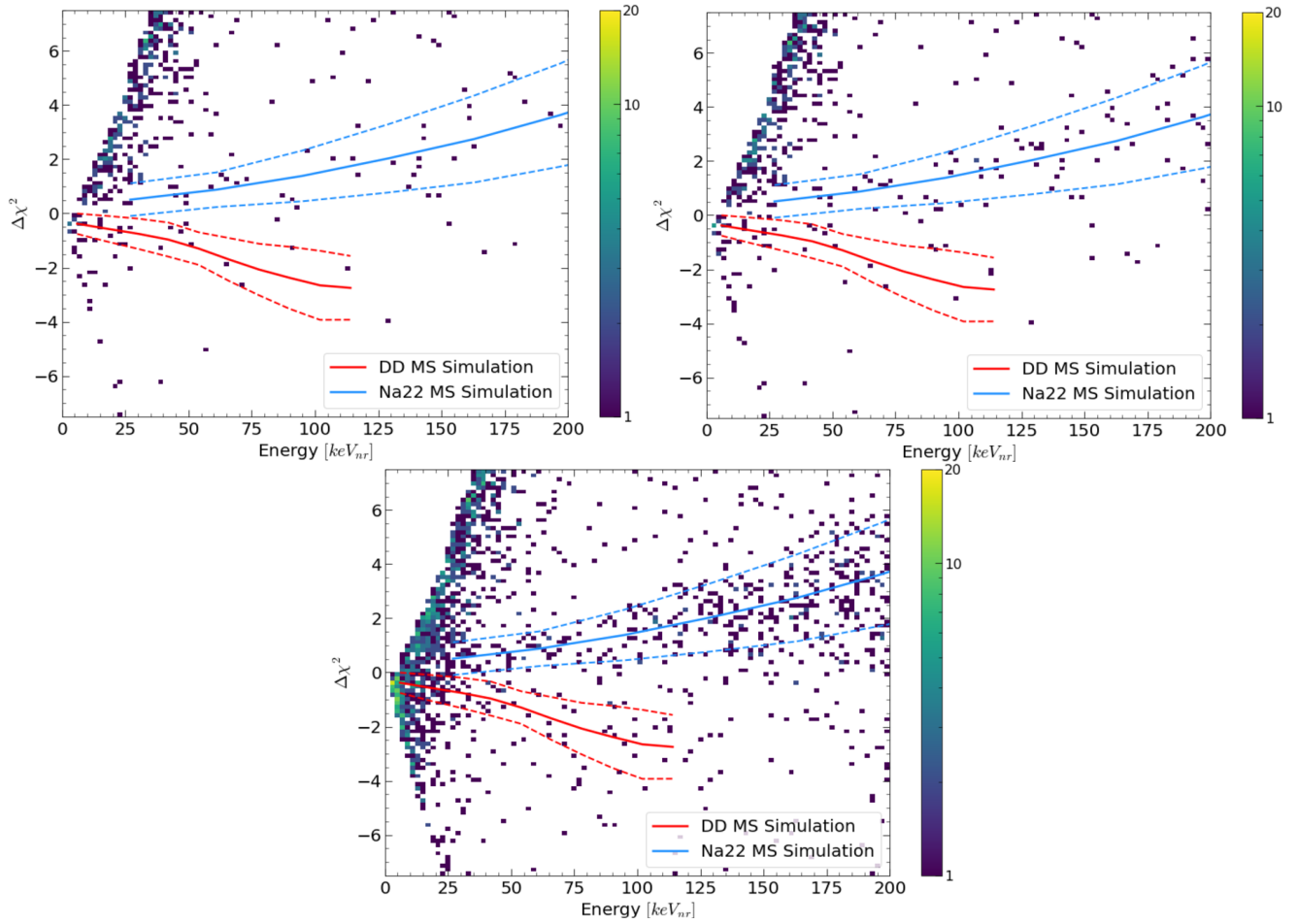


Figure 5.2: *The effect of expanding the strict FV cut on the selection of MS events from WS2024 data, specifically showing the selections with a strict FV cut (top left), a strict FV cut with the radial limit 2 cm from the ideal wall (top right), and a strict FV cut with the radial limit 0 cm from the ideal wall (bottom). All other MS data quality cuts are applied here, but the ROI is extended to be able to view higher energies. No accidental coincidence cuts are applied to these datasets. Also shown are the NR (red) and ER (blue) MS bands that were calculated from DD and Na-22 simulations respectively.*

for MS data events, so that inelastic scatter events, along with other high energy events, can also be studied. For this analysis, the ROI used for MS data requires $S1c < 1000$ phd, $S2 > (4.5 \times 47.8)$ phd, and $S2c < 10^5$ phd. As is also the case for the independent $\Delta\chi^2$ estimate, a secondary, post-fitting MS ROI is imposed, requiring events to be below 200 keV_{nr} total fitted NR energy, hence a large number of events that are in the larger initial ROI selection are not actually included in the final analysis. For SS and MS simulations, the WIMP search ROI of $3 \text{ phd} < S1c < 80 \text{ phd}$, $S2 > (4.5 \times 47.8)$ phd, and $S2c < 10^5$ phd is used.

Next, for the SS/MS ratio obtained from the neutron background simulation (analogous to section 6.4), NR band selections are made on both SS and MS events in $\log(S2c)$ vs. $S1c$ space

(with S2c pulses summed for MS events), and no $\Delta\chi^2$ analysis is performed. This means that ER leakage into the NR band is more likely, but computing time is notably reduced. Since this stage works exclusively with simulation, the majority of ER backgrounds are not a concern, unless they are produced by the process being simulated. Additionally, it was decided that the SS/MS ratio obtained from the simulation would not be given an energy dependence, and would instead be a constant value. This means that Equation 3.1 rather than Equation 3.2 is used in this case. The ROI used for MS events here is also just based on the S1c and total S2c in $\log(\text{S2c})$ vs. S1c space, since no $\Delta\chi^2$ analysis is run to be able to use the post-fitting MS ROI approach.

Another difference between the two estimates is that the LZ WS2024 estimate does not use a re-weighting factor, as was discussed in section 4.6. This factor is calculated for the $\Delta\chi^2$ WS2024 estimate in section 6.5. Instead, studies were carried out to quantify the difference in SS/MS ratio between data and simulation for different neutron calibration sources (AmLi, AmBe, and DD), and the additional error arising from this discrepancy is noted alongside the final result. It is found that the simulation underestimates the number of MS events by a factor of around 20%.

5.2 Use of the $\Delta\chi^2$ Method

The final part of the estimate again requires a measurement of the number of MS neutrons in WIMP search data. This is where the LZ WS2024 estimate utilises the increased discrimination power of the $\Delta\chi^2$ analysis for MS events, to select neutron candidates from the MS WS2024 dataset. As was mentioned at the end of the last chapter, and will be discussed further in section 6.2, for WS2024 no accidental coincidence cuts were developed for MS events, and hence there was a risk of the selected MS neutron candidates being contaminated by accidental coincidence events. For this reason, once events have been selected by the NR band of the $\Delta\chi^2$ method, candidate event waveforms are verified by hand to ensure that each looks like a viable neutron candidate. This method of candidate selection is not optimal however, as it introduces the potential for bias and human error. To minimise this, event waveforms are viewed by multiple analysers, but the preferable approach would be the use of dedicated MS accidental coincidence cuts. Examples of good and bad waveforms are shown in Figure 5.3.

Details of all of the cuts that are applied for the independent $\Delta\chi^2$ estimate are given in section 6.2 of the following chapter, and differ from those applied in this analysis only in the aforementioned ways, and in that no field cage resistor cut is used on the MS data events here, in order to increase statistics. In the $\Delta\chi^2$ analysis presented in chapter 6, the MS ROI is consistent with that used for the simulation, and the field cage resistor cut is applied. This is in order to match the cuts applied to the data and the simulation as closely as possible, and therefore minimise systematic errors in the SS/MS ratio.

A ‘good’ waveform for an MS NR candidate (the top example of Figure 5.3) has a clear S1

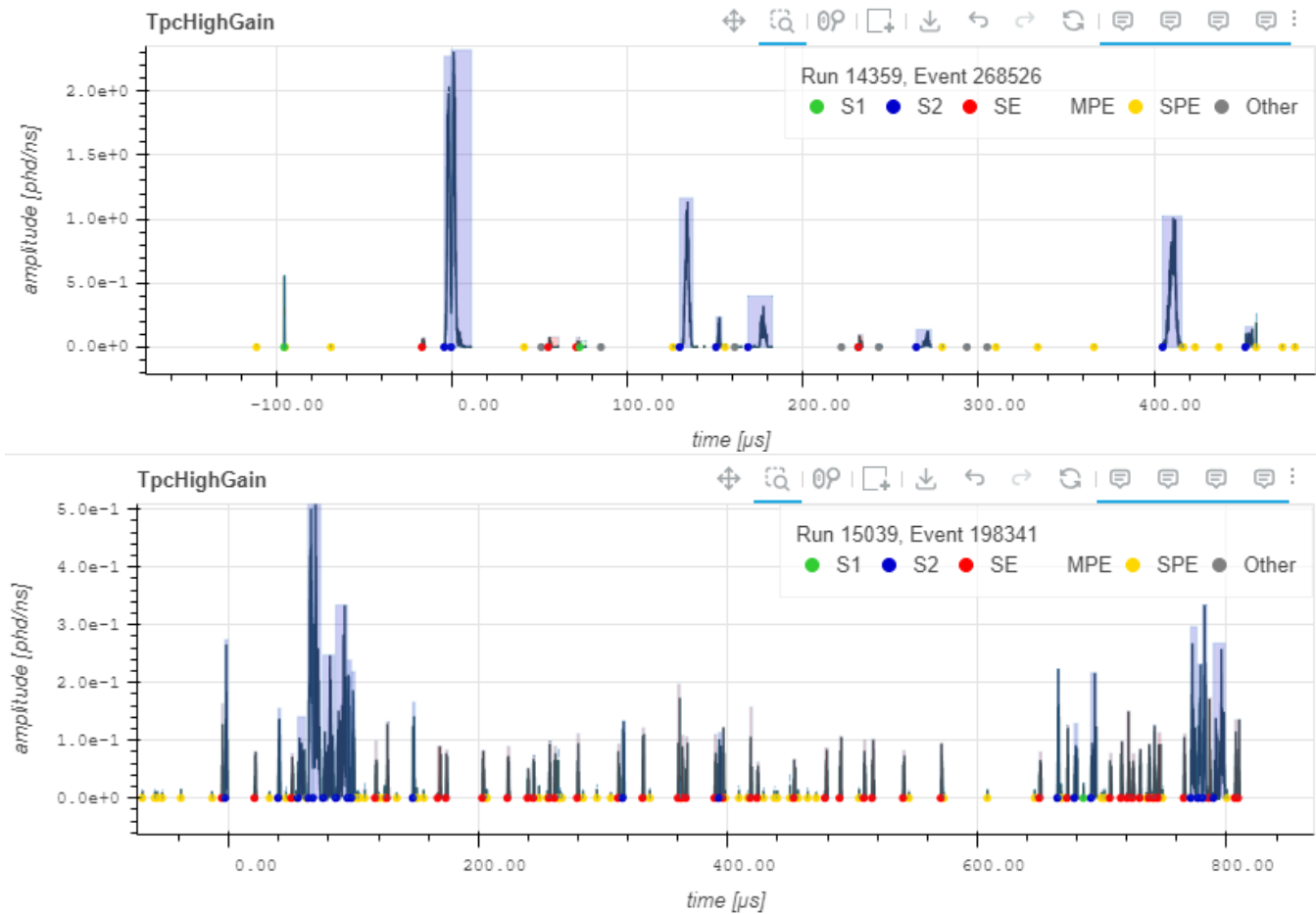


Figure 5.3: An example waveform for a good (top) and bad (bottom) MS neutron candidate. These waveforms display the pulse amplitude with time from the pulse on which the event triggered, as detected by the TPC PMTs. These waveforms are taken from the WS2024 MS NR selection. Different pulse types, as identified by LZAP, are colour-coded, with S1s in green, S2s in blue, SEs in red, SPEs in yellow, and ‘other’ pulses in grey. The ‘good’ event is classified as a good candidate due to its clear S1 and S2 pulses. For the ‘bad’ event, these pulses are much more lost in background noise, and very difficult to distinguish.

pulse followed by clear, distinguishable S2 pulses. These pulses should not merge into each other, and should be distinguishable from background noise. As can be seen in the ‘bad’ waveform (the bottom example of the figure), there are many SEs that obscure the S1 and relatively small S2s in this event. The S1 in particular is very much lost in these background signals, and occurs after many of the S2s in the event. Some more examples of what could cause an event to fail at the waveform evaluation stage are given in section 6.6, specifically relating to the $\Delta\chi^2$ WS2024 MS NR candidate selection. There are many reasons why events would not be considered good MS NR candidates, and not all of their waveforms would appear like the one shown in the figure.

5.3 Multiple Scatter Neutron Candidates in Data

Using the strict FV extending to 2 cm from the ideal wall, 14 MS neutron candidates are identified, compared to 9 using the strict FV extending to 0 cm from the wall, with an OD tag. These two selections have 7 events in common. The spatial distributions of these event selections, along with their positions in $\log(S2c)$ vs. $S1c$ space and $\Delta\chi^2$ space, are shown respectively for these two sets of MS neutron candidates in Figures 5.4 and 5.5. It should be noted that the code for plotting the boundaries of the active and fiducial volumes in these plots, and subsequent plots, was written by A. Al Musalhi, and was also used to produce plots for Ref [126].

The fact that the number of MS NR candidates decreases when the FV is increased, but a veto signal is required, could suggest that there are events among the 14 in the FV extended to 2 cm from the wall that, despite looking like acceptable neutron events, could be accidental coincidences. It is notable that a small cluster of 4 of the 14 events in the top right panel of Figure 5.4 is located at very low $S1c$ and $S2c$, in the region where accidental coincidences would be expected. It is also noteworthy that the plot in the bottom left panel of this figure shows that 2 events have at least one scatter in the region that would be cut out if the field cage resistor cut was applied, so likely originate from neutron-producing processes in the resistors.

For the 9 events selected by expanding the FV all the way to the ideal wall, but requiring a delayed OD veto signal, it can be similarly seen from the top right panel of Figure 5.5 that there is still 1 event sitting below the NR band in $\log(S2c)$ vs. $S1c$ space, in the region where accidental coincidences would be expected to be seen. This event does sit within the band in $\Delta\chi^2$ space (top left panel of the figure), but it could still be an accidental coincidence. This was illustrated by the low energy cluster of events seen during the in-depth study of the features of $\Delta\chi^2$ space during the WS2022 campaign, that was discussed in section 4.4. The bottom left plot of this figure also shows that there is still 1 event with a scatter in the field cage resistor region.

5.4 Single Scatter Neutron Estimate

The results for the two estimates with the two different FV requirements are shown in Table 5.1.

	MS NR	MS/SS Ratio	SS NR Band	SS ROI	SS WS
FV 2cm from Ideal Wall	14 ± 4	3.4 ± 0.7	4 ± 1	6 ± 2	0.5 ± 0.3
FV 0cm from Ideal Wall + OD Delayed Tag	9 ± 3 (tagged) (12 ± 3 total)	4.7 ± 0.9	3 ± 1	4 ± 2	0.3 ± 0.2

Table 5.1: LZ WS2024 MS-driven SS neutron estimate results.

These results are calculated in the following way. For the number of MS NR candidates, in the case of the strict FV 0 cm from the wall, the measured OD delayed tagging efficiency of (75

$\pm 3\%$ must be taken into account to get the total number of implied events. Details on how veto efficiencies are calculated can be found in section 2.3. Since an NR band selection is used for the SS simulation, the division of the number of MS NR candidates by the MS/SS ratio gives the expected number of SS neutrons in the NR band. $(70 \pm 10)\%$ of SS neutrons should be in this band, and so accounting for this, the overall number of SS neutrons in the ROI is calculated. Finally, only $(8 \pm 4)\%$ of SS neutrons are expected not to have a veto signal, so this gives the final estimate for the number of SS neutrons in the WIMP search dataset.

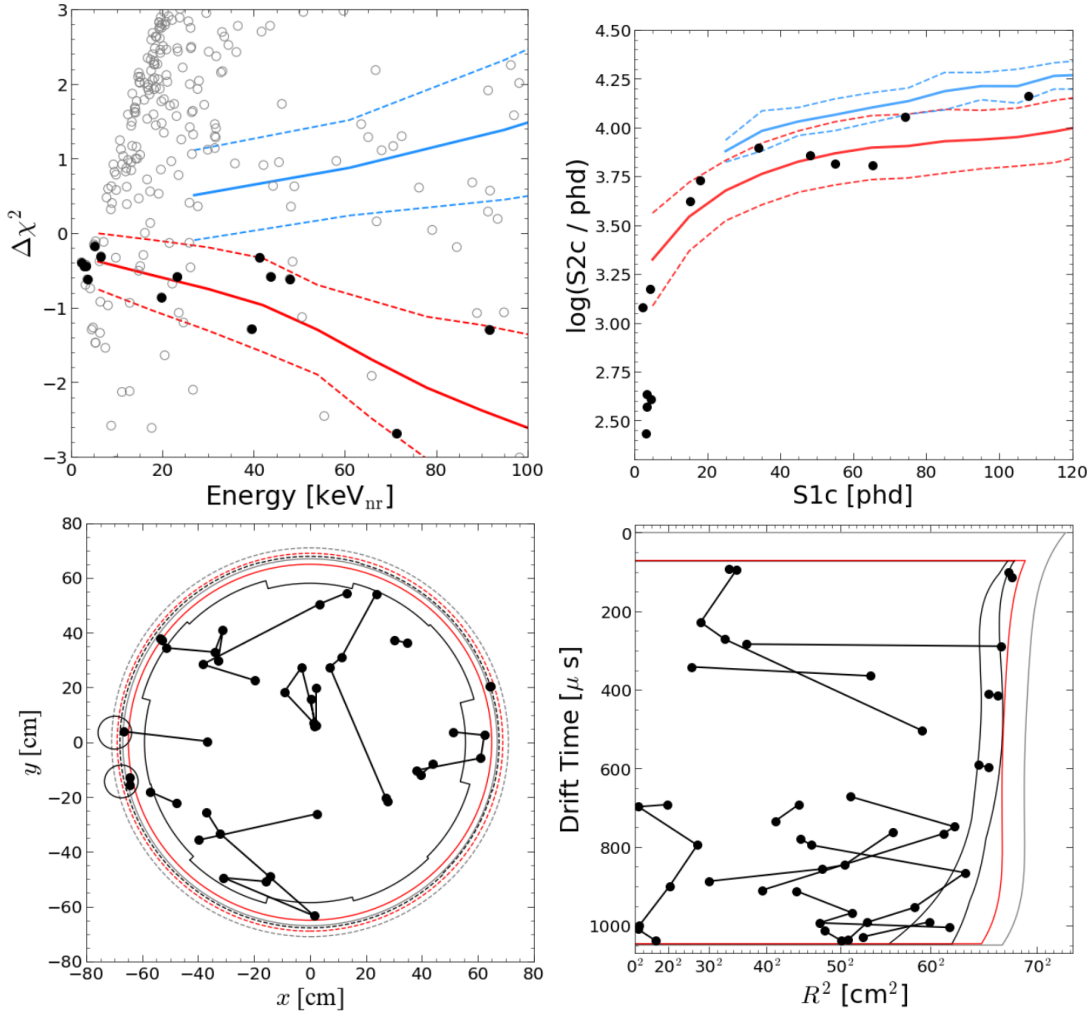


Figure 5.4: The 14 WS2024 MS NR candidates in the strict FV extended out to 2 cm from the ideal wall. Events in $\Delta\chi^2$ space are shown (top left) alongside the NR (red) and ER (blue) Gaussian 90-10 CL bands in this space, generated using DD and Na-22 simulations respectively. Events passing all cuts but not chosen as suitable candidates are shown by grey open circles. The distribution in $\log(S2c)$ vs. $S1c$ space is shown (top right) alongside Gaussian 90-10 CL bands generated from the NR (red) and ER (blue) simulations. The xy distribution of all scatters of the events is shown (bottom left), where the grey/red lines show the ϕ -averaged active volume/active volume -2 cm edges at the top (dashed) and bottom (solid) of the FV. The black lines show the ϕ -varying fiducial edges at the top (dashed) and bottom (solid) of the FV. The smaller circular regions would be the target of the field cage resistor cut. All scatters in drift time vs. R^2 are shown (bottom right), where the grey line indicates the boundary of the active volume. The black lines show the minimum and maximum squared radii of the FV, as radius varies with ϕ , for each value of drift time. The red line shows the FV boundary extended out to 2 cm from the ideal wall. Connecting lines between scatters in these plots are arbitrary.

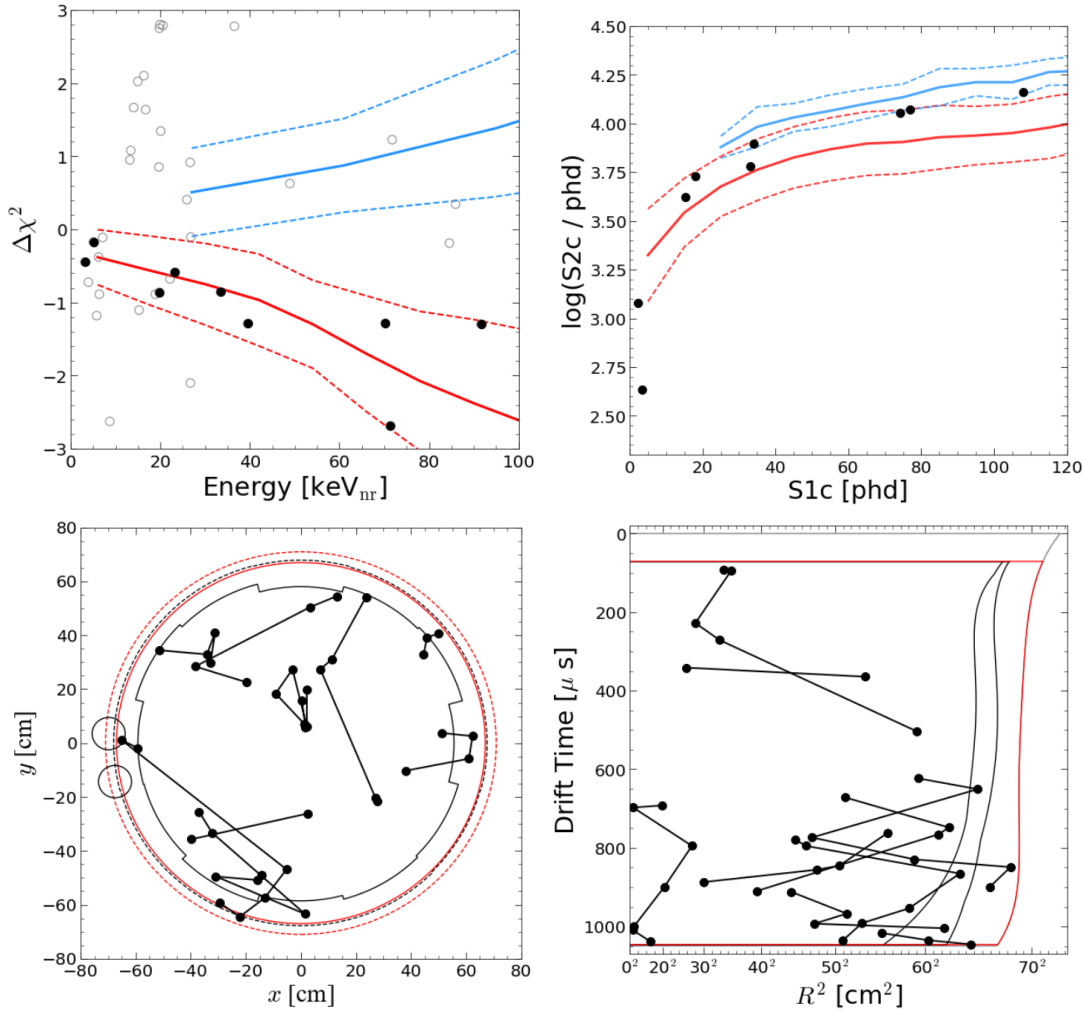


Figure 5.5: The 9 WS2024 MS NR candidates in the strict FV extended out to the ideal wall, requiring a delayed OD veto signal. Events in $\Delta\chi^2$ space are shown (top left) with the NR (red) and ER (blue) Gaussian 90-10 CL bands, generated using DD and Na-22 simulations respectively. Events passing all cuts but not chosen as suitable candidates are shown by grey open circles. Events in $\log(S2c)$ vs. $S1c$ space are shown (top right) alongside Gaussian 90-10 CL bands generated from the NR (red) and ER (blue) simulations. The xy distribution of all scatters of the events is shown (bottom left), where the red lines show the ϕ -averaged active volume edges at the top (dashed) and bottom (solid) of the FV. The black lines show the ϕ -varying fiducial edges at the top (dashed) and bottom (solid) of the FV. The smaller circular regions would be the target of the field cage resistor cut. All scatters in drift time vs. R^2 are shown (bottom right), where the grey line indicates the boundary of the active volume. The black lines show the minimum and maximum squared radii of the FV, as radius varies with ϕ , for each value of drift time. The red line shows the FV boundary extended out to 0 cm from the ideal wall. Connecting lines between scatters in these plots are arbitrary.

Chapter 6

$\Delta\chi^2$ WIMP Search 2024 Neutron Single Scatter Estimate

In addition to its use in the LZ WS2024 SS neutron estimate presented in chapter 5, the $\Delta\chi^2$ analysis is also used at all stages of an independent MS-driven SS neutron estimate, referred to as the $\Delta\chi^2$ WS2024 SS neutron estimate. This follows on from what was done for WS2022 and was presented in chapter 4. This chapter will cover the details of this estimate.

For this campaign, there was a significant update to the $\Delta\chi^2$ method in order to incorporate anti-correlations between S1 and S2 signals, due to recombination fluctuations, into the χ^2 definitions of the NR and ER models used in the method. A comparison between the performance of the updated method and the previous iteration of the $\Delta\chi^2$ method is presented in section 6.1.

6.1 $\Delta\chi^2$ Update

For the work presented in this chapter, a significant update was made to the $\Delta\chi^2$ method from the version of the algorithm that was used for the WS2022 analysis, presented in chapter 4. This update was described in section 3.3.1, and takes into account the anti-correlation between S1 and S2 signals due to recombination fluctuations when the liquid xenon is ionised. This required a reconfiguration of the χ^2 tests used in the definition of the $\Delta\chi^2$ metric to incorporate a covariance matrix that can account for these anti-correlation terms, and this new definition was given in Equation 3.11.

These changes were made in order to make the $\Delta\chi^2$ analysis more rigorous and justifiable, with the hope that it could also potentially further improve NR ER discrimination for MS events. Therefore, it is important to analyse how the performance of this new configuration of the method compares to the previous iteration, and that is what will be detailed in this section. However, it is essential to note that the detector conditions changed between WS2022 and WS2024 to have a lower drift field, and this would be expected to reduce NR ER discrimination power. Therefore, it

is difficult to disentangle changes to the $\Delta\chi^2$ method from this change in detector conditions.

There are a couple of different ways in which the performance of the $\Delta\chi^2$ analysis can be quantified. The first approach that can be taken is to consider the selection efficiency. For a sample of events of a known type (either NR or ER), the fraction that are correctly identified and fall within the appropriate band can be found. This will be affected by the fact that a 90-10 CL Gaussian band is only expected to contain 80% of events. By definition, the band will contain 80% of the simulated data on which it was tuned, in a given energy bin. This means that this is not a particularly useful metric for assessing the performance of the analysis in this case.

Another approach that can be taken to evaluating the performance of the method is to look at the leakage of events of a known type into the incorrect band. In this instance, the most important case to consider is ER events leaking into the NR band, since such events would be misidentified as NR events. For both WS2022 and WS2024, the percentage of ER simulation events leaking into the NR band is shown in Table 6.1, using an ROI selection on the ER events of $S1c < 250$ phd and $2.5 < \log(S2c / \text{phd}) < 5.0$. Note that the number of events in the WS2022 Th-232 simulation in this ROI is $\sim 12\,000$, whereas for the WS2024 Na-22 simulation there are only ~ 1500 events in this ROI, hence the WS2024 result has a larger fractional error.

	ER to NR Leakage (%)
WS2022	0.38 ± 0.06
WS2024	0.20 ± 0.12

Table 6.1: *The leakage of ER simulation events into the NR band in $\Delta\chi^2$ space for WS2022 and WS2024, for events with $S1c < 250$ phd.*

As is evident from these results, the ER to NR leakage in both WS2022 and WS2024 is less than 1% of the total simulated ER events. This shows that discrimination is effective in both iterations of the analysis. There looks to be a slight improvement in the percentage of ER leakage for WS2024, but the result is just in agreement with that for WS2022 within errors. This comparison will be affected by the aforementioned change in detector field conditions, however, that would reduce discrimination power. The fact that the WS2024 version of the method potentially shows a marginal improvement in discrimination despite the field change indicates that the introduction of the S1 S2 anti-correlation into the method causes a notable improvement in discrimination.

6.2 Analysis Cuts for the $\Delta\chi^2$ SS Neutron Estimate

As was the case in WS2022, not all of the data that was collected during the WIMP-search is useful for analysis, and this can be for a variety of different reasons. To remove this non-useful data, a number of analysis cuts are applied to the dataset, and this section will detail those cuts.

Many of the analysis cuts that are applied for WS2024 were previously used for WS2022, and hence have already been motivated in section 4.2. Where that is the case, this section will only detail any notable changes to cuts in the interest of brevity, although the cuts were individually tuned for the different campaigns. Any new cuts will be detailed in full.

6.2.1 Fiducial Volume

The active volume definition, and therefore also the FV definition, was updated from WS2022 to maximise the volume of liquid xenon used for the WIMP search, and therefore maximise the sensitivity of the detector. This followed the same procedure as in the previous WIMP search of carrying out detailed studies of the wall background and allowing only a certain amount of leakage of this background into the FV at each value of drift time. The details of this analysis are beyond the scope of this thesis. A notable change from WS2022, is that the WS2024 FV definition includes a dependence on the azimuthal angle, ϕ , within the detector.

As was the case for the WS2022 analysis, it was decided that a strict FV cut for MS events, whereby all scatters of an event are required to be within the FV, was appropriate. For SS events, the FV cut is much more straightforward, and simply requires that the event interaction occurs within the FV. It was discussed earlier, in chapter 5, that larger FVs could be considered in order to increase the number of neutrons seen, as many will interact around the edges of the detector. However, expanding the FV in this way also increases the number of backgrounds that are seen, notably the number of accidental coincidence events, as was evident from Figure 5.2. Since no MS-specific accidental coincidence cuts have yet been developed to remove these backgrounds, it was decided that the harsher cut using the standard FV definition was more appropriate for this analysis.

For the WS2024 SS FV cut used in the WIMP search, the maximum drift time (and therefore minimum z position) for the FV changed during the course of data taking. This variation was due to the change in the circulation state of the TPC from the high-mixing state to the low-mixing state, as discussed in section 2.5, and this led to drift time limits of 1034 μs and 1030 μs respectively. The two different drift time limits only introduce a percentage level effect on the FV definition.

To check which of these two limits is appropriate for a given event requires the run number, which poses an issue for simulated events since they are not allocated a run due to not being real data. The lower drift time FV limit is used for these events since this corresponded to the conditions with which they were simulated. For calibration data, for which the two different circulation conditions were not present, the more conservative limit of 1030 μs is used, in line with the simulations.

6.2.2 Field Cage Resistor Cut

As was presented in section 4.2.2, a cut is again applied for WS2024 to remove events that are in the vicinity of the high activity field cage resistors at the edge of the TPC, where the elevated rate of events effectively blinds the detector. The radius removed from around the resistor chains is again 6.0 cm, as in WS2022.

6.2.3 Region of Interest

For this analysis, the WS2024 ROI is used for SS events, since this is by definition the region in which a WIMP-like neutron signal would be problematic, and could potentially be mistaken for dark matter. This requires the S1c pulse area to be within the range $3 \text{ phd} < \text{S1c} < 80 \text{ phd}$. The introduction of this lower limit aims to minimise the number of accidental coincidence events in the ROI. There is also a requirement that the uncorrected S2 pulse area is greater than 645.25 phd. This is equivalent to 14.5 electrons, each with an SE size of 44.5 phd. This S2 threshold removes all CE ν NS events (see section 2.11.3). The final requirement for the SS ROI is that the S2c area is less than a maximum value of $10^{4.5}$ phd (reported in this way due to the traditional use of $\log(\text{S2c})$).

For MS events, the choice of ROI is less clear. As was explored in section 3.2, the $\log(\text{S2c})$ vs. S1c parameter space is not optimal for the study of MS events, and so the definition of an ROI for them in this space faces difficulties. However, when dealing with large datasets it becomes computationally demanding to run the $\Delta\chi^2$ analysis over all events, regardless of their position in $\log(\text{S2c})$ vs. S1c space. Therefore, a relaxed ROI selection is initially made, requiring events to have $3 \text{ phd} < \text{S1c} < 100 \text{ phd}$, total S2 $> 645.25 \text{ phd}$, and total S2c $< 10^{5.0}$ phd. The lower limits from the tighter SS ROI are maintained to minimise the effect of accidental coincidence events migrating into the band post-fitting (after the $\Delta\chi^2$ analysis). The $\Delta\chi^2$ analysis is run only on MS events in this ROI.

When the WS2024 ROI is applied to the SS events, a sharp drop off in the energy distribution is seen above around $60 \text{ keV}_{\text{nr}}$ and below around $2 \text{ keV}_{\text{nr}}$. For this reason, a post-fitting ROI cut in $\Delta\chi^2$ space at these energy values is applied to the MS WS2024 data. This requirement is also enforced inherently in the calculation of SS/MS in section 6.4 and r_{DD} in section 6.5, since these quantities go to zero when the SS distribution goes to zero.

By applying a looser $\log(\text{S2c})$ vs. S1c space ROI cut to MS events before the $\Delta\chi^2$ analysis is carried out, this takes into consideration events just beyond the limits of the more restricted ROI that may move into the ROI in $\Delta\chi^2$ space. If a harsher ROI cut was initially used in $\log(\text{S2c})$ vs. S1c space, events that may move into the ROI, post-fitting, could be lost.

6.2.4 OD and Skin Veto Cuts

Three results for the SS neutron estimate are produced (as they were for WS2022), namely with the requirement on the MS selections of having no veto signal, having a veto signal, and no veto requirement (veto agnostic). The SS selection in all cases requires no veto signal, as this is the requirement to be in the WIMP search dataset.

The specific conditions for a pulse in the OD or Skin to be classified as a veto signal for an event in WS2024 are as follows. A prompt veto signal in the OD is required to have an area greater than 4.5 phd, be within 300 ns either before or after the S1, and have a coincidence of more than 5 PMTs. A delayed OD veto signal must have an area greater than 32 phd, be within a time window after the S1 of between 300 ns and 600 μ s, and have a coincidence of more than 5 PMTs.

For the Skin, the prompt signal requirement is an area of at least 2.5 phd within 250 ns before or after the S1, and a coincidence of more than 2 PMTs. For a delayed Skin signal, an area greater than 46 phd is needed, the veto pulse must be within the time window of 250 ns to 600 μ s after the S1, and the coincidence must be more than 2 PMTs.

Note that the coincidence requirement is not applicable to LZLAMA simulations, as coincidence is not an RQ included in the fast chain simulation.

6.2.5 Ghost Train Veto

The so-called ‘ghost train’ veto is designed to remove periods of live time where pulse rates are very high in the wake of a large progenitor S2, just like the e-train cut. However, this cut looks at the specific instance where the progenitor S2 itself occurs in an e-train exclusion period, or another period of trigger hold-off, and therefore cannot be identified by the e-train veto.

6.2.6 PMT Trip Cut

The temporary flare up of a hotspot will produce an increased amount of light in the detector, which can sometimes cause PMTs to trip. When this occurs, it is essential that the reason for the trip is investigated, and that the tripped PMTs are ramped back up to their usual operating voltages as quickly as possible.

During time periods when PMTs are tripped, or are being re-biased, the detector conditions are temporarily abnormal, and signals from incoming particles will not quite be detected in the way in which they usually would (since fewer PMTs will be viewing the signals and contributing to the output waveforms). Therefore, these periods are also removed from the WIMP search dataset.

6.2.7 High SPE Rate Cut

If many SPEs occur at once and pile up, they can be mistaken for S1 pulses. This increased rate of isolated S1 pulses can then in turn lead to an increased rate of accidental coincidence events. To reduce the probability of this occurring, it is preferable to minimise the PMT signal rate.

The high SPE rate cut is designed to remove periods in which the rate of SPE pulses, or S1 pulses, is elevated above a given threshold. Once the e-train, muon. hotspot, and PMT trip cuts have been applied, the remaining WIMP-search live time is divided into 2 minute bins. Any bin in which the rate is above the designated threshold is excluded from the analysis by this cut, along with a 2 minute buffer on either side.

6.2.8 Additional Cuts

There are a number of cuts applied to the WS2024 dataset that were also applied for WS2022, and had no significant updates beyond tuning that are within the scope of this thesis. These cuts were already described in section 4.2, and, so for brevity, will just be listed here: the e-train veto, the OD burst noise cut, the SS window cut, the stinger cut, the muon cut, and the exclusion period cuts.

6.2.9 Accidental Coincidences

As in WS2022, accidental coincidences are an important background in WS2024. A set of dedicated cuts was developed to tackle this population for the SS WIMP search dataset, but this was not the case for MS events, and future work is aiming to address this. The WS2022 method of directly using the SS-tuned accidental coincidence cuts on the individual scatters of MS events (where possible) was seen to be potentially overly harsh, and removed all events. For this reason, no MS accidental coincidence cuts are applied for WS2024. In lieu of these cuts, all MS NR candidates selected by the $\Delta\chi^2$ NR band have their raw waveforms analysed by eye to ensure that the event looks like a good neutron MS candidate. Events with misshapen S1 or S2 pulses, or poor pulse identification, for example, are discarded.

6.3 NR and ER Band Definitions

As was done for WS2022, for WS2024 NR and ER 90-10 CL Gaussian bands are defined in $\Delta\chi^2$ space. This is done using simulations of NR and ER sources, specifically DD and Na-22 respectively.

For the DD simulation used to create the NR band, statistics are sufficiently high for MS events with energies less than around 200 keV_{nr} that cuts can be applied to this dataset, so that it better represents the data to which the band will be compared. Specifically, the cuts applied here are a strict FV cut, the field cage resistor cut, and an extended MS ROI cut requiring S1c < 500 phd

and $2.5 < \log(S2c / \text{phd}) < 5.0$. This means that an NR band is created that is longer along the energy axis than is required for the extended MS ROI used in this work, as this allows for some flexibility in the analysis. The MS NR band, and the simulated DD data from which it was created, are shown on the left of Figure 6.1. Note that the two clusters of more ER-like events in the left plot are inelastic NR events, specifically involving excitation to Xe-129 (lower energy inelastic peak) and Xe-131 (higher energy inelastic peak).

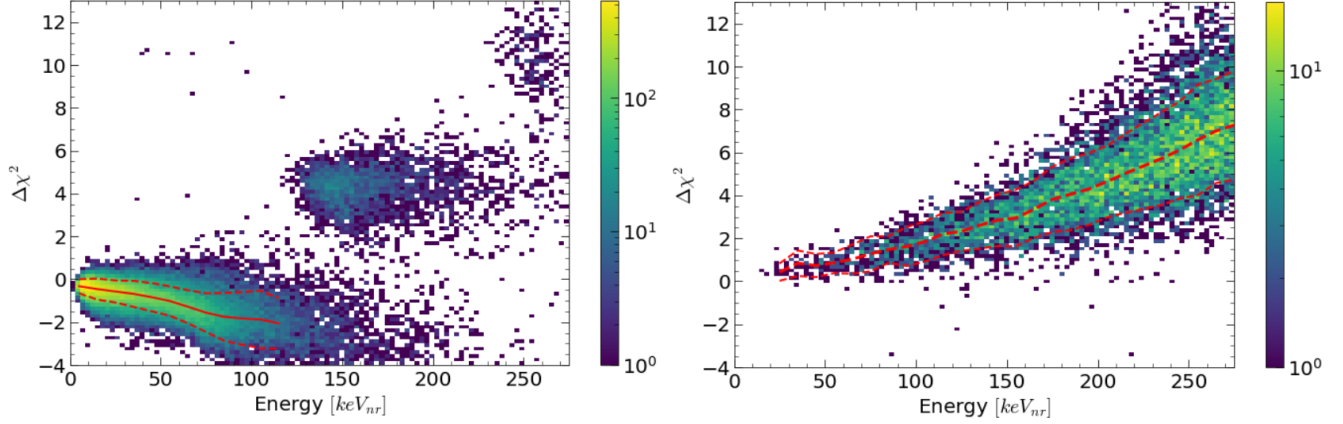


Figure 6.1: *The 90-10 CL Gaussian NR (left) and ER (right) bands (shown in red) used for the $\Delta\chi^2$ WS2024 analysis, overlaid on the respective DD and Na-22 simulations used to create them. The NR band fitting is cut short at 120 keV_{nr} to avoid effects on the band from the inelastic scatter populations. A pre-fit ROI cut of $S1c < 500$ phd and $2.5 < \log(S2c / \text{phd}) < 5.0$ is applied to both datasets, and the DD dataset has a strict FV cut and the field cage resistor cut applied. Both datasets also have a post-fit ROI of $-4 < \Delta\chi^2 < 13$ and total fitted NR energy < 275 keV_{nr} applied.*

The ER band here is created using Na-22 simulated data, rather than the Th-232 source used for WS2022, as this can be directly compared to Na-22 calibration data. The number of MS events with an energy less than 200 keV_{nr} is low, and so it was decided that no FV cut would be applied in order to maximise the statistics used in the band calculation. The same ROI cut is applied as for the DD simulation. The larger ROI allows for the study of the behaviour of the band at higher energies, where the statistics are higher for ERs, and therefore the band can be fitted more accurately.

These bands are shown again, but overlaid, in Figure 6.2, along with the simulated data used to create them. This figure also shows these same simulated events with their equivalent bands in $\log(S2c)$ vs. $S1c$ space to show the improvement in MS NR ER discrimination that is gained from using the $\Delta\chi^2$ approach. NR energy contours are again shown in $\log(S2c)$ vs. $S1c$ space for reference, but it should again be noted that these energies are not directly comparable to those in the post-fitting $\Delta\chi^2$ space, as was discussed in section 4.3. It can also be seen from the figure that in $\Delta\chi^2$ space the discrimination improves as total fitted NR energy increases, whereas

in $\log(S2c)$ vs. $S1c$ space the two distributions overlap at nearly all values of $S1c$. The energy dependent leakage of ER events into the NR band in both of these parameter spaces can once more be evaluated for the simulated data used to produce the bands, as was presented in section 4.3 for WS2022. This is shown in Figure 6.3, in which it can be seen that the leakage of ER events into the NR band increases with energy in $\log(S2c)$ vs. $S1c$ space, but is negligible at all energies in $\Delta\chi^2$ space.

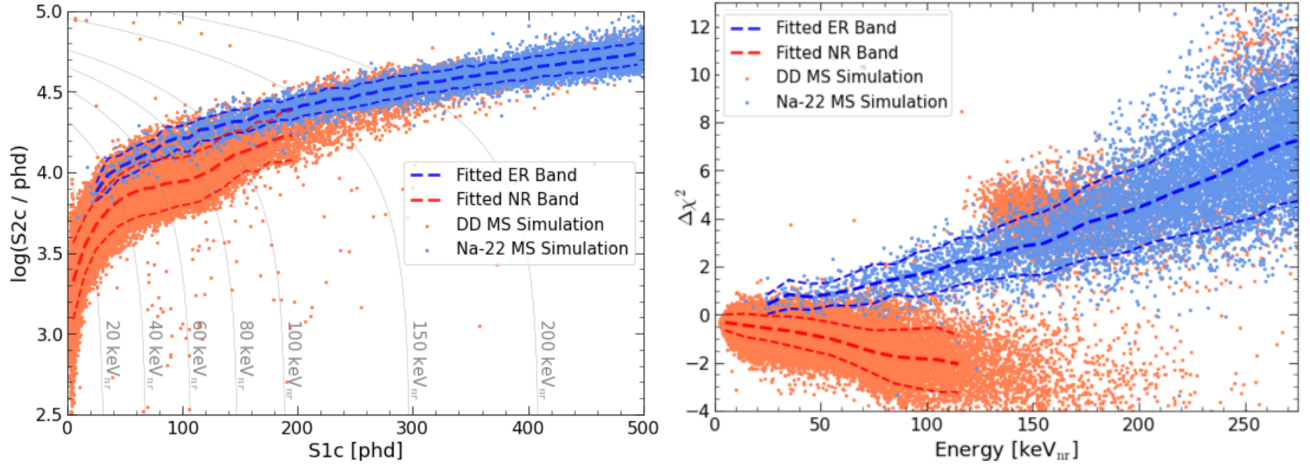


Figure 6.2: A demonstration of the difference in MS NR ER discrimination between the $\log(S2c)$ vs. $S1c$ parameter space (left), and the $\Delta\chi^2$ vs. total fitted nuclear recoil energy parameter space (right) using NR (DD, shown in light red) and ER (Na-22, shown in light blue) simulated data for WS2024. Also shown are fitted 90-10 CL Gaussian bands for each of these two datasets in each of the two parameter spaces. NR energy contours are shown in $\log(S2c)$ vs. $S1c$ space. A pre-fit ROI cut of $S1c < 500$ phd and $2.5 < \log(S2c / \text{phd}) < 5.0$ is applied to both datasets and the DD dataset has a strict FV and the field cage resistor cut applied. In $\Delta\chi^2$ space, both datasets also have a post-fit ROI of $-4 < \Delta\chi^2 < 13$ and total fitted nuclear recoil energy < 275 keV_{nr} applied.

Note that the typical values of $\Delta\chi^2$ differ from those seen in Figure 4.6 for WS2022 because of the new definition of $\Delta\chi^2$ that includes the S1 S2 anti-correlations. Since this update, the values of the individual χ^2_{NR} and χ^2_{ER} that contribute to $\Delta\chi^2$ have become more meaningful, since each should follow a χ^2 distribution for one degree of freedom, in the case where the model matches the true event type (i.e. χ^2_{NR} for a true NR event and χ^2_{ER} for a true ER event). Investigation into the χ^2 values of the two models for different datasets is carried out in section 6.9, with the aim of further optimising the method.

The NR band is simple to verify using DD calibration data, and this is shown in the top left plot of Figure 6.4, where it can be seen that the data follows the band produced by the simulation. The cuts applied to this calibration data are the strict FV, the field cage resistor cut, an extended ROI (requiring $S1c < 500$ phd) in order to see inelastic scatter events, and some DD data quality

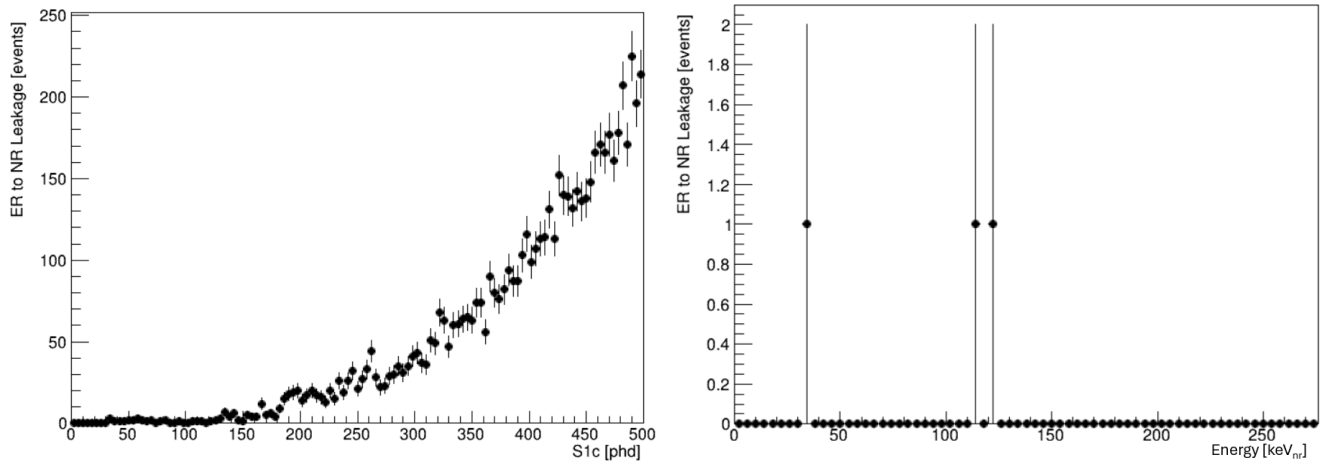


Figure 6.3: A comparison of the leakage of ER events into the NR band in $\log(S2c)$ vs. $S1c$ space (left) and $\Delta\chi^2$ vs. total fitted NR energy space (right) for WS2024. For values beyond the end of the NR band (in $S1c$ or energy), the NR band is extrapolated.

cuts to minimise backgrounds. Again, no accidental coincidence cuts are applied here, since they have not yet been developed for MS events, and hence there is evidence suggesting that this type of event is present in this dataset. Notably, the steep band feature above the ER band, and many of the events visible below the NR band. By extending the ROI, this dataset includes the inelastic scatters of DD neutrons starting from around $130 \text{ keV}_{\text{nr}}$. As was discussed for WS2022, these ER-like inelastic NR events can be used to provide some partial verification of the ER band.

AmLi and AmBe were also investigated as potential neutron sources to use for the generation of the NR band, and it was found that the bands produced by the three different sources were largely in agreement, and could be used for further validation of the NR band. The AmLi and AmBe calibration data is shown in Figure 6.4 (top right and bottom plots respectively) to illustrate that the band is valid for different neutron sources. The agreement of the AmLi data in this figure (and, to a slightly lesser extent, the AmBe data) with the DD simulation-produced NR band can be generally seen, although there are some differences in the band shape between these sources. The agreement between sources is better below $100 \text{ keV}_{\text{nr}}$, which is the upper ROI limit used in this analysis. Note that for the second two plots displayed in this figure, the population of accidental coincidence events rising steeply above the ER band is more populated than it is in the case of DD data, due to the sources producing other backgrounds, as well as neutrons, to a greater extent than DD neutron generation does. It can also be seen for AmLi and AmBe that the NR band of events does not extend as high in energy as it does for DD, which is another reason that DD simulation is selected as a more appropriate source from which to produce the NR band.

As in WS2022, once again simulation is able to produce enough low energy MS ER statistics to generate the ER band, but it is difficult to find a corresponding high-statistics source for the data. Figure 6.5 shows the WS2024 Na-22 calibration data that is used to attempt this verification. No

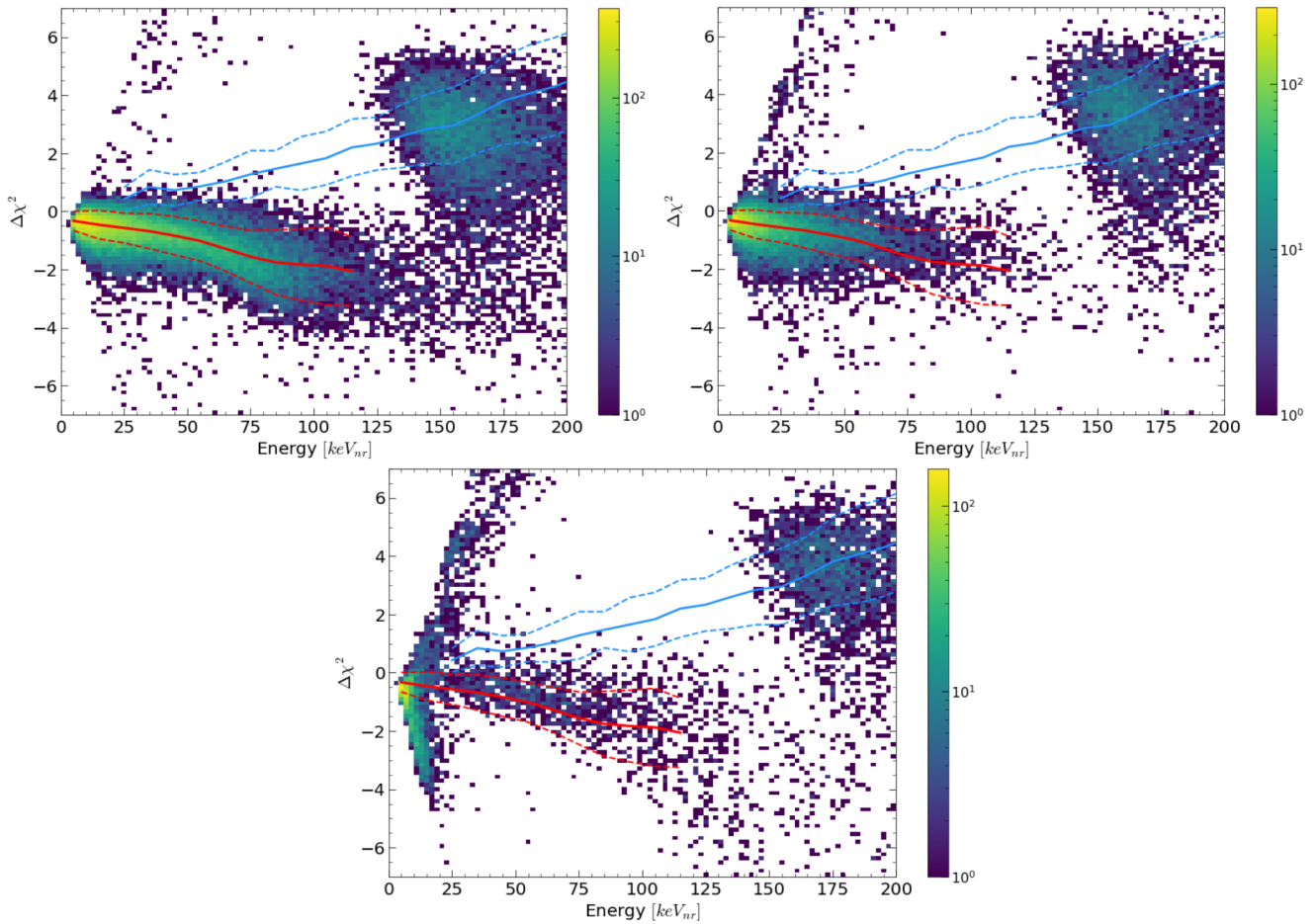


Figure 6.4: A verification of the DD simulation-produced NR band using DD (top left), AmLi (top right) and AmBe (bottom) data. The data plotted here has the following cuts applied: strict FV, field cage resistor, an extended ROI ($S1c < 500$ phd, $2.5 < \log(S2c / \text{phd}) < 5.0$, and $S2 > 645.25$ phd), and some calibration data quality cuts to minimise backgrounds. Shown here are the 90-10 CL Gaussian bands generated for NR events from DD simulation (red) and for ER events from Na-22 simulation (blue).

cuts other than an extended ROI (requiring $S1c < 500$ phd) are applied to this data to maximise the statistics. Although the top left plot of this figure shows that there are an insufficient number of events in and around the ER band in $\Delta\chi^2$ space to verify the band, there are nevertheless a couple of interesting points that can be extracted from these plots. Firstly, it can be seen that there is a population below the NR band in both $\Delta\chi^2$ space and $\log(S2c)$ vs. $S1c$ space (top right). As in WS2022, discussed in section 4.4, this population is seen to be due to gas events in the electroluminescence region of the detector. All of these events would be removed by an FV cut. However, when the events in the ER band are looked at, it is found that they also largely occur in this region, meaning that the application of such a cut would remove essentially all events.

A steep band of events above the ER band can also be seen in $\Delta\chi^2$ space, which corresponds to the accidental coincidence events at low $S1c$ in $\log(S2c)$ vs. $S1c$ space. This is again analogous

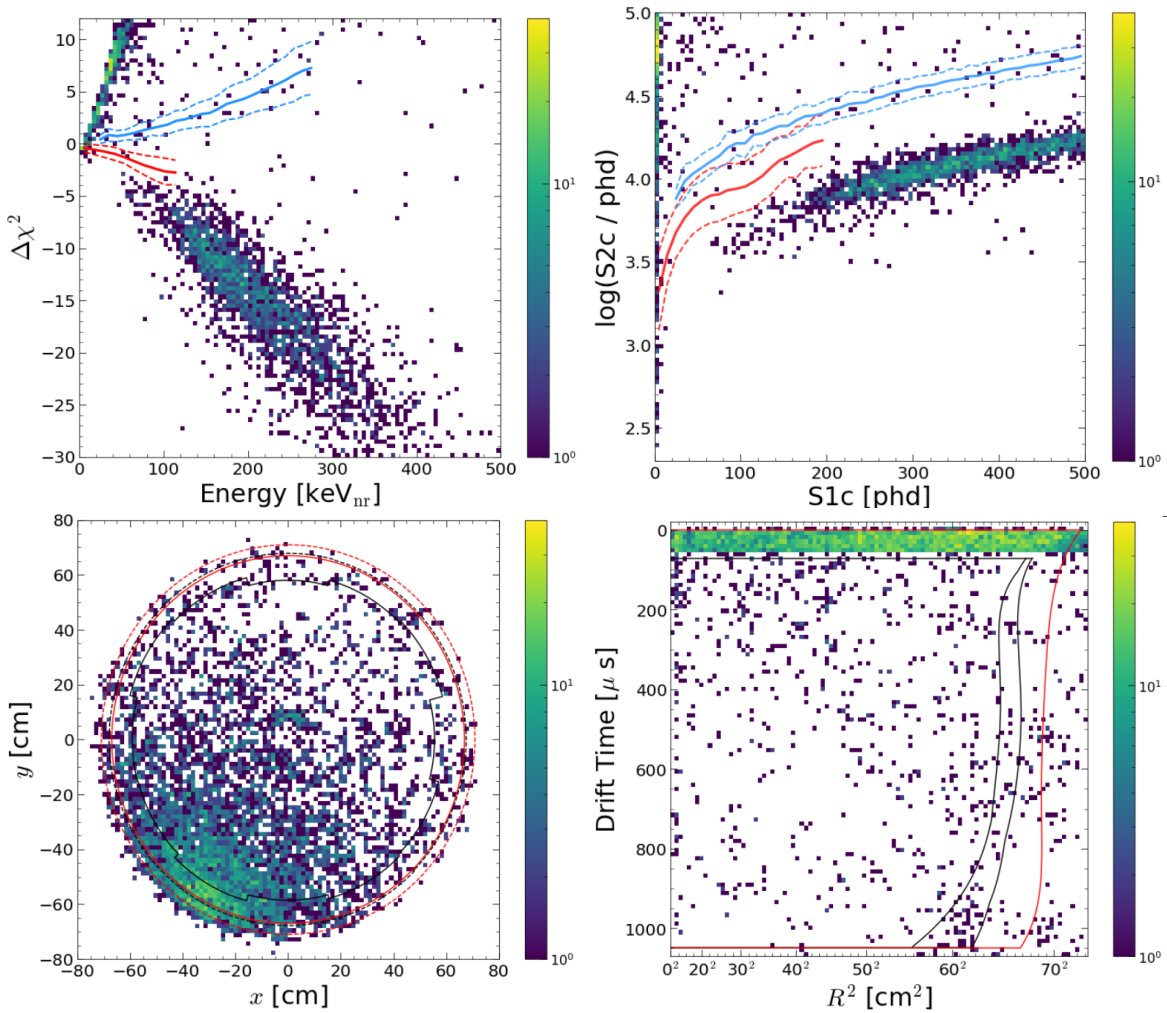


Figure 6.5: *WS2024 Na-22 calibration data, using CSD 3 with the source at 1700 mm, shown across different parameter spaces, aiming to verify the ER band. Only an extended ROI cut (requiring $S1c < 500$ phd) is applied to this data. Events in $\Delta\chi^2$ space are shown (top left) alongside the NR (red) and ER (blue) Gaussian 90-10 CL bands in this space, generated using DD and Na-22 simulations respectively. The distribution in $\log(S2c)$ vs. $S1c$ space is likewise shown (top right) alongside Gaussian 90-10 CL bands generated from the NR (red) and ER (blue) simulations. The xy distribution of all scatters of the events is shown (bottom left), where the red lines show the ϕ -averaged active volume edges at the top (dashed) and bottom (solid) of the active volume. Similarly, the black lines show the ϕ -varying FV edges at the top (dashed) and bottom (solid) of the FV. The distribution of all scatters of the events in drift time vs. R^2 is shown (bottom right), where the red line indicates the boundary of the active volume of the detector. The black lines show the minimum and maximum squared radii of the FV, as radius varies with ϕ , for each value of drift time.*

to what was discussed for WS2022 in section 4.4. These events likely constitute the majority of events that can be seen to lie outside of the active volume in the bottom two plots of the figure,

and must have an incorrectly constructed xy position from the Mercury algorithm [117].

Since this ER band verification is not successful, some further verification is achieved by using a secondary simulated source of MS ER events, namely Th-228. This produces lower statistics at low energies than the Na-22 simulation, so is less practical for producing a band, but nevertheless allows for verification of the consistency of the band across different simulated sources. This simulated data, compared to the Na-22 band, is shown in Figure 6.6. For maximum statistics, and to see the position of the ER band at higher energies, the ROI selection applied here is widened to allow S1c values up to 1000 phd. The top left plot of the figure shows the crucial verification of the ER band in $\Delta\chi^2$ space using this alternative simulated dataset. It can be seen that the data follows the Na-22 band well, and hence provides further justification for the use of this band. The traditional $\log(\text{S2c})$ vs. S1c space is shown at the top right of the figure, and illustrates that these events also sit in the ER band in this space. The positional information for these events is shown in terms of xy position (bottom left) and R^2 vs. drift time (bottom right), and it is clear that the gamma photons interact with the liquid xenon very quickly after emission from the source in the CSD tube, and the penetrating power into the TPC is much less than is seen for Na-22, as is shown for calibration data in Figure 6.5.

It should be noted that the NR and ER bands shown in the subsequent analysis differ slightly from those used in chapter 5 due to the fact that the bands have been updated in the time since this earlier work was done. These updates include using the latest versions of BACCARAT and LZLAMA, as well as applying cuts to the DD simulation, before fitting the NR band, that allow the band to better represent the data, since statistics for the DD simulation are high enough to allow for this.

6.4 Neutron Background Simulation SS/MS Ratio

Simulations of the primary neutron producing processes occurring in materials found in different detector components were run for WS2024, as they were for WS2022 (discussed in section 4.5). The analysis cuts applied to this dataset are the ROI cut, strict FV cut, and the field cage resistor cut, along with an NR band selection (in $\log(\text{S2c})$ vs. S1c space for SS events, and in $\Delta\chi^2$ space for MS events).

As was motivated in section 6.2.4, there are three SS/MS ratios calculated for the neutron background simulation due to the different veto requirements on the MS events. These requirements are that they have no veto signal, that they do have a veto signal, and finally there was a selection of all events regardless of veto signal (veto agnostic). In all three cases the SS requirement is that there is no veto signal, as this is what is used in the WIMP search. The requirement of MS events with no veto signal is preferable, since this is the SS requirement and hence would minimise systematic uncertainties in the SS/MS ratio, but this leads to datasets with low statistics and

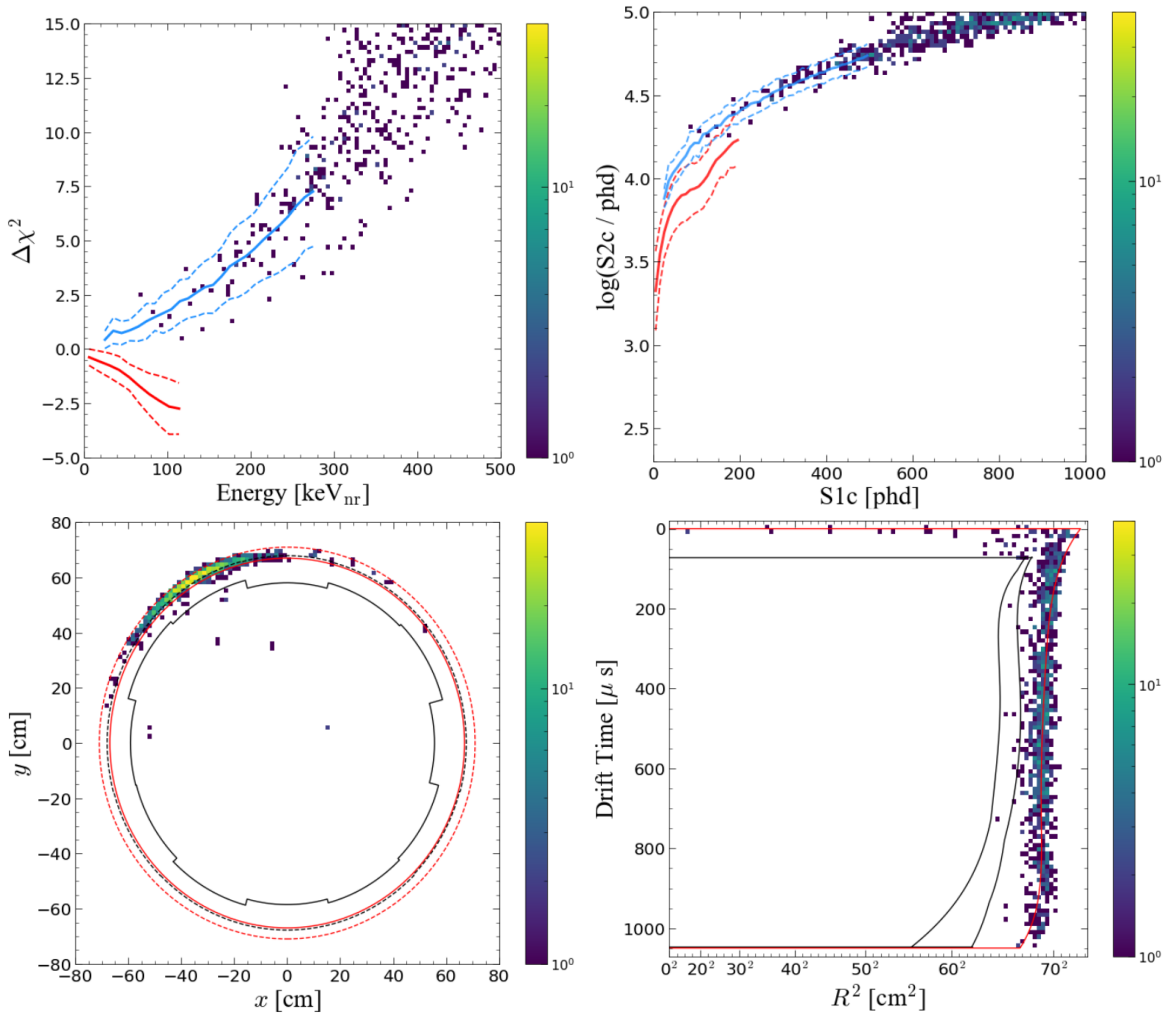


Figure 6.6: *WS2024 Th-228 simulated data, using CSD 2, shown across different parameter spaces, aiming to verify the ER band. This simulation includes data for the source at multiple different z positions in the CSD. Only an extended ROI cut is applied to this data, extending up to $S1c$ values of 1000 phd. Events in $\Delta\chi^2$ space are shown (top left) alongside the NR (red) and ER (blue) Gaussian 90-10 CL bands in this space, generated using DD and Na-22 simulations respectively. The distribution in $\log(S2c)$ vs. $S1c$ space is likewise shown (top right) alongside Gaussian 90-10 CL bands generated from the NR (red) and ER (blue) simulations. The xy distribution of all scatters of the events is shown (bottom left), where the red lines show the ϕ -averaged active volume edges at the top (dashed) and bottom (solid) of the active volume. Similarly, the black lines show the ϕ -varying FV edges at the top (dashed) and bottom (solid) of the FV. The distribution of all scatters of the events in drift time vs. R^2 is shown (bottom right), where the red line indicates the boundary of the active volume of the detector. The black lines show the minimum and maximum squared radii of the FV, as radius varies with ϕ , for each value of drift time.*

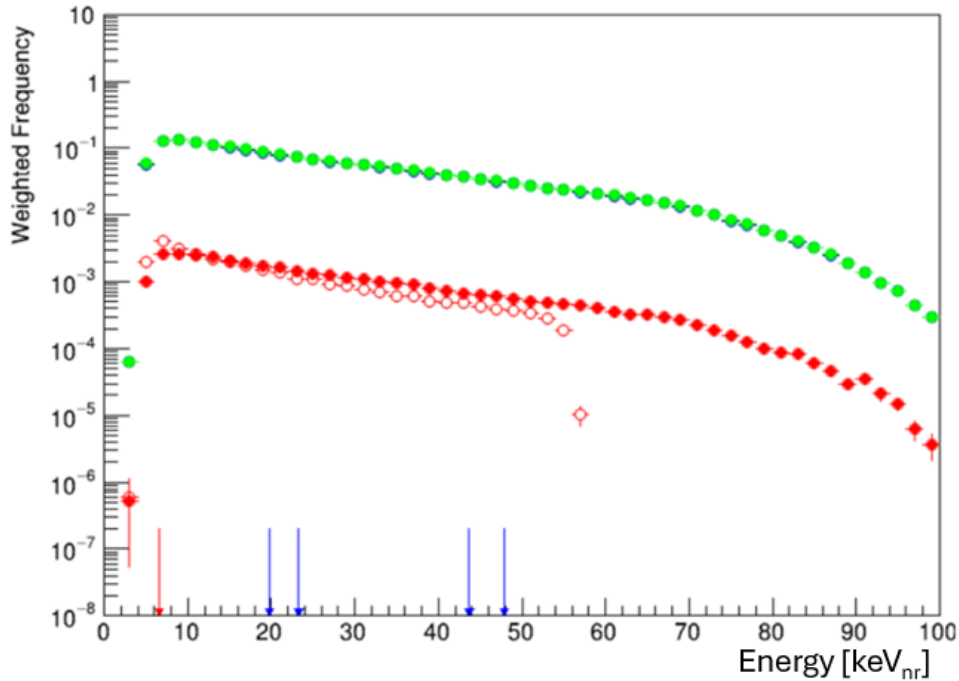


Figure 6.7: Weighted energy distributions of SS and MS events in the WS2024 neutron background simulation. The weighting is calculated as the product of the activity of the source simulated, the inverse of the number of events simulated for that source, and the number of WS2024 live days. Open circles indicate SS events and filled circles indicate MS events. The three different veto requirements included are requiring no veto signal (red), requiring a veto signal (blue), and veto agnostic (green). Also shown are arrows indicating the energies of the 5 MS neutron candidates discussed in section 6.6, with their colours corresponding to the aforementioned veto requirements. MS events have a looser ROI cut here than SS events for the reasons discussed in section 6.2.3.

therefore large relative statistical errors.

The energy distributions for these three MS selections and the SS selection are shown in Figure 6.7, where the post-fitting ROI cut for MS events is not yet applied. These distributions are weighted to account for the activity of the process simulated, the size of the simulation, and the number of live days for WS2024. As was the case for WS2022, note that the MS energy is the total fitted energy from the NR model of the $\Delta\chi^2$ analysis, but the SS energy is directly obtained from the measured S1c and S2c using Equation 3.5. The assumption of this equivalency will be investigated in section 6.5.

It can be seen in Figure 6.7 that the SS distribution cuts off before the expected SS DD endpoint of 74 keV_{nr}, and this is due to the ROI cut that is in use here, that enforces an earlier endpoint. Since the ROI cut is looser in log(S2c) vs. S1c space for MS events, and initially imposed before the $\Delta\chi^2$ analysis (and crucially before the energy fitting), the MS distributions tail off at higher energies, and do not see such a harsh cut-off due to the ROI. It can also be seen from the figure

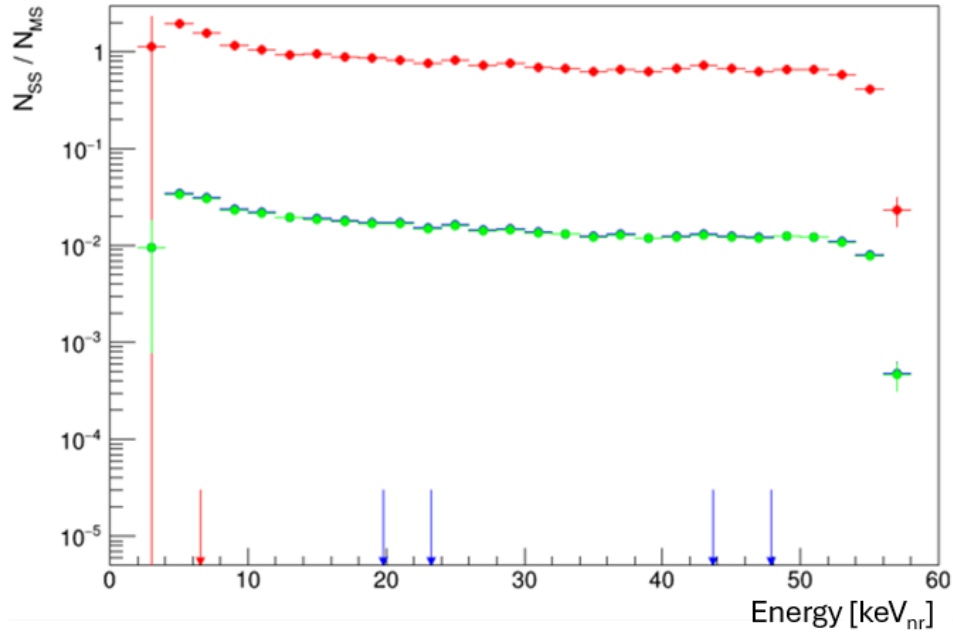


Figure 6.8: *SS/MS ratio as a function of energy, as calculated from the WS2024 neutron background simulation. The three different MS veto requirements included are requiring no veto signal (red), requiring a veto signal (blue), and veto agnostic (green). The SS veto requirement is the same in all cases and requires that there is no veto signal. Also shown are arrows indicating the energies of the 5 MS neutron candidates discussed in section 6.6, with their colours corresponding to the aforementioned veto requirements.*

(mostly for the ‘no veto’ selections) that the largest errors on the weighted frequency values are in the lowest energy bin, where statistics are lowest due to the minimum S1 and S2 requirements for an event to be within the ROI for both SS and MS events. This becomes more apparent for all selections when the SS/MS ratios are plotted in Figure 6.8.

It is also clearly illustrated by Figure 6.7 how different the number of events with the different MS veto selections are. Changing the MS requirement from no veto signal to requiring a veto signal, or being veto agnostic, increases the statistics by approximately two orders of magnitude. Because of this, the MS selection requiring a veto signal (blue) is very similar to the veto agnostic MS selection (green), that is the sum of the veto signal selection and the no veto signal selection (red). This means that the veto signal MS distribution is largely hidden behind the veto agnostic MS distribution in the figure.

From these distributions, the SS/MS ratios are calculated, giving three ratio distributions: the SS selection divided by each of the three MS selections. These ratios as a function of energy are shown in Figure 6.8. All of these distributions now have the same endpoint as the SS distribution. It can be seen from this figure that there is indeed a non-negligible energy dependence in the SS/MS ratio, which indicates that the use of the energy dependent calculation of Equation 3.2 is appropriate.

6.5 Correcting SS/MS Ratio Differences in Simulation and Data

For WS2024, the data and simulation SS/MS ratios are still not necessarily equivalent, so it was decided to keep the re-weighting factor, r_{DD} , in the SS neutron estimate, as is described by Equation 4.2. In the case where the SS/MS ratio does in fact perfectly match between data and simulation, then this factor would just be found to be 1.0 at all energies.

DD data and simulation are selected to define this re-weighting factor, as in WS2022, since DD data is seen to be the cleanest of the neutron calibration datasets, with the lowest amount of backgrounds. It is for this same reason that DD simulation and calibration data are primarily used for the respective creation and verification of the NR band in section 6.3. However, the effects of choosing different neutron sources for the reweighting factor will be further investigated. It is seen for AmLi, and especially AmBe, that the MS calibration data has a lot of events sitting in the region of $\Delta\chi^2$ space in which accidental coincidences would be expected. The additional background events in this space were shown in the plots of Figure 6.4. There are also more gammas produced from neutron sources such as AmLi and AmBe, due to the alpha absorption by the target producing a nuclide in an excited state. Many of these gamma photons can undergo multiple Compton scatters, so an elevated additional MS ER background is present. However, after calculation of the reweighting factor for a DD source in this section, the reweighting factor will also be studied for an AmLi source, and the results will be compared. It was decided that the background signals for the AmBe source are too numerous to warrant the calculation of a further reweighting factor, as can be seen by the relatively large number of events in the steep bands above the ER band and below the NR band in the bottom plot of Figure 6.4.

A comparison of the energy distributions of SS and MS events in DD data and simulation is shown in Figure 6.9, with the distributions normalised, in the left hand plots, such that the areas under the curves integrate to unity, since the simulation and calibration datasets do not contain the same number of events. These plots are also shown without the normalisation, on the right of the figure, and the difference in the number of events can be seen to not be too large. This figure shows that the ROI causes an SS cut-off at around 58 keV_{nr}, but this is less sharp in the MS distributions due to the energy fitting occurring after the looser ROI cut is applied.

These distributions are used to calculate the simulation and data SS/MS ratios that are shown in Figure 6.10, along with the ratio of these ratios (data / simulation), which is the definition of r_{DD} . As can be seen from the figure, r_{DD} has some dependence on energy up to the ROI-induced SS cut-off point, where r_{DD} also drops to zero, but overall this dependence is minimal, relative to errors. For WS2022, it was deemed that the r_{DD} distribution was sufficiently flat to be able to approximate it as energy independent. For r_{DD} in WS2024, looking at the shape of the distribution in Figure 6.10, it was decided that the variation is sufficiently small that r_{DD} can

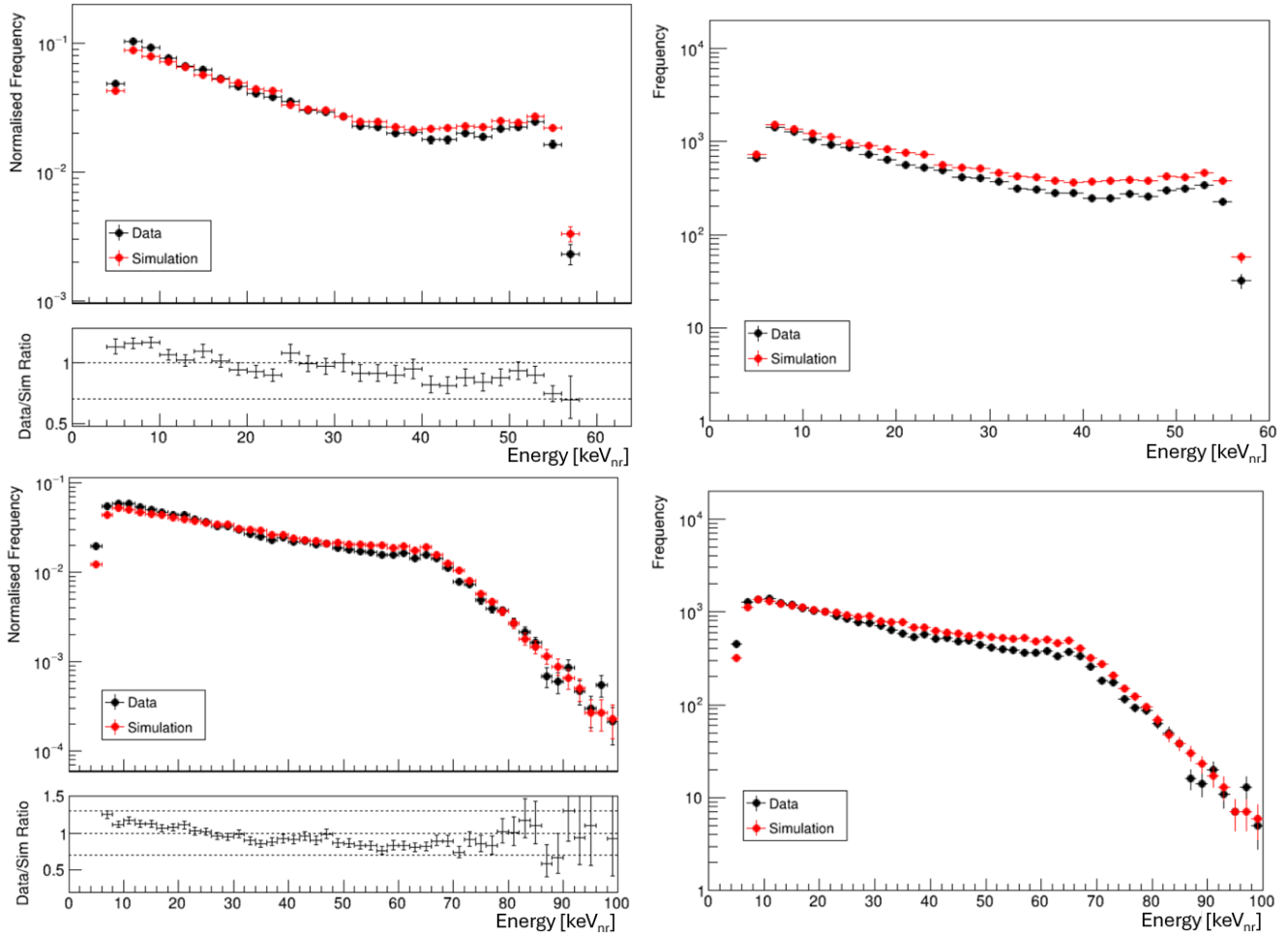


Figure 6.9: NR energy distributions of WS2024 DD SS and MS events for data and simulation after analysis cuts. Comparisons between data and simulation are shown for SS events (top) and MS events (bottom), both with normalisation (left) and without (right). Where normalisation is applied, this enforces that the distributions integrate to unity. In these normalised plots, the ratio of the distributions is also shown, with dashed lines at 1.25, 1.00, and 0.75 as a guide to the eye. Across all subplots, data is shown in black and simulation is in red.

again be considered constant. This gives a value for r_{DD} of 0.88 ± 0.01 for energies in the range (0-60) keV_{nr} . This average value is indicated on the figure by the blue dashed line. Note that the range of this single energy bin extends slightly beyond the SS cut-off.

It is also noteworthy that the left plot of Figure 6.10 shows that both DD calibration data and simulation show an energy dependent SS/MS ratio that decreases between around 6-35 keV_{nr} , then increases between around 35-55 keV_{nr} . This further justifies treating these quantities as energy dependent in this analysis. The reason for the shape of this distribution is currently unknown and could be a point for further investigation.

As previously mentioned in this section, DD calibration data and simulation are chosen for the

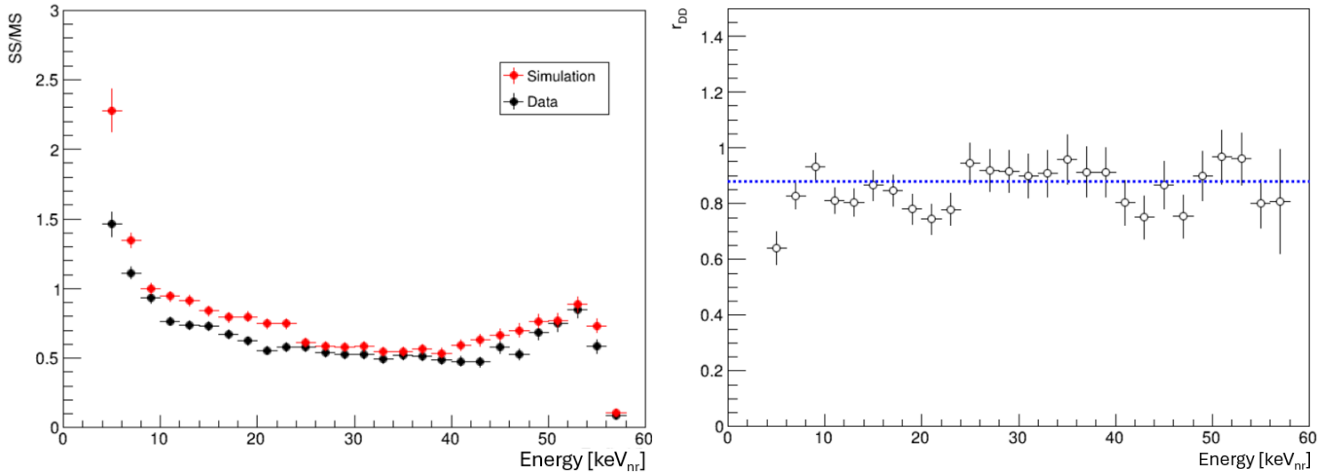


Figure 6.10: *WS2024 energy distributions of the SS/MS ratio for DD data and simulation (left) and r_{DD} (right) after analysis cuts. The SS/MS ratio plot follows the convention of Figure 6.9 where simulation is shown in red and DD calibration data is shown in black. On the r_{DD} plot, the average value across the bins is shown by the blue dashed line, and this value is 0.88 ± 0.01 .*

calculation of this re-weighting factor, largely because they provide the cleanest datasets. However, the re-weighting factor can also be calculated for an AmLi neutron source. Specifically, for the deployment of the AmLi source that was used for the simulation and calibration datasets here, a source was placed in all three CSDs and lowered to 700 mm. The same procedure as was followed above, for the calculation of r_{DD} , is used to calculate r_{AmLi} , and the equivalent plots to those shown in Figure 6.10 are shown in Figure 6.11. The constant value found for the AmLi-based reweighting factor is $r_{AmLi} = 0.80 \pm 0.03$. This value is comparable to r_{DD} , but the source of the $\sim 10\%$ discrepancy between these values would benefit from further study. It would also likely be worthwhile to investigate why, in both the DD and AmLi studies, the simulation predicts a higher SS/MS ratio in most energy bins than was seen for the calibration data.

6.5.1 SS Energy Definition Investigation

It has been mentioned previously in this analysis that when plotting the SS and MS energy distributions, the energy quoted for SS events is calculated using the NR Doke formula of Equation 3.5 for the measured S1c and S2c of the event, but for MS events the quoted energy is the sum of the NR model scatter energies after the χ^2_{NR} minimisation. These two definitions of energy are not necessarily the same, although that is ultimately what the $\Delta\chi^2$ method is aiming to achieve. The total energy cannot be directly calculated for MS events, since the individual S1c values of the scatters cannot be distinguished. However, the $\Delta\chi^2$ analysis can be run on any N scatter event, and this includes SS events where $N = 1$. However, this would not be expected to give significantly better ER NR discrimination than in $\log(\text{S2c})$ vs. S1c space, since no extra information is being

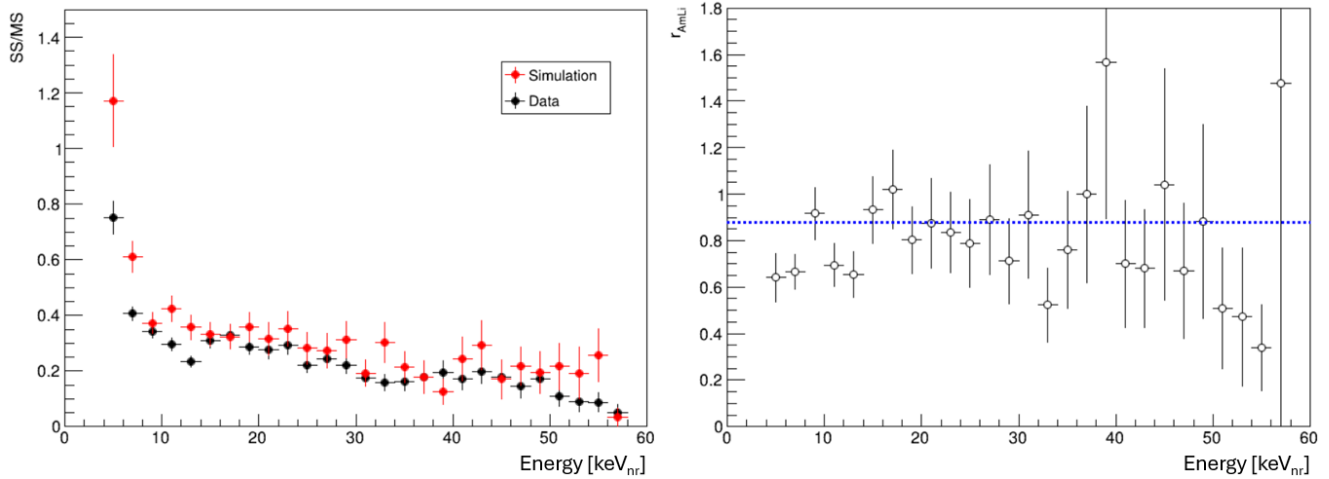


Figure 6.11: *WS2024 energy distributions of the SS/MS ratio for AmLi data and simulation (left) and r_{AmLi} (right) after analysis cuts. The SS/MS ratio plot follows the convention of Figure 6.9, where simulation is shown in red and AmLi calibration data is shown in black. On the r_{AmLi} plot, the average value across the bins is shown by the blue dashed line, and this value is 0.80 ± 0.03 .*

utilised. This is because all of the individual scatter information (about the one scatter) is already used in $\log(S2c)$ vs. $S1c$ space. Nevertheless, this can be used to obtain a post-fitting SS NR energy that is more comparable to the MS post-fitting total NR energy.

A comparison of the SS energy spectrum calculated simply by using the Doke formula given by Equation 3.5, and the energy spectrum found using the $\Delta\chi^2$ analysis is shown at the top of Figure 6.12. It can be noted that the upper energy boundary becomes more sharp with the energy fitting, but the lower boundary smears slightly due to the fact that the fitting allows energies to fluctuate below the minimum value imposed by the ROI. This figure shows the general trend of SS energies being slightly lower when the $\Delta\chi^2$ method is used in their calculation. The bottom plot of the figure shows the value of r_{DD} with the two energy definitions (blue for the Doke formula, pink for the energy fitting). It is seen that the average value of the reweighting factor does not change between the two cases, since the same SS DD events are used for both energy definitions, and hence the total number of events between 0-60 keV_{nr} is the same. Beyond this though, it can be seen from the figure that the shape of the r_{DD} distribution is broadly similar in the two cases, and therefore using the Doke formula simply based on the measured $S1c$ and $S2c$ values for an SS event is a suitable approximation for the fitted energy. This energy definition also significantly saves on computing time because the $\Delta\chi^2$ analysis does not need to be run for SS events as well as for MS events.

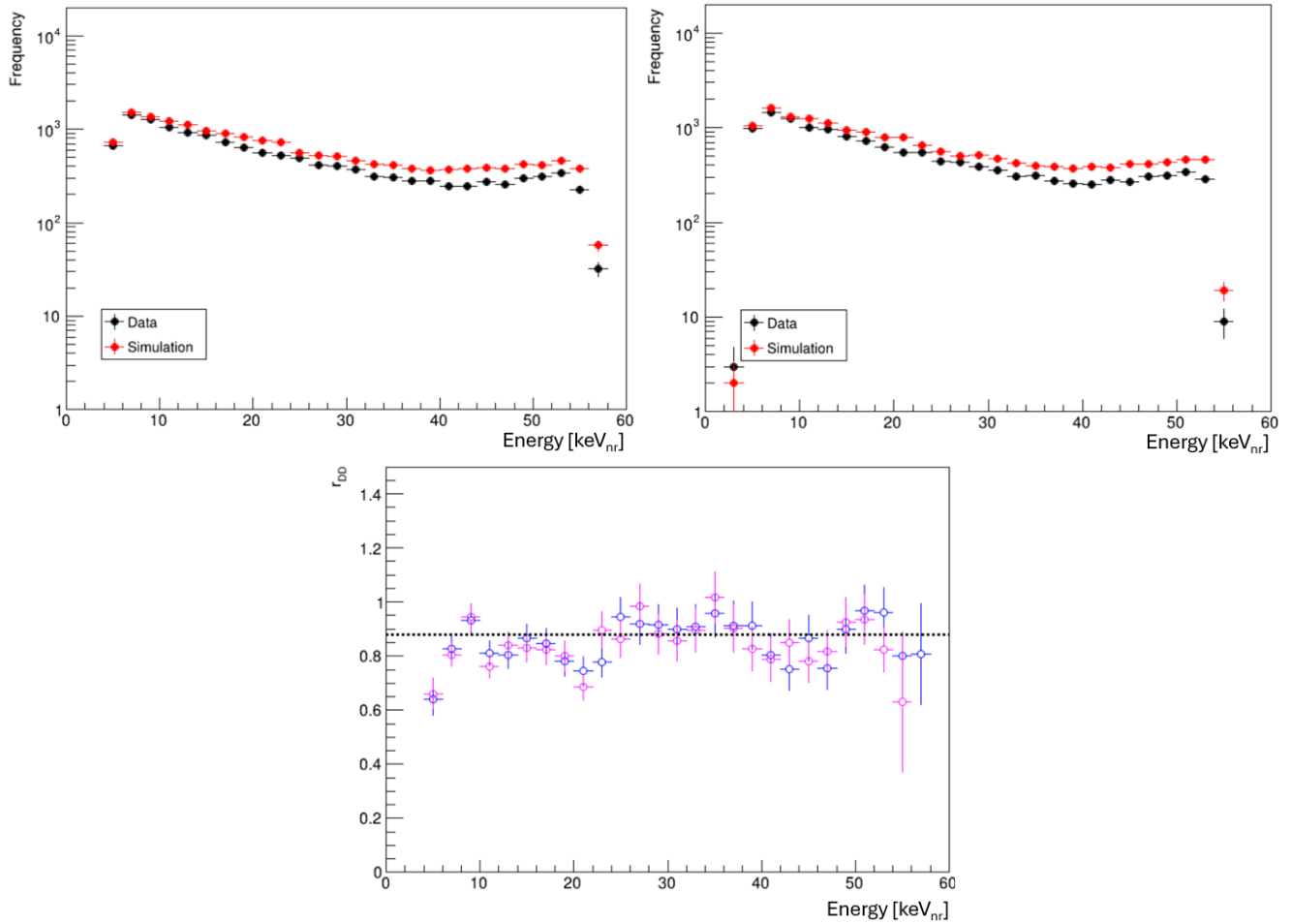


Figure 6.12: Energy distributions of WS2024 DD SS events (top), for data and simulation after analysis cuts, comparing the $\Delta\chi^2$ fitted energy definition (right) and the non-fitted energy definition (left). This is then propagated to the calculation of r_{DD} (bottom), with the fitted and non fitted distributions in pink and blue respectively. The top plots follow the convention where simulation is shown in red and calibration data is shown in black. The black dashed line in the bottom plot indicates the average value across the bins, which is the same regardless of the choice of energy definition, and this value is 0.88 ± 0.01 .

6.6 Multiple Scatter Neutron Candidates in Data

For the selection of MS neutron candidates from WIMP search data, all MS events passing all analysis cuts (with the exception of the post-fitting $\Delta\chi^2$ space MS ROI cut, which is necessarily applied later) are processed using the $\Delta\chi^2$ analysis method to establish their positions in $\Delta\chi^2$ space. Figure 6.13 shows these events in both $\Delta\chi^2$ space (top left) and $\log(S2c)$ vs. $S1c$ space (top right), as well as the spatial locations of all of their scatters in the detector in both the xy plane (bottom left) and drift time vs. R^2 space (bottom right). This figure shows these events relative to the simulated NR and ER Gaussian 90-10 CL bands (discussed in section 6.3) in the

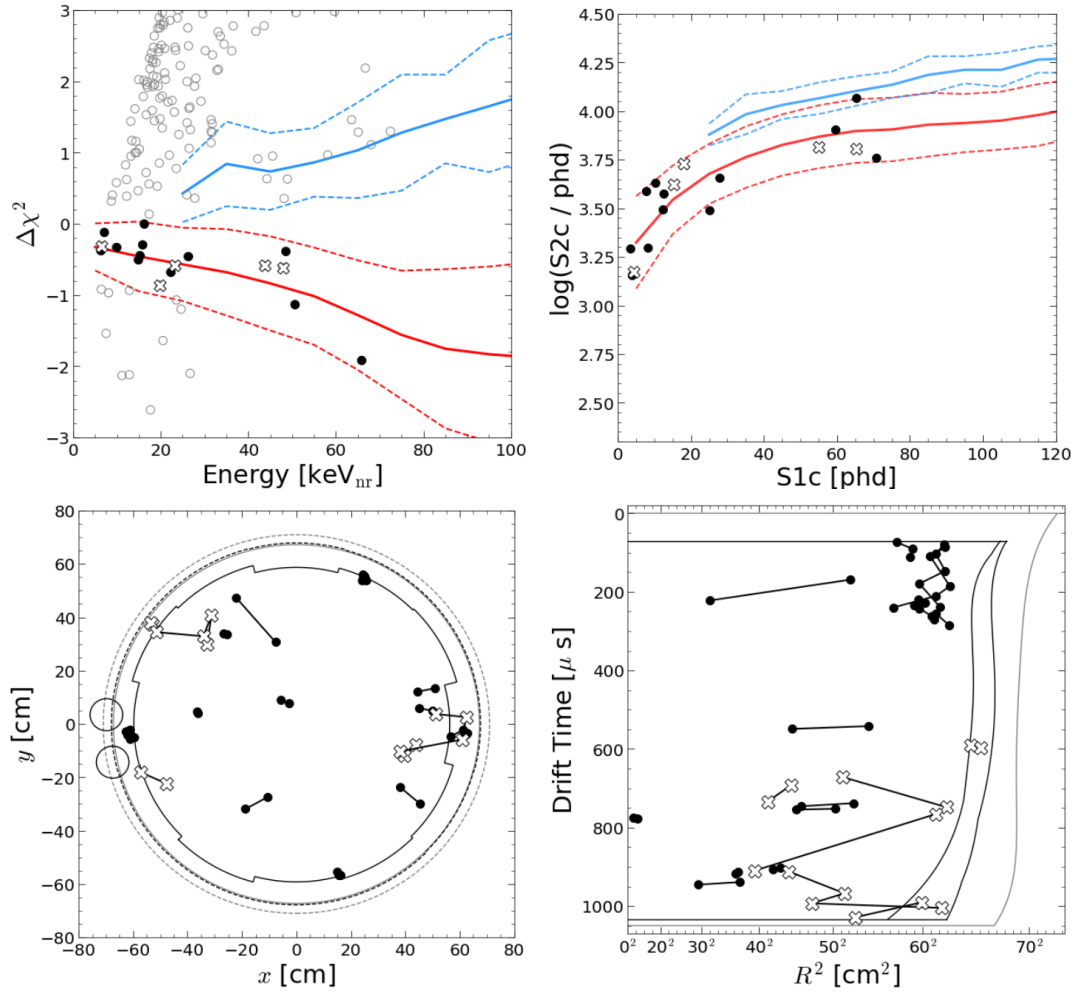


Figure 6.13: The 17 MS NR candidates selected from the WS2024 dataset. Events with no waveform issues are marked by a white cross. The distribution of the events in $\Delta\chi^2$ space is shown (top left) alongside the NR (red) and ER (blue) Gaussian 90-10 CL bands in this space, generated using DD and Na-22 simulations respectively. All events not selected by the NR band selection in this space are shown in grey. The distribution in $\log(S2c)$ vs. $S1c$ space is shown (top right) alongside Gaussian 90-10 CL bands generated from the aforementioned NR (red) and ER (blue) simulations. The xy distribution of all scatters is shown (bottom left), where the grey lines show the ϕ -averaged active volume edges at the top (dashed) and bottom (solid) of the active volume. Similarly, the black lines show the ϕ -varying FV edges at the top (dashed) and bottom (solid) of the FV. The smaller circular regions at the 9 o'clock position indicate areas where events are removed by the field cage resistor cut. The distribution of all scatters in drift time vs. R^2 is shown (bottom right), where the grey line indicates the boundary of the active volume of the detector. The black lines show the minimum and maximum squared radii of the FV, as radius varies with ϕ , for each value of drift time. Connecting lines between scatters in these plots are arbitrary.

former two of the four parameter spaces, and relative to the boundaries of the FV and active volume in the latter two parameter spaces. From the $\Delta\chi^2$ parameter space, all events sitting in the NR band are selected as potential MS neutron candidates, of which there are 17. In lieu of MS accidental coincidence cuts, the waveforms of these events are individually looked at to remove any problematic events. A list of these 17 events and their reasons for being removed from the dataset (if indeed they are) is shown in Table 6.2.

Run	Event	Good Event?	Reason
12266	115592	No	Potential alpha
12437	36545	No	Potential alpha
12550	2421	Yes	No issues
13644	41065	No	Potential alpha
13827	296682	No	Abnormal S2 shape
13994	185870	No	Gate photoionisation
14087	136917	Yes	No issues
14132	207834	No	Double S1, significant negative area
14185	173875	No	Split S2
14304	226487	Yes	No issues
14540	56532	No	S1 in etrain
14812	251461	Yes	No issues
14857	216929	No	Potential alpha
14857	92364	No	Potential split S2 or pile-up
15035	265510	No	Accidental coincidence, potential grid emission
15394	264947	No	Double S1 peak, S2s are just noise
15746	95751	Yes	No issues

Table 6.2: *WS2024 MS events in the NR band, and whether analysis of their waveform leads to their selection as a neutron candidate.*

The issues listed in Table 6.2 that warrant the removal of events from the list of MS NR candidates are exactly the type of issues that MS-specific data quality and accidental coincidence cuts would aim to target. The issues mentioned in this table will now be looked at in more detail to provide an insight as to why events are excluded from the analysis.

Gate Photoionisation

When electrons pass from the liquid phase to the gas phase of the detector, in which they undergo electroluminescence and produce S2 light, some of this light can interact with the gate grid that is just below the surface of the liquid. This can cause ionisation, releasing further electrons that

are also extracted into the electroluminescence region, and hence also produce an S2 signal. This phenomenon is referred to as gate photoionisation, and has a very distinctive waveform topology of a normal S2 pulse followed by a long, relatively flat pulse, as is shown in Figure 6.14. If this second pulse is also identified as an S2 by LZAP, then this type of event will most likely be classed as MS. This is a type of event that would be a good target for future MS-specific data quality cuts.



Figure 6.14: An example of the S2 pulses from a gate photoionisation event, where S2 light causes the emission of electrons from the gate grid.

Potential Alpha Particles

Alpha decays can be produced in the detector by sources that are attached to surfaces, such as the PTFE lining the TPC walls. The two main examples of this were previously discussed in section 2.11.4, specifically alpha particles from U-238 and Th-232 decays. In that previous section, they were presented in the context of the alpha particles subsequently interacting with other materials to produce neutrons. The decay chains from these sources can also produce radon, which will emanate away from the surfaces to which the sources are attached, and mix with the liquid xenon in the TPC. This, in itself, becomes another source of alpha radiation. Alpha decays from the radon are said to occur ‘freely’, and tend to produce a clear S1 signal, whereas those from sources attached to surfaces only produce a clear S1 signal approximately half of the time, due to the fact that the alpha particle will often deposit its energy in the material to which the source is attached. Electrons could still be liberated and produce an S2 signal, however. The MS NR candidate events marked as potential alphas have no visible S1 signal before a large, S2-like, ‘other’ pulse, and hence could be alpha events where the S1 is lost. Alternatively, if an event occurs very close to the liquid surface, the S1 could just be engulfed by the S2.

The topology of these events, of one large ‘other’ pulse followed by a comparatively flat S2, is shown in Figure 6.15. The flat top of the ‘other’ pulse suggests saturation of the PMTs, and this is likely why the shape of this pulse is sufficiently different from an S2 pulse that LZAP is not able

to recognise it as an S2, therefore classifying it as ‘other’. The relatively flat S2 following this large pulse looks to be characteristic of gate photoionisation, as was discussed previously. This could be another factor that contributes to the occurrence of this event topology.

Regardless of the specific physics causing this topology, these are not events that are suitable MS neutron candidates, and therefore are removed from the dataset. The distinctive features of this type of event make it another good target of a future MS-specific analysis cut.

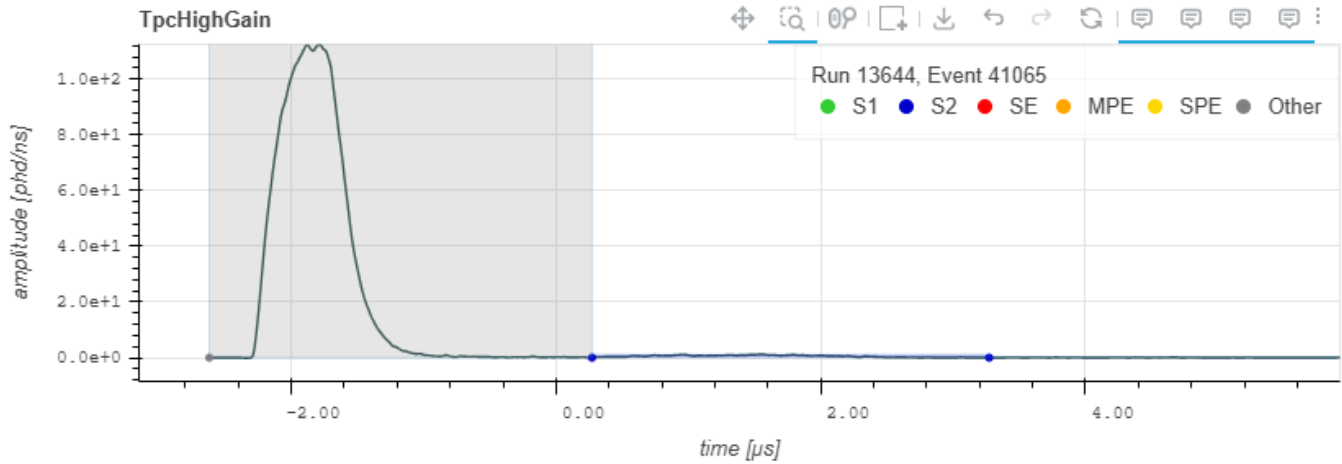


Figure 6.15: *An example of a potential alpha event, where the S1 is lost. This also looks to display saturation for the large S2-like ‘other’ pulse, and some gate photoionisation. This waveform has been zoomed in to better display the ‘other’ pulse and the flat ‘S2’ pulse.*

Negative Areas

A true physical process would not give a PMT signal with an amplitude less than zero at any point, since detection of photons would lead to the production of an electrical signal of a given positive amplitude. If no photons are being detected at a given time, no voltage is produced by the PMT, and hence the amplitude reads zero. This means that if the amplitude drops below zero, then this is an indication of electronic noise, rather than a true signal, and this will cause some of the waveform pulse area to be negative. Events with significant negative area contain notable electronic noise, and so often are not useful for analysis.

For the WS2024 WIMP search, there is a negative area cut applied to the SS dataset to remove events with a high fraction of negative pulse area, but no such cut is applied to the MS dataset. A version specifically tuned for MS events would be beneficial to develop in the future.

Split S2s

Event 14185 173875 is an example of a split S2 pulse. This occurs when a single S2 pulse, or two S2 pulses occurring too close in time to be resolved from each other, is identified by LZAP as two S2s. The S2 for event 14185 173875 is shown in Figure 6.16 as an example. Regardless of the cause, events like these are not clear MS events with resolvable, clearly defined S2 areas, and so are not included as MS NR candidates. Again, future MS data quality cuts could be developed and tuned to target this type of event, to avoid having to remove them by hand.

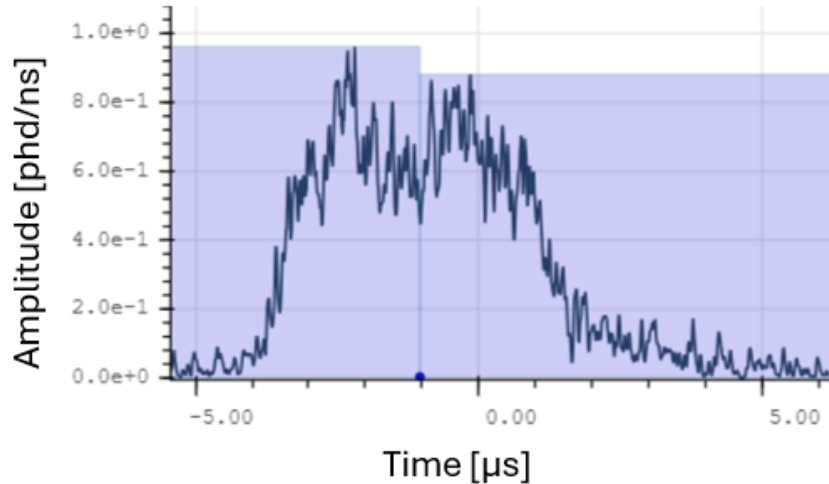


Figure 6.16: *An example of a split S2 pulse, where LZAP has identified two S2 pulses, where by eye it can be seen that two pulses cannot be clearly resolved.*

S1s in E-trains

The phenomenon of e-trains and ph-trains was introduced in section 4.2.6. The e-train cut was developed to remove periods of live time following a large S2, when there are a lot of additional SEs and SPEs.

Despite application of this cut, evidence of e-trains is still seen in the data, albeit to a less concerning extent than in the events removed by the cut. This means that some pulses can be lost in very noisy waveforms, and the event cannot be used for analysis.

MS Accidental Coincidence Events

Accidental coincidence events were discussed in section 2.11.2, and subsequently throughout this thesis, as one of the main backgrounds that must be considered for MS neutron identification. As previously considered, there are numerous potential ways in which an MS accidental coincidence event could be created. In the case of event 15035 265510, this appears to be an accidental coincidence between a lone S1 and a feature that has been identified by LZAP as multiple S2s.

The waveform for this event is shown in Figure 6.17. When this waveform is investigated, it is noted that the the alleged S2s looked more like a short period of noise, potentially due to electron emission from the grids. Therefore, it was decided that this event was not a viable MS NR candidate.

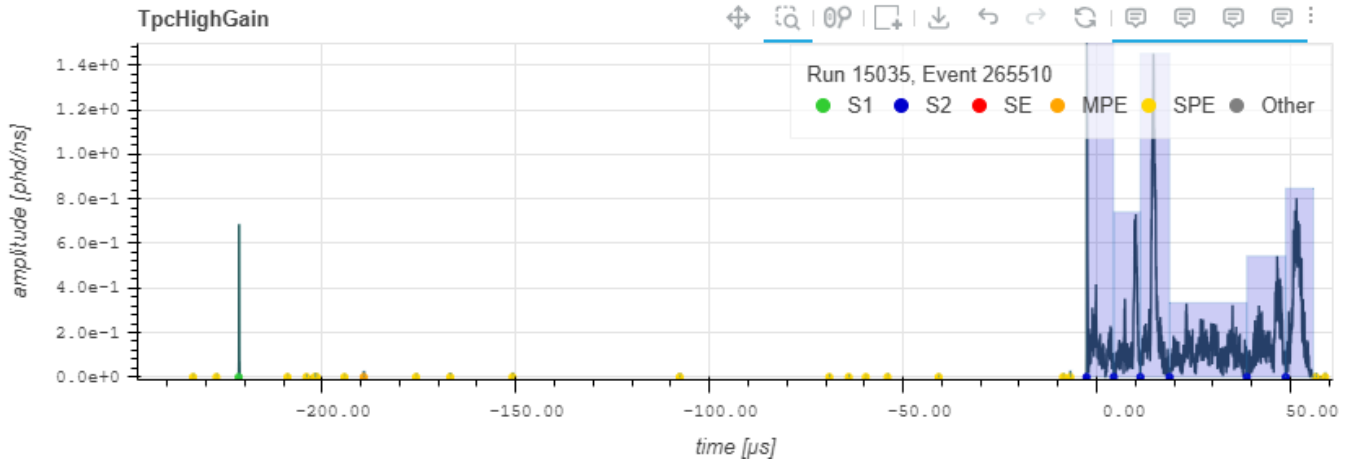


Figure 6.17: *The waveform of a suspected MS accidental coincidence event, 15035 265510.*

After the analysis of the waveforms of all NR band events presented in Table 6.2, the 5 highlighted events in the table are selected as MS neutron candidates. These events are marked on Figure 6.13 by the use of a white cross. Of these events, only one (14304 226487) does not have a prompt or delayed veto signal in either the OD or Skin veto detectors. No events have an energy higher than the SS cut-off, so none are removed from the selection in accordance with the post-fitting $\Delta\chi^2$ space MS ROI cut. This essentially would have imposed a cut on MS data events such that the maximum energy enforced by the ROI on SS events was equal to the maximum energy of MS events.

6.7 WS2024 $\Delta\chi^2$ SS Neutron Estimate

Using the total fitted NR energies of each of these events, the constant WS2024 value of r_{DD} , and the energy dependent SS/MS ratio (from Figure 6.8), the SS neutron estimate is calculated. Summing Equation 4.2 over the selected MS candidate events gives the SS neutron estimate in the NR band. Since the NR band is expected to contain $(70 \pm 10)\%$ of neutrons, the number of SS neutrons in the WIMP search ROI is able to be calculated.

The results for the three estimates are shown in Table 6.3. It should be noted that there are three sources of statistical error that contribute to the final SS NR band estimate, propagated according to Equation 4.2. The first is the error on the value of r_{DD} used, the second is the error on the value of the SS/MS ratio used, and the final source is the error on the number of MS data

events identified. The first two errors came from simulation and high statistics calibration data, and so the Poisson errors on these values are relatively low. Since the numbers of MS neutrons with the different veto requirements identified in WS2024 data are small, it is the Poisson error on these values that dominates the final error calculation.

	MS NR	SS NR Band	SS WS
No Veto Signal	1 ± 1	1.0 ± 1.0	1.0 ± 1.0
Veto Signal	4 ± 2	0.05 ± 0.03	0.07 ± 0.04
Veto Agnostic	5 ± 2	0.08 ± 0.04	0.11 ± 0.06

Table 6.3: *WS2024 $\Delta\chi^2$ SS neutron estimate results. Errors quoted are 1σ using Poisson statistics.*

Evidently, it is clear that the result produced using the MS requirement of no veto signal reveals very little information due to the very high error, driven by the sample of only one MS data event. The other two results are more useful, and it can be seen that they are just in agreement with the LZ WS2024 MS-driven SS neutron estimate that used an FV extending to 0 cm from the ideal wall, as was discussed in chapter 5. The estimates discussed in that chapter followed a slightly different method to that which was presented here, and aspects of the analysis have been refined since that work was completed. The more crucial comparison for the results found in this section is to the number of WIMP-like events found by LZ during WS2024, which was 0. The estimates calculated here are in agreement with this result, in that they predict no WIMP-like neutron events in the dataset. This all suggests that these results are accurate, and the use of this method could remove the need to explicitly apply veto efficiencies to the result, as was done for the LZ WS2024 estimate, which eliminates an additional source of systematic error.

6.8 Choice of Neutron Interaction Cross-Section Library

As was the case in WS2022, and was discussed in section 4.9, an additional systematic uncertainty that could impact the SS/MS ratios obtained from the neutron background simulation, and therefore affect the final estimates, is the choice of neutron interaction cross-section library used in the BACCARAT simulations.

Once again, it is deemed impractical, and too computationally expensive, to re-run the entire neutron background simulation with an alternative cross-section library to gauge the impact on the result, and so only the simulation that contributes the largest number of neutrons, after cuts, is selected. For WS2024, this is Th-232 (α -n) interactions in the PTFE of the bottom TPC PMT bodies (as found by A. Usón). The default library used for the simulations is still G4NDL-4.5, and the alternative library looked at is again JEFF-3.3. Future work could look at a larger range of different cross-section libraries to establish whether the differences between G4NDL-4.5 and

JEFF-3.3 are typical of different libraries, but extensive studies of this are not considered here, as the aim is just to gauge the scale of the impact of changing libraries on the final estimate.

66 000 events are simulated with the JEFF-3.3 cross-section library and 100 000 events are simulated with the G4NDL-4.5 library (running the fast chain simulation with the non-default JEFF-3.3 library encounters some issues that make generating high statistics more difficult), at the BACCARAT energy-only stage of the simulation. There is a reduction of approximately 2% of events in the LZLAMA simulation compared to the BACCARAT simulation input, as BACCARAT does not save out any event that does not have an interaction in any of the three detectors of LZ, and LZLAMA does not record any event that produces a signal that would be too small to be detected. Since this particular simulation is seen to be the greatest contributor to the WS2024 neutron background, and most neutron background simulations have the same input number of events, this percentage reduction is small relative to that seen by the neutron background simulation as a whole. It is also important to bear in mind that the number of simulated events is split across the SS, MS, and ‘other’ classifications, and hence statistics in each of these sub-datasets is lower.

Cuts are applied to the two simulations with the different cross-section libraries, as consistent as possible with those applied to the neutron background simulation in the main analysis. Specifically, this includes an ROI cut, as described in section 6.2.3, an $\log(S2c)$ vs. $S1c$ space NR band cut on the SS data, and a $\Delta\chi^2$ space NR band cut on the MS data. No FV or field cage resistor cuts are applied to these datasets in order to increase the statistics, to be able to reach a more meaningful result.

Changing the neutron interaction cross-section library in the simulation will impact SS events as well as MS events, but it is the overall impact on the SS/MS ratio, which is used in the SS neutron estimate, that is the primary concern, as it is larger differences in this value that will lead to an increased systematic uncertainty on the final estimate. Nevertheless, it is interesting to observe the impact of changing the cross-section library on the SS and MS distributions individually. Due to the different numbers of events in the simulations with the different cross-section libraries though, these comparison plots are normalised to integrate to unity, so that the shapes of the distributions can be compared. Figure 6.18 shows the normalised distribution of the NR energy of the SS events in the Th-232 (α -n) PTFE bottom TPC PMT bodies simulation. This is shown with both the G4NDL-4.5 and JEFF-3.3 interaction cross-section libraries. In the primary analysis, there was a requirement on the SS data that there was no veto signal, as would be the case for a WIMP. However, for this simulation, imposing this requirement on the SS data reduces the number of events to essentially zero. For this reason, and since only the fractional difference in the SS/MS ratio is required for this study, the SS selection here is veto agnostic.

Similarly, the individual energy distributions with the different cross-section libraries can be compared for MS events, and this is shown in Figure 6.19. As is the case for the SS events, in order

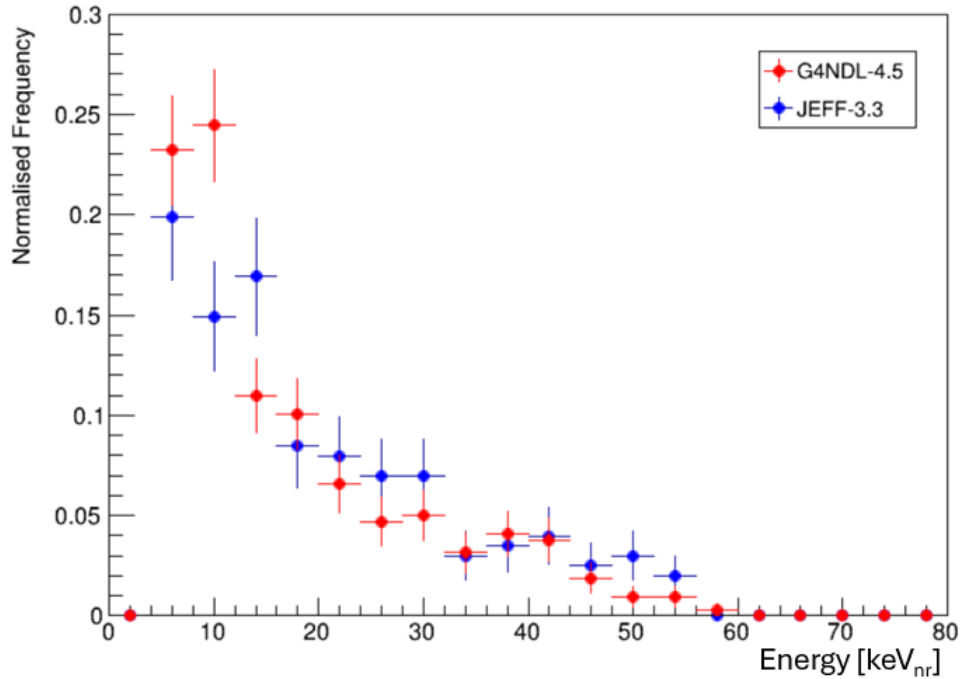


Figure 6.18: The NR energy distribution of simulated Th-232 (α -n) PTFE bottom TPC PMT bodies SS neutron events with the G4NDL-4.5 (red) and JEFF-3.3 (blue) interaction cross-section libraries. An ROI cut and an SS NR band selection are made in $\log(S2c)$ vs. $S1c$ space. No veto cuts are applied. The distributions are normalised such that the area under the curves are equal to 1.

to have a meaningful number of events in the study, the MS selection is made veto agnostic. In both of the SS and MS plots, some differences are visible between the two library choices, but the discrepancies are largely within the statistical error bars shown in the figures. The most notable departure from this is the single bin peak for the JEFF-3.3 distribution, around 10 keV_{nr} in Figure 6.19, that is not seen in the G4NDL-4.5 distribution. The differences in the two libraries causing this feature are not currently known.

The SS/MS ratios for the two libraries are found as functions of energy, and this is shown in Figure 6.20. As can be seen from the figure, the two distributions with the different cross-section libraries are not identical, and indeed they would not be expected to be, but look to be relatively similar, with the counts in most bins agreeing within the statistical errors.

The next and final step in this study is to evaluate the impact of this change in the SS/MS ratio distribution on the final SS neutron estimate. To do this, Equation 4.2 is once more used, but under the assumption that the constant value of r_{DD} and the 5 MS neutron candidates found in the WS2024 dataset remain unchanged from the main analysis. The only difference is the replacement of the energy dependent SS/MS ratio obtained from the neutron background simulation with the ratio from each of the simulations in this study. Table 6.4 shows the SS neutron estimates with the G4NDL-4.5 and JEFF-3.3 neutron interaction cross-section libraries, along with the fractional

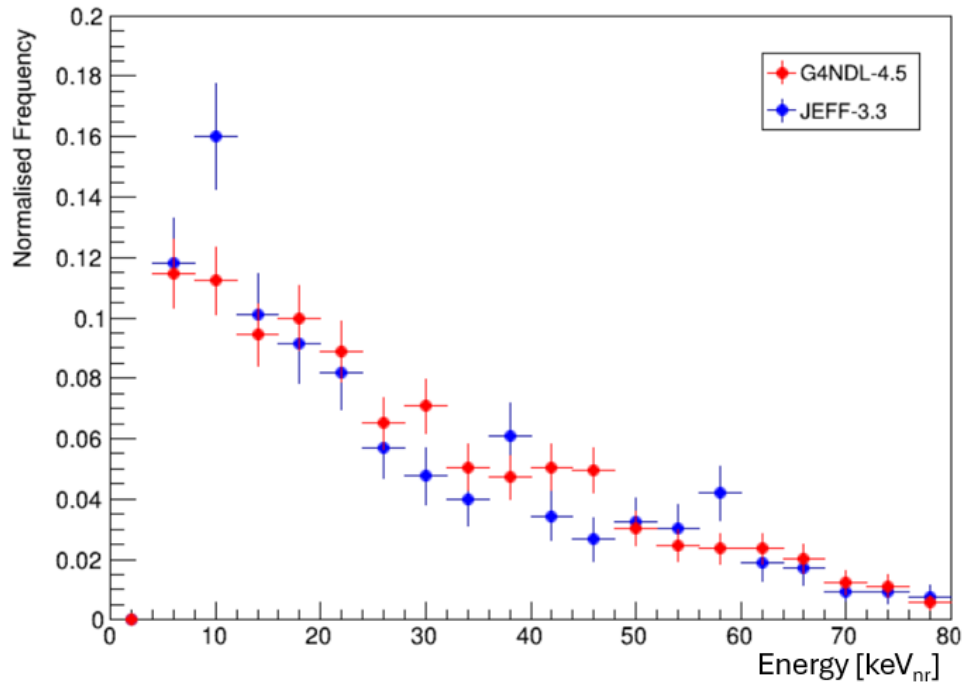


Figure 6.19: The NR energy distribution of simulated *Th-232* (α -*n*) PTFE bottom TPC PMT bodies MS neutron events with the G4NDL-4.5 (red) and JEFF-3.3 (blue) interaction cross-section libraries. These events have an extended ROI ($3 < \text{total } S1c < 100 \text{ phd}$, $S2 > 645.25 \text{ phd}$, $\log(\text{total } S2c) < 5.0$) cut and a $\Delta\chi^2$ space NR band section applied. No veto cuts are applied. The distributions are normalised such that the area under the curves are equal to 1.

error introduced by changing the library, and therefore, the systematic error on the $\Delta\chi^2$ WS2024 SS neutron estimate, along with the statistical error for comparison. Finally, the statistical and systematic errors are added in quadrature to give the final WS2024 result with the total error.

	Veto Agnostic (SS and MS)
G4NDL-4.5	1.5 ± 0.2
JEFF-3.3	2.2 ± 0.4
Fractional Error ((JEFF-G4NDL)/G4NDL)	0.5 ± 0.3
WS2024 Result (Stat. Error)	0.11 ± 0.06
WS2024 Result (Syst. Error)	$0.11 \pm (0.06 \pm 0.04)$
WS2024 Result (Total Error)	$0.11 \pm (0.08 \pm 0.04)$

Table 6.4: Results of the WS2024 neutron simulation cross-section library study.

This result is dependent on the energies of the MS candidate events found in the data, as only the SS/MS ratios in those energy bins are used in the calculation of the result. This means

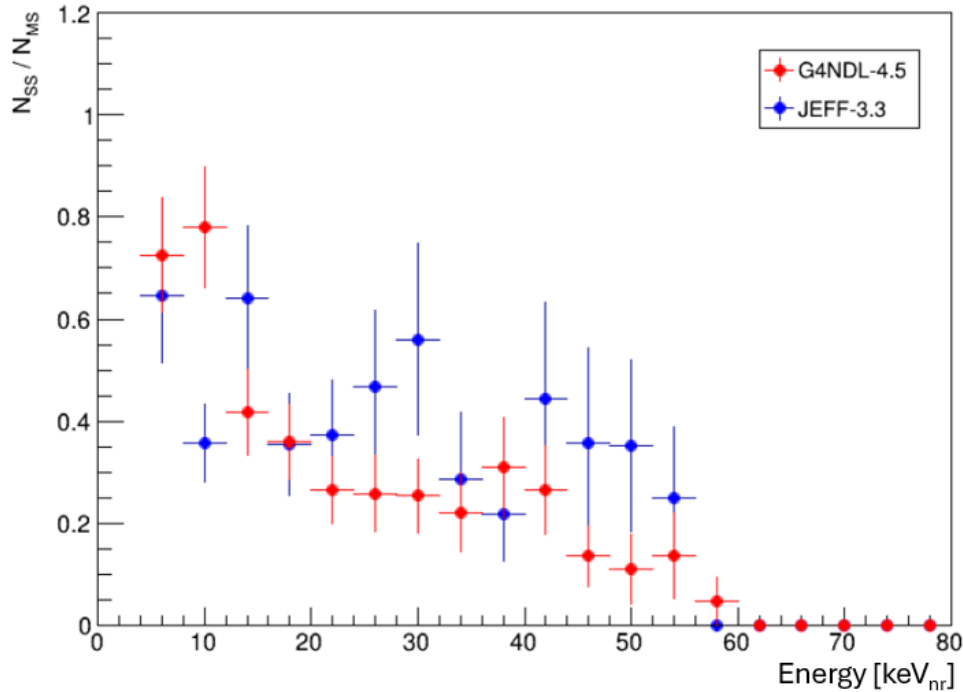


Figure 6.20: *The NR energy dependent distribution of the SS/MS ratio of simulated Th-232 (α -n) PTFE bottom TPC PMT bodies neutron events with the G4NDL-4.5 (red) and JEFF-3.3 (blue) interaction cross-section libraries.*

that larger differences between the two libraries in the distributions shown in Figure 6.20 could dominate, despite other bins being in better agreement, if MS candidates happen to sit at those energy values. Alternatively, larger differences may not be considered at all if no events lie in the bin where they occur. Using the 5 WS2024 MS events however, the fractional difference in the estimates using the two different libraries is found to be 0.5 ± 0.3 . This leads to a systematic error of the same order of magnitude as the statistical error, but when added in quadrature the overall veto agnostic estimate error is unaffected, within errors. For WS2022, the fractional difference was found to be 0.112, which is notably lower than the WS2024 result. However, it is important to consider that the simulations chosen for this study in WS2022 and WS2024 are not the same, and are Th-232 (α -n) in the ceramic of the forward field resistors and Th-232 (α -n) in the PTFE of the bottom TPC PMT bodies respectively. These findings suggest that the systematic error introduced by changing the neutron interaction cross-section library may be simulation-dependent to an extent, likely because of the different interactions occurring in different simulations. For future work, although computationally expensive, it could be worth investigating the effect of changing the cross-section library on the entire neutron background simulation, rather than just for a subset that is hoped to be representative, in order to fully understand the effect that this may have on the SS neutron estimate.

6.9 Further $\Delta\chi^2$ Method Optimisation Studies

The justification behind the introduction of the S1 S2 anti-correlations into the $\Delta\chi^2$ analysis was to make the method more robust and justifiable, and to potentially further improve discrimination. As was discussed in section 2.12.1, the χ^2 distribution depends on the number of degrees of freedom, k . The number of degrees of freedom is defined as the number of variables in the fit, minus the number of free parameters. In the case of the $\Delta\chi^2$ analysis, there are $N + 1$ (recall N is the number of scatters in an event) variables in each of the NR and ER χ^2 fits, namely the total S1c and the N S2cs. The free parameters in these fits are the N scatter energies. Therefore, the number of degrees of freedom in the ER and NR χ^2 tests is always $N + 1 - N = 1$, regardless of the number of scatters in the event. This means that a sample of true NRs, modelled and fitted as NRs, should theoretically follow a $k = 1$ χ^2 distribution, and likewise for true ER events under the ER hypothesis.

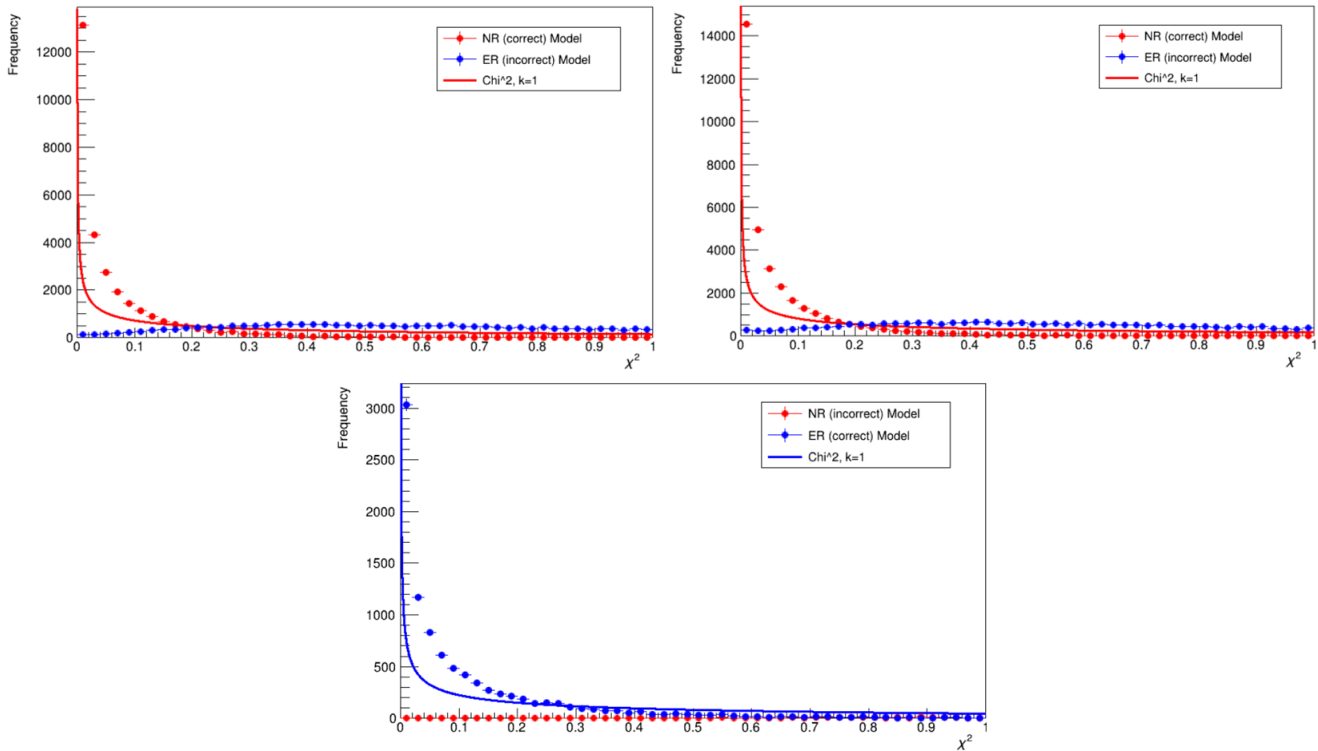


Figure 6.21: The MS χ^2 distributions from both the NR (red) and ER (blue) models of the $\Delta\chi^2$ method, compared to the theoretical $k = 1$ χ^2 distribution (red for NR data or simulation, blue for ER simulation). This is shown for DD data (top left), DD simulation (top right), and Na-22 simulation (bottom). The DD simulation has a strict FV cut, a field cage resistor cut, and the MS ROI described in section 6.2.3 applied, and the DD data has these cuts along with some DD specific data quality cuts applied. The Na-22 simulation has an extended ROI up to S1c < 500 phd applied and no further cuts.

However, it is seen that for MS DD data and simulation under the NR hypothesis, and for Na-22 simulation under the ER hypothesis (Na-22 calibration data has very low statistics at low energies, as discussed in section 6.3, so is not studied here), that this is not completely the case, as is illustrated in Figure 6.21. There are some deviations from the theoretical expected trend shown in this figure. Namely, in the plots at the top of the figure that show DD data and simulation, it was expected that the NR model χ^2 values should follow the $k = 1$ χ^2 distribution. It can be seen that, while the NR distribution does have broadly the correct shape, it does not exactly track the theoretical values. There is good agreement between the distributions for data and simulation though. The same can be seen for the ER model for the Na-22 simulation at the bottom of the figure. Both the NR and ER models look to perform comparably, and the two cases both see the model χ^2 distribution drop below the theoretical distribution at around a χ^2 value of 0.2.

The performance of the incorrect model for the data is also shown in the figure (ER for DD and NR for Na-22), and it can be seen that the shape is not at all consistent with the $k = 1$ theoretical distribution in any of the cases. This is what would be expected. Note that the χ^2 range of the Na-22 plot at the bottom of the figure is matched to the range for the DD plots at the top, and NR model counts for the Na-22 simulation only start to rise significantly above zero at higher χ^2 values, hence counts in this plot appear to all be zero. Overall, it is good that the distributions of the appropriate models have the correct form for a $k = 1$ distribution, as it was shown in Figure 2.18 in section 2.12.1 that a different number of degrees of freedom completely changes the shape of the curve. This suggests that the number of degrees of freedom in the $\Delta\chi^2$ method is well understood. Matching the gradient of the slope is a matter of tuning the uncertainties in the model. Figure 6.21 therefore suggests that there is potential for additional optimisation of the $\Delta\chi^2$ method that could perhaps further improve the discrimination power for NR and ER MS events.

To take the simplest case for this study, with the lowest possible number of variables, only SS events are initially considered. These events have only one S1c contributing to the total S1c, and only have one S2c, so only have one free parameter in the χ^2 minimisation for both ER and NR, which is the energy of the one scatter. Note again that for single scatters there is not expected to be an improvement in discrimination between the $\log(\text{S2c})$ vs. S1c space and the $\Delta\chi^2$ space, since no new information is utilised in the $\Delta\chi^2$ parameter. Firstly, it is shown in Figure 6.22 that the aforementioned observation still holds: NR events in the NR model and ER events in the ER model do not exactly follow a χ^2 distribution with $k = 1$. This means that this is not a phenomenon that is introduced by having multiple interactions. However, it is worth noting that the shape of the distributions changes slightly compared to the MS case. Once again, the NR model for DD data and simulation (top left and right of the figure respectively), and the ER model for Na-22 simulation (bottom of the figure), loosely match the shape of the theoretical curve, but the point at which the data crosses the theoretical distribution is consistently now at around 1.5 for the SS events. It is not currently clear what causes this change.

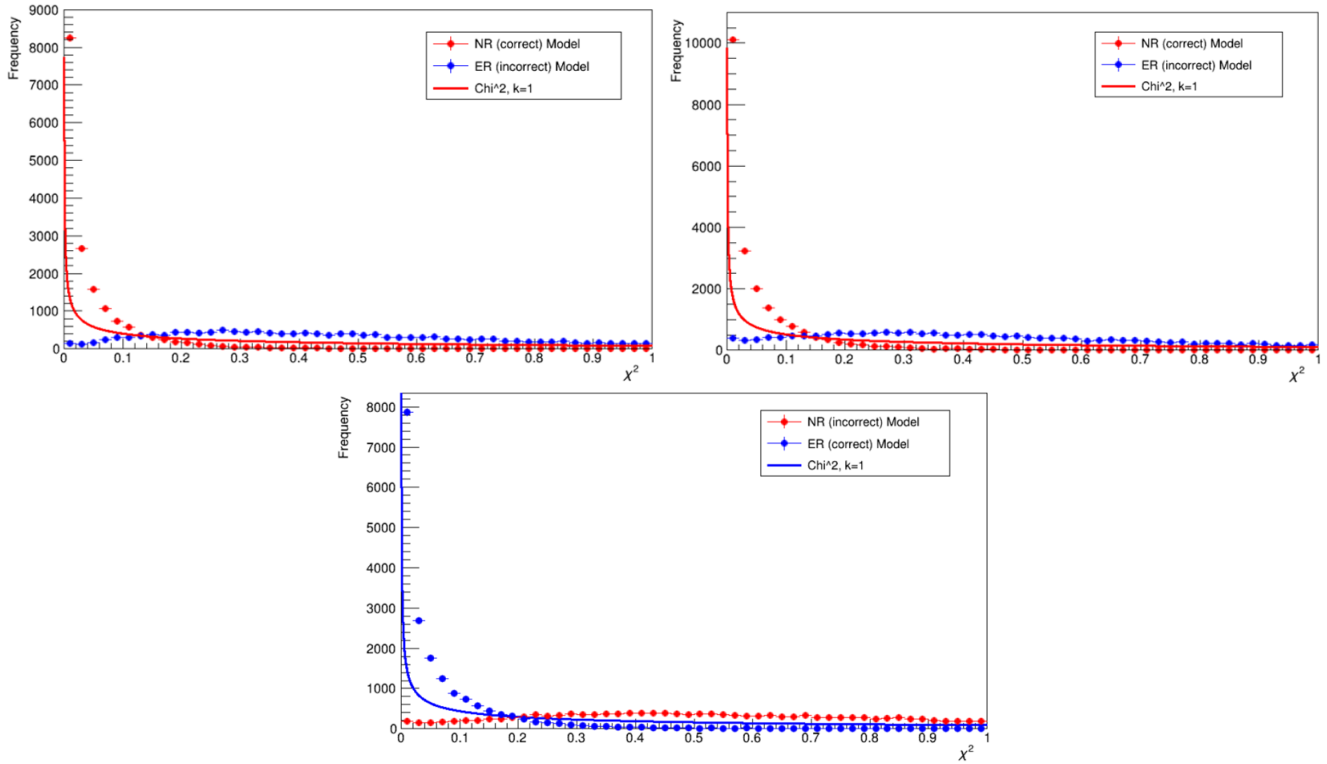


Figure 6.22: The SS χ^2 distributions from both the NR (red points) and ER (blue points) models of the $\Delta\chi^2$ method, compared to the theoretical $k = 1$ χ^2 distribution (red for NR data or simulation, blue for ER simulation), shown for DD data (top left), DD simulation (top right), and Na-22 simulation (bottom). The DD simulation has an FV cut, a field cage resistor cut, and the SS ROI described in section 6.2.3 applied, and the DD data has these cuts along with some DD specific data quality cuts. The Na-22 simulation has only the WIMP search ROI applied.

The curves used to relate $\sigma_m(S1c)$ to $S1c$, $\sigma_m(S2c)$ to $S2c$, and σ_c to $S2c$ were calculated using photopeak data from the WS2024 dataset, as was shown in Table 3.2 and discussed in section 3.3.1. Therefore, this SS dataset of ER events is used to evaluate how closely the data, under the ER model, follows the theoretical χ^2 distribution for $k = 1$. This is done individually for samples of 10 000 events from four of the photopeaks in the dataset, one of which was not measured for use in the initial calculation of $\sigma_m(S1c)$, $\sigma_m(S2c)$, and σ_c . These peaks are specifically Kr-83m (41 keV), Xe-127 (63 keV, not used for the tuning), Xe-131m (164 keV), and Xe-127 + Xe-129m (236 keV). These four χ^2_{ER} distributions are compared to the theoretical χ^2 distribution for $k = 1$ in Figure 6.23. As was stated previously, if the general model is correct, then the data will at least follow the right general function, even if the gradient is not perfectly matched. A correct gradient requires errors not to be overestimated or underestimated. For the first two photopeaks studied in this figure (top plots), the match to theory is reasonable for $\chi^2 < 1$, after which point the gradient is too steep (beyond what is shown in the figure), suggesting overestimated errors.

The lower values of χ^2 are the focus of this comparison, however, as this is where most true ER events are expected to be found.

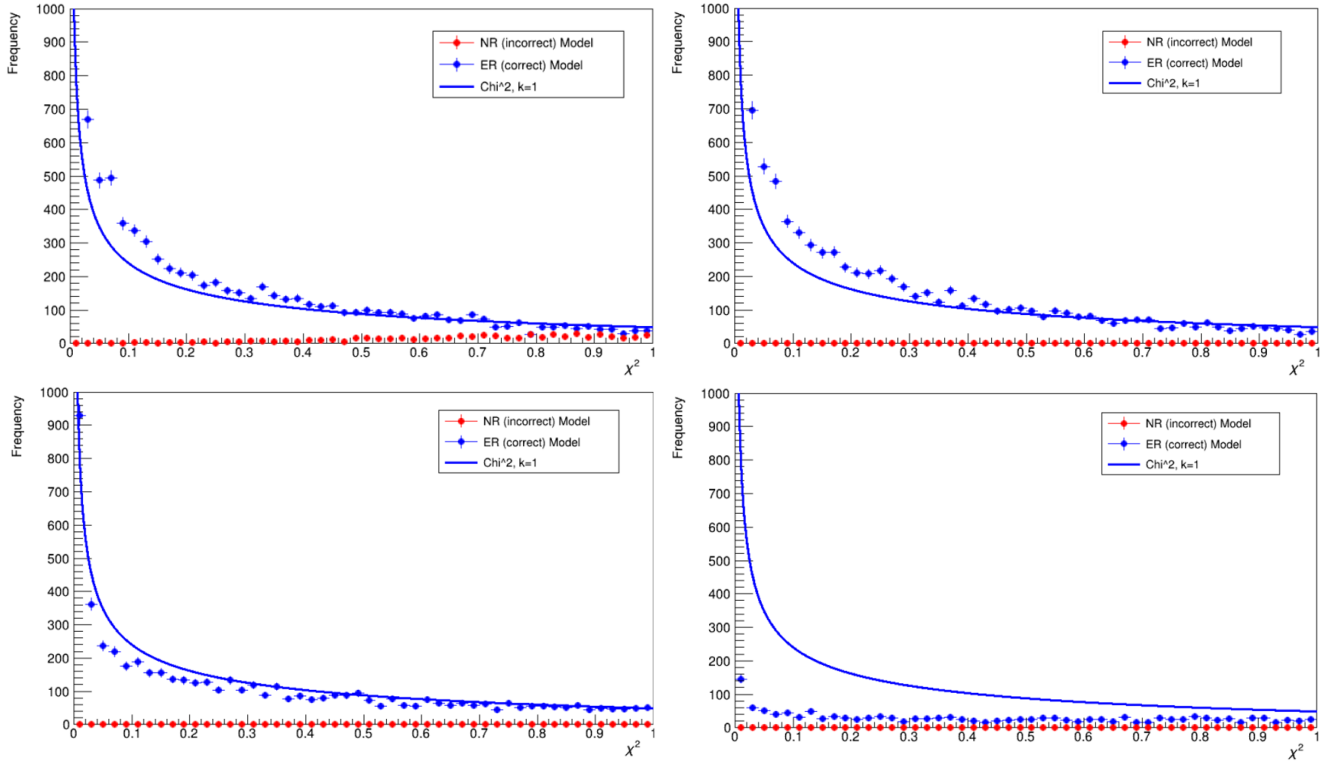


Figure 6.23: The SS χ^2 distributions from both the NR (red points) and ER (blue points) models of the $\Delta\chi^2$ method, compared to the theoretical $k = 1$ χ^2 distribution (blue line), shown for the ER photopeak data on which the $\Delta\chi^2$ algorithm was tuned. Samples of 10,000 events are taken from the following photopeaks: Kr-83m (41 keV) (top left), Xe-127 (63 keV) (top right), Xe-131m (164 keV) (bottom left), and Xe-127 + Xe-129m (236 keV) (bottom right).

For the Xe-131m peak (bottom left), the match again looks close at low χ^2 , but beyond this point (again, beyond the range of the figure) errors look to be underestimated. For the final peak, of Xe-127 + Xe-129m (bottom right), the data does not match the theory, and a fairly linear distribution can be seen. This is potentially due to the fact that, since LZ is looking for WIMPs at lower energies, everything in the detector is tuned for these energies. This means that at higher energies, such as that at which this photopeak occurs, the detector tuning may be worse. It should be noted that, in all plots of this figure, the NR model values of χ^2 are generally much larger than those for the ER model, and hence the counts in bins with a χ^2 value of less than one are generally zero, or very small. Overall, these distributions do not look unreasonable, and it can be seen that the algorithm performs as expected when run on the data on which it was tuned.

A hypothesis presented as to why the photopeak WS2024 data is a better match to the theoretical distribution than the Na-22 source of MS beta events is that the underlying xenon microphysics

of these two different types of ER interaction are sufficiently different as to alter the distribution. Since the calibration of $\sigma_m(S1c)$, $\sigma_m(S2c)$, and σ_c cannot be done with beta ERs (no peaks are formed from which to measure $\sigma(S1c)$, $\sigma(S2c)$, and $\sigma(E_{ee})$), it was accepted that, at this stage, no further improvements can be made to the ER model. This hypothesis of different xenon microphysics for beta ERs is tested using a tritiated methane (CH3T) source that was used in the main LZ WIMP search to define the SS ER band, as is a good source of SS beta particles. The distribution for these events is shown in Figure 6.24, and it can indeed be seen that the match between data and theory here is not as good as in the case of the photopeak data, but the general form of the distribution does look to be correct.

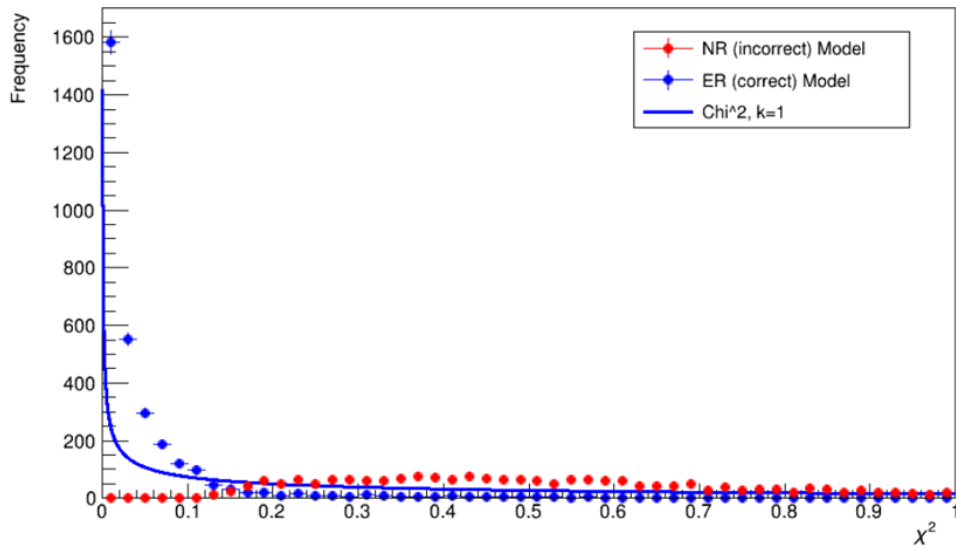


Figure 6.24: The SS χ^2 distribution from both the NR (red points) and ER (blue points) models of the $\Delta\chi^2$ method, compared to the theoretical $k = 1$ χ^2 distribution (blue line), shown for a CH3T beta source. An SS ER band selection is used to select these events, and an ROI cut is applied.

If it is true that the distributions found for $\sigma_m(S1c)$, $\sigma_m(S2c)$, and σ_c differ between photopeak ER events, and beta ER events, then this definitely calls into question the assumption that these distributions can also be used for the NR events (although the NR model does not use the non-diagonal elements in the covariance matrix). Because of this, a study is carried out to investigate an alternate definition of the covariance matrix in the case of the NR model, that does not rely on measurements made from the ER photopeak data.

Since only the diagonal elements of the covariance matrix are used in the NR model and fitting, and since these simply represent the squares of $\sigma(S1c^{total})$ and, for each scatter, $\sigma(S2c)$, these values can be acquired from SS DD simulation. In this section, S1 and S2 signals always correspond to the corrected S1c and S2c signals, so the ‘c’ notation will be dropped for simplicity. For this investigation, only an ROI cut is applied. Simulation is needed here as it is required that the true energy of the recoil is known. From this, the NEST charge and light yield curves (see

section 2.10.1) are used to obtain the mean S1 and S2 values for a given event. The difference between the observed S2, $S2_{obs}$, after having run the simulation of the interaction and detector response, and this mean (true) S2, $S2_{mean}$, is plotted against the mean (true) S2 in the left plot of Figure 6.25. The value of $\sigma(S2)$ can then be obtained for each value of the mean S2 from this left plot as simply the standard deviation of the distribution of events in that bin. Also shown, on the right of this figure, is the distribution of this measured $\sigma(S2)$ as a function of mean S2, fitted with a third degree polynomial. The four leftmost data points are not included in the fit as a good Gaussian fit to the data in these bins of mean S2 is not able to be obtained. The values and errors of most of these points are too high to appear on this plot, but just correspond to the background signals that appear in addition to the primary distribution, seen in the left plot of Figure 6.25.

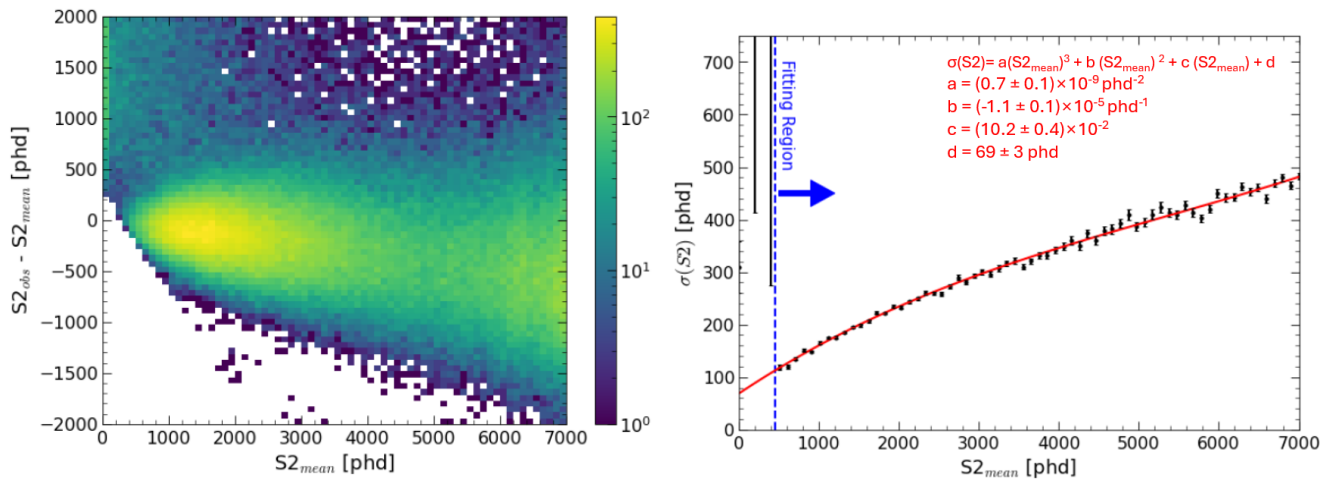


Figure 6.25: The distribution of observed minus mean S2 values as a function of the mean S2 value (left) for simulated DD data. Also shown is how the width of this distribution varies with the mean S2 value (right). This data is fitted to a cubic polynomial (red) of the form $\sigma(S2) = aS2_{mean}^3 + bS2_{mean}^2 + cS2_{mean} + d$, with $\chi^2 / ndf = 119.3 / 61$.

The same process is followed for S1 signals, and these results are displayed in Figure 6.26. The best fit function used for the $\sigma(S1)$ distribution with mean S1 is a polynomial with non-zero coefficients for the terms with exponents of 1/2 and 1. Again, the two data points with the lowest mean S1 do not have a good Gaussian fit to the data in that mean S1 bin, and so are excluded from this final fit. This fit is not perfect, as can be seen from the right plot of the figure, but for events with an S1c value less than 100 phd (the S1 ROI upper limit initially used in $\log(S2c)$ vs. S1c space for MS events) it was deemed to be a sufficient approximation of the distribution. The figure also shows a more generalised fit (blue curve) for which the power of 1/2 in the previous fit is allowed to float as a fitted parameter, but this curve is not used in the following analysis.

For an MS event, the entries for $\sigma^2(S2)$ in the NR covariance matrix are trivial, but the case is more complex for $\sigma^2(S1^{total})$. This is because the individual $\sigma^2(S1)$ values need to be known

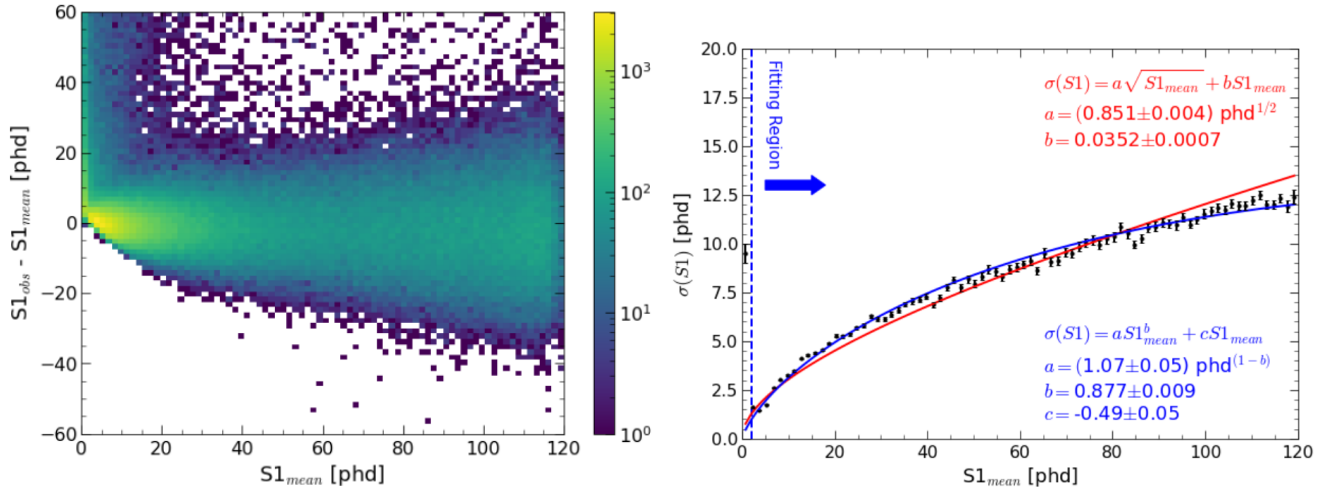


Figure 6.26: The distribution of observed minus mean $S1$ values as a function of the mean $S1$ value (left) for simulated SS DD data. Also shown is how the width of this distribution varies with the mean $S1$ value (right). This data is fitted to a polynomial (red) of the form $\sigma(S1) = a\sqrt{S1_{mean}} + bS1_{mean}$, with $\chi^2 / ndf = 3185 / 77$, and a second polynomial (blue) of the form $\sigma(S1) = aS1_{mean}^b + cS1_{mean}$, with $\chi^2 / ndf = 1358 / 76$.

first, and then their sum gives the required quantity. However, the complexity with MS events is that the individual $S1$ s from the separate scatters cannot be differentiated. For this study, the individual $S1$ s are estimated in the same way as in Equation 3.4, by apportioning the total $S1$ according to the size of the $S2$ for each of the scatters. This is used to calculate the NR covariance matrix used in the χ^2 definition in the NR model, which is constant for a given event. The results of this are shown for 10 000 events of MS DD calibration data in Figure 6.27.

As is clear from the top plot of the figure, this did not provide any drastic improvement to the match to the χ^2 distribution with $k = 1$, however it does change the the errors to being overestimated rather than underestimated (the distribution now sits below the theoretical curve). The match to the curve is arguably slightly better. However, when the $\Delta\chi^2$ values are plotted against the total fitted NR energy, this does not lead to improved MS NR ER discrimination (see the bottom plot of Figure 6.27), which is the ultimate aim of this method. The NR band now extends much further into the region of $\Delta\chi^2 > 0$, but interestingly the majority of events still follow the band as defined without this new covariance matrix for the NR model, as shown by the red NR band in the figure. This is likely due to the fact that the $\Delta\chi^2$ parameter is driven by the χ^2 value of the worse fit model, in this case ER, which is unchanged.

In order to properly evaluate the effect on discrimination, a source of ER events needs to be considered as well, hence MS Na-22 events are also plotted in this re-defined $\Delta\chi^2$ space, and this is shown in Figure 6.28. Since sufficient statistics at these low energies are not able to be obtained with Na-22 data (as previously discussed and as illustrated by Figure 6.5), this plot is produced

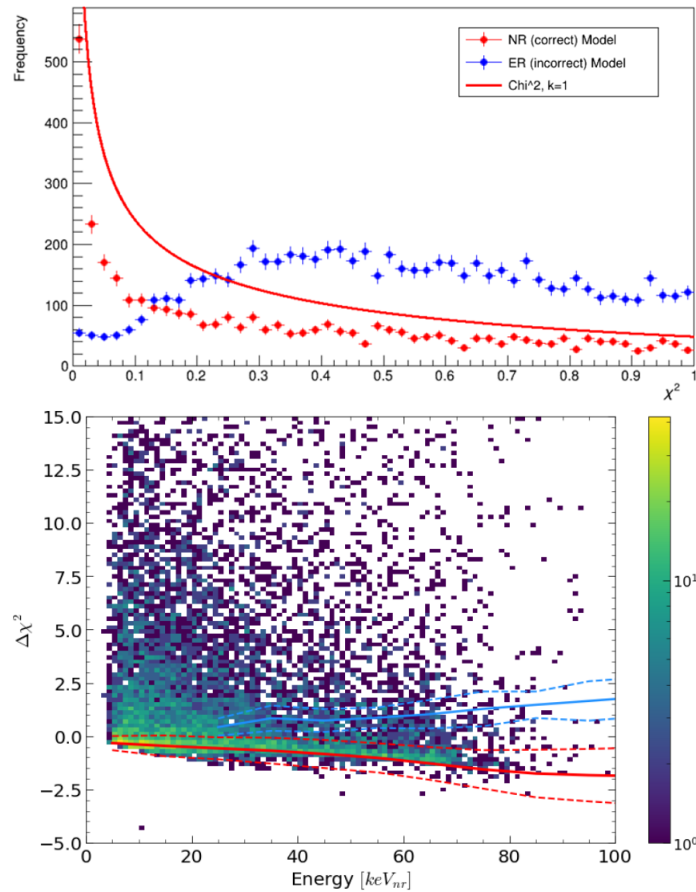


Figure 6.27: The MS χ^2 distribution from both the NR (red points) and ER (blue points) models of the $\Delta\chi^2$ method (top) using a DD simulation-based error covariance matrix for the NR model, shown for 10 000 DD calibration events. This is compared to the theoretical $k = 1$ χ^2 distribution (red line). Also shown is the $\Delta\chi^2$ space with this redefinition of the method (bottom). The NR (red) and ER (blue) bands in this space, from the previous definition of the method, are shown for reference.

using Na-22 simulation. The events seen in the figure form a much less clear band than with the previous definition of the $\Delta\chi^2$ algorithm, and discrimination power between NR and ER events now decreases with energy, because of the shape of this structure. Therefore, overall, it was decided that this attempted optimisation of the method was not successful.

The more generalised fit shown in blue in Figure 6.26 provides a better fit to the data, but given the results shown in Figures 6.27 and 6.28 obtained using the initial curve, this somewhat improved (but still imperfect) fit is not used to reproduce discrimination plots. It was not believed the relatively minor improvement in the fitting would resolve the discrimination issues present in this method.

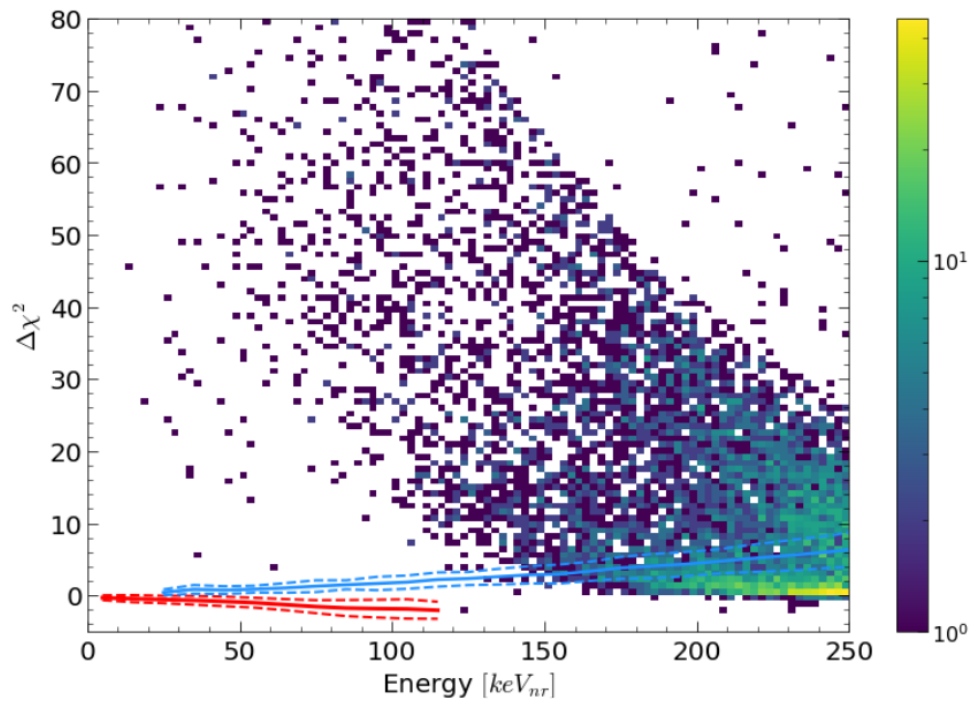


Figure 6.28: *MS Na-22 simulation events in $\Delta\chi^2$ space with the NR covariance matrix redefinition of the method. The NR (red) and ER (blue) bands in this space, from the previous definition of the method, are shown for reference.*

Chapter 7

Conclusion

Across the work presented in this thesis, it was investigated how MS events, detected in the LZ TPC, could be used to estimate the expected number of SS events in the WIMP search dataset. Such events would be indistinguishable from a WIMP signal. This is crucial for a WIMP search, as in the event of detecting a WIMP-like signal it would be necessary to prove, beyond any reasonable doubt, that any signal events were not simply non-vetoed neutrons. The OD and Skin veto detectors have a very high tagging efficiency for neutrons ($(89 \pm 3)\%$ [126]), and were also used to produce an estimate of neutrons expected in the WIMP search, but it is valuable to verify this result with an additional, independent estimate.

A barrier that presented itself in producing this MS-driven estimate was the lack of NR ER discrimination for MS events in the traditional $\log(\text{S2c})$ vs. S1c space, when the S2c pulses are simply summed. The centrepiece of this thesis was a new parameter, $\Delta\chi^2$, and a new parameter space that was developed for MS events in order to improve the NR ER discrimination. This was achieved by utilising all of the information that is known about the individual scatters of an MS event.

7.1 $\Delta\chi^2$ Method

It was shown that the $\Delta\chi^2$ method did indeed provide improved NR ER discrimination for MS events in early studies conducted during the WS2022 campaign. This early application made some general assumptions about the errors on measured S1c and S2c values, and did not take into account the anti-correlations between S1 and S2 signals. This was addressed for WS2024 however, which made the analysis method more robust and justifiable, even if there was no significant improvement in discrimination compared to the initial application of the method. This was, however, difficult to disentangle from changes in detector conditions between WS2022 and WS2024. Further work was also carried out to study the performance of this analysis method compared to theoretical expectations, to see if any further improvements to the analysis could be implemented. It was,

however, found that the MS NR ER discrimination could not be significantly improved by any of the methods explored, although a deeper understanding of the $\Delta\chi^2$ method was achieved through this work. There remains the potential for the implementation of further improvements in the future, and greater understanding of all facets of the analysis could be gained. This would be a good focus for future work with the application of the $\Delta\chi^2$ method in future WIMP searches.

7.2 WS2022 SS Neutron Estimate

During the first WIMP search of LZ (WS2022), the $\Delta\chi^2$ method was still being developed, so was not directly used in the published results. However, the WS2022 data was crucial for the development of this method, which was able to produce an SS neutron estimate that was in agreement with that which was quoted in the LZ backgrounds paper [150], and even improved the limit on the estimate of 0 SS neutrons. The main WS2022 MS-driven SS neutron estimate in the WIMP search dataset was $0^{+0.2}$.

For the $\Delta\chi^2$ based estimate, three results were quoted, and these had different veto signal requirements on the MS data and simulation throughout the process. Ideally, the MS veto requirement would be the same as for SS events (no veto signal), to minimise systematic errors in the SS/MS ratio, but when the requirement of no veto signal was applied to MS data events, very low statistics were found, which led to large errors. Therefore, estimates with the MS veto requirement of having a veto signal, and no MS veto requirement at all, were also produced. In all three of these cases, 0 MS neutrons were found in the WS2022 dataset, which enforced estimates of 0 SS neutrons in the WIMP search dataset. The differences in the number of events measured for each of these requirements led to different limits on these estimates. With the MS requirement of no veto signal, the estimate was $0^{+0.9}$. With the MS requirement of a prompt or delayed veto signal in either the OD or the Skin, the estimate was $0^{+0.01}$. With no MS veto requirement, which had very similar numbers of events to the previous requirement, due to the high tagging efficiency of the veto detectors, the estimate was also $0^{+0.01}$.

Additional studies were also carried out to investigate and evaluate the impact of different sources of systematic errors on the final result, such as the choice of neutron interaction cross-section library used for the neutron background simulation.

7.3 WS2024 SS Neutron Estimate

For WS2024, the $\Delta\chi^2$ analysis was in a sufficient state of maturity as to be used in the official WIMP search, to help provide an MS-driven estimate of the number of SS neutrons expected in the WIMP ROI that were not tagged by a veto detector. Selection of MS NR candidates was performed in $\Delta\chi^2$ space using the NR band in this space. The waveforms of these events were

then individually analysed to remove events that were not neutron-like, in the current absence of MS-specific accidental coincidence and data quality cuts. The $\Delta\chi^2$ analysis here was the aforementioned updated version that takes into account anti-correlations between S1 and S2 signals due to recombination fluctuations, described in section 3.3.1. This estimate consisted of two results, which used different radii of the strict FV, and different OD signal requirements. For a strict FV that extended to 2 cm from the ideal wall, with no veto tag requirement, the estimate for the number of SS neutrons in the WIMP ROI that were not tagged by a veto detector was 0.5 ± 0.3 . With the strict FV extending all the way to the ideal wall, and requiring a delayed OD signal, this estimate was 0.3 ± 0.2 .

In addition to the primary MS-driven SS neutron estimate produced for WS2024, a secondary estimate was also made for which the $\Delta\chi^2$ method was used at every stage of the analysis. The differences between these methods were explicitly laid out in chapter 5. For this estimate, three results using different veto requirements were again quoted, since very low statistics were again found when an MS requirement of no veto signal was applied. This meant that the estimate for the number of SS neutrons in the WIMP ROI, that were not tagged by a veto detector, using an MS requirement of no veto signal, was 1.0 ± 1.0 . This is not a useful result due to the very high error. The estimate with an MS requirement of having a prompt or delayed veto signal in either the OD or Skin was 0.07 ± 0.03 . Finally, the estimate with the highest statistics, that placed no veto signal requirements on the MS events, was 0.11 ± 0.06 .

It should be noted that all three of these results are consistent with the main WS2024 MS-driven SS neutron estimate with a strict FV extending to 0 cm from the ideal wall, and requiring a delayed OD signal. To one significant figure, the veto agnostic $\Delta\chi^2$ result is also consistent with the LZ result using the strict FV extending to 2 cm from the ideal wall. With the exception of the result requiring no veto signal however, the estimates are all slightly lower for the $\Delta\chi^2$ analysis.

In addition to this, all three results from the $\Delta\chi^2$ -driven estimates are in agreement with the primary neutron estimate quoted in the WS2024 paper [126] that was based on the number of WIMP search events tagged by the veto detectors. This estimate was $0.0^{+0.2}$ untagged SS neutrons in the ROI. Also quoted for WS2024 [126], as a verification of this estimate (alongside the MS-driven estimate discussed in chapter 5), is an additional estimate, from simulations based on detector material radioassays, of 0.05 ± 0.01 , which is in even better agreement with the $\Delta\chi^2$ results and, unlike previous comparisons, is lower than all three estimates. Since the LZ WS2024 estimate discussed in this thesis was used in the WS2024 WIMP search just as a verification of the neutron background estimate, this result will not have had an impact on the limit curve shown in Figure 5.1.

Crucially though, the $\Delta\chi^2$ -driven estimates are in agreement with what was seen in the WIMP search itself, namely that there were no WIMP-like events seen once the salt events were removed. Had there been any remaining WIMP-like events, the neutron estimates would have been used to

establish how many of the events were likely neutrons. Therefore, given a result of zero WIMP-like events, all of the aforementioned neutron estimates are in agreement with this.

7.4 WS2022, WS2024 and Implications for Future LZ Runs

MS-driven SS neutron estimates made using the $\Delta\chi^2$ method for the WS2022 and WS2024 campaigns can be compared to assess the agreement across these two estimates. This is presented in Table 7.1. Once again, a result is presented for each of the three veto requirements that were used for the MS events throughout the WS2022 and WS2024 analyses. The systematic errors evaluated in the neutron interaction cross-section library studies, in sections 4.9 and 6.8, were found to have a relatively small effect on the overall errors, and so are not included here.

	WS2022	WS2024	/Live Day	WS2022 + WS2024	1000 Live Days
No Veto Signal	$0^{+0.9}$	1.0 ± 1.0	0.005 ± 0.005	1.0 ± 1.0	5.0 ± 5.0
Veto Signal	$0^{+0.01}$	0.07 ± 0.04	0.0003 ± 0.0002	0.09 ± 0.05	0.3 ± 0.2
Veto Agnostic	$0^{+0.01}$	0.11 ± 0.06	0.0005 ± 0.0003	0.14 ± 0.09	0.5 ± 0.3

Table 7.1: Comparison of WS2022 and WS2024 $\Delta\chi^2$ SS neutron estimate results, and extrapolation of WS2024 results. WS2022 errors are 90% upper limits, and all other errors are 1σ , based on Poisson statistics.

Since the WS2022 results estimated zero SS neutrons in the WIMP search ROI, and because the analysis evolved notably between WS2022 and WS2024, an estimate for the total number of SS neutrons in LZ WIMP searches to date (WS2022 + WS2024) is made by extrapolating the WS2024 estimate to 280 live days, and this is also shown in the table, along with the counts per live day, and an extrapolation to 1000 live days, for the full projected lifetime of LZ. As was noted for the two WIMP searches individually, the result that requires no MS veto signal has a very large error, due to the high tagging efficiency of the veto detectors, and therefore low statistics of events across both simulation and data. The remaining two results are more useful, and are in agreement with each other. Due to the very low statistics seen for the result requiring no MS veto signal (the ideal case), the author believes that the most valuable of these three results is the veto agnostic result, due to the fact that it maximises statistics. For this requirement, the results show that 0.14 ± 0.09 neutrons are expected in the 280 live days of WIMP search data thus far accrued by the LZ dark matter search. Given that the target run time for LZ is around 1000 live days, the WS2024 result can again be extrapolated to estimate the total number of neutrons in the final, full dataset to be 0.5 ± 0.3 .

7.5 Future Work

While the work presented in this thesis showed the development of a novel method of discriminating MS NR and ER events, and used this new method to produce SS neutron estimates for the LZ WS2022 and WS2024 campaigns that are consistent with other estimates, that is not to say that the method is fully optimised, or even that all aspects of the method are fully understood.

At the very least, it is hoped that the $\Delta\chi^2$ method will continue to be used for TPC-only SS neutron estimates in upcoming LZ WIMP searches, but beyond that further investigations into optimisation and full comprehension of the method should be carried out. Efforts were taken to begin optimisation studies during WS2024, and were presented in section 6.9. This work was not able to further improve discrimination, but did open up some interesting avenues for future studies to address currently unanswered questions.

It would be good to study what further optimisations can be made to the $\Delta\chi^2$ method in order to make NR events modelled with the NR hypothesis (and likewise for ER events with the ER hypothesis) better follow the expected theoretical $k = 1 \chi^2$ curves discussed in section 6.9. In addition to this, it would need to be understood how these optimisations correspond to changes in $\Delta\chi^2$ space, and the effect that they have on discrimination. If the $k = 1 \chi^2$ curves match well but discrimination is worse, it would need to be understood why that was, as better discrimination is the ultimate goal.

The work presented in this thesis relies significantly on the LZAP identification of MS events, which will have introduced an additional systematic error into these studies. Future work should aim to quantify this systematic error, so that the impact that it has on the results can be assessed.

Additionally, there were a number of phenomena encountered during the course of these analyses that are not yet fully understood, as were mentioned throughout this thesis when they were encountered. In summary, the author believes that this work provides a solid foundation, and proof of concept, for the development of the $\Delta\chi^2$ method for discriminating NR and ER MS events, but further development, and deeper understanding, would be good to see in the future.

Bibliography

- [1] N. Aghanim *et al.*, “Planck 2018 Results- VI. Cosmological Parameters,” *Astronomy and Astrophysics*, vol. 641, 2020.
- [2] K. Dimopoulos, *Introduction to cosmic inflation and dark energy*. Series in astronomy and astrophysics, CRC Press, 1st ed., 2021.
- [3] L. Bergström, “Dark matter candidates,” *New Journal of Physics*, vol. 11, no. 10, p. 105006, 2009.
- [4] D. Akerib *et al.*, “The LUX-ZEPLIN (LZ) Experiment,” *Nuclear Instruments and Methods in Physics Research Section A: Accelerators, Spectrometers, Detectors and Associated Equipment*, vol. 953, p. 163047, 2020.
- [5] G. Bertone and D. Hooper, “A History of dark matter,” *Reviews of Modern Physics*, vol. 90, p. 045002, 2018.
- [6] F.Zwicky, “Die Rotverschiebung von extragalaktischen Nebeln,” *Helvetica Physica Acta*, vol. 6, pp. 110–127, 1933.
- [7] F.Zwicky and A.Ehlers (translator), “Republication of: The Redshift of Extragalactic Nebulae,” *Gen. Relativ. Gravit.*, vol. 41, pp. 207–224, 2009.
- [8] E. Hubble, “A Relation Between Distance and Radial Velocity Among Extra-Galactic Nebulae,” *Proceedings of the National Academy of Sciences*, vol. 15, pp. 168–173, 1929.
- [9] G.W. Collins II, *The Virial Theorem in Stellar Astrophysics*. Pachart Publishing House, 1978.
- [10] F.Zwicky, “On the Masses of Nebulae and of Clusters of Nebulae,” *Astrophysical Journal*, vol. 86, pp. 217–246, 1937.
- [11] S. Kent, “Dark Matter in Spiral Galaxies. II - Galaxies with H I Rotation Curves,” *Astronomical Journal*, vol. 93, pp. 816–832, 1987.

- [12] A. Bosma, “Kinematics and Dynamics of Dwarf Spirals and Irregulars,” *Dwarf Galaxies, ESO Conference and Workshop Proceedings, 1993*, pp. 187–196, 1994.
- [13] H.W.Babcock, “The Rotation of the Andromeda Nebula,” *Lick Observatory Bull.*, vol. 498, pp. 41–51, 1939.
- [14] D. Rogstad and G. Shostak, “Gross Properties of Five Scd Galaxies as Determined from 21-CENTIMETER Observations,” *Astrophysical Journal*, vol. 176, pp. 315–321, 1972.
- [15] P. Tipler and G. Mosca, *Physics for Scientists and Engineers*. W.H. Freeman and Company, 6th ed., 2008.
- [16] W. K. J. Rubin, V. C. Ford, “Rotation of the Andromeda Nebula from a Spectroscopic Survey of Emission Regions,” *Astrophysical Journal*, vol. 159, p. 379, 1970.
- [17] R. N. Roberts, M. S. Whitehurst, “The Rotation Curve and Geometry of M31 at Large Galactocentric Distances,” *Astrophysical Journal*, vol. 201, pp. 327 – 346, 1975.
- [18] C. Carignan *et al.*, “The Extended H I Rotation Curve and Mass Distribution of M31,” *The Astrophysical Journal*, vol. 641, no. 2, p. L109, 2006.
- [19] K. Freeman, “Dark Matter in the Galaxy, and the MACHO Project,” *ASP Conference Series*, vol. 117, pp. 242–248, 1997.
- [20] M. Milgrom, “MOND Theory,” *Canadian Journal of Physics*, vol. 93, no. 2, pp. 107–118, 2015.
- [21] S. Mollerach and E. Roulet, *Gravitational Lensing and Microlensing*. World Scientific, 1st ed., 2002.
- [22] M. Weisskopf, H. Tananbaum, L. V. Speybroeck, and S. O’Dell, “Chandra X-ray Observatory (CXO): Overview,” in *X-Ray Optics, Instruments, and Missions III*, SPIE, 2000.
- [23] M. Johns *et al.*, “Giant Magellan Telescope: overview,” in *Ground-based and Airborne Telescopes IV*, vol. 8444, SPIE, 2012.
- [24] H. Ford *et al.*, “Advanced camera for the Hubble Space Telescope,” in *Space Telescopes and Instruments V*, vol. 3356, SPIE, 1998.
- [25] Chandra X-ray Observatory, “1E 0657-56: NASA Finds Direct Proof of Dark Matter,” <https://chandra.si.edu/photo/2006/1e0657/>, 2006, accessed 22/10/2024.
- [26] G. Angus, B. Famaey, and H. Zhao, “Can MOND Take a Bullet? Analytical Comparisons of Three Versions of MOND Beyond Spherical Symmetry,” *Monthly Notices of the Royal Astronomical Society*, vol. 371, no. 1, pp. 138–146, 2006.

- [27] G. Angus and S. McGaugh, “The Collision Velocity of the Bullet Cluster in Conventional and Modified Dynamics: The Collision Velocity of the Bullet Cluster,” *Monthly Notices of the Royal Astronomical Society*, vol. 383, no. 2, p. 417–423, 2007.
- [28] NASA, WMAP Science Team, “Timeline of the Universe,” <https://map.gsfc.nasa.gov/media/060915/index.html>, 2012, accessed 30/05/2025.
- [29] M. Davis *et al.*, *Cosmology : a Research Briefing*. National Academy Press, 1st ed., 1995.
- [30] Y. Akrami *et al.*, “Planck 2018 results IV. Diffuse component separation,” *Astronomy and Astrophysics*, vol. 641, p. 74, 2020.
- [31] R. Sachs and A. Wolfe, “Perturbations of a Cosmological Model and Angular Variations of the Microwave Background,” *The Astrophysical Journal*, vol. 147, pp. 73–90, 1966.
- [32] S. Dodelson and F. Schmidt, “9 - The Cosmic Microwave Background,” in *Modern Cosmology (Second Edition)*, pp. 231–269, Academic Press, 2021.
- [33] A. Marcos-Caballero, R. Fernández-Cobos, E. Martínez-González, and P. Vielva, “The Shape of CMB Temperature and Polarization Peaks on the Sphere,” *Journal of Cosmology and Astroparticle Physics*, vol. 2016, no. 04, p. 058, 2016.
- [34] W. Hu, N. Sugiyamam, and J. Silk, “The Physics of Microwave Background Anisotropies,” *Nature*, vol. 386, pp. 37–43, 1997.
- [35] A. Liddle, *An Introduction to Modern Cosmology*. John Wiley Sons, Incorporated, 2nd ed., 2003.
- [36] S. Weinberg, *Cosmology*. Oxford University Press, 1st ed., 2008.
- [37] V. Singh, D. Bhowmick, and D. Basu, “Re-examining the Lithium Abundance Problem in Big-Bang Nucleosynthesis,” *Astroparticle Physics*, vol. 162, p. 102995, 2024.
- [38] R. Cyburt, B. Fields, and K. Olive, “The NACRE Thermonuclear Reaction Compilation and Big Bang Nucleosynthesis,” *New Astronomy*, vol. 6, no. 4, pp. 215–238, 2001.
- [39] R. Wagoner, “Cosmological Element Production,” *Science*, vol. 155, no. 3768, pp. 1369–1376, 1967.
- [40] Particle Data Group, “Review of Particle Physics,” *Chinese Physics C*, vol. 40, no. 10, p. 100001, 2016.
- [41] S. Navas *et al.*, “Review of Particle Physics,” *Physical Review D*, vol. 110, p. 030001, 2024.

- [42] M. Fukugita and P. Peebles, “The Cosmic Energy Inventory,” *The Astrophysical Journal*, vol. 616, no. 2, p. 643, 2004.
- [43] M. Taoso, G. Bertone, and A. Masiero, “Dark Matter Candidates: A Ten-Point Test,” *Journal of Cosmology and Astroparticle Physics*, vol. 2008, no. 03, p. 022, 2008.
- [44] A. De Rújula, S. Glashow, and U. Sarid, “Charged Dark Matter,” *Nuclear Physics B*, vol. 333, no. 1, pp. 173–194, 1990.
- [45] D. Baumann, “Cosmology: Part III Mathematical Tripos,” *University of Cambridge Lecture Notes*, <https://cmb.wintherscoming.no/pdfs/baumann.pdf>, 2021, accessed 10/03/2025.
- [46] P. Murdin, *Encyclopedia of Astronomy and Astrophysics: WIMPs and MACHOs*. CRC Press, 2001.
- [47] L. Strigari, “Galactic Searches for Dark Matter,” *Physics Reports*, vol. 531, no. 1, pp. 1–88, 2013.
- [48] C. Alcock *et al.*, “The MACHO Project: Microlensing Results from 5.7 Years of Large Magellanic Cloud Observations,” *The Astrophysical Journal*, vol. 542, no. 1, p. 281, 2000.
- [49] L. Wyrzykowski *et al.*, “The OGLE View of Microlensing Towards the Magellanic Clouds – III. Ruling out Subsolar MACHOs with the OGLE-III LMC data*,” *Monthly Notices of the Royal Astronomical Society*, vol. 413, no. 1, pp. 493–508, 2011.
- [50] É. Aubourg and N. Palanque-Delabrouille, “A Search for Galactic Dark Matter with EROS 2,” *New Astronomy*, vol. 4, no. 4, pp. 265–273, 1999.
- [51] J. Glanz, “EROS, MACHO, And OGLE Net A Haul of Data,” *Science*, vol. 268, no. 5211, pp. 642–643, 1995.
- [52] J. Bahcall, P. Hut, and S. Tremaine, “Maximum Mass of Objects that Constitute Unseen Disk Material,” *The Astrophysical Journal*, vol. 290, pp. 15–20, 1985.
- [53] C. Lacey and J. Ostriker, “Massive Black Holes in Galactic Halos?,” *The Astrophysical Journal*, vol. 299, pp. 633–652, 1985.
- [54] M. Khlopov, “Primordial Black Holes,” *Research in Astronomy and Astrophysics*, vol. 10, no. 6, p. 495, 2010.
- [55] C. Cercignani, *The Boltzmann Equation and its Applications*. Springer-Verlag, 1988.
- [56] J. Feng, “The WIMP Paradigm: Theme and Variations,” *SciPost Physics Lecture Notes*, 2023.

- [57] A. Peter, “Dark Matter: A Brief Review,” *arXiv-1201.3942*, <https://arxiv.org/abs/1201.3942>, 2012.
- [58] G. Ricciardi *et al.*, “Flavour, Electroweak Symmetry Breaking and Dark Matter: State of the Art and Future Prospects,” *The European Physics Journal Plus*, vol. 130, no. 209, 2015.
- [59] L. Roszkowski, E. Sessolo, and S. Trojanowski, “WIMP Dark Matter Candidates and Searches — Current Status and Future Prospects,” *Reports on Progress in Physics*, vol. 81, no. 6, p. 066201, 2018.
- [60] P. Fayet and S. Ferrara, “Supersymmetry,” *Physics Reports*, vol. 32, no. 5, pp. 249–334, 1977.
- [61] J. Lykken and M. Spiropulu, “Supersymmetry and the Crisis in Physics,” *Scientific American*, vol. 310, no. 5, pp. 34–39, 2014.
- [62] J. Feng, “Naturalness and the Status of Supersymmetry,” *Annual Review of Nuclear and Particle Science*, vol. 63, pp. 351–382, 2013.
- [63] M. Carena and H. Haber, “Higgs Boson Theory and Phenomenology,” *Progress in Particle and Nuclear Physics*, vol. 50, no. 1, pp. 63–152, 2003.
- [64] F. Gianotti and T. Virdee, “The Discovery and Measurements of a Higgs Boson,” *Philosophical Transactions of the Royal Society A: Mathematical, Physical and Engineering Sciences*, vol. 373, no. 2032, p. 20140384, 2015.
- [65] S. Martin, *Perspectives on Supersymmetry: A Supersymmetry Primer*, pp. 1–98. World Scientific, 1998.
- [66] M. Drees, M. Nojiri., D. Roy, and Y. Yamada, “Light Higgsino Dark Matter,” *Physical Review D*, vol. 56, pp. 276–290, 1997.
- [67] P. Grothaus, M. Lindner, and Y. Takanishi, “Naturalness of Neutralino Dark Matter,” *Journal of High Energy Physics*, vol. 2013, no. 94, 2013.
- [68] L. Hall, K. Jedamzik, J. March-Russell, and S. West, “Freeze-in Production of FIMP Dark Matter,” *Journal of High Energy Physics*, vol. 2010, no. 80, 2010.
- [69] J. Feng, A. Rajaraman, and F. Takayama, “Superweakly Interacting Massive Particles,” *Physical Review Letters*, vol. 91, p. 011302, 2003.
- [70] J. Kim and G. Carosi, “Axions and the strong CP problem,” *Reviews of Modern Physics*, vol. 82, pp. 557–601, 2010.

- [71] H. Cheng, “The Strong CP Problem Revisited,” *Physics Reports*, vol. 158, no. 1, pp. 1–89, 1988.
- [72] M. Pospelov, A. Ritz, and M. Voloshin, “Bosonic Super-WIMPs as keV-scale Dark Matter,” *Physical Review D*, vol. 78, p. 115012, 2008.
- [73] P. Graham, J. Mardon, and S. Rajendran, “Vector Dark Matter from Inflationary Fluctuations,” *Physical Review D*, vol. 93, p. 103520, 2016.
- [74] J. Feng, “Dark Matter Candidates from Particle Physics and Methods of Detection,” *Annual Review of Astronomy and Astrophysics*, vol. 48, pp. 495–545, 2010.
- [75] A. Boveia and C. Doglioni, “Dark Matter Searches at Colliders,” *Annual Review of Nuclear and Particle Science*, vol. 68, pp. 429–459, 2018.
- [76] G. Aad *et al.*, “The ATLAS Experiment at the CERN Large Hadron Collider,” *Journal of Instrumentation*, vol. 3, no. 08, p. S08003, 2008.
- [77] S. Chatrchyan *et al.*, “The CMS Experiment at the CERN LHC,” *Journal of Instrumentation*, vol. 3, no. 08, p. S08004, 2008.
- [78] A. Augusto Alves Jr *et al.*, “The LHCb Detector at the LHC,” *Journal of Instrumentation*, vol. 3, no. 08, p. S08005, 2008.
- [79] G. Bertone, *Particle Dark Matter : Observations, Models and Searches*. Cambridge University Press, 2010.
- [80] G. Vasileiadis, “The H.E.S.S Experimental Project,” *Nuclear Instruments and Methods in Physics Research Section A: Accelerators, Spectrometers, Detectors and Associated Equipment*, vol. 553, no. 1, pp. 268–273, 2005.
- [81] D. Staszak *et al.*, “Science Highlights from VERITAS,” *arXiv-1510.01269*, <https://arxiv.org/abs/1510.01269>, 2015.
- [82] T. Gaisser and F. Halzen, “IceCube,” *Annual Review of Nuclear and Particle Science*, vol. 64, pp. 101–123, 2014.
- [83] S. Fukuda *et al.*, “The Super-Kamiokande Detector,” *Nuclear Instruments and Methods in Physics Research Section A: Accelerators, Spectrometers, Detectors and Associated Equipment*, vol. 501, no. 2, pp. 418–462, 2003.
- [84] D. Cerdeño and A. Green, *Direct detection of WIMPs*, p. 347–369. Cambridge University Press, 2010.

- [85] M. Schumann, “Direct Detection of WIMP Dark Matter: Concepts and Status,” *Journal of Physics G: Nuclear and Particle Physics*, vol. 46, no. 10, p. 103003, 2019.
- [86] J. Engel and P. Vogel, “Spin-dependent Cross Sections of Weakly Interacting Massive Particles on Nuclei,” *Physical Review D*, vol. 40, pp. 3132–3135, 1989.
- [87] J. Lewin and P. Smith, “Review of Mathematics, Numerical Factors, and Corrections for Dark Matter Experiments Based on Elastic Nuclear Recoil,” *Astroparticle Physics*, vol. 6, no. 1, pp. 87–112, 1996.
- [88] A. Drukier, K. Freese, and D. Spergel, “Detecting Cold Dark-matter Candidates,” *Physical Review D*, vol. 33, pp. 3495–3508, 1986.
- [89] N. Evans, C. O’Hare, and C. McCabe, “Refinement of the Standard Halo Model for Dark Matter Searches in Light of the Gaia Sausage,” *Physical Review D*, vol. 99, p. 023012, 2019.
- [90] M. Bravin *et al.*, “The CRESST Dark Matter Search,” *Astroparticle Physics*, vol. 12, no. 1, pp. 107–114, 1999.
- [91] T. Doke *et al.*, “Absolute Scintillation Yields in Liquid Argon and Xenon for Various Particles,” *Japanese Journal of Applied Physics*, vol. 41, no. 3R, p. 1538, 2002.
- [92] T. Alexander *et al.*, “DarkSide Search for Dark Matter,” *Journal of Instrumentation*, vol. 8, no. 11, p. C11021, 2013.
- [93] M. Bossa, “DarkSide-50, a Background Free Experiment for Dark Matter Searches,” *Journal of Instrumentation*, vol. 9, no. 01, p. C01034, 2014.
- [94] D. McKinsey *et al.*, “The LUX Dark Matter Search,” *Journal of Physics: Conference Series*, vol. 203, no. 1, p. 012026, 2010.
- [95] D. Akerib *et al.*, “Results from a Search for Dark Matter in the Complete LUX Exposure,” *Phys. Rev. Lett.*, vol. 118, p. 021303, 2017.
- [96] D. Akerib *et al.*, “First Results from the LUX Dark Matter Experiment at the Sanford Underground Research Facility,” *Phys. Rev. Lett.*, vol. 112, p. 091303, 2014.
- [97] D. Akimov *et al.*, “The ZEPLIN-III Dark Matter Detector: Instrument Design, Manufacture and Commissioning,” *Astroparticle Physics*, vol. 27, no. 1, pp. 46–60, 2007.
- [98] V. Lebedenko *et al.*, “Results from the First Science Run of the ZEPLIN-III Dark Matter Search Experiment,” *Phys. Rev. D*, vol. 80, p. 052010, 2009.

- [99] E. Aprile *et al.*, “Design and Performance of the XENON10 Dark Matter Experiment,” *Astroparticle Physics*, vol. 34, no. 9, pp. 679–698, 2011.
- [100] E. Aprile *et al.*, “The XENON100 Dark Matter Experiment,” *Astroparticle Physics*, vol. 35, no. 9, pp. 573–590, 2012.
- [101] E. Aprile *et al.*, “Dark Matter Results from 225 Live Days of XENON100 Data,” *Physical Review Letters*, vol. 109, p. 181301, 2012.
- [102] E. Aprile *et al.*, “Dark Matter Search Results from a One Ton-Year Exposure of XENON1T,” *Phys. Rev. Lett.*, vol. 121, p. 111302, 2018.
- [103] Y. Meng *et al.*, “Dark Matter Search Results from the PandaX-4T Commissioning Run,” *Phys. Rev. Lett.*, vol. 127, p. 261802, 2021.
- [104] E. Aprile *et al.*, “First Dark Matter Search with Nuclear Recoils from the XENONnT Experiment,” *Phys. Rev. Lett.*, vol. 131, p. 041003, 2023.
- [105] D. Akerib *et al.*, “Projected WIMP Sensitivity of the LUX-ZEPLIN Dark Matter Experiment,” *Phys. Rev. D*, vol. 101, p. 052002, 2020.
- [106] L. Baudis, “DARWIN Dark Matter WIMP Search with Noble Liquids,” *Journal of Physics: Conference Series*, vol. 375, no. 1, p. 012028, 2012.
- [107] J. Aalbers *et al.*, “The XLZD Design Book: Towards the Next-Generation Liquid Xenon Observatory for Dark Matter and Neutrino Physics,” *arXiv-2410.17137*, <https://arxiv.org/abs/2410.17137>, 2024.
- [108] J. Aalbers *et al.*, “A Next-generation Liquid Xenon Observatory for Dark Matter and Neutrino Physics,” *Journal of Physics G: Nuclear and Particle Physics*, vol. 50, no. 1, p. 013001, 2022.
- [109] D. Akerib, “LUX, ZEPLIN and LUX-ZEPLIN: Developments in Liquid Xenon Detectors and the Search for WIMP Dark Matter,” *Nuclear Physics B*, vol. 1003, p. 116437, 2024.
- [110] L. Votano, “The Gran Sasso Laboratory,” *The European Physical Journal Plus*, vol. 127, no. 109, 2012.
- [111] G. Alner *et al.*, “First Limits on Nuclear Recoil Events from the ZEPLIN I Galactic Dark Matter Detector,” *Astroparticle Physics*, vol. 23, no. 5, pp. 444–462, 2005.
- [112] B. Mount *et al.*, “LUX-ZEPLIN (LZ) Technical Design Report,” *arXiv-1703.09144*, <https://arxiv.org/abs/1703.09144>, 2017.

- [113] J. Heise, “The Sanford Underground Research Facility,” *Journal of Physics: Conference Series*, vol. 2156, no. 1, p. 012172, 2021.
- [114] J. Aalbers *et al.*, “First Dark Matter Search Results from the LUX-ZEPLIN (LZ) Experiment,” *Physical Review Letters*, vol. 131, no. 4, 2023.
- [115] D. Akerib *et al.*, “Identification of Radiopure Titanium for the LZ Dark Matter Experiment and Future Rare Event Searches,” *Astroparticle Physics*, vol. 96, pp. 1–10, 2017.
- [116] C. Faham *et al.*, “Measurements of Wavelength-dependent Double Photoelectron Emission from Single Photons in VUV-sensitive Photomultiplier Tubes,” *Journal of Instrumentation*, vol. 10, no. 09, p. P09010, 2015.
- [117] V. Solovov *et al.*, “Position Reconstruction in a Dual Phase Xenon Scintillation Detector,” *IEEE Transactions on Nuclear Science*, vol. 59, no. 6, pp. 3286–3293, 2012.
- [118] E. Aprile and L. Baudis, *Particle dark matter : observations, models and searches: Liquid Noble Gases*. Cambridge University Press, 2010.
- [119] E. Aprile and T. Doke, “Liquid Xenon Detectors for Particle Physics and Astrophysics,” *Reviews of Modern Physics*, vol. 82, pp. 2053–2097, 2010.
- [120] M. Szydagis *et al.*, “A Review of Basic Energy Reconstruction Techniques in Liquid Xenon and Argon Detectors for Dark Matter and Neutrino Physics Using NEST,” *Instruments*, vol. 5, no. 13, 2021.
- [121] J. Lindhard, V. Nielsen, M. Scharff, and P. Thomsen, “Integral Equations Governing Radiation Effects (Notes on Atomic Collisions III),” *Kgl. Danske Videnskab., Selskab. Mat. Fys. Medd.*, vol. 33, no. 10, 1963.
- [122] S. Haselschwardt *et al.*, “A Liquid Scintillation Detector for Radioassay of Gadolinium-loaded Liquid Scintillator for the LZ Outer Detector,” *Nuclear Instruments and Methods in Physics Research Section A: Accelerators, Spectrometers, Detectors and Associated Equipment*, vol. 937, pp. 148–163, 2019.
- [123] W. Turner *et al.*, “Optical Calibration System for the LUX-ZEPLIN (LZ) Outer Detector,” *Nuclear Instruments and Methods in Physics Research Section A: Accelerators, Spectrometers, Detectors and Associated Equipment*, vol. 1010, p. 165551, 2021.
- [124] D. Akerib *et al.*, “Measurement of the Gamma Ray Background in the Davis Cavern at the Sanford Underground Research Facility,” *Astroparticle Physics*, vol. 116, p. 102391, 2020.

- [125] R. Linehan *et al.*, “Design and Production of the High Voltage Electrode Grids and Electron Extraction Region for the LZ Dual-phase Xenon Time Projection Chamber,” *Nuclear Instruments and Methods in Physics Research Section A: Accelerators, Spectrometers, Detectors and Associated Equipment*, vol. 1031, p. 165955, 2022.
- [126] J. Aalbers *et al.*, “Dark Matter Search Results from 4.2 Tonne-Years of Exposure of the LUX-ZEPLIN (LZ) Experiment,” *arXiv-2410.17036*, <https://arxiv.org/abs/2410.17036>, 2024.
- [127] M. Arthurs *et al.*, “Performance Study of Charcoal-based Radon Reduction Systems for Ultraclean Rare Event Detectors,” *Journal of Instrumentation*, vol. 16, no. 07, p. P07047, 2021.
- [128] A. Dobi *et al.*, “Study of a Zirconium Getter for Purification of Xenon Gas,” *Nuclear Instruments and Methods in Physics Research Section A: Accelerators, Spectrometers, Detectors and Associated Equipment*, vol. 620, no. 2, pp. 594–598, 2010.
- [129] N. Stojilovic, E. Bender, and R. Ramsier, “Surface Chemistry of Zirconium,” *Progress in Surface Science*, vol. 78, no. 3, pp. 101–184, 2005.
- [130] R. Myers and D. Pryor, “An Empirical Explanation of Boiling Temperatures for Nonpolar Liquids Including Noble Gases and Selected Tetrahedrals,” *Monatshefte für Chemie - Chemical Monthly*, vol. 143, p. 557–561, 2012.
- [131] J. Aalbers *et al.*, “The Data Acquisition System of the LZ Dark Matter Detector: FADR,” *Nuclear Instruments and Methods in Physics Research Section A: Accelerators, Spectrometers, Detectors and Associated Equipment*, vol. 1068, p. 169712, 2024.
- [132] D. Akerib *et al.*, “Data Acquisition and Readout System for the LUX Dark Matter Experiment,” *Nuclear Instruments and Methods in Physics Research Section A: Accelerators, Spectrometers, Detectors and Associated Equipment*, vol. 668, pp. 1–8, 2012.
- [133] J. Aalbers *et al.*, “The Design, Implementation, and Performance of the LZ Calibration Systems,” *Journal of Instrumentation*, vol. 19, no. 08, p. P08027, 2024.
- [134] A. Sazzad *et al.*, “Design and Characterization of AmLi Neutron Sources for the LZ Experiment,” *Journal of Instrumentation*, vol. 18, no. 05, p. P05006, 2023.
- [135] H. Ito *et al.*, “Analyzing the Neutron and γ Emission Properties of an Americium–beryllium Tagged Neutron Source,” *Nuclear Instruments and Methods in Physics Research Section A: Accelerators, Spectrometers, Detectors and Associated Equipment*, vol. 1057, p. 168701, 2023.

- [136] J. Vainionpaa, “Technology and Applications of Neutron Generators Developed by Adelphi Technology, Inc,” *Physics Procedia*, vol. 60, pp. 203–211, 2014.
- [137] J. Verbus, “Proposed Low-energy Absolute Calibration of Nuclear Recoils in a Dual-phase Noble Element TPC using D-D Neutron Scattering Kinematics,” *Nuclear Instruments and Methods in Physics Research Section A: Accelerators, Spectrometers, Detectors and Associated Equipment*, vol. 851, pp. 68–81, 2017.
- [138] M. Fuller *et al.*, “Long-lifetime High-yield Neutron Generators Using the DD Reaction,” *International Atomic Energy Agency*, 2010.
- [139] D. Akerib *et al.*, “Low-energy (0.7-74 keV) Nuclear Recoil Calibration of the LUX Dark Matter Experiment using D-D Neutron Scattering Kinematics,” *arXiv-1608.05381*, <https://arxiv.org/abs/1608.05381>, 2016.
- [140] D. Akerib *et al.*, “Simulations of Events for the LUX-ZEPLIN (LZ) Dark Matter Experiment,” *Astroparticle Physics*, vol. 125, p. 102480, 2021.
- [141] M. Szydagis *et al.*, “Noble Element Simulation Technique,” <https://zenodo.org/records/8215927>, version 2.4.0, 2023.
- [142] M. Szydagis *et al.*, “NEST: a Comprehensive Model for Scintillation Yield in Liquid Xenon,” *Journal of Instrumentation*, vol. 6, no. 10, p. P10002, 2011.
- [143] M. Szydagis *et al.*, “Enhancement of NEST Capabilities for Simulating Low-energy Recoils in Liquid Xenon,” *Journal of Instrumentation*, vol. 8, no. 10, p. C10003, 2013.
- [144] NEST, “NEST Benchmark plots: Xenon,” <https://nest.physics.ucdavis.edu/benchmark-plots>, 2024, accessed 24/10/2024.
- [145] S. Agostinelli *et al.*, “Geant4—a Simulation Toolkit,” *Nuclear Instruments and Methods in Physics Research Section A: Accelerators, Spectrometers, Detectors and Associated Equipment*, vol. 506, no. 3, pp. 250–303, 2003.
- [146] J. Allison *et al.*, “Recent Developments in Geant4,” *Nuclear Instruments and Methods in Physics Research Section A: Accelerators, Spectrometers, Detectors and Associated Equipment*, vol. 835, pp. 186–225, 2016.
- [147] D. Akerib *et al.*, “The LUX-ZEPLIN (LZ) Radioactivity and Cleanliness Control Programs,” *The European Physics Journal C*, vol. 80, no. 1044, 2020.
- [148] V. Kudryavtsev, “Expected Background in the LZ Experiment,” *AIP Conference Proceedings*, vol. 1672, no. 1, p. 060003, 2015.

- [149] R. Firestone and L. Ekström, “WWW Table of Radioactive Isotopes, LBNL Isotopes Project, version 2.1,” <https://web.archive.org/web/20150701215057/http://ie.lbl.gov/toi/index.asp>, 2004, accessed 13/03/2025.
- [150] J. Aalbers *et al.*, “Background Determination for the LUX-ZEPLIN Dark Matter Experiment,” *Phys. Rev. D*, vol. 108, p. 012010, 2023.
- [151] Rad Elec Inc., “Radon Decay Products,” <https://www.radelec.com/radondecay.html>, accessed 14/03/2025.
- [152] D. Akerib *et al.*, “Investigation of Background Electron Emission in the LUX Detector,” *Phys. Rev. D*, vol. 102, p. 092004, 2020.
- [153] M. Abdullah *et al.*, “Coherent Elastic Neutrino-Nucleus Scattering: Terrestrial and Astrophysical Applications,” 2022.
- [154] D. Akimov *et al.*, “Observation of Coherent Elastic Neutrino-nucleus Scattering,” *Science*, vol. 357, no. 6356, p. 1123–1126, 2017.
- [155] M. Agostini *et al.*, “Simultaneous Precision Spectroscopy of pp , ${}^7\text{Be}$, and pep Solar Neutrinos with Borexino Phase-II,” *Phys. Rev. D*, vol. 100, p. 082004, 2019.
- [156] N. Vinyoles *et al.*, “A New Generation of Standard Solar Models,” *The Astrophysical Journal*, vol. 835, no. 2, p. 202, 2017.
- [157] B. Aharmim *et al.*, “Combined Analysis of all Three Phases of Solar Neutrino Data from the Sudbury Neutrino Observatory,” *Phys. Rev. C*, vol. 88, p. 025501, 2013.
- [158] D. Baxter *et al.*, “Recommended Conventions for Reporting Results from Direct Dark Matter Searches,” *The European Physical Journal C*, vol. 81, no. 907, 2021.
- [159] J. Billard, E. Figueroa-Feliciano., and L. Strigari, “Implication of Neutrino Backgrounds on the Reach of Next Generation Dark Matter Direct Detection Experiments,” *Physical review. D*, vol. 89, no. 2, 2014.
- [160] S. Vahsen *et al.*, “CYGNUS: Feasibility of a Nuclear Recoil Observatory with Directional Sensitivity to Dark Matter and Neutrinos,” *arXiv-2008.12587*, <https://arxiv.org/abs/2008.12587>, 2020.
- [161] P. Grothaus, M. Fairbairn, and J. Monroe, “Directional Dark Matter Detection Beyond the Neutrino Bound,” *Physical Review D*, vol. 90, p. 055018, 2014.
- [162] P. Smith *et al.*, “Observation of Nuclear Recoil Events from Neutron Scattering in Low Temperature Calorimetric Detectors,” *Physics Letters B*, vol. 255, no. 3, pp. 454–458, 1991.

- [163] M. Carson *et al.*, “Neutron Background in Large-scale Xenon Detectors for Dark Matter Searches,” *Astroparticle Physics*, vol. 21, no. 6, pp. 667–687, 2004.
- [164] V. Kudryavtsev, P. Zakhary, and B. Easeman, “Neutron Production in (α, n) Reactions,” *Nuclear Instruments and Methods in Physics Research Section A: Accelerators, Spectrometers, Detectors and Associated Equipment*, vol. 972, p. 164095, 2020.
- [165] S. Dowdy, S. Wearden, and D. Chilko, *Statistics for Research*. John Wiley & Sons inc., 3rd ed., 2004.
- [166] E. Artin, *The Gamma Function*. Athena series. selected topics in mathematics, Holt, Reinhart Winston, 1964.
- [167] D. Akerib *et al.*, “Signal Yields, Energy Resolution, and Recombination Fluctuations in Liquid Xenon,” *Physical Review D*, vol. 95, p. 012008, 2017.
- [168] R. Ajaj *et al.*, “Search for dark matter with a 231-day exposure of liquid argon using DEAP-3600 at SNOLAB,” *Phys. Rev. D*, vol. 100, p. 022004, 2019.
- [169] P. Sorensen, “Electron Train Backgrounds in Liquid Xenon Dark Matter Search Detectors are Indeed Due to Thermalization and Trapping,” *arXiv-1702.04805*, <https://arxiv.org/abs/1702.04805>, 2017.

Appendices

Appendix A

$\Delta\chi^2$ Method Technical Details

There are two versions of the $\Delta\chi^2$ analysis, introduced in chapter 3 and used in chapters 4-6, that allow it to be run either in a python Jupyter Notebook or in C++. The WS2022 and WS2024 versions of both of these scripts can be found at https://gitlab.com/luxzeplin/users/jorpwood1/ms_neutron_delta_chi-squared.git. This appendix will give the technical details required for running this code for the benefit of future work.

A.1 Python

The python implementation of this code for both WS2022 and WS2024 is written in a Jupyter Notebook and requires, as an input, a ROOT file of events containing an ‘ms’ tree with S1c and S2c vectors (S1c is a vector due to corrections for each of the different drift times). The S2c-averaged S1c value is used in this analysis:

```
avg_S1, tot_S2 = 0., 0.  
for j in range(Scatters):  
    avg_S1 += S1s[j] * S2s[j]  
    tot_S2 += S2s[j]
```

```
avg_S1 /= tot_S2
```

Some constants for the analysis need to be defined. Specifically:

$$W = 13.5/1000$$

For WS2022:

$$g1 = 0.1136$$

$$g2 = 47.07$$

$$SE = 58.5$$

For WS2024:

$$g1 = 0.1122$$

$$g2 = 34.09$$

Initial scatter energy estimates are made for all events with both the NR and ER hypotheses. This is done by assuming S1 light is apportioned across the scatters in the same ratio as the S2 light:

$$\text{Est_event_energies_er} = W * ((((S2s/tot_S2)*avg_S1) / g1) + (S2s / g2))$$

For WS2022:

$$\text{Est_event_energies_nr} = (((((S2s/tot_S2)*avg_S1) / g1) + (S2s / g2)) / 11)**(1/1.1)$$

For WS2024:

$$\text{Est_event_energies_nr} = (((((S2s/tot_S2)*avg_S1) / g1) + (S2s / g2)) / 11)**(1/1.1)$$

Values taken from the NEST NR and ER charge and light yield curves (Figure 2.14) are loaded in (not included in full here as they are long lists):

For WS2022:

$$\text{ERLYEnergy} = [0.09891080977945985, 0.5342015120612374, \dots]$$

$$\text{ERLY} = [0.13861386138613863, 0.27722772277227725, \dots]$$

$$\text{ERCYEnergy} = [0.12304030339927341, 0.1513891626058525, \dots]$$

$$\text{ERCY} = [80.3076923076923, 80, 79.6923076923077, \dots]$$

$$\text{NRLYEnergy} = [0.09917711784736, 0.21036162024716162, \dots]$$

$$\text{NRLY} = [0.03264925373134328, 0.06529850746268656, \dots]$$

$$\text{NRCYEnergy} = [0.1048678107958792, 0.2089075464428825, \dots]$$

$$\text{NRCY} = [0.01593625498007968, 0.03187250996015936, \dots]$$

For WS2024:

$$\text{ERLYEnergy} = [0.10196211844775045, 0.11457023135101989, \dots]$$

$$\text{ERLY} = [0, 0, \dots]$$

$$\text{ERCYEnergy} = [0.1029449409541541, 0.12371917026384399, \dots]$$

$$\text{ERCY} = [79.59044211300905, 79.59044211300905, \dots]$$

$$\text{NRLYEnergy} = [0.11244893869618479, 0.12552379393680851, \dots]$$

$$\text{NRLY} = [0, 0, \dots]$$

$$\text{NRCYEnergy} = [0.10070449361523451, 0.11188723796714249, \dots]$$

$$\text{NRCY} = [0, 0, \dots]$$

The values taken are extrapolated to give continuous curves:

```

y_interpERLY = scipy.interpolate.interp1d(ERLYEnergy, ERLY, kind='linear',
bounds_error=False, fill_value='extrapolate', axis=0)
y_interpERCY = scipy.interpolate.interp1d(ERCYEnergy, ERCY, kind='linear',
bounds_error=False, fill_value='extrapolate', axis=0)
y_interpNRLY = scipy.interpolate.interp1d(NRLYEnergy, NRLY, kind='linear',
bounds_error=False, fill_value='extrapolate', axis=0)
y_interpNRCY = scipy.interpolate.interp1d(NRCYEnergy, NRCY, kind='linear',
bounds_error=False, fill_value='extrapolate', axis=0)

```

Functions are defined to find S1c and S2c from these curves, given the scatter energies ('newE'):

```

def lineER(N_index,*newE):
    totalS1 = 0.0
    everyS2 = np.zeros([len(newE[0])])
    for i in range(len(newE[0])):
        S2 = g2 * newE[0][i] * y_interpERCY(newE[0][i])
        S1 = g1 * newE[0][i] * y_interpERLY(newE[0][i])
        totalS1 += S1
        everyS2[i] = S2
    totalS1 = np.array([totalS1])
    return np.concatenate((totalS1, everyS2))

def lineNR(N_index,*newE):
    totalS1 = 0.0
    everyS2 = np.zeros([len(newE[0])])
    for i in range(len(newE[0])):
        S2 = g2 * newE[0][i] * y_interpNRCY(newE[0][i])
        S1 = g1 * newE[0][i] * y_interpNRLY(newE[0][i])
        totalS1 += S1
        everyS2[i] = S2
    totalS1 = np.array([totalS1])
    return np.concatenate((totalS1, everyS2))

```

Define χ^2 . For WS2024 the covariance matrix used in the definition of χ^2 also needs to be defined, along with the curves used to characterise $\sigma_m(S1)$, $\sigma_m(S2)$, and σ_c shown in section 3.3.1:

For WS2022:

```

def chi2(data1, data2, error):

```

```

chi2 = 0
for i in range(len(data1)):
    chi2_i = ((data1[i] - data2[i])**2) / (error[i]**2)
    chi2 += chi2_i
return chi2

```

For WS2024:

```

abc1 = [1.2737603636892538, 0.028944856249924045, -0.014800122087204612]
mc3 = [0.10439930782190743, 0.0005438817430916676]

```

```

def S1Sigma_m(S1):
    return S1 * math.sqrt( ( abc1[0] / math.sqrt(S1) )**2
        + (abc1[1] / S1)**2 + abc1[2]**2)

```

```

def S2Sigma_m(S2):
    return 0

```

```

def Sigma_c(S2):
    return mc3[0] * math.sqrt(S2 / g2) + (mc3[1] * (S2 / g2))

```

```

def CalcInvCovMat(N, S1, S2s, NR):

```

```

    CovMat = np.zeros([N+1, N+1])
    for diag in range(N+1):
        if diag == 0:
            CovMat[diag][diag] = (S1Sigma_m(S1) / g1)**2
            for scat in range(N):
                CovMat[diag][diag] += (Sigma_c(S2s[scat]) / W)**2
        else:
            CovMat[diag][diag] = (S2Sigma_m(S2s[diag-1]) / g2)**2
                + (Sigma_c(S2s[diag-1]) / W)**2

```

```

    if NR == False:
        for cols in range(N):
            CovMat[0][cols+1] = -(Sigma_c(S2s[cols]) / W)**2
        for rows in range(N):
            CovMat[rows+1][0] = -(Sigma_c(S2s[rows]) / W)**2

```

```

InvCovMat = np.linalg.inv(CovMat)
return InvCovMat

```

```

class CorrLeastSquares:

```

```

    """

```

```

    Chi-Squared cost function for dealing with S1 and S2 correlation.

```

```

    """

```

```

    errordef = Minuit.LEAST_SQUARES # for Minuit to compute errors correctly

```

```

    def __init__(self, model, x, y, ICM):

```

```

        self.model = model

```

```

        self.x = np.asarray(x)

```

```

        self.y = np.asarray(y)

```

```

        self.ICM = np.asarray(ICM)

```

```

    def __call__(self, *par):

```

```

        ym = self.model(self.x, *par)

```

```

        Scatters = len(self.x) - 1

```

```

        yvec = np.array([self.y - ym])

```

```

        yvec[0][0] /= g1

```

```

        for s2 in range(1, len(yvec[0])):

```

```

            yvec[0][s2] /= g2

```

```

        yvectrans = np.transpose(yvec)

```

```

        return np.matmul(np.matmul(yvec, self.ICM), yvectrans)

```

```

    def CorrChi2(data1, data2, ICM):

```

```

        ym = data2

```

```

        yvec = np.array([data1 - ym])

```

```

        yvec[0][0] /= g1

```

```

        for s2 in range(1, len(yvec[0])):

```

```

            yvec[0][s2] /= g2

```

```
yvectrans = np.transpose(yvec)
```

```
return np.matmul(np.matmul(yvec, ICM), yvectrans)
```

The $\Delta\chi^2$ analysis is now ready to be run over events. This requires the estimated NR energies as ‘NREnergies’, the estimated ER energies as ‘EREnergies’, where each entry is a list of scatter energies for that event. Also required is the S1 and S2 data for the event in the format of $[S1c_{avg}, S2c_1, S2c_2, \dots, S2c_N]$ for an N scatter event. Each entry in ‘goodlist’, corresponding to each event, should be in this format.

```
datalength = len(everyS1avg)
```

```
print("Running over", str(datalength), "events")
```

```
AllChiDiffs, AlltotNREnergies = [], []
```

```
for data in tqdm(range(datalength)):
```

```
    Scatters = len(goodlist[data]) - 1
```

```
    everyS1er, everyS2er, everyEer = [], [], []
```

Calculate the initial estimates for S1c and the S2cs for both of the ER and NR models:

```
    for i in range(Scatters):
```

```
        Eer = EREnergies[data][i]
```

```
        S2 = g2 * Eer * y_interpERCY(Eer)
```

```
        S1 = g1 * Eer * y_interpERLY(Eer)
```

```
        everyS1er.append(S1)
```

```
        everyS2er.append(S2)
```

```
        everyEer.append(Eer)
```

```
tot_S1er = 0.0
```

```
for j in range(len(everyS1er)):
```

```
    tot_S1er += everyS1er[j]
```

```
tot_S1er = [tot_S1er]
```

```
NESTer_data = tot_S1er + everyS2er
```

```

everyS1nr , everyS2nr , everyEnr = [] , [] , []

for i in range(Scatters):
    Enr = NREnergies[data][i]
    S2 = g2 * Enr * y_interpNRCY(Enr)
    S1 = g1 * Enr * y_interpNRLY(Enr)

    everyS1nr.append(S1)
    everyS2nr.append(S2)
    everyEnr.append(Enr)

tot_S1nr = 0.0
for j in range(len(everyS1nr)):
    tot_S1nr += everyS1nr[j]

tot_S1nr = [tot_S1nr]
NESTnr_data = tot_S1nr + everyS2nr

```

Calculate errors and run least squares fits using Minuit:

For WS2022:

```

N_index = np.linspace(0, Scatters, Scatters+1)
a = 1.0
b = 1.0

y_err = [a*math.sqrt(goodlist[data][0])]
for j in range(Scatters):
    y_err.append(b*(1 / math.sqrt(goodlist[data][j+1]/SE))
                *goodlist[data][j+1])

least_squaresER = LeastSquares(N_index, goodlist[data],
                                y_err, lineER)
mer = Minuit(least_squaresER, everyEer)
parlim = []
for i in range(Scatters):
    parlim.append((min(ERCYEnergy), max(ERCYEnergy)))
mer.limits = parlim

```

```

mer.migrad()
mer.hesse()

least_squaresNR = LeastSquares(N_index, goodlist[data],
                                y_err, lineNR)
mnr = Minuit(least_squaresNR, everyEnr)
parlim = []
for i in range(Scatters):
    parlim.append((min(NRCYEnergy), max(NRCYEnergy)))
mnr.limits = parlim
mnr.migrad()
mnr.hesse()

```

For WS2024:

```

N_index = np.linspace(0, Scatters, Scatters+1)
InvCovMatER = CalcInvCovMat(Scatters, goodlist[data][0],
                             goodlist[data][1:Scatters+1], False)
InvCovMatNR = CalcInvCovMat(Scatters, goodlist[data][0],
                             goodlist[data][1:Scatters+1], True)

least_squaresER = CorrLeastSquares(lineER, N_index,
                                    goodlist[data], InvCovMatER)
mer = Minuit(least_squaresER, everyEer)
parlim = []
for i in range(Scatters):
    parlim.append((0, None))
mer.limits = parlim
mer.migrad()
mer.hesse()

least_squaresNR = CorrLeastSquares(lineNR, N_index,
                                    goodlist[data], InvCovMatNR)
mnr = Minuit(least_squaresNR, everyEnr)
parlim = []
for i in range(Scatters):
    parlim.append((0, None))
mnr.limits = parlim

```

```
mnr.migrad()
mnr.hesse()
```

Calculate final values of $\Delta\chi^2$ and the total fitted NR energies:

For WS2022:

```
ER_NEST_data = lineER(N_index, mer.values)
ER_chi2 = chi2(goodlist[data], ER_NEST_data, y_err)

NR_NEST_data = lineNR(N_index, mnr.values)
NR_chi2 = chi2(goodlist[data], NR_NEST_data, y_err)

chiDiff_i = NR_chi2 - ER_chi2
AllChiDiffs.append(chiDiff_i)
AlltotNREnergies.append(sum(mnr.values))
```

For WS2024:

```
ER_NEST_data = lineER(N_index, mer.values)
ER_chi2 = CorrChi2(goodlist[data], ER_NEST_data,
                  InvCovMatER)

NR_NEST_data = lineNR(N_index, mnr.values)
NR_chi2 = CorrChi2(goodlist[data], NR_NEST_data,
                  InvCovMatNR)

chiDiff_i = NR_chi2[0][0] - ER_chi2[0][0]
NRChis.append(NR_chi2[0][0])
ERChis.append(ER_chi2[0][0])
AllChiDiffs.append(chiDiff_i)
AlltotNREnergies.append(sum(mnr.values))
```

A.2 C++

The C++ implementation of the $\Delta\chi^2$ analysis broadly follows the same structure and logic as the Python implementation (where possible the same variable notation was used in both implementations to minimise confusion), but required the definition of some additional functions. Firstly,

checking if an event is in the $\Delta\chi^2$ NR band:

```

bool NRBandChecker(double dchi2, double enrtot){

bool NRBandPass = false;
vector<double> bincenters = NRBanddata.at(0);
vector<double> means = NRBanddata.at(1);
vector<double> widths = NRBanddata.at(2);
vector<double> widths2 = NRBanddata.at(3);

vector<double> top(means.size()); vector<double> bottom(means.size());
std::transform (means.begin(), means.end(), widths2.begin(),
    top.begin(), std::plus<double>());
std::transform (means.begin(), means.end(), widths.begin(),
    bottom.begin(), std::minus<double>());

double thresh = 10000;
int close_index = 0;
double finDiff;
for (int j = 0; j < bincenters.size(); j++){
    double Ediff = enrtot - bincenters.at(j);
    if (abs(Ediff) < thresh){thresh = abs(Ediff); close_index = j;
        finDiff = Ediff;}
}
int secclose_index;
if (finDiff > 0.){secclose_index = close_index + 1;}
else if (finDiff < 0.){secclose_index = close_index - 1;}

double EFrac = (enrtot - bincenters[close_index]) /
    (bincenters[secclose_index] - bincenters[close_index]);
double Chitop = top[close_index] + (EFrac *
    (top[secclose_index] - top[close_index]));
double Chibottom = bottom[close_index] + (EFrac *
    (bottom[secclose_index] - bottom[close_index]));

if (dchi2 > Chibottom && dchi2 < Chitop &&
    enrtot > 12 && enrtot < bincenters.at(bincenters.size()-1)){
    NRBandPass = true;}

```

```
return NRBandPass;
}
```

Calculate S1 and S2 from the NEST curves:

```
vector<vector<double>>
  QLCalc(vector<double> newE, bool NR, int Scatters){

  vector<double> LYEnergy; vector<double> CYEnergy;
  vector<double> LY; vector<double> CY;
  if (!NR){LYEnergy = ERLYEnergy; CYEnergy = ERCYEnergy;
    LY = ERLY; CY = ERCY;}
  if (NR){LYEnergy = NRLYEnergy; CYEnergy = NRCYEnergy;
    LY = NRLY; CY = NRCY;}

  std::vector<double> everyS1; std::vector<double> everyS2;

  for (int i = 0; i < Scatters; i++){

    std::vector<double> LYEnergy_nearest;
    std::vector<double> LY_nearest;
    std::vector<double> CYEnergy_nearest;
    std::vector<double> CY_nearest;
    double LYEn_thresh = 10000; double CYEn_thresh = 10000;
    int LYEn_index = 0; int CYEn_index = 0;

    for (int j = 0; j < LYEnergy.size(); j++){
      double LYdiff = abs(newE[i] - LYEnergy[j]);
      if (LYdiff < LYEn_thresh){LYEn_thresh = LYdiff;
        LYEn_index = j;}
    }
    for (int j = 0; j < CYEnergy.size(); j++){
      double CYdiff = abs(newE[i] - CYEnergy[j]);
      if (CYdiff < CYEn_thresh){CYEn_thresh = CYdiff;
        CYEn_index = j;}
    }
  }
}
```

```

if (LYEnergy[LYEn_index] < newE[i]){
    LYEnergy_nearest.push_back(LYEnergy[LYEn_index]);
    if (LYEnergy[LYEn_index] == LYEnergy[(LYEn_index+1)]){
        LYEnergy_nearest.push_back(LYEnergy[(LYEn_index + 2)]);}
    else {LYEnergy_nearest.push_back(LYEnergy[(LYEn_index + 1)]);}
    LY_nearest.push_back(LY[LYEn_index]);
    LY_nearest.push_back(LY[LYEn_index + 1]);}
else {
    LYEnergy_nearest.push_back(LYEnergy[LYEn_index - 1]);
    LYEnergy_nearest.push_back(LYEnergy[LYEn_index]);
    LY_nearest.push_back(LY[LYEn_index - 1]);
    LY_nearest.push_back(LY[LYEn_index]);}
if (CYEnergy[CYEn_index] < newE[i]){
    CYEnergy_nearest.push_back(CYEnergy[CYEn_index]);
    CYEnergy_nearest.push_back(CYEnergy[CYEn_index + 1]);
    CY_nearest.push_back(CY[CYEn_index]);
    CY_nearest.push_back(CY[CYEn_index + 1]);}
else {
    CYEnergy_nearest.push_back(CYEnergy[CYEn_index - 1]);
    CYEnergy_nearest.push_back(CYEnergy[CYEn_index]);
    CY_nearest.push_back(CY[CYEn_index - 1]);
    CY_nearest.push_back(CY[CYEn_index]);}

double LYfrac = (newE[i] - LYEnergy_nearest[0]) /
    (LYEnergy_nearest[1] - LYEnergy_nearest[0]);
double L = LY_nearest[0] + (LYfrac * ((LY_nearest[1] -
    LY_nearest[0])));
double CYfrac = (newE[i] - CYEnergy_nearest[0]) /
    (CYEnergy_nearest[1] - CYEnergy_nearest[0]);
double C = CY_nearest[0] + (CYfrac * ((CY_nearest[1] -
    CY_nearest[0])));

double E = newE[i];
double S2 = g2 * E * C;
double S1 = g1 * E * L;

everyS1.push_back(S1); everyS2.push_back(S2);

```

```

}

vector<vector<double>> S1S2;
S1S2.push_back(everyS1);
S1S2.push_back(everyS2);

return S1S2;
}

```

Calculate total S1 and S2s from the scatter energies, using the previous function:

```

vector<double>
lineERNR(vector<double> newE, int Scatters, bool NR){

double totalS1 = 0.0;
vector<double> data;
vector<vector<double>> S1sS2s = QLCalc(newE, NR, Scatters);
vector<double> S1s = S1sS2s[0];
vector<double> S2s = S1sS2s[1];

for (int i = 0; i < Scatters; i++){
double S1 = S1s[i];
double S2 = S2s[i];
totalS1 += S1;
data.push_back(S2);}
data.insert(data.begin(), totalS1);
return data;
}

```

Calculate χ^2 for the NR model, for the ER model, and generally:

For WS2022:

```

void fcnNR(Int_t &npar, Double_t *gin,
Double_t &f, Double_t *par, Int_t iflag)
{
int Scatters = allScatters.at(Event_num);
bool NR = true;

```

```

vector<double> newE;
for (int i=0; i<Scatters; i++){newE.push_back(par[i]);}
vector<double> data = lineERNR(newE, Scatters, NR);

double chi2 = 0;
for (int i = 0; i < Scatters + 1; i++){
    double chi2_i = pow(allRealdata.at(Event_num).at(i) -
        data.at(i),2) / pow(ally_err.at(Event_num).at(i),2);
    chi2 += chi2_i;}

f = chi2;
}

void fcnER(Int_t &npar, Double_t *gin,
    Double_t &f, Double_t *par, Int_t iflag)
{
    int Scatters = allScatters.at(Event_num);
    bool NR = false;
    vector<double> newE;
    for (int i=0; i<Scatters; i++){newE.push_back(par[i]);}
    vector<double> data = lineERNR(newE, Scatters, NR);

    double chi2 = 0;
    for (int i = 0; i < Scatters + 1; i++){
        double chi2_i = pow(allRealdata.at(Event_num).at(i) -
            data.at(i),2) / pow(ally_err.at(Event_num).at(i),2);
        chi2 += chi2_i;}

    f = chi2;
}

double chi2(vector<double> realdata, vector<double> modeldata,
    vector<double> error)
{
    int Scatters = allScatters.at(Event_num);
    double chi2 = 0;
    for (int i = 0; i < Scatters + 1; i++){

```

```

    double chi2_i = pow(allRealdata.at(Event_num).at(i) -
        modeldata.at(i),2) / pow(ally_err.at(Event_num).at(i),2);
    chi2 += chi2_i;}
return chi2;
}

```

For WS2024:

Additional functions are needed here to define $\sigma_m(S1)$, $\sigma_m(S2)$, and σ_c , as well as to allow for matrix multiplication and subtraction:

```

double S1Sigma_m(double S1){
    return S1 * sqrt( pow(( abc1[0] / sqrt(S1) ), 2) +
        pow((abc1[1] / S1), 2) + pow(abc1[2], 2));
}

double S2Sigma_m(double S2){
    return 0;
}

double Sigma_c(double S2){
    return mc3[0] * sqrt(S2 / g2) + (mc3[1] * (S2 / g2));
}

vector<vector<double>>
MultMat(vector<vector<double>> Mat1, vector<vector<double>> Mat2){

    int N1_row = Mat1.size();
    int N1_col = Mat1.at(0).size();
    int N2_row = Mat2.size();
    int N2_col = Mat2.at(0).size();

    int Nprod_row = min(N1_row, N2_row);
    int Nprod_col = min(N1_col, N2_col);

    vector<vector<double>>
        ProdMat(Nprod_row, vector<double>(Nprod_col));
    for(int i = 0; i < Nprod_row; i++){

```

```

        for(int j = 0; j < Nprod_col; j++){
            ProdMat[i][j] = 0;
            for(int k = 0; k < N1_col; k++){
                ProdMat[i][j] += Mat1[i][k] * Mat2[k][j];
            }
        }
    }

    return ProdMat;

}

vector<double>
SubtractVect(vector<double> Vect1, vector<double> Vect2){

    int N = Vect1.size();
    vector<double> OutVect(N);
    for(int i = 0; i < N; i++){
        OutVect[i] = Vect1[i] - Vect2[i];
    }

    return OutVect;

}

void fcnNR(Int_t &npar, Double_t *gin,
           Double_t &f, Double_t *par, Int_t iflag){

    int Scatters = allScatters.at(Event_num);
    bool NR = true;
    vector<double> newE;
    for (int i=0; i<Scatters; i++){newE.push_back(par[i]);}

    vector<double> ym = lineERNR(newE, Scatters, NR);
    vector<double> y = allRealdata.at(Event_num);

    vector<double> yvec = SubtractVect(y, ym);

```

```

    yvec[0] /= g1;
    for (int s2=1; s2<yvec.size(); s2++){yvec[s2] /= g2;}
    vector<vector<double>> yvec_2d;
    yvec_2d.push_back(yvec);
    vector<vector<double>> yvectrans = transpose_vector(yvec_2d);

    vector<vector<double>>
        chi2 = MultMat(MultMat(yvec_2d, NRICM), yvectrans);

    f = chi2[0][0];
}

void fcnER(Int_t &npar, Double_t *gin,
    Double_t &f, Double_t *par, Int_t iflag){

    int Scatters = allScatters.at(Event_num);
    bool NR = false;
    vector<double> newE;
    for (int i=0; i<Scatters; i++){newE.push_back(par[i]);}
    vector<double> ym = lineERNR(newE, Scatters, NR);
    vector<double> y = allRealdata.at(Event_num);

    vector<double> yvec = SubtractVect(y, ym);
    yvec[0] /= g1;
    for (int s2=1; s2<yvec.size(); s2++){yvec[s2] /= g2;}
    vector<vector<double>> yvec_2d;
    yvec_2d.push_back(yvec);
    vector<vector<double>> yvectrans = transpose_vector(yvec_2d);

    vector<vector<double>>
        chi2 = MultMat(MultMat(yvec_2d, ERICM), yvectrans);

    f = chi2[0][0];
}

double chi2(vector<double> realdata, vector<double> modeldata,
    vector<vector<double>> ICM){

```

```

int Scatters = realdata.size() - 1;
vector<double> ym = modeldata;
vector<double> y = realdata;

vector<double> yvec = SubtractVect(y, ym);
yvec[0] /= g1;
for (int s2=1; s2<yvec.size(); s2++){yvec[s2] /= g2;}
vector<vector<double>> yvec_2d;
yvec_2d.push_back(yvec);
vector<vector<double>> yvectrans = transpose_vector(yvec_2d);

vector<vector<double>>
    chi2 = MultMat(MultMat(yvec_2d, ICM), yvectrans);
return chi2[0][0];
}

```

```

vector<vector<double>>
CalcInvCovMat(int N, double S1, vector<double> S2s, bool NR{

vector<vector<double>> CovMat(N+1, vector<double>(N+1));

for (int diag; diag < N+1; diag++){
    if (diag == 0){
        CovMat[diag][diag] = pow((S1Sigma_m(S1) / g1), 2);
        for (int scat=0; scat < N; scat++){CovMat[diag][diag]
            += pow((Sigma_c(S2s[scat]) / W), 2);}
    }
    else {CovMat[diag][diag] =
        pow((S2Sigma_m(S2s[diag-1]) / g2), 2) +
        pow((Sigma_c(S2s[diag-1]) / W), 2);}
}

if (NR == false){
    for (int cols=0; cols < N; cols++){CovMat[0][cols+1] =
        -pow((Sigma_c(S2s[cols]) / W), 2);}
}
}

```

```

    for (int rows=0; rows < N; rows++){CovMat[rows+1][0] =
        -pow((Sigma_c(S2s[rows]) / W), 2);}
}

```

```

TMatrixD TCovMat(N+1, N+1);
fillTMatrixFromVectors(CovMat, TCovMat);
TMatrixD TInvCovMat = TCovMat.Invert();
vector<vector<double>> InvCovMat(N+1, vector<double>(N+1));
GetVectorsfromMatrix(TInvCovMat, InvCovMat);

```

```

return InvCovMat;

```

```

}

```

With these functions defined, the $\Delta\chi^2$ analysis runs as follows:

```

vector<double> Realdata;
for (int i = 0; i < Scatters; i++){
Realdata.push_back( MS_S2c_all.at(i) );}
Realdata.insert( Realdata.begin(), MS_S1c );
allRealdata.push_back( Realdata );

std::vector<double> EREnergyEst;
std::vector<double> NREnergyEst;

for (int i = 0; i < Scatters; i++){
EREnergyEst.push_back(W * (
    ((( MS_S2c_all.at(i)/MS_S2c)*MS_S1c) / g1) +
    ( MS_S2c_all.at(i) / g2)));
NREnergyEst.push_back(pow(((
    ((( MS_S2c_all.at(i)/MS_S2c)*MS_S1c) / g1) +
    ( MS_S2c_all.at(i) / g2)) / 10.19), (1/1.11)));
}

std::vector<double> everyS1er; std::vector<double> everyS2er;
std::vector<double> everyS1nr; std::vector<double> everyS2nr;

vector<vector<double>> NRS1S2 =
    QLCalc(NREnergyEst, true, Scatters);
vector<vector<double>> ERS1S2 =

```

```

    QLCalc(EREnergyEst, false, Scatters);

double S1tot_er = 0; double S1tot_nr = 0;
for (int i = 0; i < Scatters; i++){
    S1tot_er += ERS1S2.at(0).at(i);
    S1tot_nr += NRS1S2.at(0).at(i);
}

std::vector<double> NESTER_data; std::vector<double> NESTNR_data;
NESTER_data.push_back(S1tot_er);
NESTNR_data.push_back(S1tot_nr);
for (int i = 0; i < Scatters; i++){
    NESTER_data.push_back(ERS1S2.at(1).at(i));
    NESTNR_data.push_back(NRS1S2.at(1).at(i));}

auto gNRMinuit = std::make_unique<TMinuit>(20);
gNRMinuit->SetFCN(fcnNR);
gNRMinuit->SetPrintLevel(-1);
Double_t NRarglist[10];
Int_t NRierflg = 0;

// Set starting values and step sizes for parameters
static vector<Double_t> NRstep;
for (int i=0; i<Scatters; i++){
    NRstep.push_back(0.1);
    std::string i_string = std::to_string(i);
    gNRMinuit->mnparm(i, "E"+i_string, NREnergyEst[i],
    NRstep[i], *min_element(NRCYEnergy.begin(), NRCYEnergy.end()),
    *max_element(NRCYEnergy.begin(), NRCYEnergy.end()), NRierflg);
}

// Now ready for minimization step
NRarglist[0] = 500;
gNRMinuit->mnexcm("MIGRAD", NRarglist, 1, NRierflg);
vector<double> Enr_out; vector<double> errnr_out;
double NRoutpar[Scatters], NRerr[Scatters];
for (int i=0; i<Scatters; i++){

```

```

    gNRMinuit->GetParameter(i, NRoutpar[i], NRerr[i]);
    Enr_out.push_back(NRoutpar[i]);
    errnr_out.push_back(NRerr[i]);}

//and again for ER.
auto gERMinuit = std::make_unique<TMinuit>(20);
gERMinuit->SetFCN(fcnER);
gERMinuit->SetPrintLevel(-1);
Double_t ERarglist[10];
Int_t ERierflg = 0;

// Set starting values and step sizes for parameters
static vector<Double_t> ERstep;
for (int i=0; i<Scatters; i++){
    ERstep.push_back(0.1);
    std::string i_string = std::to_string(i);
    gERMinuit->mnparm(i, "E"+i_string, EREnergyEst[i],
    ERstep[i], *min_element(ERCYEnergy.begin(), ERCYEnergy.end()),
    *max_element(ERCYEnergy.begin(), ERCYEnergy.end()), ERierflg);
}

// Now ready for minimization step
ERarglist[0] = 500;
gERMinuit->mnexcm("MIGRAD", ERarglist, 1, ERierflg);
vector<double> Eer_out; vector<double> errer_out;
double ERoutpar[Scatters], ERerr[Scatters];
for (int i=0; i<Scatters; i++){
    gERMinuit->GetParameter(i, ERoutpar[i], ERerr[i]);
    Eer_out.push_back(ERoutpar[i]);
    errer_out.push_back(ERerr[i]);}

vector<double> NRmodel = lineERNR(Enr_out, Scatters, true);
vector<double> ERmodel = lineERNR(Eer_out, Scatters, false)

```

For WS2022:

```

double NRChi2 = chi2(Realdata, NRmodel, y_err);
double ERChi2 = chi2(Realdata, ERmodel, y_err);
double DeltaChi2 = NRChi2 - ERChi2;

```

For WS2024:

```
ERICM = CalcInvCovMat(Scatters, MS_S1c, MS_S2c_all, false);
NRICM = CalcInvCovMat(Scatters, MS_S1c, MS_S2c_all, true);
double NRChi2 = chi2(Realdata, NRmodel, NRICM);
double ERChi2 = chi2(Realdata, ERmodel, ERICM);
double DeltaChi2 = NRChi2 - ERChi2;
```

Finally, calculate the total fitted NR energy and check if the event is in the MS NR band:

```
double totEnr = 0.;
for (int i=0; i<Scatters; i++){totEnr += Enr_out.at(i);}

bool InNRBand = NRBandChecker(DeltaChi2, totEnr);
```

Appendix B

Derivation of the $\sigma_m(\mathbf{S1})$, $\sigma_m(\mathbf{S2})$, and σ_c Equations

Equations 3.14-3.16 from section 3.3.1 are derived in this appendix. From Equation 2.1, the S1 and S2 components of energy can be defined as:

$$E = W \left(\frac{S1}{g_1} + \frac{S2}{g_2} \right) \equiv E_1 + E_2, \quad (\text{B.1})$$

hence:

$$E_1 = \frac{WS1}{g_1}, \quad E_2 = \frac{WS2}{g_2}. \quad (\text{B.2})$$

Similarly:

$$\sigma(E_1) = \frac{W\sigma(S1)}{g_1}, \quad \sigma(E_2) = \frac{W\sigma(S2)}{g_2}. \quad (\text{B.3})$$

Since $\sigma(E) \equiv \sigma(E_1) + \sigma(E_2)$:

$$\sigma^2(E) = \sigma^2(E_1) + \sigma^2(E_2) + 2\rho\sigma(E_1)\sigma(E_2), \quad (\text{B.4})$$

where ρ is the correlation coefficient of the E_1 and E_2 errors. Two components of the error are expected: an anti-correlated ($\rho = -1$) component due to recombination fluctuations at the recoil site, and an uncorrelated ($\rho = 0$) component due to the measurement of the S1 and S2 signals. These components are referred to as σ_c and σ_m respectively. σ_c is the same for E_1 and E_2 (and equivalently S1 and S2) since they are anti-correlated, but each has their own σ_m , denoted $\sigma_m(E_1)$ and $\sigma_m(E_2)$. These can of course be converted to S1 and S2 in the same manor as in Equation B.3. Therefore, using the same expansion as Equation B.4 for $\sigma_m(E_1)$ and $\sigma_m(E_2)$ with $\rho = 0$:

$$\sigma^2(E_1) = \sigma_c^2 + \sigma_m^2(E_1), \quad \sigma^2(E_2) = \sigma_c^2 + \sigma_m^2(E_2). \quad (\text{B.5})$$

It then follows that:

$$\begin{aligned}\sigma^2(E) &= \sigma_m^2(E_1) + \sigma_m^2(E_2) + 2\sigma_c^2 + 2\rho(\sigma_c + \sigma_m(E_1))(\sigma_c + \sigma_m(E_2)), \\ \sigma^2(E) &= \sigma_m^2(E_1) + \sigma_m^2(E_2) + 2\sigma_c^2 - 2\sigma_c^2, \\ \sigma^2(E) &= \sigma_m^2(E_1) + \sigma_m^2(E_2),\end{aligned}\tag{B.6}$$

so the overall energy width is simply the quadrature sum of the measurement component widths. Rearranging B.5 gives:

$$\sigma_c^2 = \sigma^2(E_1) - \sigma_m^2(E_1) = \sigma^2(E_2) - \sigma_m^2(E_2),\tag{B.7}$$

therefore:

$$\sigma^2(E_1) - \sigma^2(E_2) = \sigma_m^2(E_1) - \sigma_m^2(E_2)\tag{B.8}$$

Finally, combining Equations B.6, B.7, and B.8 the final expressions for $\sigma_m^2(E_1)$, $\sigma_m^2(E_2)$, and σ_c^2 are obtained:

$$\sigma_m^2(E_1) = \frac{1}{2}(\sigma^2(E) + \sigma^2(E_1) - \sigma^2(E_2)),\tag{B.9}$$

$$\sigma_m^2(E_2) = \frac{1}{2}(\sigma^2(E) - \sigma^2(E_1) + \sigma^2(E_2)),\tag{B.10}$$

$$\sigma_c^2 = \frac{1}{2}(\sigma^2(E_1) + \sigma^2(E_2) - \sigma^2(E)).\tag{B.11}$$